



HAL
open science

Two experiments on quantum correlations in gases of metastable helium: fermion antibunching and a study of boson pair correlations in the collision of two condensates

Valentina Krachmalnicoff

► **To cite this version:**

Valentina Krachmalnicoff. Two experiments on quantum correlations in gases of metastable helium: fermion antibunching and a study of boson pair correlations in the collision of two condensates. Atomic Physics [physics.atom-ph]. Université Paris Sud - Paris XI, 2009. English. NNT : . tel-00441654

HAL Id: tel-00441654

<https://pastel.hal.science/tel-00441654>

Submitted on 16 Dec 2009

HAL is a multi-disciplinary open access archive for the deposit and dissemination of scientific research documents, whether they are published or not. The documents may come from teaching and research institutions in France or abroad, or from public or private research centers.

L'archive ouverte pluridisciplinaire **HAL**, est destinée au dépôt et à la diffusion de documents scientifiques de niveau recherche, publiés ou non, émanant des établissements d'enseignement et de recherche français ou étrangers, des laboratoires publics ou privés.

LABORATOIRE CHARLES FABRY DE L'INSTITUT D'OPTIQUE

UNIVERSITE PARIS XI
U.F.R. SCIENTIFIQUE D'ORSAY

THESE

présentée pour obtenir

le GRADE DE DOCTEUR EN SCIENCES
DE L'UNIVERSITE PARIS XI

par

Valentina KRACHMALNICOFF

Sujet:

**DEUX EXPERIENCES DE CORRELATIONS QUANTIQUES
SUR DES GAZ DE HELIUM METASTABLE :
DEGROUPEMENT DE FERMIONS ET ETUDE DE PAIRES DE BOSONS
CORRELES PAR COLLISION DE CONDENSATS**

Soutenue le 22 Juin 2009 devant le jury composé de :

Mr. C. WESTBROOK	Directeur de thèse
Mr. J. DALIBARD	Rapporteur
Mme H. PERRIN	Rapporteur
Mr. P. GRANGIER	Examineur
Mr. M. INGUSCIO	Examineur
Mr. A. ASPECT	Membre invité
Mr. D. BOIRON	Membre invité

à Luigi et Anna

Remerciements

Ces travaux de thèse se sont déroulés au Laboratoire Charles Fabry de l'Institut d'Optique. Je remercie son directeur Pierre Chavel de m'y avoir accueilli et d'avoir suivi avec intérêt mon travail de recherche tout au long de mon doctorat.

Je remercie de tout coeur le directeur du groupe d'Optique Atomique Alain Aspect, mon directeur de thèse Chris Westbrook et le responsable de l'équipe Hélium Denis Boiron pour m'avoir donné la possibilité de vivre cette expérience très enrichissante, non seulement du point de vue scientifique mais aussi du pont de vue humain. J'ai eu la chance de pouvoir apprécier à plusieurs reprises les qualités pédagogiques d'Alain, lors des réunions de groupe, quand il se soucie que les "plus jeunes" du groupe comprennent les discussions, et lors de la rédaction d'articles, quand il a plusieurs fois contribué à clarifier des idées qui étaient encore embrouillées dans ma tête. Je le remercie aussi pour le soutien et les précieux conseils qu'il a su me donner lors du choix de mon post-doc.

Dès ma première visite à l'Institut d'Optique, j'ai été frappée par l'enthousiasme de Chris et par sa curiosité, qui ne s'arrête devant rien. Les nombreuses discussions sur les manips en cours et sur les manips futures, là où on peut voyager avec la créativité et la fantaisie, sans pour cela oublier la physique, démontrent sa fraîcheur d'esprit dont j'espère m'inspirer dans la suite. Je remercie aussi Chris pour m'avoir transmis son optimisme lors des moments difficiles : quand les caprices de la manip semblaient insurmontables ou quand rien ne semblait marcher selon le plan rationnel qu'on s'attendrait, très naïvement, devoir guider une expérience de physique.

Je remercie Denis pour la rigueur, la constance et la patience qu'il a démontré tous les jours et en toute occasion. J'ai toujours été pleine d'admiration pour sa capacité à répondre à toutes les questions des thésards (sans jamais se scandaliser ni pour leur naïveté ni par le fait que la question lui avait déjà été posée auparavant!) et pour la grande clarté de ses explications. De plus sa présence quotidienne en salle de manip, sa capacité à rester calme et à rire aussi des situations qui semblent désespérées, ont été d'une grande aide pendant toute ma thèse. Je le remercie aussi de tout coeur pour ses nombreuses relectures du manuscrit.

Hélène Perrin et Jean Dalibard ont eu la gentillesse d'accepter de rapporter cette thèse. Je les remercie pour le vif intérêt qu'ils ont montré envers mon travail ainsi que pour leurs remarques intéressantes sur le manuscrit, qui ont constitué un moment important de réflexion. Je remercie également Philippe Grangier pour l'enthousiasme

avec lequel il a accepté d'être président du jury. Massimo Inguscio a fait partie du jury en tant que examinateur. Je souhaite le remercier non seulement pour avoir fait l'impossible pour concilier la date de ma soutenance de thèse avec son emploi du temps, mais surtout pour avoir toujours suivi avec intérêt et affection mes travaux. Je ne peux pas oublier quand, avec un grand sourire, il m'a dit qu'Alain Aspect cherchait des doctorants, déclenchant ainsi mon aventure sur les mesures des corrélations dans des condensats d'Hélium métastable.

Quand j'ai rejoint l'équipe Hélium, j'ai été accueillie par les deux thésards qui étaient sur la manip à ce moment là, Martijn Schellekens et Aurélien Perrin. Avec une grande patience ils m'ont tout appris sur la manip. Avec un enthousiasme inébranlable Martijn m'a dévoilé tous les secrets du détecteur et de l'analyse des données, en initiant au langage de root et C++ une italienne qui connaissait très peu de programmation. Je crois que je n'aurais pas pu avoir un meilleur collègue pour la préparation et la réalisation de l'expérience des corrélations sur les fermions qui s'est déroulée à Amsterdam. S'acharner jour et nuit pour voir un tout petit creux dans une fonction de corrélation n'aurait pas été possible sans l'optimisme de Martijn, auquel sans doute la réalisation de cette expérience doit beaucoup. Je souhaite remercier aussi l'équipe Hélium d'Amsterdam, son chef Wim Vassen et les deux thésards qui étaient sur la manip au moment de la collaboration, Tom Jelts et John McNamara. Merci pour nous avoir accueilli dans leur équipe et pour l'enthousiasme avec lequel ils ont participé à cette collaboration, pour les nuits passées à chercher le "bon" nuage froid et à dormir sur un petit matelas gonflable à côté de la salle de manip.

Merci à Aurélien pour m'avoir aidé à comprendre la manip des paires corrélés, et pour avoir su attaquer avec profondeur et rigueur toutes les points obscurs de cette expérience. C'est aussi grâce à ça que nous avons été poussé à vouloir étudier en profondeur les phénomènes physiques qui règlent la génération des paires corrélées. Ainsi les idées présentées dans le dernier chapitre de cette thèse lui doivent beaucoup. Encore merci à Aurélien pour avoir ouvert le chemin de la collaboration avec les théoriciens, Karen Kheruntsyan, Piotr Deuar, Pawel Zin et Marek Trippenbach, que je remercie pour la contribution qu'ils apportent en continu à la compréhension de la physique des collisions et des corrélations. Merci aussi à Klaus Mølmer pour les nombreuses discussions sur l'expérience des collisions et pour la fraîcheur de ses explications.

Merci à Hong Chang, Vanessa Leung, Jean-Christophe Jaskula, Guthrie Partridge et Marie Bonneau, les autres thésards et post-docs avec qui j'ai eu le plaisir de travailler. Avec Hong j'ai partagé une partie de l'aventure d'Amsterdam, les longues nuitées passées à aligner le laser pour défocaliser le nuage d'atomes et (je ne pourrais jamais l'oublier!) la dernière nuit de prise des mesures, lorsque nous avons pris des données jusqu'à 3h00 du matin et démonté tout le matériel pour le charger sur le camion qui partait pour Orsay à 7h30... Avec Jean-Christophe et Vanessa j'ai partagé les joies et les douleurs du déménagement de la manip d'Orsay à Palaiseau et de sa reconstruction. Je les remercie pour leur aide dans ce moment difficile. Je veux remercier particulièrement Jean-Christophe pour les nombreuses et fructueuses discussions que nous avons eu lors de l'analyse des données des collisions. L'équipe Hélium,

maintenant formée par Jean-Christophe, Guthrie et Marie a déjà démontré qu'elle est exceptionnelle et je souhaite de tout coeur à ce trio d'obtenir de nombreux résultats, bien mérités!

La bonne ambiance qui règne dans le groupe d'Optique Atomique a constitué un fort point d'appui pour moi pendant ces années de thèse. Pour cela je veux remercier de tout coeur tous les thésards, post-docs et permanents que j'ai rencontré : Martijn, Aurélien, Jean-Baptiste, David C., Andrès, Carlos, Rob (Joana et le Square de Port Royal), Isabelle (et les régates du CNRS), Martin, Jean-Christophe, Alain, Julien, Simon, Thomas B., Thomas V., Andrea, Guthrie, Jean-François et Juliette (et les séances de psychanalyse), Vanessa, Hong, David D., Karim (vive les mariés!), Vincent, Patrick, Antoine, Gaël (et Emmanuelle), Marie, Sébastien, Karen, Jean-Philippe, Ben, Pierre, Laurent, William, Thorsten, José, Hari, Luca, Nathalie, Philippe, Zhanchun, Guillaume, Rémi, Jocelyn (et Matt), Ronald... Ils ont été de très bons collègues de travail et ils sont et resteront de très bons amis. Et merci aussi à nos électroniciens, Frédéric Moron et André Villing, qui sont toujours à l'écoute des besoins (très souvent urgents) de nos manip. Pendant ma thèse j'ai eu plus souvent l'occasion de travailler avec Frédéric et je tiens à le remercier pour la patience avec laquelle il a toujours répondu à mes questions, pour la clarté de ses explications et pour ce qu'il m'a appris (et je ne cache pas que j'aurais voulu en apprendre encore plus!).

Un remerciement spécial à Francesca Arcara et Eleni Diamanti pour leur bonne humeur et pour les "chiacchierate", à Antoine Browaeys pour ses précieux conseils, à Marco Barbieri pour son cours accéléré d'Optique Quantique et à Yvan Sortais pour sa sympathie. Merci à Paolo Maioli pour sa gentillesse et pour l'aide lors du choix de mon post-doc.

Pendant ma thèse j'ai eu aussi la chance de pouvoir enseigner. Je remercie à ce propos Lionel Jacobowicz (et sa bonne humeur!) pour m'avoir permis d'enseigner les TPs de polarisation et Thierry Avignon, Cédric Lejeune, Jérôme Beugnon, Delphine Sacchet, François Marquier pour avoir été d'une grande aide pour la préparation des cours et pour clarifier les points plus difficiles.

Je remercie chaleureusement l'ensemble des personnes qui travaillent à l'Institut d'Optique, les administratifs, les gens des services techniques, service info, et des ateliers pour leur disponibilité.

Je tiens à dire un grand merci à ma famille qui m'a toujours soutenu, à partir du moment où j'ai choisi de faire une thèse à l'étranger et ensuite, tout au long du déroulement de mon doctorat, dans les moments heureux et dans les moments difficiles. Merci aussi à tous mes amis, Beatrice, Alessandro, Cristina, Irene, Agathe, Arnaud, Ania, Sara, Sylvain, Lydie, Esther, Marie, à la famille Tort, à tous les frères de la Paroisse de Notre Dame de Bonne Nouvelle à Paris et de la Parrocchia di San Bartolo in Tuto à Scandicci, à Don Raffaello, Padre Carlo, Père Julio, Père Mikel et Père Antoine pour l'inébranlable soutien qu'ils m'ont apporté pendant toutes ces années.

Et pour finir je veux remercier de tout coeur mon mari Luigi pour sa patience et ses conseils qui m'ont accompagné et soutenu tout au long de cette thèse, même quand nous étions à plus de 1000 km de distance. Je le remercie aussi pour son aide précieuse

IV

pendant la rédaction de ce manuscrit : pour les fois où il m'a aidé à transcrire une idée qui était claire dans ma tête mais qui n'arrivait pas à être claire sur le papier, pour toutes les fautes d'anglais qu'il a corrigé et pour avoir été toujours à mon côté et prêt à m'aider, à n'importe quelle heure du jour et de la nuit. Et je dis merci aussi à la petite Anna, pour avoir su supporter, inconsciemment, le stress de ma dernière année de thèse. C'est à elle et à Luigi que je dédie de tout mon coeur ce manuscrit.

Contents

Introduction	5
I The Hanbury Brown Twiss effect for fermions	9
1 The Hanbury Brown Twiss effect	11
1.1 Brief history of the Hanbury Brown Twiss effect	11
1.2 To bunch or not to bunch?	15
1.3 Experiments with fermions	17
1.3.1 Experiments with charged fermions	18
1.3.2 Experiments with neutral fermions	20
1.4 Theory for a ballistically expanding fermionic cloud	25
1.4.1 Correlation function for a trapped cloud	25
1.4.2 Density and correlation function for a harmonic trap	27
1.4.3 Density and correlation function for a degenerate sample	28
1.4.4 Correlation function after the time-of-flight	31
1.4.5 Effect of the resolution and the detectivity of the detector	34
1.5 Conclusion	36
2 Amsterdam Experimental Setup	39
2.1 Helium atomic structure	39
2.2 A Bose-Fermi mixture of metastable atoms	40
2.3 Experimental sequence	42
2.3.1 Source and recycling system	43
2.3.2 Laser cooling transitions and laser system	45
2.3.3 Atomic beam collimation	47
2.3.4 The Zeeman slower	48
2.3.5 The two species magneto-optical trap	48
2.3.6 The Magnetic Trap	50
2.3.7 Detection	54
2.4 Conclusion	56

3	Amsterdam-Palaiseau Experimental Results	57
3.1	Acquired Data	58
3.1.1	Data analysis	60
3.2	Experimental results	65
3.2.1	Bosons-Fermions comparison	65
3.2.2	Other temperatures	68
3.2.3	Comments	70
3.3	Defocusing experiment	71
3.3.1	Experimental setup	72
3.3.2	Experimental results	73
3.3.3	Theory	74
3.3.4	Dipolar force	75
3.3.5	Calculation of the demagnification factor	77
3.3.6	Results	77
3.4	Conclusion	78
II	Correlated Atom Pairs	81
4	First Generation Experiment	83
4.1	Correlated pairs of photons	84
4.1.1	Burnham and Weinberg (1970)	84
4.1.2	Theory of the non-degenerate parametric amplifier	85
4.1.3	Experiments with correlated photon pairs	88
4.2	Correlated pairs of atoms	90
4.3	Analogy with the parametric amplifier	92
4.4	A more refined theory	94
4.4.1	Analytical approach	94
4.4.2	Numerical approach	96
4.5	Experimental setup	97
4.5.1	Production of two colliding condensates	97
4.6	Experimental results	100
4.6.1	Observation of the collision sphere	100
4.6.2	Sphere thickness	102
4.6.3	Back to back correlation	104
4.6.4	Collinear correlation	106
4.6.5	Mode occupancy	109
4.6.6	Influence of the gain of the detector	109
4.7	Comparison with theory	110
4.7.1	Analytical calculation	110
4.7.2	Positive-P calculation	113
4.8	Conclusion	116

5	Second Generation Experiment	119
5.1	Motivations for an upgraded experiment	119
5.1.1	Sphere thickness and density	119
5.1.2	Relative number squeezing	120
5.2	New collision geometry	123
5.2.1	Number of scattered atoms	124
5.3	Experimental setup	128
5.3.1	Theory of the Bragg transitions	131
5.3.2	Spontaneous emission	136
5.4	Preliminary results	140
5.5	Conclusion	142
	Conclusion and outlooks	145
A	The detector	149
A.1	The micro-channel plate	149
A.2	The delay-line anode	151
A.2.1	Working principle	151
A.2.2	Electronic chain	153
A.2.3	Determination of the position of the atoms in 3D	154
A.3	Detector characteristics	155
A.3.1	Pulse-height distribution	155
A.3.2	Flux saturation	156
A.3.3	Background noise	158
A.3.4	Detection homogeneity	159
A.3.5	Detection efficiency	159
A.3.6	Detector resolution	163
A.4	Influence of the resolution on the correlation function	164
B	Publications	167
	Bibliography	215

Introduction

Optical interferometry was at the heart of the scientific revolution which led to the new era of the twentieth century. Probably the most renowned example is the Michelson interferometer that was used to show that there is no detectable motion relative to “ether”, a key point in support of special relativity [1], [2]. In the same way Young’s interference experiments played a central role in the early discussion of the dual nature of light. At the end of the nineteenth century Young’s double slit interferometer could be completely described according to the classical theory of electromagnetism based on Maxwell’s equations and the wave nature of light seemed to be affirmed [3]. However, the situation changed radically in 1901 when M. Planck explained the ultraviolet catastrophe problem by assuming that black-body radiation is emitted in discrete energy packets called *quanta* [4]. The first serious attempt to demonstrate the quantum nature of light was performed by G. I. Taylor in 1909. He set up a Young’s slit experiment and he reduced the intensity of the incident light beam to such an extent that there would be one photon incident on the slits at a time [5]. However, he didn’t see any difference between the interference pattern registered at low and high intensity. In fact the classical explanation based in the interference of electric field amplitudes and the quantum explanation based on the interference of probability amplitudes both explain this phenomenon. In order to see a difference between classical and quantum theory one should consider higher order interference experiments, such as intensity interference.

The pioneering experiment in intensity interferometry was performed by R. Hanbury Brown and R. Q. Twiss in 1956 [6]. This experiment studied the correlations between photons arriving at two different detectors. Hanbury Brown and Twiss showed an enhancement of the probability for two photons, coming from a thermal light source, to arrive together on the two detectors, a phenomenon called photon bunching. Their experiment provoked a storm of controversy in the contemporary scientific community and the quantum explanation of the bunching effect was accepted only after the publication of a fundamental paper by E. M. Purcell [7]. Although their results may be derived from both classical and quantum theory, the Hanbury Brown Twiss experiment marked the birth of the modern quantum optics, since the quantum theory makes additional unique predictions. This was pointed out by R. Glauber in 1963 [8]. His work on quantum formulation of optical coherence theory was awarded in 2005 with the Nobel Prize [9]. One such prediction is photon antibunching, that was first observed by Kimble et al. [10] on photons spontaneously emitted by single atoms. At the same time,

the advent of laser sources gave access to other interesting quantum states of light, such as entangled states. The extraordinary character of entanglement, that has no classical counterpart, was at the center of debates since the early years of the quantum era [11], [12], [13], [14]. Realization of entangled states paved the way to new developments in quantum information and, in particular in quantum teleportation. These topics are nowadays still an open frontier of quantum physics. Other quantum effects such as amplitude and frequency squeezing were observed in four wave mixing and parametric down conversion occurring in non-linear crystals and offered new possibilities for precision measurements and interferometry [15].

In parallel with the explosion of quantum optics, the recent progress in the manipulation of atomic states [16], [17], [18], [19] has led to several proposal for generating atomic states with properties similar to the ones of the nonclassical states of light. Photons and atoms are complementary under several points of view and experiments that are possible with atoms could not be possible with photons and vice-versa. For example, photons are well suited for transmission over long distances, but are difficult to store at a fixed location, while the reverse is true for atoms. In order to take advantage of the good properties of each system, there are several proposition of quantum atom optics experiments, involving single atoms, atomic ensembles or atom-photon pairs. Furthermore, a point of great interest for the development of quantum atom optics relies on a sharp distinction between photons and atoms: atoms can obey both quantum statistics, i.e. there are bosonic and fermionic atoms. This opens interesting perspectives for the realization of tests of fundamental principles of quantum mechanics with fermions and for a comparison of quantum effects for bosons and fermions, as in the case of the experiment described in the first part of this thesis.

Historically, the first candidates for quantum atom optics have been trapped ions. Since the early 1990s it has been possible to cool and trap single ions for a very long time (several days) and to perform quantum logic operations on them [20], [21]. An enormous amount of progress in this field has been made in the past twenty years and trapped ions are at the moment a leading candidate for quantum information and computing [22]. On the other hand, the achievement of Bose-Einstein condensation [23], [24], [25], made available to quantum atom optics the material analogue of laser. This analogy has been firmly established experimentally with the demonstration of spatial and temporal coherence of Bose-Einstein condensates [26], [27], which therefore deserve the name of matter waves. Not surprisingly as condensates became readily available in laboratories across the world, quantum atom optics saw the same kind of explosion as quantum optics after the developement of laser. The realization of atom lasers [28], atom mirrors and beam splitters [29] and atom interferometers [30], constitute a good example of the analogy between light and matter waves. Furthermore, the achievement of degenerate Fermi gases of neutral atoms [31], [32], [33] is particularly important for the reasons pointed out above.

Another significant step in the analogy between quantum optics and quantum atom optics has been made with the observation of four-wave mixing of matter waves [34], [35], [36]. In addition the generation of correlated atom pairs in the dissociation of cold

molecules [37] and in the collision of Bose-Einstein condensates [38] was demonstrated. The latter of these experiments has been performed in our group and is described in the second part of this thesis.

The simplest atomic system that has a bosonic and a fermionic isotope is Helium. Due to the fact that the ground state of Helium has no magnetic moment and that the only transition available for optical cooling is in the UV part of the spectrum, Bose-Einstein condensation is hard to achieve in the ground state. However, the triplet metastable state, that has a life time of the order of 7000 s, can be magnetically trapped and has atomic transitions suitable for laser cooling. Metastable Helium has been Bose-Einstein condensed for the first time in the Atom Optics group of the Laboratoire Charles Fabry de l'Institut d'Optique [39]. The metastable Helium experiment is supervised by C. Westbrook, D. Boiron and A. Aspect. It constitutes an original setup for the study of atom optics especially for its detector. In fact the large internal energy of the metastable state makes possible to perform single atom detection, resolved in space and time. This detector allows us to reproduce quantum optics experiments that involve single photon counting.

When I joined the He* team in october 2005 to start my PhD thesis, the detector had been installed one year earlier and the Hanbury Brown Twiss effect on a cold cloud of bosons above and below the condensation threshold had been observed [40]. Almost at the same time the group of W. Vassen at the Laser Centre of the Vrije Universiteit succeeded in the production of degenerate Fermi gas of metastable Helium [41]. Therefore in July 2006 we brought the detector to Amsterdam for two months and, after having inserted it in the existent experimental apparatus, we measured the Hanbury Brown Twiss effect on a cold cloud of fermions [42]. Furthermore we could compare the correlation functions for clouds of bosons and fermions at the same temperature, created in the same experimental apparatus, highlighting the different statistics obeyed by the two systems. The preparation of the collaboration was committed to Martijn Schellekens, another PhD student, and me. We spent the ten months before leaving for Amsterdam in studying in detail the characteristics of the detector.

At the same time Aurélien Perrin as PhD student and Hong Chang as a post-doc performed an experiment aimed at the creation of correlated pairs of atoms by the collision of two Bose-Einstein condensates. The correlation between pairs of atoms was demonstrated and the correlation function was studied in detail in three dimensions, thanks to the use of our detector [38]. This experiment constitutes the atomic analogue of the generation of correlated photon pairs in parametric down conversion or four-wave mixing [43].

In order to perform a more detailed study on correlated pairs we decided to repeat the experiment in an improved version. Unfortunately, the moving from Orsay to Palaiseau in June 2007 imposed a break in our scientific activity. For the dismantling and the reconstruction of the setup in the new building I was helped by Jean-Christophe Jaskula and Vanessa Leung that recently have joined our team as a PhD student and a post-doc respectively. After producing a Bose-Einstein condensate in February 2008, the experimental setup was again fully functional. In 2008, another post-doc, Guthrie

Partridge, and a PhD student, Marie Bonneau, joined our group. Together we finally succeeded in fixing the experimental problems and we started data acquisition. The data analysis is cumbersome and has to be done with great care. Some preliminary results are available at this moment and are reported at the end of this thesis.

Outline of this thesis

This thesis is devoted to the description of the two experiments performed during my PhD, the observation of fermionic antibunching and the creation of correlated atom pairs by condensate collision.

This thesis is divided in two parts. The first part is devoted to the fermionic Hanbury Brown Twiss effect and is divided in three chapters. In the first chapter an historical overview of the Hanbury Brown Twiss effect is given, together with an explanation of the Hanbury Brown Twiss effect in terms of quantum theory. A more refined theory is derived in order to describe the correlation function for a gas of fermions above and below degeneracy in an harmonic trap. In the second chapter we describe the experimental setup used during the collaboration with the group of W. Vassen. A comparison with our experimental setup is drawn and a special attention is payed to the upgrades that would be necessary on our experiment in order to cool the fermionic Helium isotope. In the third chapter we show the experimental results obtained during the collaboration.

The second part of this thesis is devoted to the correlated pairs experiment. It is divided in two chapters. In the first one we describe the quantum optics analogue of our experiment and some fundamental experiments in quantum optics and quantum atom optics that are useful to set the context of our measurements. We then describe the experimental setup and the obtained results. In the second chapter we explain in detail the motivation for the upgraded version of the experiment and we thoroughly compare the two experiments. The new experimental setup is then described and some preliminary results are showed.

Part I

The Hanbury Brown Twiss effect for fermions

Chapter 1

The Hanbury Brown Twiss effect

This chapter is devoted to the Hanbury Brown Twiss effect. We will first give an historical overview, highlighting the reasons why the experiment carried out by the two astronomers in the 1950's, was seminal in the development of the modern quantum optics. In the second part of the chapter we will show the substantial difference in the Hanbury Brown Twiss effect for bosons and fermions. Since the Hanbury Brown Twiss effect for bosons has been studied in several other thesis of the group ([44], [45]), we will concentrate on the experiments done on fermionic samples, as electrons in semiconductors, electrons in vacuum, neutrons and neutral atoms. In the third part we will present the theory that describes the experiment done in a collaboration between our group and the group of W.Vassen in Amsterdam, where we observed the Hanbury Brown Twiss effect on a cold cloud of ^3He (fermionic Helium isotope) and of ^4He (bosonic Helium isotope) [42]. We will concentrate on the theoretical formula of the 2-body correlation function for a fermionic sample of ultracold atoms released from a harmonic trap, indicating in particular the influence of the finite detector resolution on the correlation length and on the antibunching height. The experimental apparatus and the experimental results will be described in details in chapters 2 and 3.

1.1 Brief history of the Hanbury Brown Twiss effect

The radar technology developed during the Second World War opened the field of radio astronomy and led very quickly to the discovery of bright radio sources in the sky. Since their size was unknown, astronomers raised the problem of how to measure it. Since then, the angular size of a star was measured with Michelson interferometer, that is based on a Young's double slit like interferometer. The Michelson stellar interferometer is sketched in figure 1.1.

In Michelson interferometry one compares the amplitudes of the light landing at two separated points. The distance between the two points is equal to the distance between the two slits drawn in figure 1.1. If the separation is not too large, the two signals can be superposed using a lens. The produced diffraction pattern varies as a function of the separation of the slits. At a given point P on the screen the amplitude

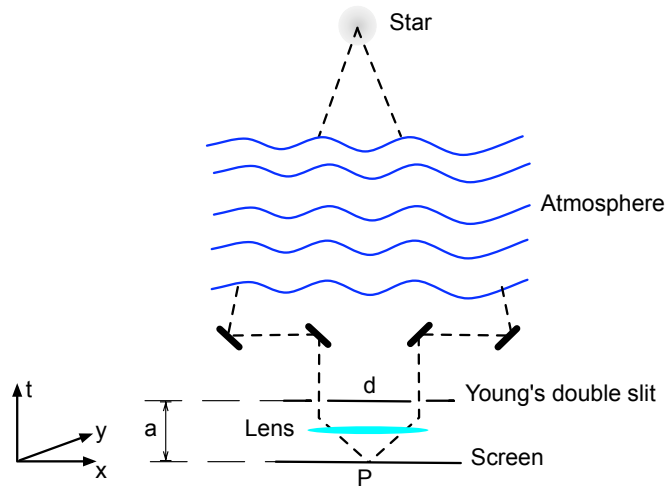


Figure 1.1: Michelson stellar interferometer. The outer mirrors send the light through a Young's double slit interferometer. The distance between the slits and the screen is a and the distance between the two slits is called d . The diffraction pattern is detected on the screen below the double slit.

of the light will be given by the sum of the amplitudes transmitted by the two slits, $A_1(t)$ and $A_2(t + \tau)$. The time τ represents the time difference for the light to reach P from each slit. The intensity observed on the screen at the point P will then be given by

$$\begin{aligned} I_P &= \langle |A_1 + A_2|^2 \rangle_t = I_1 + I_2 + 2\text{Re}(\Gamma_{12}(\tau)) \\ \Gamma_{12}(\tau) &= \langle A_1(t)^* A_2(t + \tau) \rangle_t \end{aligned} \quad (1.1)$$

The latter term takes account of the observed interference pattern. In case of an extended source the interference pattern varies over a typical distance, called coherence length of the source, of the order of λ/θ , where θ is the angular size of the source. A more detailed treatment of the Michelson interferometer can be found in [3] and [46].

It is clear that, in order to perform a measurement with an amplitude interferometer it is crucial to precisely measure the phase difference between A_1 and A_2 . If atmospheric perturbations or mechanical instabilities in the telescope make the path difference change during the acquisition time, interference fringes can be blurred out. In addition, the resolution in amplitude interferometry at a given wavelength is given by the distance over which one is able to compare the amplitudes and their phases. Therefore, if the star has a small angular size, it can be necessary to separate the mirrors (i.e. the two slits) by very large distances. In this case it might be impossible to recombine the signals on the same point of the screen and the use of coherent independent oscillators might be necessary. Since this technology was not available in the early 1950's, R. Hanbury Brown and R. Twiss decided to perform the measurement in an alternative way, by doing intensity interferometry [47]. A schematic view of the intensity interferometer is drawn in figure 1.2.

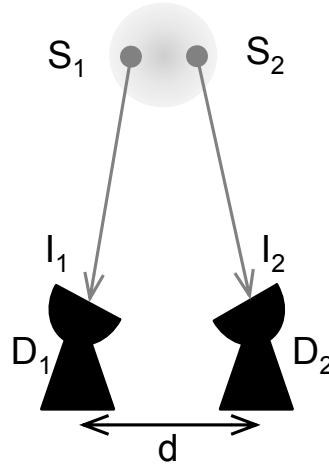


Figure 1.2: Scheme of the intensity interferometer. The light coming from a star is detected on two detectors separated by a distance d . The correlation between the detected intensities I_1 and I_2 is then measured.

The radiation emitted by the star is collected on two independent detectors. The intensities measured at the two detectors are: $I_1 = A_1^* A_1$ and $I_2 = A_2^* A_2$. Then one measures the correlations between the two detected intensities as a function of the distance between the detectors, i.e., the quantity $\langle I_1 I_2 \rangle$ where $\langle \rangle$ indicates the average over random phases. Since the correlated signal varies as a function of the detector separation d on a distance of the order of the correlation length, an intensity interferometric measurement gives the angular size θ of the star. A more detailed explanation of the Hanbury Brown Twiss effect in terms of classical electromagnetic waves can be found in [48]. A familiar example of the Hanbury Brown Twiss observation is the speckle pattern. When a non-pointlike incoherent light source illuminates a screen, a large number of patches appears on the screen and the image is not homogeneous as one would naively expect. This random intensity pattern is produced by the interference between the optical waves. The characteristic size of the speckle grain on the plane of the screen is of the order of the spatial coherence of the beam and it is called correlation length. The characteristic time over which this pattern changes is called coherence time. We will come back on this three-dimensional aspect of the correlation in the following sections.

The radio sources that the Hanbury Brown Twiss interferometer was intended to measure, turned out to be resolvable within few kilometers, therefore the measurement could have been performed with an amplitude interferometer as well. R. Hanbury Brown was so disappointed that he described intensity interferometry as “a steam roller to crack a nut” [49]. However, the importance of the intensity interferometer was not only related to astronomical measurements. In fact, while it was accepted and demonstrated theoretically and experimentally that intensity interferometry worked for radio waves, it was not clear that the effect should also work for light. The fact that

light was made by photons was still debated at that time and Hanbury Brown and Twiss decided to test their intensity interferometer in a table-top experiment in which they measured the intensity correlation of the light emitted by a mercury lamp [6]. The experimental setup and the obtained results are reported in figure 1.3.

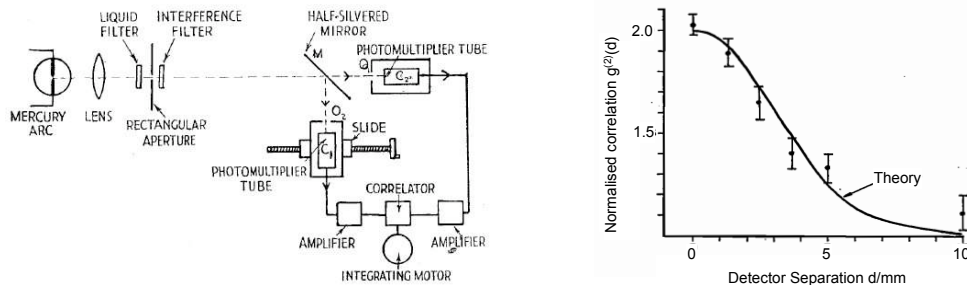


Figure 1.3: On the left: Experimental setup used by Hanbury Brown Twiss for the table-top experiment that proves the particle nature of light. The figure has been taken from [6]. On the right: Experimental results. The intensity correlation for coincident detectors results to be twice bigger than the value obtained when the detectors are far apart. In this case we find the value that we would have obtained for statistically independent particles. This figure has been taken from [50] and has been adapted from the data obtained in [6].

The light of the mercury lamp was split into two beams on a half silvered mirror and the intensity of each beam was measured on a photomultiplier. One of the photodetector could be spatially moved, so that the angular separation of the two detectors as seen from the source could be changed. Therefore it was possible to measure the intensity correlation as a function of the detector separation like in the stellar interferometer. From the point of view of a stream of photons, measuring intensity correlation amounts to measure the joint detection probability of two independently emitted photons on two independent detectors. The measurement showed that the detection probability, when the detectors are close together, is twice larger than the value obtained when they are far apart. When the detectors are far apart one finds the value that one would have obtained for statistically independent particles. The “photon bunching” was therefore demonstrated and quantum optics was born. In a second table-top experiment Hanbury Brown, Twiss and Little [50] measured the time correlation between photons emitted from the same source. The experimental setup was similar to the one of fig. 1.3, but a time-delay could be inserted before one detector in order to measure the correlation as a function of time. The obtained results showed again a photon bunching. The scientific community was sceptical about their results and several experiments were done to disprove them. At the end Hanbury Brown and Twiss won the day, helped by an important paper of E. M. Purcell [7], that explained the effect in terms of quantum mechanics. In addition to a mathematical explanation, Purcell gave a strong example to prove that the observed effect was a pure quantum mechanical effect:

“Were we to carry out a similar experiment with a beam of electrons, we should, of course, find a slight suppression of the normal fluctuations instead of a slight enhance-

ment; the accidentally overlapping wave trains are precisely the configurations excluded by the Pauli principle. Nor would we be entitled in that case to treat the wave function as classical field.” [7]

If for photons, that are bosons, bunching can be explained with a semi-classical theory, it is impossible to explain antibunching for fermions without the aid of quantum mechanics. Fermions are, in this sense, "more quantum" than bosons. In the next section we will explain the Hanbury Brown Twiss effect for bosons and fermions with a simple calculation of quantum mechanics.

1.2 To bunch or not to bunch?

As we said in the previous section, in order to understand the Hanbury Brown and Twiss effect we have to answer the questions:

“How large is the joint detection probability of two particles on two detectors?” and:

“Does it depend on the statistics of the considered particle?”

To find the answer one has to calculate the two-body correlation function $g^{(2)}(d)$, where d , as in the previous section, is the distance between the two detectors.

Consider two particles emitted by two source points S_1 and S_2 and two detectors D_1 and D_2 (see figure 1.4). If we record a click on D_1 and one on D_2 , we could have

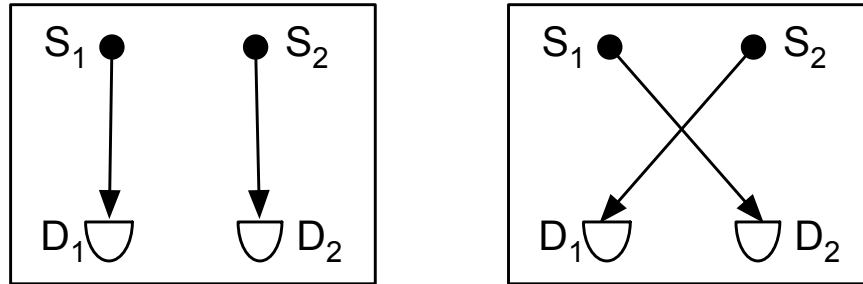


Figure 1.4: Two particles emitted by the two source points S_1 and S_2 are detected at D_1 and D_2 . The two particles can follow two paths that are sketched in this figure. The interference between the two paths leads to the Hanbury Brown Twiss effect.

detected a particle emitted from S_1 on D_1 and a particle from S_2 on D_2 (configuration sketched in figure 1.4 left), or a particle emitted from S_1 on D_2 and vice versa (see figure 1.4 right). The source state vector, for two identical particles, can be written as:

$$|\psi(S_1, S_2)\rangle = \frac{1}{\sqrt{2}}(|S_1 S_2\rangle \pm |S_2 S_1\rangle) \quad (1.2)$$

If the two particles are identical bosons the state vector has to be symmetric for particle exchange (+ sign in the equation above), if they are identical fermions it has to be antisymmetric (− sign). When the two particles are detected, the source state vector,

after temporal evolution, is projected on the two detector state $|D_1 D_2\rangle$. The joint detection probability is then given by:

$$\begin{aligned}
P(D_1, D_2) &= |\langle D_1 D_2 | \psi(S_1, S_2) \rangle|^2 \\
&= \frac{1}{2} (|\langle D_1 D_2 | S_1 S_2 \rangle|^2 + |\langle D_1 D_2 | S_2 S_1 \rangle|^2 \pm \\
&\quad \pm 2 \operatorname{Re} \langle D_1 D_2 | S_1 S_2 \rangle \langle D_1 D_2 | S_2 S_1 \rangle)
\end{aligned} \tag{1.3}$$

where the + sign holds for bosons and the - sign holds for fermions.

If the two particles are statistically independent, then:

$$P_{Indep}(D_1, D_2) = \frac{1}{2} (|\langle D_1 D_2 | S_1 S_2 \rangle|^2 + |\langle D_1 D_2 | S_2 S_1 \rangle|^2) \tag{1.4}$$

irrespective of the distance between the two detectors. On the other hand, for a sample of identical particles, the correlation function (i.e. $P(D_1, D_2)$) will depend on the detector separation and its value, for a small distance between the detectors, will depend on the nature of the particle. For null detector separation, we will have $\langle D_1 D_2 | S_2 S_1 \rangle = \langle D_1 D_2 | S_1 S_2 \rangle$ and the joint detection probability will be:

$$P_{Bose}(D_1 \equiv D_2) = (|\langle D_1 D_2 | S_1 S_2 \rangle|^2 + |\langle D_1 D_2 | S_2 S_1 \rangle|^2) = 2 \times P_{Indep} \tag{1.5}$$

if the two particles are identical bosons, and

$$P_{Fermi}(D_1 \equiv D_2) = 0 \tag{1.6}$$

if the two particles are identical fermions. As we pointed out in the previous section, bosons arrive bunched on the detector and the probability of finding two bosons is twice the probability for independent particles. On the other hand, fermions tend to “antibunch”, because for the Pauli exclusion principle they cannot occupy the same quantum state.

In the case of an extended source, as we increase the detector separation, the correlation function will tend in both cases to the value obtained for independent particles with a shape that is given by the interference term in equation 1.3. The typical distance over which the correlation function goes to the independent particles value is called correlation length. In section 1.4.1 we will derive the formula of the correlation function of a cold fermionic cloud released from a harmonic trap. Figure 1.5 sketches the shape of the correlation function for a sample of identical bosons, fermions and independent particles.

In the treatment above we assumed an ideal detector, i.e., with arbitrarily good resolution. The effect of the finite detector resolution and efficiency will be treated at the end of the chapter (section 1.4.5). For the moment we just note that, if the correlation length is too small to be resolved, the correlation function will be broader and the contrast will be smaller than 1. In other words, the finite resolution makes the measured correlation length larger, but doesn’t change the number of correlated pairs, i.e. the bunching (antibunching) area.

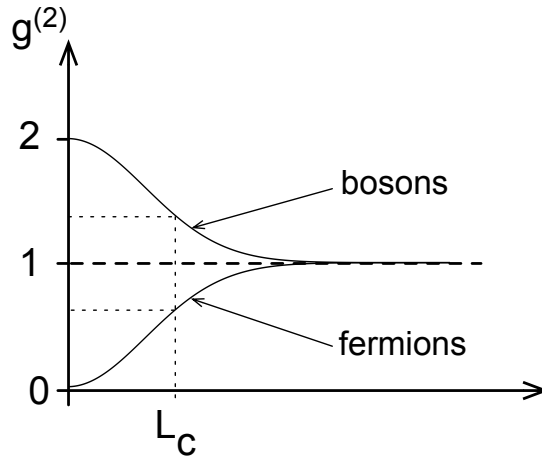


Figure 1.5: Correlation function for a sample of statistical independent particles (dashed line), a sample of identical non-interacting bosons and identical fermions. The correlation function has been normalized with respect to the value obtained for statistical independent particles.

1.3 Experiments with fermions

The Hanbury Brown Twiss effect for fermions has been observed with electrons, neutrons and neutral atoms. The peculiarity of the last system is that the same atomic species can have bosonic and fermionic isotopes and a direct comparison of the two correlation functions can be made. It is the case of the experiment done in the collaboration between our group and the Amsterdam group with ^3He and ^4He [42]. We will treat the theory underlying the measurement at the end of this chapter, while the experimental apparatus and experimental results will be described in chapter 2 and 3 respectively.

In this section we will describe the other experiments where the Hanbury Brown Twiss effect was measured on a sample of fermions. An overview of the experiments done with bosons can be found in [44].

Before starting this brief review, we want to clarify the three dimensional character of the two-body correlation function that we noted in section 1.1. We can identify two kinds of experiments, the ones where the detectors receive a continuous flux of particles and the ones where the entire sample is probed with a snap shot image. If the Hanbury Brown Twiss measurement is done over a continuous flux of particles, one has access to $g^{(2)}(\Delta x, \Delta y, \Delta t)$, i.e., to the measurement of the spatial correlation length on the plane xy , orthogonal to the particle propagation direction, and to the time correlation length along the direction of propagation. This is the case of the speckle measurement that we described in section 1.1, as well as of the Hanbury Brown Twiss table-top experiment and, in the following overview, of the experiments done with electrons [51],[52],[53] and neutrons [54]. On the other hand, if the experiment is carried out on a pulsed beam of particles and the detection time is small with respect to the dynamics of the system

(the detection is a snap shot), then the three directions of space are equivalent and one will have access to $g^{(2)}(\Delta x, \Delta y, \Delta z)$. This is the case of the experiments done with cold atoms [55], [42], where either absorption imaging or a micro-channel plate is used to perform the detection. In the case of the micro-channel plate detection, what we said is valid only under the condition that the cloud doesn't expand while passing through the plate, as we will see in section 1.4.4.

1.3.1 Experiments with charged fermions

Electrons in mesoscopic conductors

The first experiments that observed the antibunching were carried out with electrons in mesoscopic conductors [51], [52], [56], more than 40 years after the first observation on photons. In fact, the statistical effects measured in the correlation function depend on the occupation of the available states. Reaching the degeneracy regime, i.e. unit occupation of all the states below the Fermi energy, was possible in 1999 for electrons in mesoscopic conductors at very low temperature. In this year, Henny et al. [52] and Oliver et al. [51] performed two very similar experiments. The scheme of the experimental setup is shown in figure 1.6.

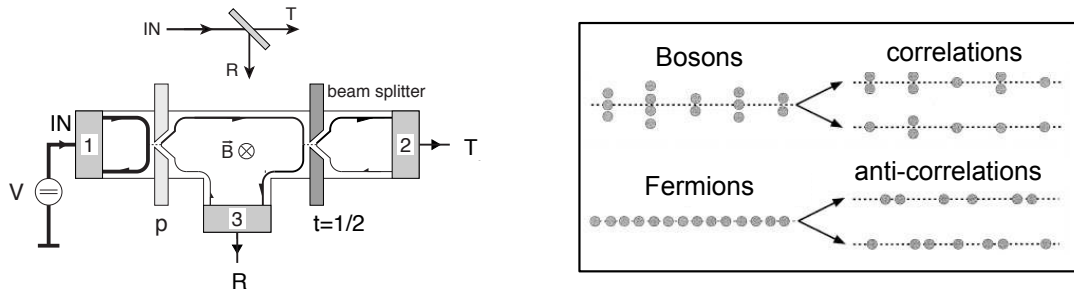


Figure 1.6: On the left, simplified scheme of the setup used by Henny et al. and Oliver et al. to measure the Hanbury Brown Twiss effect on a beam of electrons in a mesoscopic conductor. The figure has been taken from [57]. On the right, an illustration of the different statistics describing bosons and fermions and the expected correlations (anticorrelations) at the output of the beam splitter.

The current injected in the mesoscopic conductor from contact 1 travels in the conductor until reaching a 50% beam splitter. The transmitted beam is then collected on the contact 2 and the reflected beam is collected on contact 3 and the correlation between the transmitted and reflected current is measured. The variable transmission of the barrier between contacts 1 and 3 allows to vary the coherence of the electron currents. To understand this let's imagine a system of electrons where all the states are occupied by one fermion (i.e. at zero temperature). The system will be fully anticorrelated. Varying the transmission through the first barrier, amounts to empty some of the states, with a distribution that is random in time. Therefore, if the sample

was degenerate for a 100% transmission efficiency (i.e. all the states with a temperature smaller than the Fermi temperature were occupied), it is no longer the case when the efficiency is reduced. In other words one can artificially increase the temperature of the sample thereby decreasing its time correlation length.

Both groups were able to demonstrate that, varying the transmission of the first barrier, it is possible to pass from a regime where the currents measured at contacts 2 and 3 are fully anticorrelated to a regime where the statistic of the beam incident on the beam splitter is Poissonian and the anticorrelation vanishes.

Beam of free electrons

A few years later (2002) the Hanbury Brown Twiss effect was observed on a beam of electrons in vacuum by Kiesel and collaborators [53], [58]. Due to the difficulty to achieve the degeneracy, observing anticorrelations in vacuum was more difficult than in mesoscopic conductors. In order to perform the experiment, Kiesel et al. used a very bright source, where the states occupation was close to one electron per interval of coherence time. Their experiment mimics the stellar interferometer (see figure 1.7, left): an electron field emitter illuminates two detectors and coincidences in the arrival time of the electrons at the two detectors are measured.

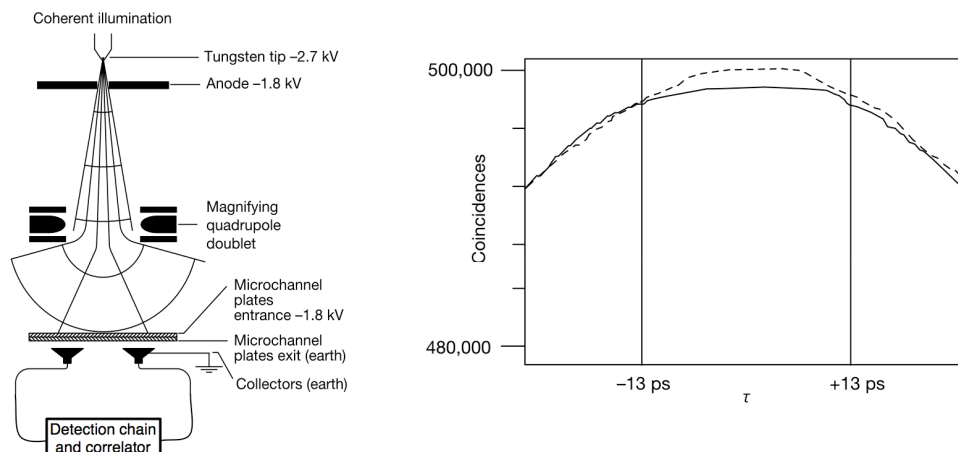


Figure 1.7: On the left, simplified scheme of the setup used by Kiesel et al. to measure the Hanbury Brown Twiss effect on a beam of electrons in vacuum. The figure has been adapted from [53]. On the right, time coincidences for incoherent illumination (dashed lines) compared to coherent illumination (full line). A reduction of the number of coincidences is shown.

Before arriving on the detectors, the electron beam passes through a lens. Changing the magnification amounts to vary the effective lateral distance between the detectors and their illumination changes from incoherent to coherent. The authors repeated the correlation measurement for different magnification factors, showing a reduction of the number of coincidences for a coherent illumination with respect to an incoherent

illumination (see figure 1.7, right). As expected from theory, the antibunching height was only of 10^{-3} , but it was enough to demonstrate the existence of anticorrelation.

1.3.2 Experiments with neutral fermions

Since electrons are affected by Coulomb repulsion, one can argue that anticorrelations observed in charged system are due to electrostatic repulsion. Actually the Coulomb force is small and cannot explain the observed antibunching, but scientists found interesting to repeat the Hanbury Brown Twiss experiment with samples of non-interacting fermions, such as neutrons or cold atoms. In the following sections we will describe those experiments.

Beam of free neutrons

In the “*News and Views*” [58] associated to the paper of Kiesel et al., J. C. H. Spence affirms that reaching the degeneracy in a beam of neutrons would have been even more difficult than for electrons, “*making the observation of neutron anti-bunching a hopeless endeavour*”. Nevertheless, the observation of neutron antibunching by means of coincidence measurements on a neutron beam was realized in 2006, thanks to technology development, that made precise instrumentation and a precise knowledge of the statistical properties of the source available. In an experiment carried out in Grenoble, Iannuzzi et al. [54] measured the Hanbury Brown Twiss effect on such a beam, observing the antibunching and measuring the correlation time of the source. The experimental setup is sketched in figure 1.8 on the left.

A monochromatic beam of thermal neutrons is split in two by a beam splitter. The intensity of each beam is then measured on two detectors and the intensity correlation is measured as a function of the relative distance of the detectors from the source. In order to vary the detector separation, one of the detectors can be moved, parallel to the beam propagation. This amounts to introduce a delay between the detection of the two beams and therefore it gives access to $g^{(2)}(0, 0, \Delta t)$. Care was taken in the choice of the beam splitter and the detectors in order to reduce any additional spread of the signal. The authors repeated the experiment with two kinds of detector, a gas detector and a scintillator. The major difference between the two resides in the time resolution, that is worse for the gas detector than for the scintillator, and in the translation step, that is bigger for the gas detector than for the scintillator. The first quantity has to be compared to the coherence time and will determine the antibunching height. The number of coincidences as a function of the detector separation is reported in figure 1.8 on the right. The top panel reports the measurements obtained with the scintillators and the bottom panel with the gas detector. With an accurate fit the authors can determine the correlation time and the antibunching height, that are consistent with theory.

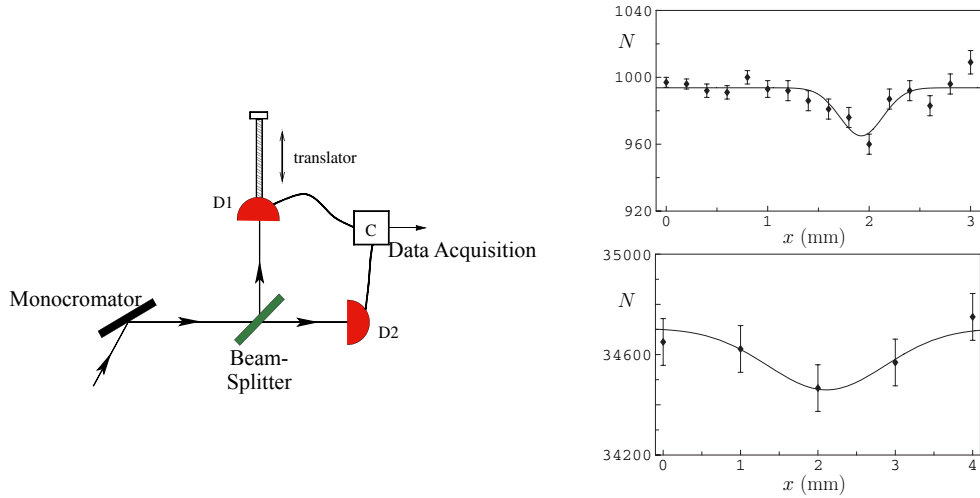


Figure 1.8: On the left, scheme of the setup used by Iannuzzi et al. to measure the Hanbury Brown Twiss effect on a thermal beam of neutrons. The figure has been adapted from [54]. On the right, number of coincidences N as a function of the detector separation. In the top panel the measurements done with the scintillator detector are reported, in the bottom panel the measurements done with the gas detector. The detector separation can be converted in time difference with the formula $t = (x - x_0)/v$ where x_0 is the dip center (that depends on detector calibration) and v is the neutron speed (about 630 m/s).

Cold atoms in an optical lattice

The group of I. Bloch performed in Mainz in 2006 a measurement of the Hanbury Brown Twiss effect in a degenerate Fermi gas of ^{40}K released from an optical lattice [55]. This experiment is the fermionic counterpart of an experiment done by the same group one year earlier on the Mott insulator phase of a rubidium Bose gas [59]. In the fermionic experiment, the atoms are first cooled below the Fermi temperature and then loaded in a three-dimensional optical lattice. The lattice is suddenly switched off and, after a time-of-flight of 10 ms, the atoms are imaged on a CCD camera via standard absorption imaging along the vertical axis. The position of the atoms after the time-of-flight corresponds to their momentum distribution in the trap.

In the lattice, the atoms occupy Bloch states in the lowest energy band. Each Bloch state is characterised by a crystal momentum $\hbar q$, where q is the crystal wave vector, defined in the first Brillouin zone of the reciprocal lattice. Due to the periodicity of the Brillouin zone, each Bloch state is a superposition of states with momentum $\hbar q + 2n\hbar k$, with n an integer number and k the wave vector of the laser used to create the lattice. When a particle with quasi-momentum $\hbar q$ is released from the lattice, it has equal probability to be detected at any of the positions $x_n = (\hbar q + 2n\hbar k)t/m$, where t is the duration of the time-of-flight and m is the mass of the particle. Conversely, if a particle has been detected at the position x_n , it has to come from a state of the crystal with quasi-momentum $\hbar q$. Now, since we are dealing with identical fermions, the occupation

of a single Bloch state by two particles is not allowed by the Pauli principle. Therefore it will be impossible to detect a particle in the position x_n and a particle in the position $x_{n'}$. Since the positions x_n are equally spaced by $l = 2\hbar kt/m$, the spatial correlation will vanish for any distance $|x_n - x_{n'}|$ integer multiple of l .

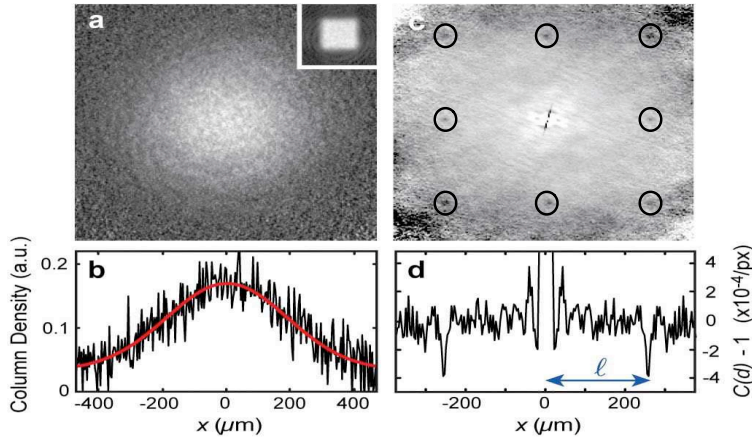


Figure 1.9: On the left: a. Single shot absorption image of the fermionic cloud released from an optical lattice. The inset shows the occupation of the Brillouin zones, demonstrating that only the lowest is occupied. b. Horizontal cut of image a. No spatial structure is present. On the right: c. Correlation measured on 158 shots like that of figure a. A rectangular periodic array of black dots is visible, the dots are circled by a solid black line. The horizontal profile through the centre of the correlation shows that the the dots correspond to dips, spaced by l . The figure has been taken from [55].

In figure 1.9 we show the experimental results. On the left the image recorded after the time-of-flight is reported. No periodic structure is present (as shown by the one-dimensional cut through the image centre, figure 1.9 bottom left). On the right is shown the correlation function obtained from the analysis of 158 images. A rectangular periodic array of peaks is visible. A horizontal profile through the centre of the image (bottom right) shows that the amplitude of the peaks is negative and that they are spaced by a multiple of l , as expected as a signature of the Hanbury Brown Twiss effect.

It is interesting to make a few comments on the imaging technique that has been used in this experiment. In general absorption imaging allows one to measure the column density of the atomic cloud, but it is not a single particle detection. The measurement of second order correlations is then tricky and, in 2004, Altman et al. [60] proposed for the first time to use this technique to measure spatial correlations in fermionic superfluids and clouds released from an optical lattice. They proposed to measure atom shot noise in the time-of-flight images. This is possible only if atomic shot noise dominates over the shot noise of the absorbed beam and on the technical noise. This requirements are hard to achieve with current CCD cameras.

In this perspective the enormous advantage of using metastable helium atoms is that one can easily perform single atom detection in three dimensions. Measuring

second order correlation functions is much easier with a single atom detector, than with absorption imaging. With this kind of detector our group measured, in 2005, the correlation function of a thermal cloud of bosons and of a Bose-Einstein condensate [40]. In 2006 we were able to measure the same quantity for a cloud of bosons and fermions [42]. As we already pointed out this will be the subject of chapters 2 and 3. Here we only briefly outline it in order to complete our review of the measurements of the HBT effect on fermions.

Amsterdam-Palaiseau experiment

An artistic view of the setup is reported in figure 1.10. A cold cloud of metastable ^3He (fermions) or ^4He (bosons) atoms can be prepared with standard cooling techniques in a magnetic, cigar shaped, trap (see chapter 2). When the desired temperature is reached the trap is suddenly switched off and the atoms fall, under the effect of gravity, on the detector, situated 63 cm below the trap centre. The trap frequencies are $\omega_x/2\pi = 54$ Hz and $\omega_{yz}/2\pi = 506$ Hz for ^3He and $\omega_x/2\pi = 47$ Hz and $\omega_{yz}/2\pi = 440$ Hz for ^4He . We acquired data with samples of ^3He and ^4He at a temperature of $0.5 \mu\text{K}$ in order to be able to make a comparison between the correlation function of bosons and fermions at the same temperature. We also acquired ^3He cold clouds at $1 \mu\text{K}$ and $1.5 \mu\text{K}$ to follow the change of the fermionic correlations as a function of the temperature.



Figure 1.10: Sketch of the experimental setup used in the Amsterdam-Palaiseau experiment. A metastable helium cloud is released at the switch-off of the magnetic trap. The atoms fall under the effect of gravity on a 3D single atom detector situated 63 cm below the trap.

The detector is a micro-channel plate with a delay-line anode (see appendix A for technical details), capable to record the position of the single atoms on the xy plane and their arrival time on the detector (i.e. the vertical position). The time-of-flight is very long (about 360 ms) and the position of the atoms measured on the detector reflects the momentum of the atoms in the trap. After the detection we can measure the two-body

correlation function of the atomic cloud by just measuring the probability of finding an atom at a certain distance from another one (all the details of the data analysis will be given in chapter 3). In the next section we will derive the theoretical formulation of the second order correlation function that we will compare with the obtained experimental results presented in chapter 3. The major result obtained in this collaboration is the

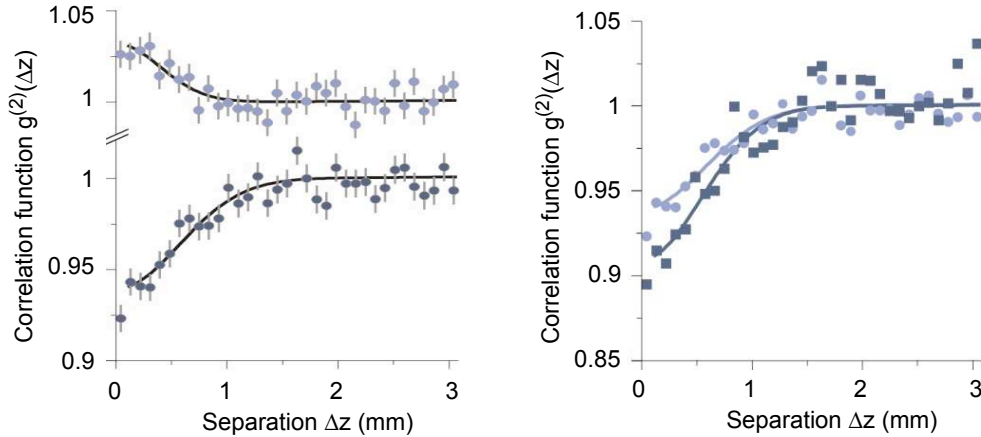


Figure 1.11: On the left: Two-body correlation function along the z direction for a cloud of ^4He (upper graph) and a cloud of ^3He (lower graph) at $0.5 \mu\text{K}$. The different quantum behavior of bosons and fermions is clearly visible. The error bars correspond to the square root of the number of entries in each bin. On the right: Correlation function along the z axis measured on a fermionic cold cloud at $0.5 \mu\text{K}$. The light blue curve is the same as the one shown on the left side of the figure. The dark blue is the correlation obtained when the effective size of the source is made smaller by the application of a blue detuned laser during the time-of-flight. The contrast of the correlation function is increased.

measurement of the two-body correlation function in three dimensions in space for a sample of fermions and a sample of bosons at the same temperature and in the same experimental apparatus. Our detector allows us to perform quantitative measurements of the correlation lengths. The two-body correlation function along the z (vertical) axis is shown in figure 1.11 (left). As expected we observe a bunching for bosons (upper graph) and an antibunching for fermions (lower graph). The correlation lengths resulted to be inversely proportional to the angular size of the source as seen from the detector. The comparison between correlation measured for bosons and fermions showed that the correlation lengths are different due to the different mass of the two isotopes. The contrast of the correlation function is limited by the detector resolution. We also measured the correlation length for fermions as a function of the temperature of the sample. The measured values are in good agreement with the theory developed in section 1.4.

In a second experiment we artificially changed the size of the source by shining a blue-detuned laser on the atomic cold cloud during the time-of-flight. The effective source is then smaller than the trapped source and the correlation length at the detector is larger. This way one can hope to increase the correlation length to a value larger

than the detector resolution and to see the correlation function going down to zero. The performances of our atomic lens were not that good but we could observe an increase in the contrast of the correlation function of a factor 1.4. In figure 1.11 (right) we report the measured correlation function along the z axis with (in blue) and without (in light blue) the application of the atomic lens. The difference is clearly visible. In section 3.3 we will discuss this experiment in detail.

1.4 Theory for a ballistically expanding fermionic cloud

In this section we will derive the theoretical expression of the two-body correlation function for a cloud of ultracold non-interacting fermions released from a harmonic trap.

In section 1.4.1 we will derive the expression of the correlation function for a non-interacting gas of fermions at thermal equilibrium in a trapping potential. Among the data acquired during our collaboration the ^3He clouds at $0.5 \mu\text{K}$ were degenerate ($T/T_F \approx 0.66$), therefore we will derive the expression of the correlation function for a degenerate trapped cloud and we will compare it with the result found for a non-degenerate cloud.

In section 1.4.4 we will derive the expression of the correlation function after a ballistic expansion.

At the end of the chapter we will discuss the effect of the finite detector resolution and the finite detectivity on the correlation function (sec. 1.4.5).

1.4.1 Correlation function for a trapped cloud

Consider a cold cloud of identical (spin polarized) fermions confined in a trapping potential. The sample is at thermal equilibrium at the temperature T . The trapping potential is characterised by the parameters ϵ_j and ϕ_j , the energy and the wave function of the level j . In second field quantisation, the field operators are defined as:

$$\hat{\Psi}^\dagger(\mathbf{r}) = \sum_j \phi_j^*(\mathbf{r}) \hat{a}_j^\dagger, \quad \hat{\Psi}(\mathbf{r}) = \sum_j \phi_j(\mathbf{r}) \hat{a}_j \quad (1.7)$$

The operator \hat{a}_j^\dagger (\hat{a}_j) annihilates (creates) a particle in the state j and the field operator $\hat{\Psi}^\dagger$ ($\hat{\Psi}$) annihilates (creates) a particle at the position \mathbf{r} . Since we are dealing with fermions, the system follows the Fermi-Dirac distribution and $\langle \hat{a}_j^\dagger \hat{a}_k \rangle = \delta_{jk} (1 + \exp\{\beta(\epsilon_k - \mu)\})^{-1}$, where $\beta = (k_B T)^{-1}$, with k_B the Boltzmann constant. The quantity μ is the chemical potential and its value ensures that $\sum_j \langle \hat{a}_j^\dagger \hat{a}_k \rangle = N$, the total number of particles in the system. In addition the field operators defined above will obey to the following commutation rules:

$$\begin{aligned} \{\hat{\Psi}(\mathbf{r}), \hat{\Psi}^\dagger(\mathbf{r}')\} &= \delta(\mathbf{r} - \mathbf{r}') \\ \{\hat{\Psi}(\mathbf{r}), \hat{\Psi}(\mathbf{r}')\} &= 0 \\ \{\hat{\Psi}^\dagger(\mathbf{r}), \hat{\Psi}^\dagger(\mathbf{r}')\} &= 0 \end{aligned}$$

If one neglects the shot noise term, the second order correlation function is given by:

$$G^{(2)}(\mathbf{r}, \mathbf{r}') = \langle \hat{\Psi}^\dagger(\mathbf{r}) \hat{\Psi}(\mathbf{r}) \hat{\Psi}^\dagger(\mathbf{r}') \hat{\Psi}(\mathbf{r}') \rangle. \quad (1.8)$$

We shall define two other quantities that will be useful in the calculation of 1.8, the first order correlation function $G^{(1)}(\mathbf{r}, \mathbf{r}')$ and the density of the sample $\rho(\mathbf{r})$:

$$G^{(1)}(\mathbf{r}, \mathbf{r}') = \langle \hat{\Psi}^\dagger(\mathbf{r}) \hat{\Psi}(\mathbf{r}') \rangle \quad (1.9)$$

$$\rho(\mathbf{r}) = \langle \hat{\Psi}^\dagger(\mathbf{r}) \hat{\Psi}(\mathbf{r}) \rangle = G^{(1)}(\mathbf{r}, \mathbf{r}) \quad (1.10)$$

If we go back to the beginning of this chapter, we see that equation 1.9 is the quantum formulation of equation 1.2 (the product of two amplitudes), while $G^{(2)}$ is the quantity measured in intensity interferometry (the product of two intensities). If we inject 1.7 in 1.8 we obtain:

$$G^{(2)}(\mathbf{r}, \mathbf{r}') = \sum_{j,k,l,n} \phi_j^*(\mathbf{r}) \phi_k(\mathbf{r}) \phi_l^*(\mathbf{r}') \phi_n(\mathbf{r}') \langle \hat{a}_j^\dagger \hat{a}_k \hat{a}_l^\dagger \hat{a}_n \rangle \quad (1.11)$$

The Wick's theorem [61] allows to write:

$$\langle \hat{a}_j^\dagger \hat{a}_k \hat{a}_l^\dagger \hat{a}_n \rangle = \langle \hat{a}_j^\dagger \hat{a}_j \rangle \langle \hat{a}_k^\dagger \hat{a}_k \rangle (\delta_{jl} \delta_{kn} - \delta_{jn} \delta_{kl}) + \langle \hat{a}_j^\dagger \hat{a}_j \rangle \delta_{kl} \delta_{jn} \quad (1.12)$$

that, injected into 1.11, using the definitions 1.9 and 1.10, leads to:

$$G^{(2)}(\mathbf{r}, \mathbf{r}') = \rho(\mathbf{r})\rho(\mathbf{r}') - |G^{(1)}(\mathbf{r}, \mathbf{r}')|^2 + \rho(\mathbf{r})\delta(\mathbf{r} - \mathbf{r}'). \quad (1.13)$$

The last term is called shot-noise term and will be neglected in the following because it is proportional to the number of atoms N while the other terms are proportional to N^2 . We can now calculate the normalized correlation function:

$$g^{(2)}(\mathbf{r}, \mathbf{r}') = \frac{G^{(2)}(\mathbf{r}, \mathbf{r}')}{\rho(\mathbf{r})\rho(\mathbf{r}')} = 1 - \frac{|G^{(1)}(\mathbf{r}, \mathbf{r}')|^2}{\rho(\mathbf{r})\rho(\mathbf{r}')} \quad (1.14)$$

We can make some remarks about the expression of $g^{(2)}$ that we just found. For a bosonic sample far from the critical temperature the expression of $g^{(2)}$ is the same as for fermions, but with a + sign instead of a - sign in front of the last term. It is this sign that gives rise to bunching for bosons and antibunching for fermions. In fact, for $\mathbf{r} = \mathbf{r}'$, $|G^{(1)}(\mathbf{r}, \mathbf{r})|^2 = \rho(\mathbf{r})\rho(\mathbf{r})$ and then $g^{(2)}(\mathbf{r}, \mathbf{r}) = 2$ for bosons and $g^{(2)}(\mathbf{r}, \mathbf{r}) = 0$ for fermions. Moreover, if the cloud has a finite correlation length, $G^{(1)}(\mathbf{r}, \mathbf{r}') \rightarrow 0$ when $|\mathbf{r} - \mathbf{r}'| \rightarrow \infty$ and $g^{(2)}$ tends to 1, the value obtained for two independent particles.

If the temperature is closed or below the transition temperature (the Fermi temperature for fermions, the critical temperature for bosons), the equation 1.14 is still valid for fermions but not for bosons. In fact the population of the ground state is macroscopic for bosons close to the condensation threshold and the second order correlation function becomes [62]:

$$g_{BEC}^{(2)}(\mathbf{r}, \mathbf{r}') = 1 + \frac{|G^{(1)}(\mathbf{r}, \mathbf{r}')|^2}{\rho(\mathbf{r})\rho(\mathbf{r}')} - \frac{\rho_0(\mathbf{r})\rho_0(\mathbf{r}')}{\rho(\mathbf{r})\rho(\mathbf{r}')} \quad (1.15)$$

where $\rho_0(\mathbf{r})$ is the ground state density. Since for a Bose-Einstein condensate at $T = 0$ only the ground state is occupied, then $|G^{(1)}(\mathbf{r}, \mathbf{r}')|^2 = \rho(\mathbf{r})\rho(\mathbf{r}') = \rho_0(\mathbf{r})\rho_0(\mathbf{r}')$ and therefore $g_{BEC}^{(2)}(\mathbf{r}, \mathbf{r}') = 1$.

For a degenerate gas of fermions this doesn't occur and equation 1.14 is still valid. In the following section we will derive the expression of $g^{(2)}(\mathbf{r}, \mathbf{r}')$ for a sample of fermions trapped in a harmonic trap, as in case of the Amsterdam-Palaiseau experiment, and we will study the behaviour of the correlation function close to the Fermi temperature.

1.4.2 Density and correlation function for a harmonic trap

Calling ω_α the trap oscillation frequencies along the α direction, we can write the hamiltonian of the system as:

$$\hat{H} = \frac{\hat{\mathbf{p}}^2}{2m} + \frac{1}{2}m(\sum_\alpha \omega_\alpha^2 r_\alpha^2) \quad (1.16)$$

The eigenfunctions of the system, for the level j with energy ϵ_j will be given by:

$$\phi_j(\mathbf{r}) = \prod_{\alpha=x,y,z} A_{j_\alpha} \exp\{-r_\alpha^2/2\sigma_\alpha^2\} H_{j_\alpha}(r_\alpha/\sigma_\alpha) \quad (1.17)$$

where $\sigma_\alpha = \sqrt{\hbar/m\omega_\alpha}$ is the harmonic oscillator ground state size, H_{j_α} is the Hermite polynomial of order j_α and $A_{j_\alpha} = [\sqrt{\pi}\sigma_\alpha 2^{j_\alpha} (j_\alpha)!]^{-1/2}$ is the normalization factor. According to [62] we can write the density and the first order correlation function in the trap, for an ideal gas of fermions, as follows:

$$\begin{aligned} \rho_{trap}(\mathbf{r}) &= \frac{1}{\pi^{3/2}} \sum_{l=1}^{\infty} (-1)^{l+1} e^{l\beta\tilde{\mu}} \prod_\alpha \frac{1}{\sigma_\alpha \sqrt{1 - e^{-2l\tau_\alpha}}} e^{-\tanh(l\tau_\alpha/2)(r_\alpha^2/\sigma_\alpha^2)} \quad (1.18) \\ G_{trap}^{(1)}(\mathbf{r}, \mathbf{r}') &= \frac{1}{\pi^{3/2}} \sum_{l=1}^{\infty} (-1)^{l+1} e^{l\beta\tilde{\mu}} \prod_\alpha \frac{1}{\sigma_\alpha \sqrt{1 - e^{-2l\tau_\alpha}}} \\ &\times \exp \left[-\tanh\left(\frac{\tau_\alpha l}{2}\right) \left(\frac{r_\alpha + r'_\alpha}{2\sigma_\alpha}\right)^2 - \coth\left(\frac{\tau_\alpha l}{2}\right) \left(\frac{r_\alpha - r'_\alpha}{2\sigma_\alpha}\right)^2 \right] \quad (1.19) \end{aligned}$$

with $\tau_\alpha = \beta\hbar\omega_\alpha = \hbar\omega_\alpha/k_B T$ and $\tilde{\mu} = \mu - \frac{1}{2} \sum_\alpha \hbar\omega_\alpha$ where μ is the chemical potential. The size of the trapped cloud is $s_\alpha = \sigma_\alpha/\sqrt{\tau_\alpha} = \sqrt{k_B T/m\omega_\alpha^2}$. Note that formulas 1.18 and 1.19 are valid only if $\tilde{\mu} < 0$. As the temperature decreases the number of terms that contributes to the sum increases. For a temperature well above the Fermi temperature, $\tilde{\mu} \rightarrow -\infty$ and one finds the Maxwell-Boltzmann distribution. In this case the density and the first order correlation function are:

$$\rho_{trap}(\mathbf{r}) = \frac{N}{\lambda^3} \prod_\alpha \tau_\alpha e^{-(\tau_\alpha/2)(r_\alpha^2/\sigma_\alpha^2)} \quad (1.20)$$

$$G_{trap}^{(1)}(\mathbf{r}, \mathbf{r}') = \frac{N}{\lambda^3} \prod_\alpha \tau_\alpha e^{-(\tau_\alpha/2)((r_\alpha+r'_\alpha)/2\sigma_\alpha)^2} e^{-\pi((r_\alpha-r'_\alpha)/\lambda)^2} \quad (1.21)$$

where $\lambda = \hbar\sqrt{2\pi}/\sqrt{mk_B T}$ is the thermal De Broglie wavelength and N is the number of trapped atoms.

Injecting the two expressions in equation 1.14, we find:

$$\begin{aligned} g_{trap}^{(2)}(\mathbf{r}, \mathbf{r}') &= 1 - \prod_{\alpha} \exp\left\{\left(\frac{1}{4s_{\alpha}^2} - \frac{2\pi}{\lambda^2}\right)(r_{\alpha} - r'_{\alpha})^2\right\} \\ &\approx 1 - \prod_{\alpha} \exp\left\{-\frac{2\pi}{\lambda^2}(r_{\alpha} - r'_{\alpha})^2\right\} \end{aligned} \quad (1.22)$$

where the last equality holds because $4s_{\alpha}^2(2\pi/\lambda^2) = 4(k_B T/\hbar\omega_{\alpha})^2 \gg 1$. The normalized correlation function (plotted in figure 1.12) has a Gaussian shape and the correlation length in the trap is $l_{trap} = \lambda/\sqrt{2\pi}$ (at $1 - 1/e$). For bosons we find the same result but with a $+$ sign in front of the second term of 1.22.

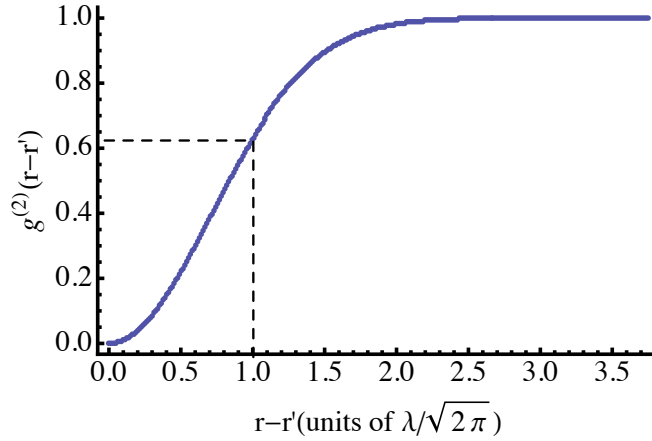


Figure 1.12: Second order normalized correlation function for a non degenerate gas of fermions in a harmonic trap.

When the temperature is below the Fermi temperature, it is easier to calculate the atomic density and the correlation function in the semiclassical approach, as we will see in the next section.

1.4.3 Density and correlation function for a degenerate sample

As the sample is cooled below the Fermi temperature T_F , the probability for the lowest energy states to be occupied becomes higher and higher. However, the probability for two fermions to occupy the same energy level is zero, due to the Pauli principle and the atoms occupy one by one the lower energy levels. At zero temperature, the energy of the higher occupied state defines the Fermi energy, $E_F = k_B T_F$. At finite temperature some of the levels below the Fermi energy are empty and some of the levels above the Fermi energy are occupied. From the experimental point of view, as the sample is cooled, the cloud initially shrinks, but as the temperature approaches T_F , the cloud

eventually stops shrinking and its size remains larger than the size of a classical gas with the same number of atoms at the same temperature. This is the effect of the so-called Fermi pressure and it is a direct consequence of the Pauli principle [32]. For the same reason the density distribution is flattened in the central part and the distribution is no longer Gaussian. The density of the trapped cloud is written, in the semiclassical approximation, as:

$$\rho_{trap}(\mathbf{p}) = \frac{1}{h^3} \int d\mathbf{R} \frac{1}{\exp\{\beta(\mathbf{p}^2/2m + V(\mathbf{R}) - \mu)\} + 1} \quad (1.23)$$

where $V(\mathbf{R})$ is the trapping potential. The effect of the Fermi pressure is shown in figure 1.13, where we plot the density of a cloud of atoms using the Maxwell-Boltzmann and the Fermi-Dirac distribution at fixed temperature and number of atoms. Since the wings of the cloud are less dependent on the statistics, the Maxwell-Boltzmann distribution and the Fermi-Dirac distribution coincide on the wings.

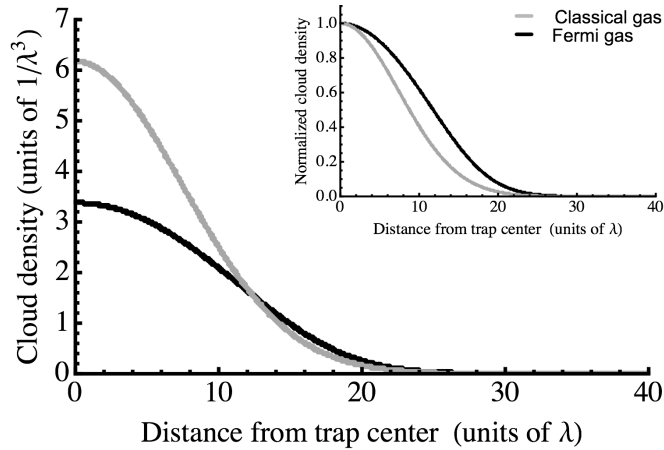


Figure 1.13: Density of a cloud of fermions at $T/T_F = 0.3$ with 40×10^4 atoms as a function of the distance to the trap center. The grey line is the density calculated using the Maxwell-Boltzmann distribution. The black line is the density calculated using formula 1.23 that takes into account the fact that the atoms follow the Fermi-Dirac statistics. The effect of the Fermi pressure is well visible close to the trap center. In the inset we show the two normalized density distributions. Each curve is normalized to its peak density, in order to make evident that the size of a cloud of fermions is larger than the size of a classical gas.

One can then ask what is the second order correlation function for a gas of fermions below T_F . As we said in the previous section, equation 1.14 holds and $g^{(2)}$ goes to zero for $\mathbf{r} = \mathbf{r}'$ and to 1 when $|\mathbf{r} - \mathbf{r}'| \rightarrow \infty$. The second order correlation function can be calculated, in the semiclassical approximation, as follows. At equilibrium, inside the trap, the following equality holds [62]:

$$\int d\mathbf{R} G^{(1)}(\mathbf{R} - \mathbf{r}/2, \mathbf{R} + \mathbf{r}/2) = \int d\mathbf{p} \rho_{trap}(\mathbf{p}) e^{-i\mathbf{p}\cdot\mathbf{r}/\hbar} \quad (1.24)$$

Injecting 1.23 in 1.24 we find [62]:

$$G^{(1)}(\mathbf{R} - \mathbf{r}/2, \mathbf{R} + \mathbf{r}/2) = \frac{1}{h^3} \int d\mathbf{p} \frac{1}{\exp\{\beta(\mathbf{p}^2/2m + V(\mathbf{R}) - \mu)\} + 1} e^{-i\mathbf{p}\cdot\mathbf{r}/\hbar} \quad (1.25)$$

The integral can be calculated numerically and the normalized second order correlation function is given by:

$$g^{(2)}(\mathbf{R} - \mathbf{r}/2, \mathbf{R} + \mathbf{r}/2) = \frac{G^{(2)}(\mathbf{R} - \mathbf{r}/2, \mathbf{R} + \mathbf{r}/2)}{\rho_{trap}(\mathbf{R} + \mathbf{r}/2) \rho_{trap}(\mathbf{R} - \mathbf{r}/2)} \quad (1.26)$$

where the density is given by:

$$\rho_{trap}(\mathbf{r}) = -\frac{1}{\lambda^3} g_{3/2} \left[-\exp \left\{ \frac{1}{k_B T} \mu - \frac{m\omega^2}{k_B T} \mathbf{r}^2 \right\} \right] \quad (1.27)$$

In figure 1.14 we show the result of this calculation for a cloud of 4×10^4 atoms at $T = 0.3T_F$. The calculation has been made for an isotropic trap with trapping frequency equal to the geometric average of the trapping frequencies of the Amsterdam-Palaiseau experiment. We calculate the correlation function at three different positions: at the center of the cloud, $\mathbf{R} = \mathbf{0}$ (black line), at a distance equals to 12λ from the trap center (light grey line), and for a classical gas (grey line). Defining the correlation length l_c as

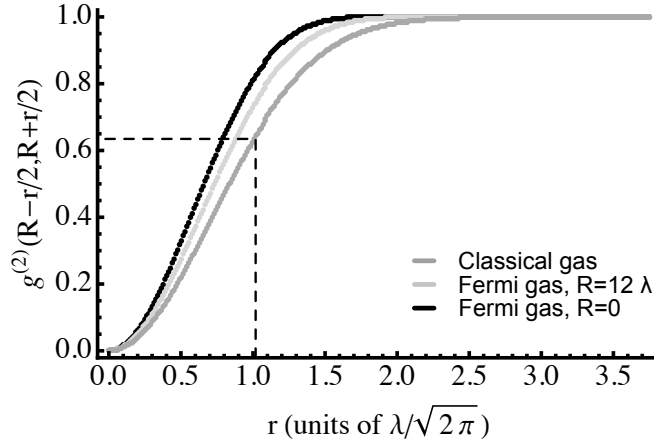


Figure 1.14: Correlation function for a cloud of fermions at $T/T_F = 0.3$. The correlation function has been calculated in the center of the cloud ($\mathbf{R} = \mathbf{0}$), black line, at $\mathbf{R} = 12\lambda$, light grey line and for a classical gas, grey line. As long as we go far from the trap center the effect of the Fermi pressure is less strong and the correlation approaches the one obtained for a classical gas.

the length at which $g^{(2)}(l_c) = 1 - 1/e$, we see that the correlation length obtained for the Fermi-Dirac distribution is smaller than the one obtained for a Maxwell-Boltzmann distribution. In addition, the effect of the Fermi pressure is stronger close to the center of the cloud, while the correlation function approaches that of a classical gas on the

wings of the cloud. The relative difference in l_c between a classical and a Fermi gas is 22% at the center of the cloud and 14% at $\mathbf{R} = 12\lambda$.

We can study what happens if we measure the average of the correlation function over all the atomic cloud, which we define as follows:

$$g^{(2)}(\mathbf{r}) = \frac{\int d\mathbf{R} G^{(2)}(\mathbf{R} - \mathbf{r}/2, \mathbf{R} + \mathbf{r}/2)}{\int d\mathbf{R} \rho_{trap}(\mathbf{R} + \mathbf{r}/2) \rho_{trap}(\mathbf{R} - \mathbf{r}/2)} \quad (1.28)$$

where $G^{(2)}(\mathbf{R} - \mathbf{r}/2, \mathbf{R} + \mathbf{r}/2)$ is defined in equation 1.13. The averaged correlation function defined above corresponds to the quantity measurable in the experiment, as we will see in chapter 3. The averaging procedure has the effect of partially washing out the effect of the Fermi pressure. In figure 1.15 we show the normalized second order correlation function for 4×10^4 trapped atoms at different values of T/T_F between 1.5 and 0.3. The calculation has been made for an isotropic trap with trapping frequency equals to the geometric average of the trapping frequencies of the Amsterdam-Palaiseau experiment. In each graph of figure 1.15 we report the second order correlation function calculated with equation 1.28 and for a gas following the Maxwell-Boltzmann distribution (equation 1.22). As the figure shows, for $T \geq T_F$ the correlation function calculated using 1.28 coincides with the one calculated with the Maxwell-Boltzmann distribution, as we have derived. The correlation length is $\lambda/\sqrt{2\pi}$, as derived in the section above. On the other hand, for $T \leq T_F$ the gas doesn't follow the Maxwell-Boltzmann distribution and the two correlation functions are different. In particular the correlation length is not $\lambda/\sqrt{2\pi}$, but is smaller because, due to the Fermi pressure, the size of the trapped cloud is larger. The relative difference is 7.5% for $T/T_F = 0.5$ (bottom left graph in figure 1.15) and 19% for $T/T_F = 0.3$ (bottom right graph in figure 1.15). If we compare this result with the values obtained for the local correlation function for $T/T_F = 0.3$ we see that, as expected, the averaging process washes out the effect of the Fermi pressure.

In the next section we will show how the second order correlation function varies during the time-of-flight.

1.4.4 Correlation function after the time-of-flight

In our experiment the atoms are detected when they cross the detector plane, that we fix for simplicity at the position $z = 0$. The second order correlation function is then:

$$G_{det}^{(2)}(\mathbf{r} = \{x, y, z = 0\}, t; \mathbf{r}' = \{x', y', z = 0\}, t') \quad (1.29)$$

This is different from the experiments where absorption imaging is used, because in that case an image of the entire cloud is taken at an instant t . However, if the detection is done in both cases after a long time-of-flight and one can neglect the expansion of the cloud as it passes through the detector, the two correlation functions are nearly the same. The complete calculation of the density and the correlation functions during the expansion can be found in [62]. Here we just recall the idea of the calculation and the expression of $g^{(2)}$ at the detector. First of all, one has to calculate the

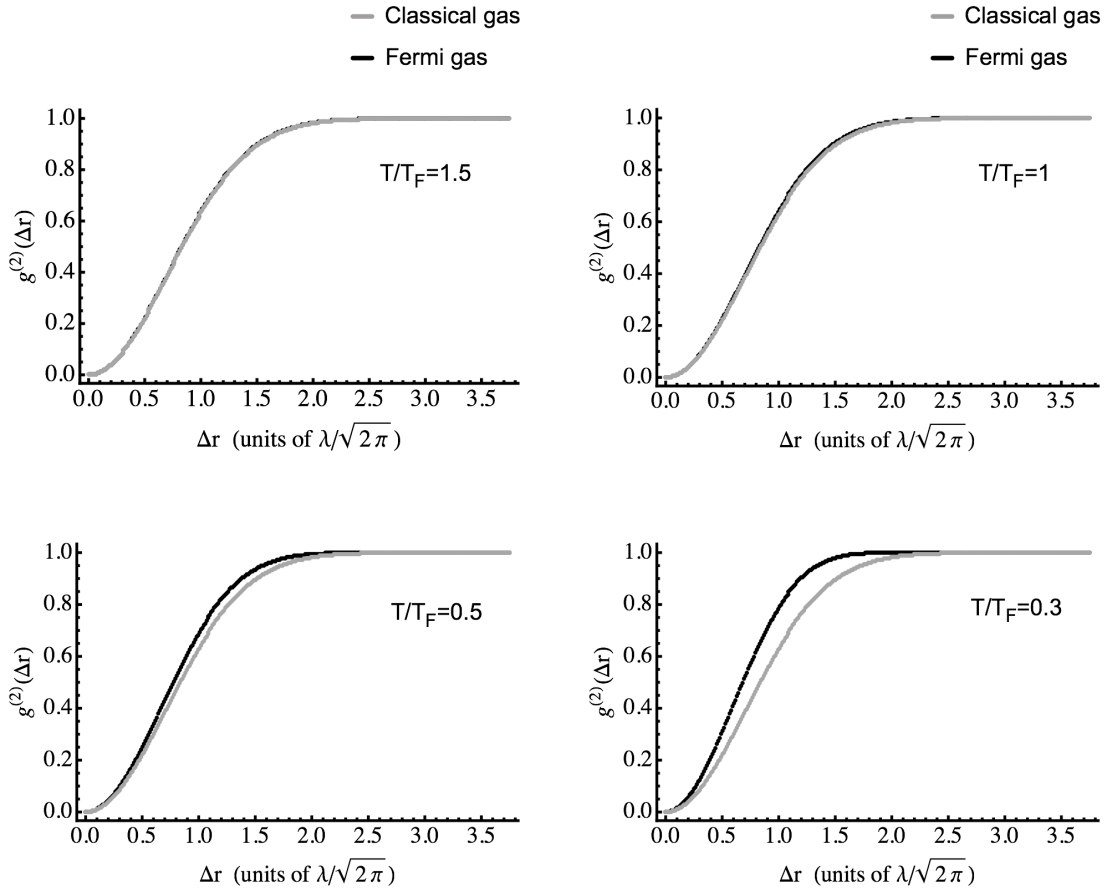


Figure 1.15: Second order normalized correlation function for a gas of fermions trapped in an harmonic isotropic potential. In each graph we plotted in grey $g^{(2)}(\mathbf{r})$ calculated with equation 1.22 and in black the result of the numerical evaluation of 1.28. The two correlation functions show a significant difference for $T/T_F < 1$.

ballistic expansion of the wave functions of the stationary harmonic oscillator state. This can be done analytically and one finds that the interesting part (with respect to intensity interferometry) of the wave function is identical to that in the trap except for a time-dependent scaling factor in the positions. Thereafter one can calculate $G^{(2)}(\mathbf{r} = \{x, y, z = 0\}, t; \mathbf{r}' = \{x', y', z = 0\}, t')$ by using a flux operator that describes the flux of atoms passing through the detector. Finally one finds:

$$G_{det}^{(2)}(\mathbf{r}, t; \mathbf{r}', t') = \frac{2gH}{\prod_{\alpha} \sqrt{(1 + \omega_{\alpha}^2 t^2)(1 + \omega_{\alpha}^2 t'^2)}} [\rho_{trap}(\tilde{\mathbf{r}})\rho_{trap}(\tilde{\mathbf{r}}') - |G^{(1)}(\tilde{\mathbf{r}}, \tilde{\mathbf{r}}')|^2] \quad (1.30)$$

where H is the vertical coordinate of the trap. The expression 1.30 is obtained under two conditions that are verified in our experiment: the size of the cloud after expansion (several mm in our case) has to be much larger than the size of the cloud in the trap

(several tens of μm) and the velocity spread of the cloud (of the order of 6 cm/s) has to be much smaller than the velocity acquired during the time-of-flight (about 3 m/s). It is interesting to note that, under these conditions, we find the same correlation function as in the trap, rescaled by the following factors:

$$\begin{aligned}\tilde{x} &\approx x/(\omega_x t_0) \\ \tilde{y} &\approx y/(\omega_y t_0) \\ \tilde{z} &\approx g(t_0 - t)/\omega_z\end{aligned}\tag{1.31}$$

where $t_0 \approx 358$ ms is the mean time-of-flight. Note that there is a direct correspondence between the arrival time of the atoms and their vertical position with respect to the trap position, for each time t . In fact, since we are neglecting the expansion of the cloud while it passes through the detector, there are two equivalent ways to model the detection process: either the detector is kept at a fixed position ($z = 0$) and the cloud passes through it during a time Δt , or the cloud is frozen at the instant t and the detector moves along the vertical axis measuring the coordinate z of the atoms with respect to its initial position.

Now we can calculate the normalized second order correlation function at the detector. The formulation is analytical for a Maxwell-Boltzmann distribution and is shown in the following part of this section.

Using the equivalence between z and t , we can write, for a cloud of atoms that follows the Maxwell-Boltzmann distribution:

$$\begin{aligned}g_{det}^{(2)}(\mathbf{r}, \mathbf{r}') &= 1 - \prod_{\alpha} \exp\left\{\frac{1}{\omega_{\alpha}^2 t_0^2} \left(\frac{1}{4s_{\alpha}^2} - \frac{2\pi}{\lambda^2}\right) (r_{\alpha} - r'_{\alpha})^2\right\} \\ &\approx 1 - \prod_{\alpha} \exp\left\{-\frac{2\pi}{\lambda^2 \omega_{\alpha}^2 t_0^2} (r_{\alpha} - r'_{\alpha})^2\right\}\end{aligned}\tag{1.32}$$

Again, the formula for bosons will be the same but with a + sign instead of $-$. We find that the correlation length is related to the one in the trap:

$$l_{\alpha} = l_{trap} \times \omega_{\alpha} t_0.\tag{1.33}$$

The scaling law will be the same for the correlation length of a degenerate Fermi gas. In addition, by substituting the expression of the De Broglie wavelength in the expression just obtained for the correlation length we find:

$$l_{\alpha} = \frac{\hbar \omega_{\alpha} t_0}{\sqrt{mk_B T}} = \frac{\hbar t_0}{ms_{\alpha}}\tag{1.34}$$

where s_{α} is the size of the trapped sample. It is interesting to note that, even if the density distribution at the detector is isotropic, the antibunching is not. The correlation function at the detector is related to the correlation in the trap and to the density distribution in the trap. In particular, since the correlation length is inversely proportional to the size of the trapped sample, the antibunching anisotropy is inverted with respect to the trap anisotropy.

In figure 1.16 we plot the correlation length along the three axis as a function of the temperature of the atomic cloud. The trap oscillation frequencies are the ones of the cigar shape trap of the Amsterdam-Palaiseau experiment and the temperature range corresponds to the data acquired during the collaboration. The smaller oscillation frequency is along the x axis and is about ten times smaller than the oscillation frequencies along the y and z axis. Therefore l_x is about ten times smaller than l_{yz} . As we will see in the following section, l_x is much smaller than the detector resolution along x and this has some important consequences on the observed correlation function.

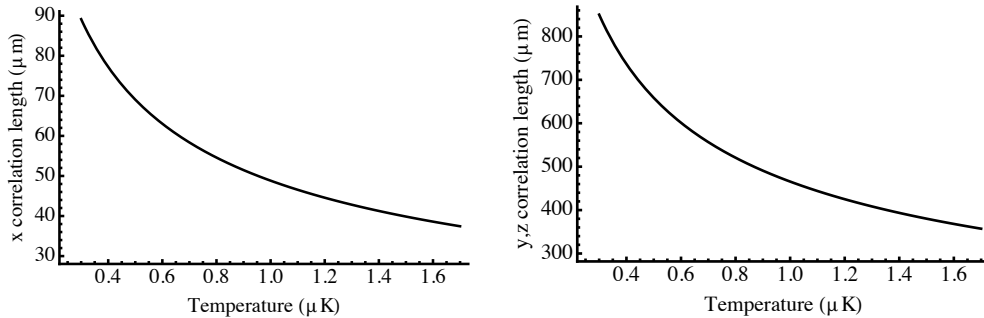


Figure 1.16: On the left: Correlation length along the x axis as a function of the atomic cloud temperature for the experimental parameters of the Amsterdam-Palaiseau experiment. On the right: Correlation length along the y and z axis as a function of the atomic cloud temperature for the experimental parameters of the Amsterdam-Palaiseau experiment.

1.4.5 Effect of the resolution and the detectivity of the detector

In the previous sections we assumed to have an ideal detector, with arbitrarily good resolution and detectivity. In this section we will see how an imperfect detector can affect the measurement of the correlation function.

Imperfect detectivity

Consider first a detector with a detection efficiency homogeneous, but smaller than 100%. The measurement of the correlation function will not be affected. In fact, the detection efficiency can change the number of detected atom pairs, but doesn't change the statistical properties of the sample. If the probability for two atoms to occupy the same quantum state is zero (or two in the case of bosons), it will stay zero (two), even with an finite detectivity.

On the other hand, if the detection efficiency is not homogenous, we have to distinguish between the measurement of the local correlation function and of the correlation function averaged over all the detector. If we call ϵ_r the detection efficiency at the position \mathbf{r} we have:

$$g^{(2)}(\mathbf{R} - \mathbf{r}/2, \mathbf{R} + \mathbf{r}/2) = \frac{\epsilon_{(R-r/2)}\epsilon_{(R+r/2)} G^{(2)}(\mathbf{R} - \mathbf{r}/2, \mathbf{R} + \mathbf{r}/2)}{\epsilon_{(R-r/2)}\epsilon_{(R+r/2)} \rho_{trap}(\mathbf{R} - \mathbf{r}/2) \rho_{trap}(\mathbf{R} + \mathbf{r}/2)} \quad (1.35)$$

Therefore the detection efficiency doesn't affect the normalized correlation function, due to the fact that the detectivity appears at both the numerator and the denominator and it cancels out. In the experiment we measure the correlation averaged over all the detector. In this case the detection efficiency doesn't cancel out in the normalization process and we have:

$$g^{(2)}(\mathbf{r}) = \frac{\int d\mathbf{R} \epsilon_{(R+r/2)} \epsilon_{(R-r/2)} G^{(2)}(\mathbf{R} - \mathbf{r}/2, \mathbf{R} + \mathbf{r}/2)}{\int d\mathbf{R} \epsilon_{(R+r/2)} \epsilon_{(R-r/2)} \rho_{trap}(\mathbf{R} + \mathbf{r}/2) \rho_{trap}(\mathbf{R} - \mathbf{r}/2)} \quad (1.36)$$

If the detection efficiency varies slowly with respect to the correlation length, it can be considered as constant and can be pulled out from the integral. In this case the contribution at the numerator and at the denominator of the normalized correlation function cancels out. Our experiment falls in this last case.

Finite detector resolution

If the detector has a finite resolution, the measured two-body correlation function will result in the convolution between the function that describes the resolution and the expression of $g^{(2)}(\Delta\mathbf{r})$ calculated above (equation 1.32):

$$g_{res}^{(2)}(\Delta\mathbf{r}) = f_{res}(x, y, z) \otimes g^{(2)}(\Delta\mathbf{r}) \quad (1.37)$$

In the following we will refer to the particular case of our detector, but the formula that we will find can be used in a more general context. The resolution of our detector is not the same in the three directions. It is very good, about 3 nm, along the z direction and it is negligible with respect to the correlation length in this direction (between 700 and 400 μm for our samples and our trap frequencies, see figure 1.16). Therefore the expression 1.32 still holds along the z axis. On the xy plane however the resolution is not very good. The method that we use to measure the resolution is explained in appendix A. In first approximation the resolution function of our detector is a Gaussian with standard deviation of about $d_{xy} \approx 250 \mu\text{m}$. It means that the two-atom resolution (at $1/e$) is $\sqrt{2} \times \sqrt{2} \times d_{xy} \approx 500 \mu\text{m}$ ¹. The correlation length (value at $1 - 1/e$, defined by equation 1.34) along the x axis is one order of magnitude smaller as shown in figure 1.16 and it is of the same order of magnitude of the resolution along the y axis. It is then already clear that the resolution will heavily affect the measurement of the correlation lengths, making impossible the measurement along the x direction and delicate the measurement along the y direction. It is interesting to see if the resolution affects only the correlation length or the antibunching height as well. To understand it we calculate the convolution between $g^{(2)}(\Delta x, \Delta y)$ and $f_{res}(x, y)$. Since we are far from degeneracy, the three directions are independent and we can treat them separately. With $f_{res}(xy) = 1/(2\pi d_{xy}^2) \exp\{-(x^2 + y^2)/2d_{xy}^2\}$ one finds:

$$g_{res}^{(2)}(\Delta x, \Delta y, \Delta z) = 1 - \eta \exp\left\{-\frac{\Delta x^2}{L_x^2} - \frac{\Delta y^2}{L_y^2} - \frac{\Delta z^2}{L_z^2}\right\} \quad (1.38)$$

¹The first $\sqrt{2}$ comes from the fact that d_{xy} is the one particle resolution (and not the two-particle resolution) and the second $\sqrt{2}$ comes from the fact that d_{xy} is an rms value instead of the value at $1/e$

where L_x, L_y, L_z are the measured correlation length, convoluted with the detector resolution. The deconvolution gives: $l_\alpha = \sqrt{L_\alpha^2 - (2d_{xy})^2}$ for $\alpha = x, y$. Note that, since $l_x \ll 2d_{xy}$, measuring the correlation length on the x direction is equivalent to measure the two-particle resolution of the detector. Due to the very good resolution on the vertical axis, $l_z = L_z$. The contrast of the correlation function η is given by:

$$\begin{aligned} \eta &= g_{res}^{(2)}(0, 0, 0) - 1 = -\prod_{\alpha} \sqrt{\frac{1 + d_{xy}^2/s_{det}^2}{1 + (2d_{xy})^2/l_\alpha^2}} \\ &\approx -\prod_{\alpha} \sqrt{\frac{1}{1 + (2d_{xy})^2/l_\alpha^2}} \end{aligned} \quad (1.39)$$

with s_{det} the size of the cloud at the detector.

In fact, a careful examination reveals that the resolution function of our detector is not well approximated by a Gaussian because the wings are too broad. A possibility would have been to try with a Lorentzian function, but, as we wanted to keep the expression of $g_{res}^{(2)}(\Delta x, \Delta y, \Delta z)$ simple, we approximated the resolution function with the sum of three Gaussians. The exact formula for the correlation function in this case is given in appendix A. This correlation function has been used to analyse the data presented in chapter 3.

1.5 Conclusion

In this chapter we briefly reviewed the history of the Hanbury Brown Twiss effect and we set the context of the birth of the modern quantum optics. Thereafter we have derived a simple quantum mechanics explanation of the Hanbury Brown Twiss effect for two point-like sources, that allows to highlight the different statistics followed by bosons and fermions: bosons tend to arrive bunched on the detector, while fermions tends to stay far apart. This is a consequence of the Pauli exclusion principle. If a classical explanation of the Hanbury Brown Twiss effect exists for photons, that are bosons, it is not the case for fermions, that don't have a classical counterpart. For this reasons it is interesting to repeat the Hanbury Brown Twiss experiment with a sample of fermions. Experiments have been carried out on electrons in solids and in vacuum, on neutrons and on samples of ultracold atoms. The experiment we made within a collaboration with the group of W. Vassen joins this stream. We measured the correlation function for a cold cloud of bosons and fermions produced in the same experimental apparatus and at the same temperature and we were able to quantitatively compare the results obtained for the two species.

Since the shape of the correlation function depends on the characteristics of the sample on which it is measured, we derived the expression of the second order correlation function for a cold cloud in a harmonic trap. We discussed the difference between the correlation obtained for a thermal sample and for a degenerate cloud of fermions. Due to the Fermi pressure, the size of a trapped cloud cooled below the Fermi temperature is larger than the size of a non degenerate cloud and the density distribution

is no longer Gaussian. Therefore the shape of the correlation function is not Gaussian and the correlation length is smaller than the one obtained for a degenerate sample. However we showed that this effect is small if we average over all the cloud.

Finally we derived the expression of the correlation function after the time-of-flight and we discussed the effect of the finite detector resolution and of an imperfect detection efficiency on the measured correlation function.

In chapter 3 we will compare the theoretical results derived here with our experimental data. In the next chapter we will describe the experimental setup used in the Amsterdam-Palaiseau collaboration.

Chapter 2

Amsterdam Experimental Setup

At the beginning of July 2006 we started a collaboration with the group of Wim Vassen, at the Laser Centre of the Vrije Universiteit, in Amsterdam. The goal was to measure the Hanbury Brown Twiss effect on a fermionic cold cloud in order to study antibunching in an ultracold Fermi gas of neutral atoms.

The Amsterdam group recently succeeded in the production of a Fermi gas of ^3He , becoming the only group in the world having a degenerate Bose-Fermi mixture of metastable helium [63], [41]. At the same time the ability of the Orsay detector in measuring 2-body correlation functions in 3 dimensions had already been demonstrated [40]. Therefore we just needed to combine the expertise of the two groups and perform the experiment. Indeed, we installed the Orsay detector in the Amsterdam vacuum apparatus and, after a short bake-out of the chamber, we performed the experiment. We produced cold clouds of ^3He and ^4He at different temperatures between $0.5\ \mu\text{K}$ and $1.5\ \mu\text{K}$ in a magnetic trap. After the desired temperature was reached, we switched off the trap, let the clouds fall on the detector under the effect of gravity, and we measured the two body correlation function in three dimensions.

Working on this experimental setup has been an enriching experience. Not only it gave us the possibility to look into a setup similar, rather not identical, to ours, but also to deeply investigate the differences in the production of degenerate cloud of ^3He and of ^4He . Since our group is planning to introduce ^3He in our experimental setup, this experience was useful to point up the changes we should make in the Palaiseau setup to cool ^3He as well. The detail of these upgrades together with an outlook of the Amsterdam setup are the main topic of this chapter. In addition we will compare the experimental parameters used in the two experiments. In the next chapter we will describe the data analysis and the obtained results.

2.1 Helium atomic structure

Helium lines were observed for the first time in 1868 by the French astronomer Pierre Janssen in the solar spectrum. Since this element was unknown on the Earth (where it was isolated only 27 years later) it was decided to call it Helium, from the name of

the mythological greek god of sun.

Helium is the lighter of the rare gases, its atomic number is equal to 2 and it is present in nature with two isotopes, ^3He and ^4He . While ^4He has nuclear spin equal to zero, ^3He has nuclear spin equal to $\frac{1}{2}$ and therefore exhibits hyperfine structure (see section 2.3.2).

Since helium has two electrons, its energy spectrum consists of two nearly independent systems of levels, one made of singlet states and the other made of triplet states. Because intercombination lines are highly forbidden, helium has two metastable states, one in the triplet and one in the singlet spectrum, which have a very long lifetime: since the ground state is a singlet state, singlet metastable state has a lifetime of 19.6 ms, while triplet metastable state has a lifetime of 7900 s. This makes metastable triplet helium a good candidate to obtain a Bose-Einstein condensate. In addition, since unlike the ground state its magnetic moment is different from zero, it can be magnetically trapped and it has several optical transitions that are available for laser cooling.

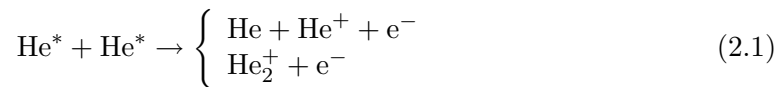
Another important feature of helium is that the internal energy of the metastable state is 19.8 eV. This makes metastable helium very interesting because one can use a micro-channel plate to detect clouds of neutral atoms (see appendix A for a description of the detector).

2.2 A Bose-Fermi mixture of metastable atoms

Before the achievement of the Fermi gas in Amsterdam, there were two open questions about the possibility of cooling ^3He to degeneracy. The first one concerned the suppression of Penning ionization in ^3He - ^3He and ^3He - ^4He collisions in a polarized sample, the second one concerned the ^3He - ^4He scattering length, responsible of the efficiency of the ^3He cooling process.

Penning ionizations

Due to the large energy of the metastable state, metastable Helium (He^*) shows an important inelastic collision rate. When two He^* atoms collide, the energy of the system is enough to ionize one of the atoms (the ionization energy is 25 eV), leading to Penning ionizations:



Penning ionizations induce losses in the sample during all the phases of its preparation and are enhanced by the presence of the MOT laser [64] (see section 2.3.5). In the absence of the laser, the ionisation rate for an unpolarized sample decreases by a factor of ≈ 100 , but is still of the order of $5 \times 10^{-10} \text{ cm}^3/\text{s}$ for ^4He . However, atoms in a magnetic trap are spin-polarized (see section 2.3.6) and in this case Penning ionization for ^4He are suppressed by 5 orders of magnitude, due to spin conservation [65], [66].

This makes possible the achievement of high densities in the magnetic trap and ^4He Bose-Einstein condensation can be realized through evaporative cooling.

Since the Penning ionization rate was unknown for ^3He - ^3He collision as well as for ^3He - ^4He collisions, a similar suppression of losses for a mixture loaded in a magnetic trap was not certain and the lifetime of the mixture in the trap was unpredictable. Even if a precise measurement of the 2-body losses rate for a polarized sample of ^3He or ^3He - ^4He has not been done yet, the achievement of a degenerate Fermi gas of ^3He atoms shows that 2-body losses are suppressed in a ^3He - ^4He mixture as well. A rough measurement of the 2-body losses rate can be inferred from [41]. The Amsterdam team measured a lifetime of a pure polarized sample of either ^3He or ^4He in a magnetic trap of ≈ 110 s, limited by collisions with residual background gas, while they measured a lifetime of a polarized mixture of ≈ 100 s. From [41] we can extract the value of the density of the clouds and their temperature and give an estimation of the ^3He - ^4He ionization rate. The density was 2.2×10^{11} at/cm³ for ^4He and 6×10^8 at/cm³ for ^3He , while the temperature was the same for the two gases (130 μK). With these numbers a rough calculation gives a 2-body heteronuclear ionization rate of $\leq 4 \times 10^{-12}$ cm³/s. This rate is larger than the ^4He - ^4He ionization rate ($\approx 5 \times 10^{-15}$ cm³/s for a spin polarized sample), but the induced losses are still small with respect to the losses induced by collisions with the background gas. Close to degeneracy the density gets higher and the 2-body and 3-body ionizations become the dominant loss cause. With the heteronuclear ionization rate calculated above, the lifetime of a mixture with a density of 10^{12} at/cm³, would be of the order of few hundreds ms, which is still reasonable.

Heteronuclear scattering length

The second important issue was the ^3He - ^4He s-wave scattering length. In order to obtain a Bose-Einstein condensate, bosons are usually first trapped in a magnetic trap and then cooled by sweeping an RF frequency that couples the trapped state to a non-trapped state and that selectively removes the hotter atoms (see section 2.3.6). Elastic collisions then thermalize the sample, that is brought in this way to quantum degeneracy. This cooling process is called evaporative cooling.

At the temperature of interest these collisions are primarily s-wave in nature and are then forbidden for identical fermions. The method generally used to cool a fermionic sample is called sympathetic cooling [67], [31], [33] and consists in immersing the fermions in a bath of bosons. When bosons are evaporatively cooled, they collide with fermions that then thermalize at the bosons temperature (see section 2.3.6). The efficiency of the cooling process depends on the value of the heteronuclear scattering length and on the density of the samples. This value has been predicted by theory to be $a_{34} = 28.8_{-3.3}^{+3.9}$ nm [68], but has not been measured yet. An estimation of the scattering length is given by the measurement of the lifetime of the ^4He condensate in presence and in absence of ^3He . In fact, such a large value for the heteronuclear scattering length leads to expect that 3-body losses rate will be large, because it scales as a^4 [69], [41]. The theoretical estimation of the boson-boson-fermion rate constant

and the measured lifetime of a pure condensate and of a degenerate mixture seem to confirm the value of the scattering length given above [41]. In addition, no evidence for mixture collapse seems to confirm the positive value for the scattering length.

2.3 Experimental sequence

In this section we will concentrate on the production of a cold cloud of ^3He and, as we said in the introduction, we will underline the important changes we should make on the French setup in order to cool ^3He .

For the reasons explained above, reaching the Fermi temperature is possible by sympathetically cooling the ^3He with ^4He . Consequently the two species must be loaded together in the magnetic trap. The experimental steps are the following:

1. A ^3He - ^4He mixture at room temperature is first prepared in a reservoir, filled with a given percentage of the two gases.
2. The mixture is then excited to the metastable state by using a DC discharge.
3. The atomic beam at the output of the discharge is then collimated transversally.
4. A Zeeman slower, that connects the source chamber to the magneto-optical-trap (MOT) chamber, is then used to slow the atoms from a velocity of ≈ 1050 m/s to ≈ 60 m/s.
5. A two species MOT is then loaded.
6. The sample is transferred in a magnetic trap where it is cooled by using 1D Doppler cooling (see section 2.3.6).
7. The magnetic trap is then compressed (in order to increase the atomic density and the collision rate). ^4He is cooled by a RF evaporation ramp and ^3He is sympathetically cooled by collisions with ^4He .
8. ^4He is expelled from the trap by a RF sweep. The magnetic trap is switched off and ^3He time-of-flight is detected.

A sketch of the experimental setup is shown in figure 2.1. The experimental sequence used to prepare a ^4He sample is the same as the one used to prepare a ^3He sample. However in this case only ^4He atoms enter the source chamber and are loaded in the magnetic trap. The sample is then cooled to the desired temperature and the time-of-flight is detected by switching off the magnetic trap.

The Amsterdam experimental sequence has no fundamental differences from the Palaiseau sequence. Differences in the experimental parameters will be pointed out throughout this section.

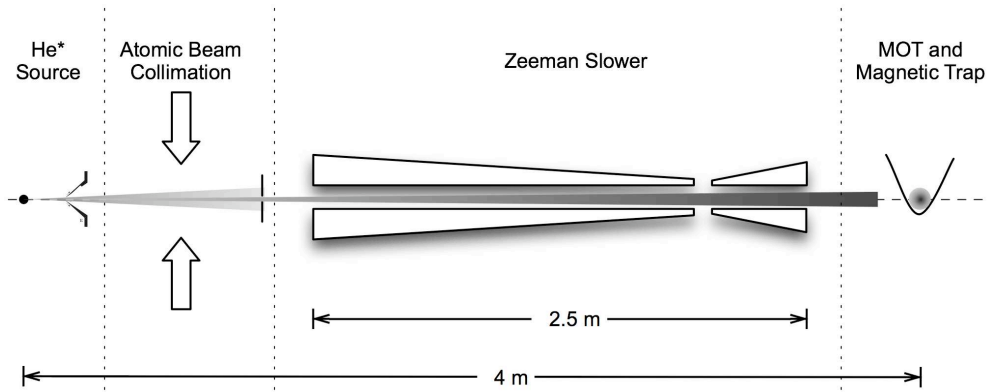


Figure 2.1: Sketch of the experimental setup.

2.3.1 Source and recycling system

The source used in Amsterdam to excite the atoms in the metastable state is similar to the one used in Palaiseau. Helium gas at room temperature is injected in the vacuum chamber where it is excited by an electric DC discharge maintained between a needle (held at high voltage) and a skimmer (grounded), as shown in figure 2.2. The discharge

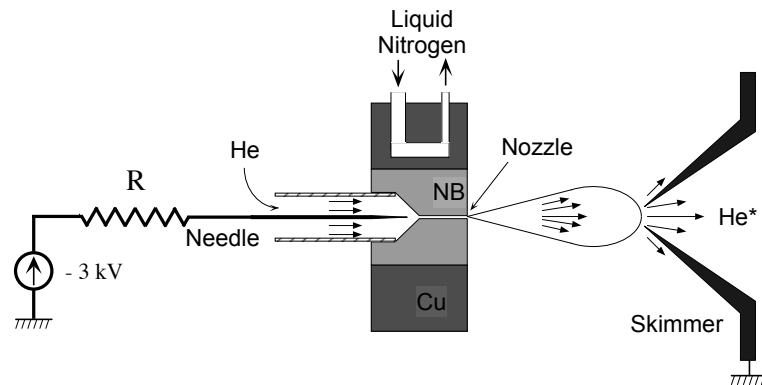


Figure 2.2: Sketch of the source used to excite helium atoms to the metastable state (see text). The Boron nitride block (light grey) is inserted in a copper block (dark grey) that is cooled by liquid Nitrogen.

is maintained through a nozzle, situated very close to the needle. The nozzle is a narrow and long canal (diameter $\approx 200 \mu\text{m}$, length $\approx 1 \text{ cm}$) drilled in a piece of boron-nitride cooled by liquid nitrogen. Boron nitride is a material that presents poor electric conductivity and good thermal conductivity. The collisions between the atoms and the Boron nitride walls decrease the initial velocity of the atoms and create a supersonic beam at the end of the canal. The excitation efficiency is of the order of one atom

excited out of 10^4 atoms remaining in the ground state. Typical beams contain 10^{12} atoms/s with a longitudinal velocity of 1200-1300 m/s.

Since the natural abundance of ^3He is just 1.4×10^{-6} , ^3He is very expensive. Then, when the source is used for ^3He or for a ^3He - ^4He mixture a recycling apparatus is used to purify and recycle the gas. This is one of the major modification we need to introduce in the French setup in order to cool ^3He . During the moving of the laboratory from Orsay to Palaiseau we have already prepared the installation of the recycling system. In fact, we replaced the diffusion and rotary pumps used to make the vacuum in the source chamber with turbo and dry pumps. The absence of oil in the recycling system is an advantage when the gas has to be kept clean (see for comparison [70]).

In the Amsterdam setup the recycling apparatus is connected to the source chamber so that the gas that does not end up in the beam is pumped out, filtered and then re-injected in the source chamber. Figure 2.3 shows a sketch of the recycling system.

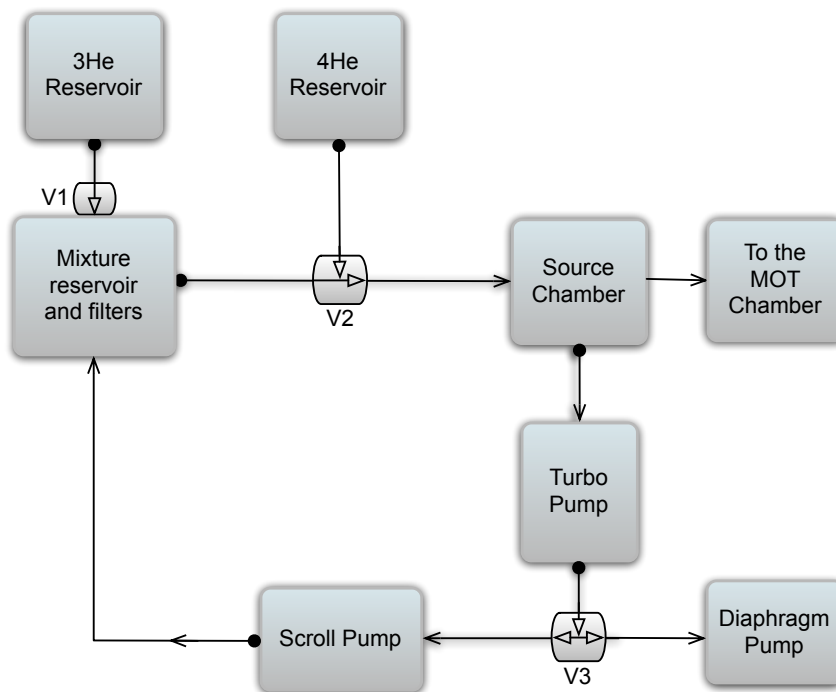


Figure 2.3: Sketch of the recycling system used in the Amsterdam setup when ^3He is injected in the apparatus (see text).

When the recycling system is in operation, helium is injected into the chamber from the ^3He - ^4He reservoir that is prefilled with a given percentage of ^3He and ^4He . Atoms that do not go into the atomic beam are pumped by a turbo pump that is backed by a scroll pump. The exhaust of the scroll pump is injected in a two stage filter, liquid nitrogen cooled, that contains two different kinds of sodium zeolites. This filter

traps everything but helium. At the output of the filter, the gas passes in the needle valve (V2) and is injected in the source chamber. Valves 1 and 2 allow to change the percentage of ^3He and ^4He in the system during the operation. If the experiment is run with ^4He the scroll pump and the filters are excluded from the system, by commuting valve 2 and 3, and the turbo pump is backed by a membrane pump. The output of the latter is the atmosphere and the helium is lost. The use of a scroll pump instead of a membrane pump in the recycling system is related to the requirement to have a closed circuit: scroll pumps allow a larger exhaust pressure, ensuring a better ultimate vacuum and a higher pumping speed, all things that can benefit to the working of a turbo pump in a closed circuit.

2.3.2 Laser cooling transitions and laser system

The transition used to laser cool ^3He and ^4He is the $2^3\text{S}_1 \rightarrow 2^3\text{P}_2$ at a wavelength of 1083 nm. The level scheme for this transition is shown in figure 2.4. The line width is $\Gamma/2\pi = 1.6$ MHz. The isotopic shift is about 30 GHz for the transition used for laser cool ^3He and ^4He . The use of two laser systems is then necessary when one wants to cool a ^3He - ^4He mixture. Therefore, in view of the introduction of ^3He in the Palaiseau setup, we should double the actual laser system and reorganise it in order to install all the optics on the same optical table.

As one can see in figure 2.4, the excited state is split in 3 fine structure components with $J=0,1,2$. The multiplet is inverted so that the 2^3P_0 has a energy higher than the 2^3P_1 . ^3He structure is a bit more complicated due to hyperfine level splitting. The metastable state is split in two (with $F=1/2$ and $F=3/2$) and the 2^3P_2 and the 2^3P_1 are both split into two hyperfine components. Due to the isotopic shift the ^3He levels have on average an energy smaller than ^4He levels. The $2^3\text{P}_{0,1/2}$ is higher than the 2^3P_2 by 811 MHz. Since the laser cooling transitions are the $2^3\text{S}_1 \rightarrow 2^3\text{P}_2$ for ^4He and the $2^3\text{S}_{1,3/2} \rightarrow 2^3\text{P}_{2,5/2}$ for ^3He , this can cause some depumping during the laser cooling phase. We will address this problem in the section 2.3.5.

Laser system

In the Palaiseau setup four distributed Bragg reflector (DBR) diode lasers at 1083 nm are used, in order to generate collimation, Zeeman slower, MOT, spin polarization and 1D Doppler cooling beams. DBR lasers have an output power of ≈ 40 mW and a linewidth of ≈ 2 MHz.

In the Amsterdam setup the lasers used during the cooling steps are of different type. The largest part of the light power is provided by a fiber laser for ^3He and by a solid state LNA laser for ^4He [71].

The ^3He laser (IPG YLD-1BC-1083) is an Ytterbium fiber laser, it has a nominal output power of 1 W and a linewidth of ≈ 2 MHz. It provides all the power needed for ^3He trapping, but for spin-polarization. For the latter a Toptica DL100 external cavity diode laser is used. The output power is ≈ 40 mW [71].

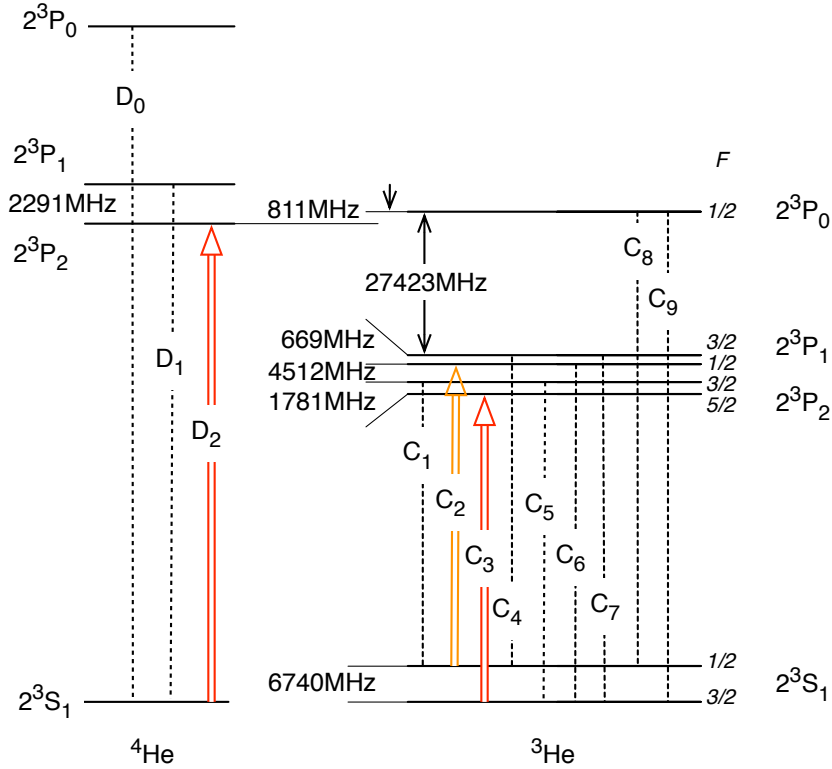


Figure 2.4: On the left, scheme of the optical transitions used to laser cool ^4He . On the right, scheme of the optical transition used to cool ^3He . Since the isotopic shift is about 30 GHz, a double laser system is needed. The transitions C_3 and D_2 are used to cool ^3He and ^4He respectively. An additional laser resonant with the transition C_2 of the ^3He is needed as a repumper.

For the ^4He laser, an LNA crystal is the active medium and is placed inside a ring cavity. The crystal is pumped with a 4 W laser at 532.2 nm. To force the system to operate on a single mode at 1083 nm a system of filters and etalons is used. The output power at 1083 nm is 250 mW. The cavity is locked to a Fabry-Perot interferometer which is locked to the $2^3\text{S}_1 \rightarrow 2^3\text{P}_2$ line. When locked, the laser has a linewidth of ≈ 160 kHz [71]. Due to cavity instability (induced for example by room temperature drifts), the LNA laser is quite unstable and difficult to lock and turned out to be one of the more time demanding device of the Amsterdam setup, during the Hanbury Brown Twiss data acquisition.

The LNA laser is used to generate collimation, Zeeman slower, and MOT beams. For spin-polarization and 1D Doppler cooling two DBR lasers are used, the one for the Doppler cooling in extended cavity configuration (linewidth ≈ 500 kHz).

In both setup lasers are locked with a saturated absorption scheme on He^* cells. The laser power available in the Amsterdam setup is much larger than the total power

available in the Palaiseau setup. This can explain why our experiment is less stable and, on average, the number of trapped atoms is smaller than in the other setup. Recently, a laser amplifier has been implemented in our experimental apparatus, improving these two aspects in agreement with our expectations.

2.3.3 Atomic beam collimation

After leaving the source the atoms enter in a second vacuum chamber, separated by the first one by the small opening in the skimmer, where the atomic beam is collimated in horizontal and vertical direction. Collimation is useful for two reasons: it increases the metastable beam intensity and separates metastable and ground state atoms.

Collimation is made applying the so-called curve-wavefront technique [72], [73]. The radiation pressure force exerted on the atoms by two pairs of counter-propagating laser beams is used to change the atomic trajectory. The laser beams are resonant with the $2^3S_1 \rightarrow 2^3P_2$ transition for ^4He and with $2^3S_{1,3/2} \rightarrow 2^3P_{2,5/2}$ for ^3He , are linearly polarized and have an elliptical profile with the long axis parallel to the atomic beam propagation direction. In order to keep the Doppler shift constant, the beams are convergent and have a curvature radius that matches the curvature of the atomic trajectory. In this way the atoms are always in resonance with the laser and the collimation process is efficient over all the interaction region.

In the Amsterdam setup the curvature radius is 15 m for the vertical beam and 11 m for the horizontal beam. The total amount of power in the collimation section is 190 mW and the length of the interacting region is about 19 cm. The curvature radius used in Palaiseau is larger (about 30 m), the total power is approximately 30 mW and the length of the interaction region is about 10 cm. Since the parameters used for the collimation of the atomic beam depends on the divergence of the atomic beam and therefore on the particular geometry of the source, it is hard to compare the two experimental setups.

In the Amsterdam setup the metastable beam is not only collimated but also deflected on the horizontal plane. The first half of the horizontal beam is used for collimation while the second half of the retroreflected beam is blocked, in order to deflect the atomic beam by about 1° . A knife edge is positioned close enough to the metastable beam axis, so that it blocks the beam of ground state atoms. In addition the metastables propagate in the Zeeman slower towards the trap chamber in the shadow-area of the knife edge. Therefore, when the collimation laser is off, hardly any atom will enter the trap chamber and perturb the trapped cloud. These two expedients have the result of increasing the lifetime of the magnetically trapped cloud.

In the French setup the atomic beam is only collimated and not deflected. Therefore both ground state atoms and metastable atoms can eventually reach the science chamber. However, since ground state atoms are not resonant with the collimation laser, their divergence is larger than for atoms in the metastable state. By subsequently passing the atom beam through small pinholes inserted inside the Zeeman slower tube (see section 2.3.4), a large fraction of the ground state atoms are filtered away. In addition, to avoid a perturbation of the experiments in the ultrahigh vacuum chamber due to the

continuous atomic beam, a mechanical shutter situated at the end of the collimation stage is closed once a sufficient number of atoms has been collected in the MOT. At the same time the collimation beams are switched off.

2.3.4 The Zeeman slower

After leaving the collimation region the atoms enter the Zeeman slower, a 2.5m long tube that connects the source chamber with the trap chamber. In the Zeeman slower the atoms experience a longitudinally decreasing magnetic field that, in combination with a counter-propagating laser beam, slows the atoms down, due to the simultaneous presence of Zeeman and Doppler effect. Owing to their different masses ^3He and ^4He have two different velocity distributions after the skimmer. Therefore, the capture velocity of the Zeeman slower has to be increased in order to slow ^3He . The Zeeman slower of the Amsterdam setup can be used to slow both isotopes (at the same time or separately) by using the two cycling transitions used for the collimation with a detuning with respect to the atomic resonance of -250 MHz. The magnetic field goes from 517 G to -140 G, consequently the atoms are slowed from 1055 m/s to 58 m/s [74]. The quantity of atoms slowed by the Zeeman slower depends of course on the velocity distribution of the atoms at the beginning of it. The velocity distribution depends in turn on the operation mode of the source. Assuming a similar velocity distribution for the atoms issued from the French and the Dutch source, the French Zeeman slower should be able to slow the ^3He as well: with a magnetic field ranging from 450 G to -280 G and a detuning of -400 MHz the atoms are brought from 1116 m/s to 80 m/s [75].

In the Amsterdam setup, the Zeeman slower beam has a power of ≈ 15 mW, it has a diameter in the trap chamber region of 3 cm and it focuses on the source chamber skimmer, as in the French setup. A $\lambda/4$ waveplate assures a perfect σ^+ polarization: without this, due to a level crossing between ^3He and ^4He occurring at 200 G, ^3He atoms are pumped to non-slowed magnetic substates and are lost [76].

At the end of the Zeeman slower the atoms can be loaded in the magneto-optical trap.

2.3.5 The two species magneto-optical trap

The magneto-optical trap (MOT) uses the combination of a gradient of the magnetic field with 3 pairs of counter-propagating beams to cool and trap the atoms. The field gradient is generated by two coils in anti-Helmholtz configuration. In the Amsterdam setup its value is 19 G/cm on the axis, while in the Palaiseau setup it is 50 G/cm. The gradient of the magnetic field on the radial axis is equal to half these values.

The light beams are generated, in both setups, from a single beam split into three pairs of retroreflected beams: one propagates along the horizontal axis (perpendicularly to the Zeeman slower), the others propagate in the vertical plane that contains the Zeeman slower. As we have already mentioned, the optical power available in the Dutch setup is larger than the power available in the French setup. The MOT beams

have a total power of 15 – 30mW in Amsterdam and a diameter of 3 – 4 cm, while they have a total power of 10 mW and a smaller diameter (about 2 cm) in Palaiseau. Their intensity is about the same in both experiments, corresponding to 5 – 10 mW/cm² ($I_{sat} = 160 \mu\text{W}/\text{cm}^2$).

The detuning of the MOT beams is quite large ($\Delta = -35 \text{ MHz} \approx -22\Gamma$ in Amsterdam and $\Delta = -54 \text{ MHz} \approx -34\Gamma$ in Palaiseau) with respect to the detuning used for other atomic species (for example, the detuning of Rubidium MOT beams is typically about -3Γ). This allows us to minimize light assisted Penning ionizations (see section 2.2), where the two colliding atoms are one in the 2^3S_1 state, the other in the 2^3P_2 state. A larger detuning decreases the population of the 2^3P_2 state and therefore light assisted collisions. The drawback is a relatively high temperature. In fact, the temperature of an helium MOT in the experimental conditions described above is about 1mK, much higher than the Doppler temperature ($40\mu\text{K}$), obtained for $\Delta = -\Gamma/2$.

The Amsterdam setup is able to trap about 1.5×10^9 ^4He atoms at a temperature of about 1mK [41], while the number of atoms trapped in the Palaiseau setup is about 5×10^8 at the same temperature. We would like to point out that a comparison between the two MOT is not possible for several reasons. First, our actual detection system makes the measurement of the number of atoms in the MOT quite inaccurate. This is mainly due to the long distance between the micro-channel plate and the centre of the trap (46 cm in Palaiseau). The observed time-of-flight of the MOT has a strange shape that does not follow the shape obtained theoretically by just assuming a ballistic expansion of the atomic cloud. In addition we do not know the detection efficiency of our micro-channel plate (see appendix A). The number given above refers to an old measurement made with an absorption imaging system [75].

Due to the fact that ^4He has no hyperfine structure, a repumper is not needed during the MOT phase. The situation for ^3He is different as we saw above (section 2.3.2). As one can see in figure 2.4, if one loads a single specie ^3He MOT, the large intensity of the trapping light excites C5 transition that populates the $2^3\text{S}_{1,1/2}$ state. However a repumper is not explicitly needed because C2 and C4 transitions are close enough to Zeeman slower and MOT light to be excited as well and to repump the atoms in the $2^3\text{S}_{1,3/2}$ level [76].

The loading of a two species MOT is more tricky. The ^4He MOT light is almost resonant with the C9 ^3He transition that brings the atoms in the $2^3\text{P}_{0,1/2}$ state. From there they can decay in $2^3\text{S}_{1,1/2}$. At that point the repumping via C2 and C4 already present is not enough to compensate losses and a repumping light is needed [41]. To generate it a part of the Zeeman slower light is reflected back in the AOM that provides the -250MHz Zeeman slower detuning. After the second passage in the AOM the detuning is double and the light generated is almost in resonance with C2 [71].

The Dutch setup is able to trap 7×10^8 ^3He atoms at a temperature of about 1mK [41]. The relative number of atoms can be changed by adjusting the ratio in the ^3He - ^4He reservoir or by loading ^3He and ^4He MOT for a different time. As we will see in the following sections, in order to further cool the sample we need an excess of ^4He : the number of ^3He atoms in the two species MOT is therefore reduced to $\approx 10^7$.

2.3.6 The Magnetic Trap

The two species are then loaded in a Ioffe-Pritchard magnetic trap, in clover-leaf configuration [77]. The magnetic trap used in the Dutch setup is the same as the one used in the French setup. The magnetic field is generated by 12 coils that are inserted in two re-entrant flanges to be as close as possible to the center of the chamber. The trapping potential has a cylindrical symmetry and is obtained by superposing a dipolar field along the x axis to a quadrupole field on the yz plane¹. The magnetic field is different from zero at the center of the magnetic trap, a very important feature to avoid Majorana spin flips. The magnetic field is given by:

$$\mathbf{B} = B_0 \begin{pmatrix} x \\ 0 \\ 0 \end{pmatrix} + B' \begin{pmatrix} 0 \\ -y \\ z \end{pmatrix} + B'' \begin{pmatrix} x^2 - \frac{1}{2}(y^2 + z^2) \\ -xy \\ -xz \end{pmatrix} \quad (2.2)$$

where B_0 is the bias field and B' and B'' are the gradient and the curvature of the magnetic field respectively. If $|x| \ll \sqrt{\frac{B_0}{B''}}$ and $\sqrt{y^2 + z^2} \ll \frac{B_0}{B'}$, the modulus of the field is given by:

$$B(x, y, z) = B_0 + B''x^2 + \left(\frac{B'^2}{2B_0} - \frac{B''}{2} \right) (y^2 + z^2) \quad (2.3)$$

and the trap is harmonic. This approximation is valid if $k_B T \ll 2\mu_B B_0$ [78], i.e. for large values of the bias field or for low temperature of the sample, when the atoms explore just a small region of the trapping potential, near to the center of the trap. It is evident from equation 2.3 that the confinement along the radial direction can be increased simply by decreasing the value of B_0 .

The trapped states are the $2^3S_{1,3/2}$, $m_F = 3/2$ for ^3He and the 2^3S_1 , $m_J = 1$ for ^4He . In order to have a good transfer efficiency from the MOT to the magnetic trap, the latter has to match the shape of the cloud previously trapped in the MOT. Therefore, the magnetic trap has to be very shallow (large B_0) and its depth has to be several mK, when it is switched on. In addition, prior to magnetic trapping, the two species are further cooled by applying a phase of three-dimensional molasses and they are spin polarized in the trapped states, in order to suppress Penning ionizations. During the molasses phase the MOT beams are switched on for a duration of few ms with a smaller intensity and a smaller detuning with respect to the MOT phase. At the same time a magnetic field is switched on to compensate any spurious magnetic field. At the end of this phase the temperature of the cloud is smaller and the transfer in the magnetic trap is more efficient.

The trapping potential can be written as:

$$U(\mathbf{x}) = \frac{1}{2} M_{4(3)} (\omega_x^2 x^2 + \omega_y^2 y^2 + \omega_z^2 z^2) \quad (2.4)$$

$$= \mu_B g_{4(3)} m_{J(F)} B(\mathbf{x}) \quad (2.5)$$

¹Note that, for the sake of uniformity with other chapters, the axis of the trap is denoted with x instead of z as more customary.

where $M_{4(3)}$ is the ^4He (^3He) mass, $g_{4(3)}$ is the gyromagnetic ratio for ^4He (^3He) in the trapped states. $B(\mathbf{x})$ is the modulus of the magnetic field given by eq.2.3. From equation 2.5 one can deduce the trapping frequencies:

$$\omega_x = \sqrt{\frac{2\mu_B g_{4(3)}}{M_{4(3)}} B'' m_{J(F)}} \quad (2.6)$$

$$\omega_{y,z} = \sqrt{\frac{2\mu_B g_{4(3)}}{M_{4(3)}} \left(\frac{B'^2}{2B_0} - \frac{B''}{2} \right) m_{J(F)}} \quad (2.7)$$

Since both ^3He and ^4He are trapped in the fully stretched states, the gyromagnetic ratios are $g_4 = 2$ and $g_3 = \frac{4}{3}$ and the two isotopes feel the same trapping potential. However, due to the mass difference, the trap frequencies will be different and they will scale with the square root of the inverse mass ratio.

When the atoms are in the magnetic trap they are further cooled in two steps: a first phase of Doppler cooling made at high bias field (≈ 25 G in the two experimental setups), followed by a phase of evaporative and sympathetic cooling where the trap is compressed by decreasing the bias field (to a value of 0.75 G in the Amsterdam setup and to a value of 0.25 G in the Palaiseau setup) in order to increase the density of the sample and hence the collision rate.

1D Doppler cooling

1D Doppler cooling starts after the spin polarization phase. A very weak laser σ^+ polarized is switched on along the x direction. The beam is retroreflected and it is red-detuned with respect to the atomic resonance at the center of the trap. The intensity of the beam is about 1% of the saturation intensity. During the Doppler cooling phase the bias field is high (25 G) in order to well define the quantization axis and hence the beam polarization. As said above, if the polarization is not pure, the laser light will depolarize the sample, introducing losses. Photons in the laser beam are absorbed by the atoms moving towards the beam direction, resulting in the cooling of the sample in the x direction. The sample is then denser and optically thicker. Cooling in the other directions can be induced by two mechanisms: thermalizing elastic collisions and reabsorption of spontaneously emitted photons [79], [63]. The importance of the second mechanism is proved by the fact that when only ^3He is loaded in the magnetic trap and therefore elastic collisions are forbidden, 1D Doppler cooling still reduces the temperature in all directions. This effect is also apparent in the mixture. In fact, even if the application of 1D Doppler cooling to ^4He reduces the temperature of ^3He through sympathetic cooling, the simultaneous application to ^3He increases the efficiency of the process [41], meaning that the reabsorption of spontaneously emitted photons plays a role.

The intensity and the bias field used in both experimental setups are the same. The duration of the application of the Doppler cooling laser can vary depending on the initial atom number and therefore on the cloud density. It is normally shorter (2 – 6 s) in the Amsterdam setup than in the Palaiseau setup (4 – 10 s). The cloud temperature

reached in Amsterdam at the end of the Doppler cooling phase is of the order of $150 \mu\text{K}$ without loss of atoms [41], while in Palaiseau we normally reach temperatures of the order of $300 \mu\text{K}$.

Evaporative cooling

After the Doppler cooling phase, the bias field is lowered, compressing the trap. This way the density of the sample increases and the collision rate gets larger. When we acquired the data for the Hanbury Brown Twiss experiment, the trapping frequencies, when the trap was fully compressed, were $\omega_x/2\pi = 54 \text{ Hz}$ and $\omega_{y,z}/2\pi = 506 \text{ Hz}$ for ^3He and $\omega_x/2\pi = 47 \text{ Hz}$ and $\omega_{y,z}/2\pi = 440 \text{ Hz}$ for ^4He . The final trapping frequencies in the Palaiseau setup are different: $\omega_x/2\pi = 47 \text{ Hz}$ and $\omega_{y,z}/2\pi = 1150 \text{ Hz}$ for ^4He .

As previously said, since ^3He is a fermion, s-wave collisions are forbidden and ^3He is cooled by thermalizing via elastic collisions with ^4He , which in turn is cooled by evaporative cooling. If the mixture is in thermal equilibrium ^3He reaches the same temperature as ^4He . This process is called sympathetic cooling.

The idea behind evaporative cooling is to remove from the trap the most energetic atoms. The remaining atoms will undergo elastic collisions and will thermalize at a temperature lower than the initial one [80]. The larger the collision rate, the faster the thermalization process will be. For this reason the trap is compressed before starting the evaporative cooling process. Experimentally the atom ejection is made by coupling the trapped state (2^3S_1 with $m_J = 1$) with a non-trapped state (2^3S_1 with $m_J = 0$) with a RF (see figure 2.5, left). The frequency is progressively lowered to the value corresponding to the desired temperature of the sample.

During the Hanbury Brown Twiss data acquisition, the evaporation ramp consisted in two pieces: the first one, exponential, started at a frequency of 30 MHz and ended at 3.2 MHz ; the second one, linear, went from 3.2 MHz to a frequency closed to the bottom of the trap. The final value of the second ramp was decided according to the temperature of the sample that we wanted to obtain and also on the isotope we wanted to observe, as we will explain in the following section. The duration of the RF evaporation stage depends on the initial number of atoms and on the initial temperature and was adapted day by day to the experimental conditions. Typically ramps of 10 s were used during Hanbury Brown Twiss data acquisition.

In Palaiseau the evaporation ramp normally consists in three linear pieces, depending on the initial number of atoms and on the initial temperature of the sample. The initial value of the RF is 50 MHz . The first ramp ends at 10 MHz and has a speed of 5 MHz/s , the second one ends at 2 MHz with a speed of 1 MHz/s and the third one starts from 2.5 MHz and ends at a value close to the bottom of the trap, depending on the desired final temperature. The speed of the final ramp is about 1 MHz/s .

Observation of a ^3He or ^4He time-of-flight

As it is shown in figure 2.5, due to the different gyromagnetic ratio, a given RF that outcouples ^4He from $m_J = 1$ to $m_J = 0$ drives the ^3He transition from $m_F = 3/2$ to

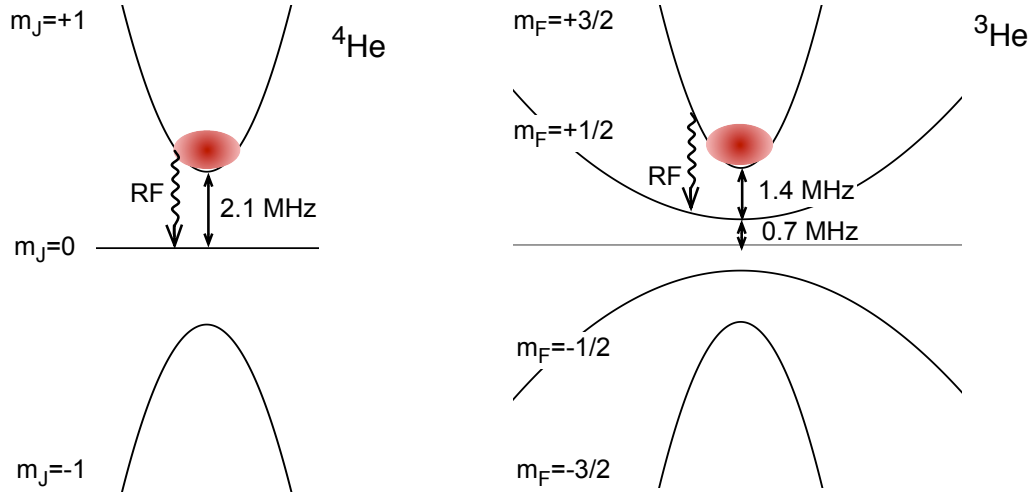


Figure 2.5: Potential energy of the different magnetic substates of ${}^4\text{He}$ (left) and ${}^3\text{He}$ (right) in a Ioffe-Pritchard magnetic trap. ${}^4\text{He}$ atoms in the trapped magnetic substate are coupled to the $m_J = 0$ substate with a RF frequency. The bottom of the ${}^4\text{He}$ trap corresponds, with the Amsterdam values for the magnetic confinement, to a frequency of 2.1 MHz. Due to the different magnetic moment, a given RF that outcouples ${}^4\text{He}$ from $m_J = 1$ to $m_J = 0$ drives the ${}^3\text{He}$ transition from $m_F = 3/2$ to $m_F = 1/2$ at a field which is 1.5 times larger.

$m_F = 1/2$ at a field which is 1.5 times larger. While ${}^4\text{He}$ atoms in the $m_J = 0$ state are no longer confined and leave the trapping region, ${}^3\text{He}$ atoms in $m_F = 1/2$ are still confined and could harm the evaporation process. This is almost not the case, because Penning ionizations for two atoms in $m_F = 1/2$, or an atom in $m_F = 1/2$ and one in $m_F = 3/2$, are no longer spin forbidden. Therefore these atoms are ejected from the trap.

Furthermore, for the trap used during the Hanbury Brown Twiss data acquisition, the bias field was equal to 0.75 G corresponding to a frequency resonant with the center of the cloud of 2.1 MHz for ${}^4\text{He}$ atoms and to 1.4 MHz for ${}^3\text{He}$ atoms. As soon as the temperature of the gas is such that $10k_B T \leq h\nu_{RF}$, the population of ${}^3\text{He}$ atoms resonant with the transition becomes vanishingly small. As a consequence, once the mixture is at $T \simeq 3 \mu\text{K}$, we can easily remove ${}^4\text{He}$ by sweeping the RF ramp through the bottom of the trap, without affecting ${}^3\text{He}$. Typically, for a mixture of $\approx 10^5$ atoms at $\leq 1.5 \mu\text{K}$, a RF sweep going from 3 MHz to 1.9 MHz was able to empty the ${}^4\text{He}$ trap without affecting the ${}^3\text{He}$ cloud. In order to observe the time-of-flight of a ${}^3\text{He}$ cold cloud we then switched off the magnetic trap to let the atoms fall on the detector under effect of gravity.

This feature was important for our measurements because, since the micro-channel plate is not able to distinguish between ${}^3\text{He}$ and ${}^4\text{He}$, it provides a simple way to separate the two isotopes. Of course more complicated ways can be imagined, for

example one could use a laser to drive a Raman transition to eject one of the species from the trap, or in the case of absorption imaging excite a transition resonant with just one of the isotopes.

To observe a ^4He cold cloud time-of-flight, we repeated the whole experimental procedure described above loading a MOT containing only ^4He atoms. Once the sample reached the desired temperature a RF knife was kept on at a constant frequency for 500 ms. Then, after 100 ms, the trap was switched off and the atoms fell on the detector.

An important difference between the French and the Dutch experiment resides in the trap switch off. In both experiments, the current flowing in the magnetic trap coils is cut abruptly, but the magnetic field does not go suddenly to zero. In Palaiseau the bias field becomes negative for a duration of the order of $150\ \mu\text{s}$, thereafter it goes to zero in $1 - 2\ \text{ms}$. The passage of the magnetic field from zero causes atomic spin-flips. As a result, about 10% of the atoms goes in the level $m_J = 0$. Since these atoms are insensitive to the magnetic field, they fall and they are detected. Atoms in the other magnetic sublevels are pushed towards the walls of the science chamber and are not detected. In section 4.5.1 we will see how we tried to avoid the problems caused by the trap switched off by transferring all the trapped atoms in the $m_j = 0$ substate with a Raman transition.

In Amsterdam the magnetic trap switch off is driven in order to detect atoms with $m_J = 1$. This is achieved by changing the delay between the switch off of the radial and axial confinement. The fact that detected atoms are in a magnetic sensitive sublevel can be a source of error in the measurement of the Hanbury Brown Twiss effect, as we will see in section 3.2.3. In fact, eddy currents or residual curvatures of the magnetic field can perturb the cloud during the fall making the definition of the relation between the source and the correlation seen at the detector difficult.

Observation of a Bose-Einstein condensate

In order to observe a Bose-Einstein condensate of ^4He we follow exactly the same experimental procedure as for the creation of a ^4He cold cloud, but we lower the final frequency of the RF evaporation ramp to a value closer to the bottom of the trap. Depending on the number of trapped atoms the condensation threshold will be reached for different final values of the RF. By further lowering the final RF, we are able to eliminate the residual thermal component and the atoms are all in the condensed state. When the RF ramp reaches the final value the trap is switched off and the atoms fall under the effect of gravity on the detector.

2.3.7 Detection

As we said above (section 2.1), one of the most interesting features of Helium is the high energy of the metastable state, that allows the use of micro-channel plates to detect the atoms. The Amsterdam setup uses two micro-channel plates to detect both metastable

atoms and helium ions. In addition the Amsterdam group uses a CCD camera to detect the atoms by using absorption imaging [71].

The two micro-channel plates used in the Amsterdam setup have a diameter of 14.5 mm. The one used to detect ions is situated above the trap and detects the ions produced at the different stages of laser cooling and trapping due to Penning ionizations. The one used to detect atoms is 11 cm below the trap. When the trap is switched off the atoms fall on the micro-channel plate and are then detected. This micro-channel plate is mounted on a translation stage that allows to move the detector horizontally by ≈ 5 cm. The translation stage was originally used to move the detector out of the path of the imaging laser beam, and it resulted to be very useful when we decided to install the position-sensitive detector in the setup.

The position-sensitive detector has a diameter of 8 cm and was installed 63 cm below the trap center (for more technical details about the detector see appendix A). The translation of the small micro-channel plate was necessary in order to detect the entire cloud on the Palaiseau detector. In addition, thanks to this translation stage, we could use the small micro-channel plate to optimize the experiment and use the position-sensitive detector only during the data acquisition.

Installation of the position-sensitive micro-channel plate

In order to install the micro-channel plate in the Amsterdam setup, the design of a vacuum chamber was required. A sketch of the used vacuum chamber is shown in figure 2.6. The vacuum chamber is cross-shaped with a port for a cold cathode gauge and a port for a turbo pump. The micro-channel plate was installed on the bottom flange and the top flange was connected to the Amsterdam science chamber. Before our arrival the bottom flange of the science chamber was replaced by a valve (as shown in figure 2.6). In this way, after having installed the detector vacuum chamber and having pumped it out, we could bake only the part of the chamber below the valve, the upper one having been kept under vacuum by closing the valve. Owing to the small volume of the new chamber, three days of baking at about 120°C allowed us to attend a pressure of $\approx 10^{-11}$ mbar and the valve could be opened without any danger for the vacuum in the upper part. Unfortunately, after the baking, the micro-channel plate dark count was quite high and it took almost another week for the detector to be functional again. During this time we could optimize the experiment by using the small micro-channel plate and we obtained a ^3He and ^4He cold cloud.

In addition to the detector we needed to bring from Palaiseau and to install all the electronics necessary for the detection, power supplies, constant-fraction-discriminator, time-to-digital converter (see appendix A), as well as a computer with all the acquisition programs already installed. The time-to-digital converter and the computer were triggered by the system driving the Amsterdam experiment and the data were saved on the local acquisition pc and then copied to the server in Palaiseau for analysis.

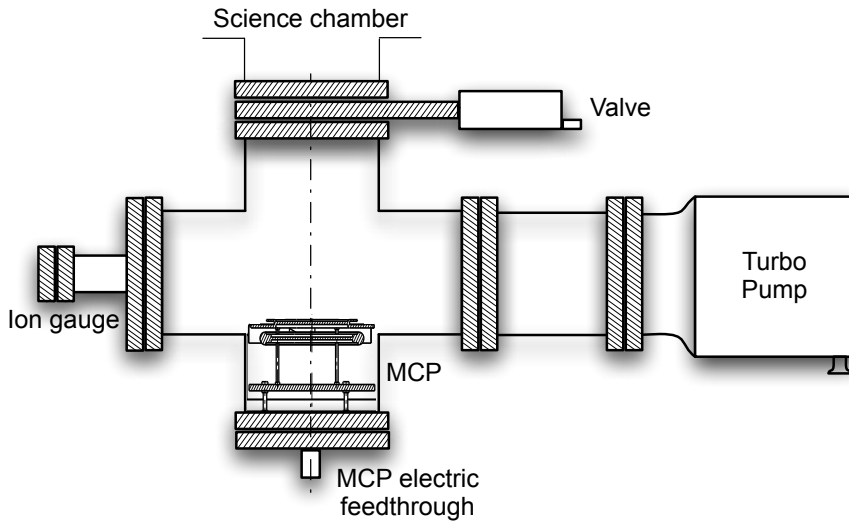


Figure 2.6: Sketch of the vacuum chamber brought to Amsterdam to perform the measurement of the Hanbury Brown Twiss effect. The valve in the upper part of the chamber was installed in the Amsterdam science chamber before our arrival, in order to separate the science chamber from the detector chamber. As the figure shows, the detector was fixed on the bottom flange of the chamber. The distance between the trap center and the micro-channel plate is 63 cm. The chamber was pumped by a turbo pump and the pressure could be measured by a cold cathode ion gauge.

2.4 Conclusion

In this chapter we described the experimental apparatus used to perform the measurement of the Hanbury Brown Twiss effect on a sample of bosons and fermions produced in the same apparatus at the same temperature. This measurement has been done within a collaboration between our group and the group of W. Vassen in Amsterdam. The capability of our detection system, based on a micro-channel plate with delay-line anode, of measuring correlations was joined to the capacity of the Amsterdam group to create ultracold samples of ^4He (bosons) and ^3He (fermions) atoms.

In the description of the experimental apparatus a particular attention was drawn to the changes we should bring to the French experimental setup in order to cool ^3He . In addition, a comparison between the parameters used in the two experimental sequences was carried out.

Chapter 3

Amsterdam-Palaiseau Experimental Results

In this chapter we will present the experimental results obtained in the framework of the Amsterdam-Palaiseau collaboration. At the beginning of July 2006, M. Schellekens and I brought the micro-channel plate and all the electronics needed for the detection in Amsterdam and, after about ten days, the detector was fully functional. Thereafter we spent a few days to optimize the experiment, with T. Jeltens and J. McNamara, two PhD students of Vassen's group. On the 14th of July, the first cold cloud of ^3He fell on the position-sensitive detector. We started the data acquisition on the spot and, twelve hours later, we had the first signature of the fermionic antibunching. During the second half of July we acquired and analysed data simultaneously. The experiment was running almost continuously day and night, with three people working in shifts. T. Jeltens and J. McNamara were taking charge of the optimization and the stability of the experiment, whereas another person of the Palaiseau group (M. Schellekens, A. Perrin, PhD students, and H. Chang, post-doc, and I) was taking charge of the data acquisition. I was responsible of the data analysis, helped by the experience acquired by M. Schellekens during the analysis of the data taken in Orsay one year before to measure the Hanbury Brown Twiss effect on a cold cloud of ^4He [40]. At the end of July, we already had some preliminary results for the comparison of the Hanbury Brown Twiss effect for ^3He and ^4He , but we still needed some data to study the behavior of the correlation function as a function of the temperature. In order to have a precise idea of the data we still had to acquire, we allotted two weeks to data analysis, pursuing data acquisition during the second half of August. During this break we also decided to perform a second experiment (see section 3.3), in order to see a bigger antibunching. The second half of August was enough to reach our objective and we went back to Palaiseau, where we completed the data analysis.

In this chapter we will show the acquired dataset and we will explain in detail the procedure used to analyse them. We will show the measured correlation function and we will compare it with theory. At the end of the chapter we will describe the experimental setup used to perform the defocusing experiment and we will show and

comment the experimental results.

3.1 Acquired Data

As we said in the introduction, during the four weeks of data acquisition, the experiment was running day and night. The experiment was more stable during the night, probably because of a better room temperature stability and a more quiet environment. Thanks to the high repetition rate of the experiment (a cold cloud each 25 seconds) it was possible to take several sets of data, for ^3He and ^4He and for different temperatures. In total, we acquired about 6500 ^3He clouds at three different temperature and 3000 ^4He clouds. A post-acquisition analysis allowed us to select about a half of these clouds on the basis of several criteria, like the temperature range, number of atoms, detector saturation.

The first step of the data analysis consists in fitting the clouds one by one with a Maxwell-Boltzmann distribution in order to measure the temperature, the mean arrival time of the atoms on the detector and the peak atom rate. The detected atom number is registered in this first part of data treatment as well. Subsequently the arrival time distribution is plotted in order to eliminate any aberrant data and the temperature distribution is plotted in order to decide what temperature range to use. The mean temperature of the chosen set and its standard deviation are then measured. Thanks to the good stability of the experimental setup, the cloud temperature was not fluctuating too much around the target value and the temperature distributions are quite sharply peaked around the mean. In table 3.1 we report the number of shots used to measured the correlation function for each temperature, the fitted temperature and the detected atom number.

Atomic Species	Temperature (μK)	Detected Atoms	Number of TOFs
^4He	0.52 ± 0.03	2000 – 14000	964
^3He	0.53 ± 0.05	5000 – 9000	1078
^3He	0.99 ± 0.06	6000 – 10000	1005
^3He	1.4 ± 0.1	5000 – 12000	1468

Table 3.1: In this table we report the temperature, the detected atom number and the number of time-of-flights for each set of data that we used to measure the correlation function. The detection efficiency is estimated to be of the order of 10 – 15% (see appendix A). The number of atoms was adjusted in order to limit the saturation of the detector.

We registered clouds of both ^3He and ^4He around $0.5\mu\text{K}$ in order to be able to compare the bosonic and fermionic correlation functions. In addition we acquired clouds of fermions at $1\mu\text{K}$ and $1.5\mu\text{K}$ in order to show the trend of the correlation function as a function of the temperature. The number of acquired shots is adjusted for each data set in order to have a good signal to noise ratio [44].

A parameter that can be checked in this first analysis step is the saturation of

the detector. If the detector saturates, the time-of-flight is deformed and the central part of the cloud (the more dense) is not properly detected (see appendix A). This can affect the measured correlation length and the bunching or antibunching height, as we will see later on (section 3.2.1). The saturation is small on a cold cloud and is difficult to measure by studying the shape of the time-of-flight. However, we know from an independent measurement [44] (see also appendix A), that the micro-channel plate used during the collaboration saturates for a flux of incident particles larger than 80×10^3 particles/s/cm². Therefore, knowing the number of detected particles during the time-of-flight, we can have an estimation of the saturation of the detector. In figure

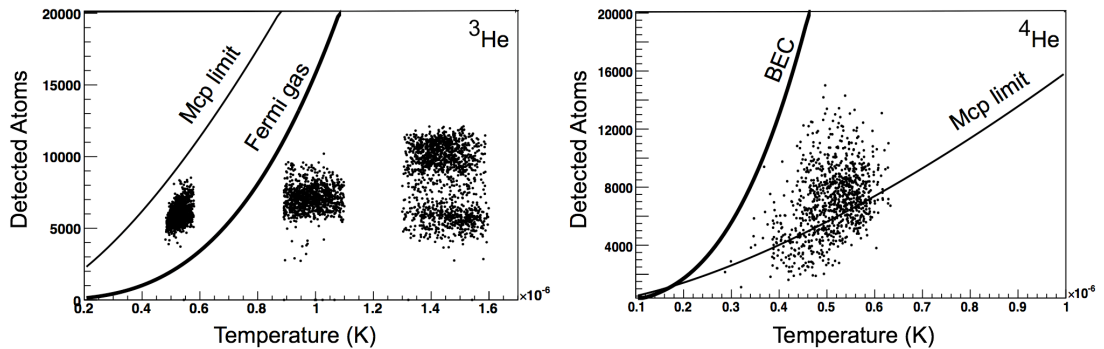


Figure 3.1: Number of detected atoms as a function of the temperature for the data used to measure the two-body correlation function. The experimental data are the black spots. In the same graph we plot the curve that indicates the saturation limit of the micro-channel plate. Saturation occurs above the line labelled “MCP limit”. We also report the critical temperature and the Fermi temperature as a function of the detected atom number. Degenerate regime is reached above the lines labelled “Fermi gas” and “BEC”. The detection efficiency is assumed to be of 15%.

3.1 we show the dataset selected for the measurement of the Hanbury Brown Twiss effect. In the same graph we plot the curve corresponding to the saturation of the micro-channel plate. As one can see, some of the ⁴He clouds are slightly above the saturation limit, while the fermionic clouds are all well below. In section 3.2.1 we will comment on the effect it can have on the correlation function. However, since we had to compromise between reducing the statistical error by retaining more data and dealing with saturation, all the displayed points were included in the data analysis. In the same graph we plot the curve for the critical temperature and the Fermi temperature as a function of the detected atom number. In the case of bosons the function that we plot takes into account atomic interactions and the effect of finite sample size [81]. The plot shows that the ⁴He clouds were not condensed. The case of fermions is different and the clouds at 0.5 μ K are all in the degenerate regime. The Fermi temperature is defined by

$$k_B T_F = \hbar\bar{\omega} (6N)^{1/3} = \hbar\bar{\omega} (6N_{det}/\alpha)^{1/3} \quad (3.1)$$

where $\bar{\omega}$ is the geometrical average of the trap frequencies along the three axis and α is the detection efficiency. In figure 3.1 we set $\alpha = 15\%$. Although the real value

of the detection efficiency is still not very well known, we have several experimental determinations indicating that it is of this order of magnitude (see appendix A and [82]). In this case, fig. 3.1 shows that all the ^3He clouds at a temperature around $0.5\mu\text{K}$ are degenerate, with $T/T_F \approx 0.66$. As we have shown in section 1.4.3, a degenerate Fermi gas does not obey the Boltzmann statistics and, due to the Fermi pressure, the shape of the time-of-flight is no longer Gaussian. Since the density distribution is flattened in the central part, a Gaussian fit of the entire time-of-flight overestimates the temperature of the gas. The wings are independent on the statistics (see figure 1.13), therefore, in order to have a precise estimation of the cloud temperature, one could make a Gaussian fit of the wings of the density distribution [83], [41]. However, the calculation of section 1.4.3 shows that the temperature obtained by fitting the entire time-of-flight differs only by approximately 8% from the one obtained by fitting the wings and that the deviation of the correlation length from the one obtained with a Maxwell-Boltzmann distribution is less than 4% (if we average over all the detector). This discrepancy being within our error bars, we decided to fit the entire cloud with a Gaussian function and to fit the correlation function with a Gaussian as well. In addition, since the value of the detection efficiency is not well known, this seems a sensible decision.

In addition, we paid a special attention to the detector resolution. As we explained in section 1.4.5, the resolution has a strong effect on the measured correlation and it affects both the correlation length and the bunching height. During the data acquisition we noticed that the resolution differed by up to 30% from day to day. We still do not understand the reason for this, as we never observed a similar behavior in Orsay. In order to minimize the errors in the measurement of the correlation function caused by these day by day fluctuations, we acquired the data at a given temperature in the shortest possible delay. In this way we did not have to average over different days (and therefore over data with different detector characteristics). In addition, we always measured the resolution just before or after the acquisition of one data set and we used the obtained value to correct the correlation function.

3.1.1 Data analysis

For the data analysis, we proceeded with the same scheme as for the measurement of the Hanbury Brown Twiss effect on bosonic cold clouds made in Orsay in 2005 [40]. The procedure has been detailed in [44] and here we will recall the most important points. The analysis steps are the following:

- Measurement of the three dimensional correlation function $G^{(2)}(\Delta x, \Delta y, \Delta z)$.
- Normalisation of the correlation function.
- Measurement of the correlation length along the z axis.
- Measurement of the correlation length along the x and y axis and of the bunching/antibunching height.

In the following sections we will explain the analysis procedure step by step.

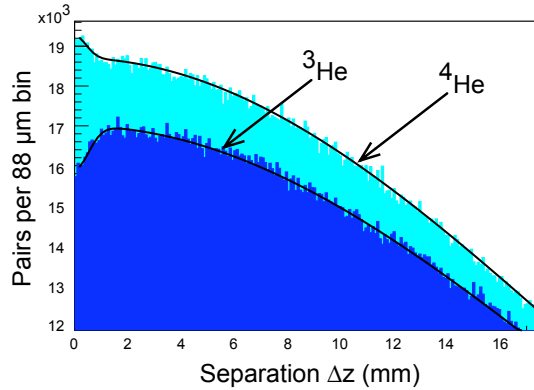


Figure 3.2: Correlation histogram along the z axis for bosons (light blue) and fermions (dark blue) at $0.5 \mu\text{K}$. The time separation has been converted in spatial separation with the formula $z = \sqrt{2gH}(t-t_0)$, where $t_0 = 358 \text{ ms}$ is the mean arrival time of the atoms on the detector. We note the double structure, made by the superposition of two Gaussians. The broader is the autocorrelation of the cold cloud, while the smaller one is the bunching/antibunching. The black curve is a fit made with the sum of two Gaussians.

Measurement of $G^{(2)}(\Delta x, \Delta y, \Delta z)$

The correlation procedure simply consists in histogramming all the differences in time and position between any couple of atoms hitting the detector. Background noise is low and is concentrated in a few hot spots on the edge of the detector. Therefore it can be easily excluded from the data before measuring the correlation function.

On the xy plane, the bin size of the correlation histogram is fixed by the pixel size, that is equal to $133 \mu\text{m}$. In order to decrease the computation time, we consider only particles that are at most 15 pixels away, that is about three times the correlation length along the y axis and thirty times the correlation length along the x axis. On the time axis, the pixel size is very small (of the order of 1 ns) and the bin size is fixed at $25 \mu\text{s}$ to increase the signal to noise ratio. In addition we introduce a dead-time of 300 ns in order to prevent spurious counts due to electronic noise, such as for example reflections on the delay-lines (the maximum atom rate is about 1.2 Matoms/s).

At the end of this procedure we have a 3D histogram for each acquired time-of-flight, that corresponds to the non-normalized correlation function $G^{(2)}(\Delta x, \Delta y, \Delta t)$ averaged over all the detector. We recall here that, as we said in section 1.4.4, the arrival time of the atoms on the micro-channel plate can be translated into a vertical position. The scaling factor is the mean velocity of the cloud falling on the detector $v = \sqrt{2gH}$, with g the acceleration of gravity and H the height of the trap above the detector. In the following, we will always refer to the vertical coordinate as a position.

In figure 3.2 we show the correlation histogram along the z axis obtained with the procedure described above, for bosons and fermions at $0.5 \mu\text{K}$. In order to increase the signal to noise ratio we average over 10 couples $(\Delta x, \Delta y)$ that are included in

the coherence zone. The black curve is a fit made with the sum of two Gaussians, one broader and one narrower on the top of the first one. The broader one is the result of the correlation between atoms that are far away and that behave like independent particles. In other words it is the autocorrelation of the cold cloud. Its width is proportional to the temperature of the cloud. The narrower Gaussian distribution is the quantum effect we are looking for: we see a small bunching on the top of the bosonic correlation histogram and an antibunching on the top of the fermionic correlation histogram. The height of the small Gaussian is only a few percent of the height of the autocorrelation and to measure properly the height and the correlation length we will have to normalize the correlation histogram. In particular, we note that the height of the correlation function cannot be measured directly on figure 3.2 because we averaged over $(\Delta x, \Delta y)$ to obtain this figure. The averaging procedure has the effect of lowering the bunching/antibunching height.

In the following section we will explain our normalization procedure.

Normalization procedure

In order to normalize the correlation histogram $G^{(2)}(\Delta x, \Delta y, \Delta z)$ we want to divide it by the correlation between particles that are statistically independent, in other words we want to divide it by the autocorrelation of the cold cloud seen in the previous section. The rigorous way to compute this quantity, would be to sum up all the time-of-flights acquired for a given temperature (that are used to compute $G^{(2)}(\Delta x, \Delta y, \Delta z)$) and to calculate the correlation between all the atoms of all the time-of-flights. Finally one would end up with the quantity:

$$\langle g^{(2)}(\Delta x, \Delta y, \Delta z) \rangle = \frac{\sum_i G_i^{(2)}(\Delta x, \Delta y, \Delta z)}{\langle \sum_i \rho_i(x, y, z) \sum_i \rho_i(x + \Delta x, y + \Delta y, z + \Delta z) \rangle} \quad (3.2)$$

where $\langle \rangle$ indicates the average over all the detector. Unfortunately, the computation of the denominator of equation 3.2 is very long. To have an order of magnitude, the calculation of $G^{(2)}(\Delta x, \Delta y, \Delta z)$ for a cloud of 5×10^3 atoms takes about a minute, therefore the correlation between all the atoms of 10^3 time-of-flights ($\simeq 5 \times 10^6$ atoms) would take 10^6 min ≈ 2 years, that is definitely too long. We decided to simplify the procedure, exploiting the very good resolution of our detector on the vertical axis and the fact that, as shown in section 1.4.5, in the correlation function the three directions x, y and z are independent.

First of all, we normalize the correlation function along the vertical axis. To do this we calculate the auto-correlation along z for $(\Delta x, \Delta y) = (0, 0)$ of the sum of the time-of-flights. In practice, for each pixel (x, y) of the histogram that contains the sum of all the time-of-flights, we calculate the autocorrelation of the z column and we average the result over all the (x, y) pixels. We end up with a 1-dimensional function that we use to normalize the 3-dimensional correlation histogram $G^{(2)}(\Delta x, \Delta y, \Delta z)$. To do this, we divide the z column of $G^{(2)}(\Delta x, \Delta y, \Delta z)$ by this function. The normalization in the z direction is achieved in this way.

We note that in the normalization procedure described above, we divided all the z columns of the histogram $G^{(2)}(\Delta x, \Delta y, \Delta z)$ by the autocorrelation measured for $(\Delta x, \Delta y) = (0, 0)$. One can therefore ask whether it is correct to do it for the z columns having $(\Delta x, \Delta y) \neq (0, 0)$. The answer can be found in the fact that the autocorrelation Gaussian is much broader than the bunching (antibunching) Gaussian, therefore the autocorrelation function does not evolve a lot in the coherence region. This allows us to divide the z column by the normalization function obtained for $(\Delta x, \Delta y) = (0, 0)$ even for pairs with $(\Delta x, \Delta y) \neq (0, 0)$.

The normalized correlation function along the z axis is plotted in figure 3.3 for ^4He (left) and ^3He (right) at $0.5 \mu\text{K}$. We note that the normalized correlation is not flat for large separation Δz . This is due to the fact that the normalization method discussed above works as long as all the time-of-flights have the same shape, i.e. if the temperature and the number of atoms do not change from a realization to another. Experimental fluctuations make this condition impossible to fulfill and the temporal correlation function shows a curvature. This is taken into account in the data analysis by fitting the normalized correlation function with a second order polynomial, in a zone that excludes the bunching (or the antibunching) and that is shown in figure 3.3. We fix the first order of the polynomial to zero and we fit the constant value with the zeroth order and the curvature with the second order. Then we scale the data points by the fitted value of the zeroth order (that is of the order of 0.98 instead of 1). In this way the correlation function is equal to 1 for $\Delta z = 0$ in absence of quantum bunching. Figure 3.3 shows that the curvature is not important (the fit gives values between 10^{-5} and 10^{-4}) and it is not taken into account in the rescaling.

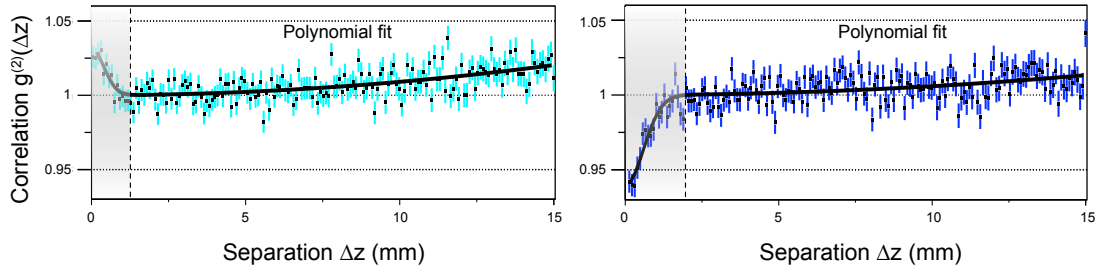


Figure 3.3: Normalised correlation function along the z axis for bosons (on the left) and fermions (on the right) at $0.5 \mu\text{K}$. In this figure the correlation function has been averaged over 10 couples $(\Delta x, \Delta y)$ in order to increase the signal to noise ratio. The part of the graph in shadow is the bunching/antibunching and it is not fitted with the polynomial function. The error bars correspond to the square root of the number of entries in each bin.

Measurement of L_z

The correlation length L_z is obtained by fitting the normalized correlation function computed above with a Gaussian plus the second order polynomial. The parameters

of the polynomial are fixed at the values found during the normalization procedure. In order to increase the signal to noise ratio the correlation histogram is averaged over 10 pairs $(\Delta x, \Delta y)$ around the position $(\Delta x, \Delta y) = (0, 0)$ and included in the coherence zone. The averaging procedure decreases the uncertainty in the fitted value of L_z but it decreases the contrast of the correlation function η . Therefore η cannot be measured in this way. We recall that, since the resolution of our detector along the z axis is very good, the value of the correlation length along this axis is fairly well defined by the result of the Gaussian fit (see section 1.4.5).

Measurement of L_x , L_y and of the contrast of the correlation function

In order to measure the height of the correlation function and the correlation length along x and y , we measure $g^{(2)}$ on the xy plane. We proceed as follows: for each couple $(\Delta x, \Delta y)$ we fit the z correlation function with a Gaussian of fixed width L_z , then we report the fitted value of the bunching/antibunching height versus $(\Delta x, \Delta y)$. The result of this measurement is reported in figure 3.4 for fermions at $0.5\mu\text{K}$. As we

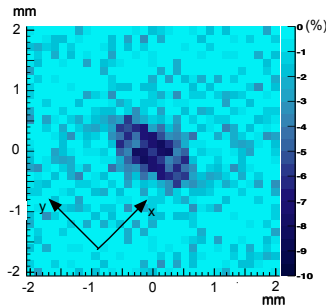


Figure 3.4: Normalised correlation function on the xy plane for fermions at $0.5\mu\text{K}$. A fit with the convolution of the correlation function and the resolution function gives the values of l_x , l_y and η . The axis of the detector are rotated by 45° with respect to the trap axis (indicated by the arrows). As one can see the antibunching is anisotropic and the aspect ratio is inverted with respect to inside the trap.

expected the correlation function shows a hole. The correlation function is not isotropic, but it is cigar-shaped. In addition the anisotropy is inverted with respect to the trap anisotropy. This is what we expect from theory (see section 1.4.4 and equation 1.34), since the correlation length is inversely proportional to the size of the trapped cloud. However, the trap aspect ratio, of the order of 10, is not reproduced in the correlation function, because of the finite detector resolution. In section 1.4.5 we saw that the measured correlation function is the convolution between the theoretical correlation function (1.32) and the detector resolution function. As a consequence, the measured correlation length L_i is the convolution between the correlation length obtained with a perfect detector l_i and the resolution along the same axis d_i , i.e. $L_i = \sqrt{l_i^2 + (2d_i)^2}$, with $i = x, y$. In our experiment the detector has a resolution $d_i \simeq 250\mu\text{m}$ on the xy plane (RMS value). The two-particle detector resolution (at $1/e$) is $2d_i \simeq 500\mu\text{m}$

and is about one order of magnitude larger than the expected value of the correlation length along the x axis (see figure 1.16). Therefore, measuring L_x is equivalent to measure the detector resolution. The correlation length along the y axis is of the same order of magnitude than the resolution (see figure 1.16) and a deconvolution will be necessary in order to properly measure it. It is evident that the accurate knowledge of the resolution function is important for the correct measurement of η , L_x and L_y . In section 1.4.5 we derived the correlation function for a Gaussian resolution. However, a careful examination reveals that the resolution function of our detector is not well approximated by a Gaussian but by the sum of three Gaussians. The exact formulation of the obtained correlation function is given in appendix A, together with the explanation of the procedure used to measure the detector resolution. A fit of the measured $g^{(2)}(\Delta x, \Delta y)$ with the correlation function obtained by the convolution with the three-Gaussians resolution gives the value of η and the values of the correlation lengths l_x and l_y already deconvoluted with the resolution. In the following section we will give the values measured with this more refined correlation function.

3.2 Experimental results

3.2.1 Bosons-Fermions comparison

As we said at the beginning of this chapter, we acquired about 2000 cold clouds of ^3He and ^4He at around $0.5\mu\text{K}$ (see table 3.1). Therefore we are able to compare the correlation functions for the two species at the same temperature. In figure 3.5 we report the measured correlation functions for bosons and fermions along the z axis and on the xy plane. As expected we observe a bunching for bosons and an antibunching for fermions. The contrast of the two correlation functions is not the same as well as the correlation lengths. It is interesting to check if the difference between the two correlation functions agrees with theory (see section 1.4.5).

Table 3.2 summarizes the values obtained with the analysis procedure described above. In the last line of the table we report the ratio between the bosonic and the fermionic correlation lengths as well as between the measured heights of the correlation functions.

The correlation length is theoretically given by (see section 1.4.4):

$$l_i = \frac{\hbar\omega_i t_0}{\sqrt{k_B T m}} = \frac{\hbar t_0}{m s_i} \quad (3.3)$$

where t_0 is the mean arrival time of the atoms on the detector, ω_i is the trap frequency along the i axis, T is the temperature of the cloud and m the mass of the atoms. s_i is the RMS size of the trapped cloud. Since the size of the trapped clouds is the same for the two isotopes (same Zeeman shifts, see section 2.3.6), the ratio between the two correlation lengths is inversely proportional to the mass ratio, i.e.

$$\frac{{}^3l_i}{{}^4l_i} = \frac{m_4}{m_3} = 1.3 \quad (3.4)$$

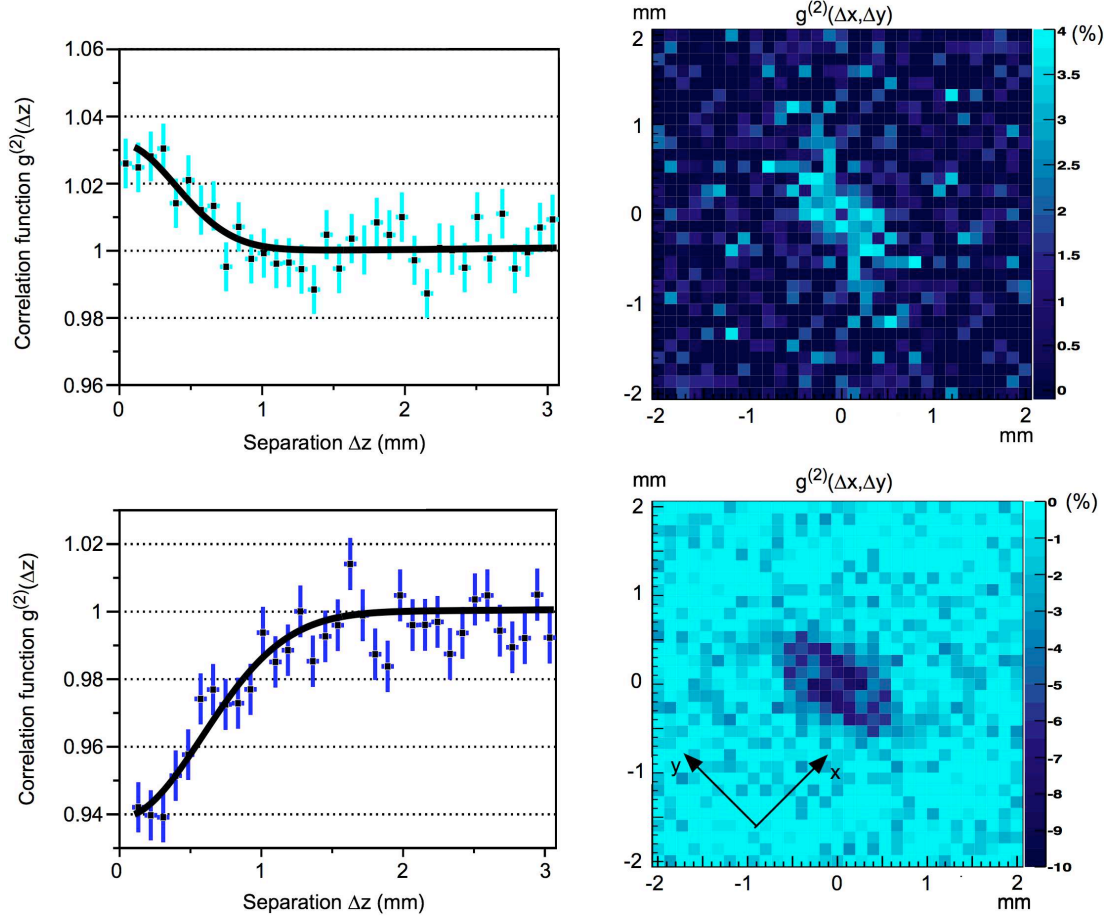


Figure 3.5: Normalised correlation function along the z axis and on the xy plane for bosons (top) and fermions (bottom) at $0.5 \mu\text{K}$. For the correlation along the z axis the error bars correspond to the square root of the number of entries in each bin. The black curve is a fit to a Gaussian function. For the xy correlation function we note that the axis of the detector on the xy plane are rotated by 45° with respect to the trap axis, that are indicated by the arrows (in the bottom right figure).

The theoretical expectation for the contrast of the correlation function with the resolution function of our detector is given in appendix A. The ratio η_3/η_4 is estimated to be 1.2 with the resolution function obtained for these two sets of data. In table 3.3 we report the theoretical expectation for l_i and η . The error bars on the theoretical values take account of the uncertainty on the sample temperature.

Generally the data are in good agreement with the theoretical values obtained with the ideal gas model and they are consistent with theory within 2 standard deviations. In addition the ratio ${}^3l_z/{}^4l_z$ is equal to 1.3 ± 0.2 and it is in very good agreement with the expected value of 1.3 ± 0.1 . Despite of that, we can observe two small anomalies: first, the contrast of the correlation function is, for ${}^4\text{He}$, smaller than expected. This results in a ratio $\eta_3/\eta_4 = 2.4 \pm 0.2$ instead of 1.2 ± 0.1 . Second, the measured value of

Data	l_y (μm)	l_z (μm)	η
${}^3\text{He}$, $0.53 \pm 0.05\mu\text{K}$	565 ± 47	750 ± 65	0.078 ± 0.003
${}^4\text{He}$, $0.52 \pm 0.03\mu\text{K}$	570 ± 100	560 ± 80	0.033 ± 0.003
	${}^3l_y/{}^4l_y$	${}^3l_z/{}^4l_z$	η_3/η_4
	0.99 ± 0.19	1.3 ± 0.2	2.4 ± 0.2

Table 3.2: Measured values for the correlation length along the y and z axis and for the contrast of the correlation function, for a sample of ${}^3\text{He}$ at $0.53 \pm 0.05\mu\text{K}$ and a sample of ${}^4\text{He}$ at $0.52 \pm 0.03\mu\text{K}$. The correlation lengths have already been deconvoluted with the resolution function and can be directly compared with theory. The value of l_x is consistent with zero and is not reported. In the last line we report the ratio between the correlation length and the contrast of ${}^3\text{He}$ and ${}^4\text{He}$.

Theory	l_y (μm)	l_z (μm)	η
${}^3\text{He}$, $0.53 \pm 0.05\mu\text{K}$	630 ± 30	630 ± 30	0.072 ± 0.003
${}^4\text{He}$, $0.52 \pm 0.03\mu\text{K}$	480 ± 14	480 ± 14	0.058 ± 0.002
	${}^3l_y/{}^4l_y$	${}^3l_z/{}^4l_z$	η_3/η_4
	1.3 ± 0.1	1.3 ± 0.1	1.2 ± 0.1

Table 3.3: Theoretical expectations for l_y , l_z and η for a sample of ${}^3\text{He}$ and a sample of ${}^4\text{He}$ at around $0.5\mu\text{K}$. The uncertainty is due to the error on the temperature. The value of η is calculated for a convolution of the correlation function with the three-Gaussian resolution function.

the fermionic correlation length along the y direction is low and not consistent with the correlation length along z , leading to a ratio ${}^3l_y/{}^4l_y = 0.99 \pm 0.19$ instead of 1.3 ± 0.1 .

The small height of the ${}^4\text{He}$ bunching can be due to the detector saturation. In figure 3.1, we have shown that some of the ${}^4\text{He}$ clouds at $0.5\mu\text{K}$ saturate the detector, while the ${}^3\text{He}$ clouds do not. If a saturation occurs, the probability to detect two particles close together is smaller than the probability to detect two particles far apart. This is due to the locality of such phenomenon. It is then easy to understand that the unnormalized correlation function is affected by that. In fact the bunching (or the antibunching) will show a flatter top and the height will be smaller. On the other hand the correlation at large distance will be less affected by the saturation, because it results of the correlation between atoms that are far apart. It is interesting then to understand what happens when we normalize the correlation function. We said that the normalization is made by calculating the correlation on a sample of statistically independent atoms, i.e. the sum of all the time-of-flights used to calculate $G^{(2)}(\Delta x, \Delta y, \Delta z)$. In this process we will calculate again the correlation between atoms that are close together. However, in this case, the correlation at small distances is calculated between atoms that belong to different clouds, and the correlation (probability to detect a pair of atoms) is less affected by saturation. Therefore, the normalization should not cancel the effect of saturation for small pair separation and the bunching height should be smaller.

Concerning the second observed anomaly, there are several possible ways to explain

the disagreement with theory. We will address them in section 3.2.3. In the following section we will show the results for the correlation functions measured at $1\mu\text{K}$ and $1.5\mu\text{K}$.

3.2.2 Other temperatures

As shown in table 3.1, we acquired about 1000 clouds of ^3He at $0.99 \pm 0.06 \mu\text{K}$ and 1500 clouds of ^3He at $1.4 \pm 0.1 \mu\text{K}$. With these data it was possible to study the trend of the correlation length and of the antibunching height as a function of the temperature. When the temperature of the sample increases, the size of the source increases with the square root of the temperature and the correlation length decreases, as shown by equation 3.3 and as discussed in section 1.4.4. The contrast of the correlation function decreases as well.

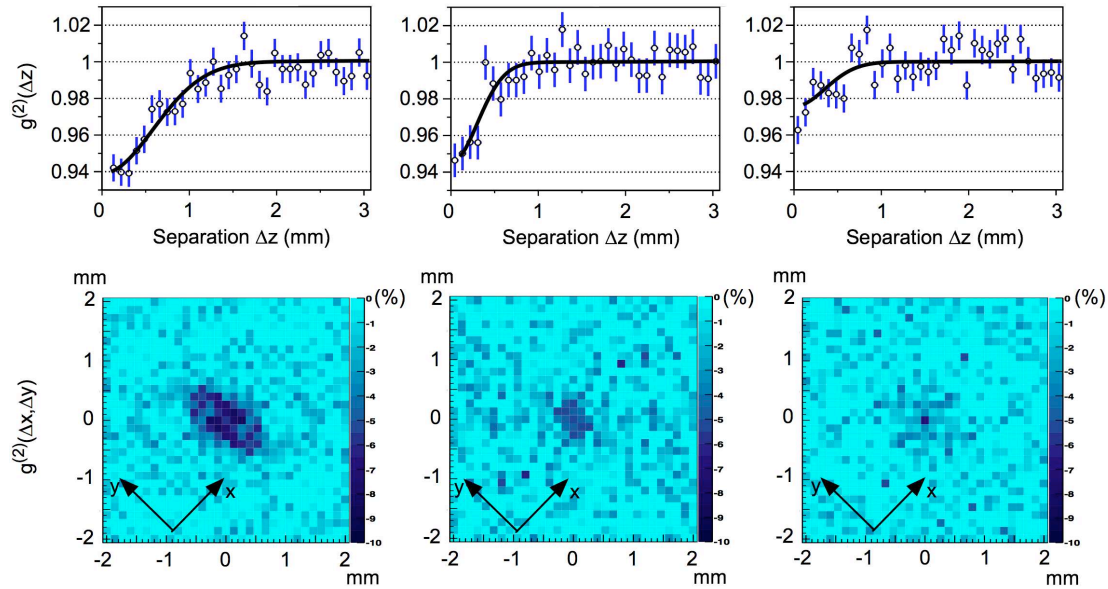


Figure 3.6: Correlation measured on the z axis and on the xy plane for ^3He at $0.53 \pm 0.05 \mu\text{K}$, $0.99 \pm 0.06 \mu\text{K}$ and $1.4 \pm 0.1 \mu\text{K}$ (from left to right).

The procedure used to measure the correlation function on these sets of data is the one explained at the beginning of the chapter. In figure 3.6 we show the correlation function for the three temperatures on the z axis and on the xy plane. The resolution function has been measured independently for each set of temperatures in order to have the best accuracy in the determination of the correlation length along y and the antibunching height. The measured values are reported in table 3.4 and plotted in figure 3.7, together with the theoretical expectations. The error bars are the root-mean-square errors provided by the fitting procedure.

In order to directly compare our results with theory, we plot also equation 3.3 on

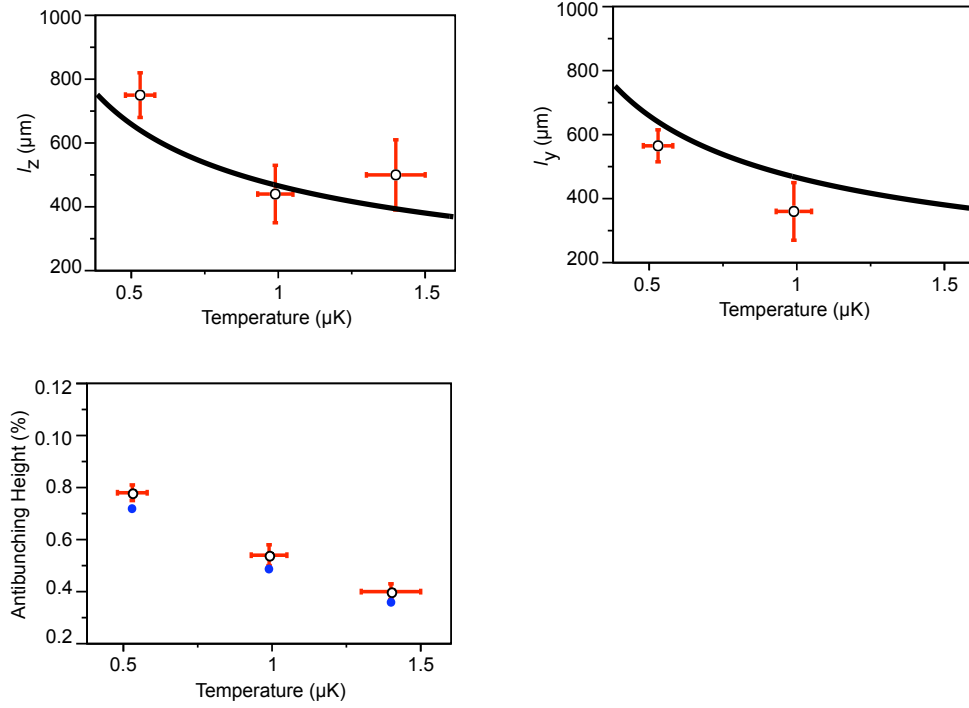


Figure 3.7: Plot of the measured values of l_y , l_z and η as a function of the temperature. The black curve in the two upper graphs is the theoretical expectation, given by equation 3.3. In the plot of the antibunching height the filled dots are the theoretical value calculated with the resolution function measured for each data set. All the measured values are in good agreement with theory.

Data	l_y (μm)	l_z (μm)	η
^3He , $0.53 \pm 0.05 \mu\text{K}$	565 ± 47	750 ± 65	0.078 ± 0.003
^3He , $0.99 \pm 0.06 \mu\text{K}$	360 ± 90	440 ± 90	0.054 ± 0.004
^3He , $1.4 \pm 0.1 \mu\text{K}$	0	500 ± 110	0.040 ± 0.003
Theory	l_y (μm)	l_z (μm)	η
^3He , $0.53 \pm 0.05 \mu\text{K}$	630 ± 30	630 ± 30	0.072 ± 0.003
^3He , $0.99 \pm 0.06 \mu\text{K}$	470 ± 14	470 ± 14	0.049 ± 0.001
^3He , $1.4 \pm 0.1 \mu\text{K}$	390 ± 14	390 ± 14	0.036 ± 0.001

Table 3.4: Measured and theoretical values for the correlation length along the y and z axis and for the contrast of the correlation function, for a sample of ^3He at $0.53 \pm 0.05 \mu\text{K}$, $0.99 \pm 0.06 \mu\text{K}$ and $1.4 \pm 0.1 \mu\text{K}$. The measured correlation lengths have already been deconvoluted with the resolution function and can be directly compared with theory. The value of l_x is consistent with zero and is not reported. The value of l_y for the sample at $1.4 \pm 0.1 \mu\text{K}$ is smaller than the resolution and is therefore consistent with zero. In the theoretical data the uncertainty takes into account the error on the temperature.

the graph for l_y and l_z and, for the antibunching height, we plot the theoretical values obtained, with the measured resolution function.

The agreement with theory is quite good again. The measured values are always consistent with theory within less than two standard deviations. We do not plot the value of l_y for the set at $1.5\mu\text{K}$ because the measured value is consistent with zero, i.e. the correlation length is smaller than the resolution.

In the next section we will give some possible explanation of the observed discrepancies with theory.

3.2.3 Comments

In summary the measured correlation lengths and heights are in agreement with theory within two standard deviations. The only measurement that shows a large discrepancy is the ^4He bunching height and consequently the ratio η_3/η_4 . We already gave a possible explanation for that in section 3.2.1. Here we would like to comment on some other experimental problems that could affect the correlation function measurement and that could take account of the other observed disagreement.

There are four phenomena that can affect our measurements: the saturation of the detector, an anomaly in the switch off of the magnetic trap, a spin polarization impurity of the sample and a wrong (or not accurate enough) measurement of the detector resolution. The first of those can explain the too small contrast measured for the ^4He correlation function, as explained previously (section 3.2.1).

The second and the third phenomena can affect ^3He and ^4He in a different way. During the data acquisition we measured the magnetic field during the switch off of the trap in the radial and axial direction. We measured it with a gaussmeter from the outside of the chamber. We observed that the switch off of the radial confinement is slower than the one of the axial (with a time constant of some ms) and we also measured a delay between the two. It is quite difficult to theoretically predict the behavior of the atoms in such magnetic field, but naively we can expect a deformation of the cloud that can affect our temperature measurement or the effective size of the source viewed from the detector. We tried to measure the aspect ratio of the detected clouds, but we did not see any anisotropy, within our error bars. Furthermore, due to the different mass, the force generated by a magnetic field acts differently on fermions and bosons, and this can explain the inconsistencies pointed out above. In the Amsterdam experiment, the atoms are released from the magnetic trap in a magnetic sensitive state ($m_J = 1$ for ^4He and $m_F = 3/2$ for ^3He) and the presence of eddy currents or residual curvatures of the magnetic field, can affect the correlations. This is not the case in the Palaiseau setup, where the ^4He atoms were falling in the $m_J = 0$ state. Therefore the correlation function measured on ^4He in Palaiseau in 2005 [40], was not affected by this problem.

The third phenomenon that can decrease the correlation is the spin impurity of the sample. As we explained in the first chapter, in order to observe the Hanbury Brown Twiss effect, the particles have to be identical. In our case it is equivalent to say that they have to be all in the same magnetic substate. When the magnetic trap is switched off all the Zeeman substates are degenerate and have the same probability of being

occupied. As we said, in the Amsterdam experiment the largest part of the atoms are transferred in the state $m_J = 1$ for ^4He and $m_F = 3/2$ for ^3He and fall on the detector. During the data acquisition we checked that the samples were pure when they reached the detector, by applying magnetic fields gradients during the time-of-flight. Therefore this possible problem was ruled out.

The observed discrepancies can also be due to an error in the measurement of the detector resolution. Even if all the methods that we use to measure it give approximately the same results (see appendix A), we are still not confident in our estimation. As we have already said, in Amsterdam we noticed that the resolution was not stable and differed by up to 30% from day to day. This behavior had never been observed when the detector was in Orsay and we have not an explanation for it. An error on the resolution determination would affect both the contrast of the correlation function and the correlation length. A confirmation of that can be seen in the fact that the value of l_z , that is not affected by the resolution on the xy plane, is in good agreement with theory.

3.3 Defocusing experiment

As we saw in the previous sections, as long as the detector resolution is not negligible with respect to the correlation lengths the bunching (antibunching) height is smaller than 1 (see section 1.4.5). The antibunching height as a function of the correlation length is given by equation 1.39 in case of Gaussian detector resolution. As we said our resolution function is given by the sum of three Gaussians, but equation 1.39 can still be used to have an idea of the behavior of η as a function of the correlation length. Equation 1.39 tells us that in order to observe a larger contrast of the $g^{(2)}$ function one can try either to have a better resolution or to increase the correlation length. However, getting a better detector resolution would require an hard work on each part of the electronic chain and, far from being easy, would have taken a lot of time. Since at the moment of our collaboration we just had few weeks to take data, we decided to increase the contrast of the correlation function by increasing the correlation length. As we explained in section 1.4.5 the antibunching height is governed by the ratio between the correlation lengths on the xy plane and the resolution. We then tried to increase l_x and l_y . Equations 3.3 show that it is equivalent to make the source smaller in these two directions.

In optics a smaller source can be obtained by using a divergent lens. As shown on the left side of figure 3.8, a divergent lens will create a virtual source smaller than the original one situated between the original source and the lens.

In order to create a divergent lens for an atomic cold cloud one can use a blue detuned laser beam. The dipolar force pushes the atoms towards regions of small intensity. Since we want to modify the source size on the xy plane, we can apply a vertically propagating beam, forcing the atoms away from the vertical axis. If the lens does not suffer from aberrations, the correlation length at the detector is increased by the lens demagnification factor and the antibunching height is increased consequently.

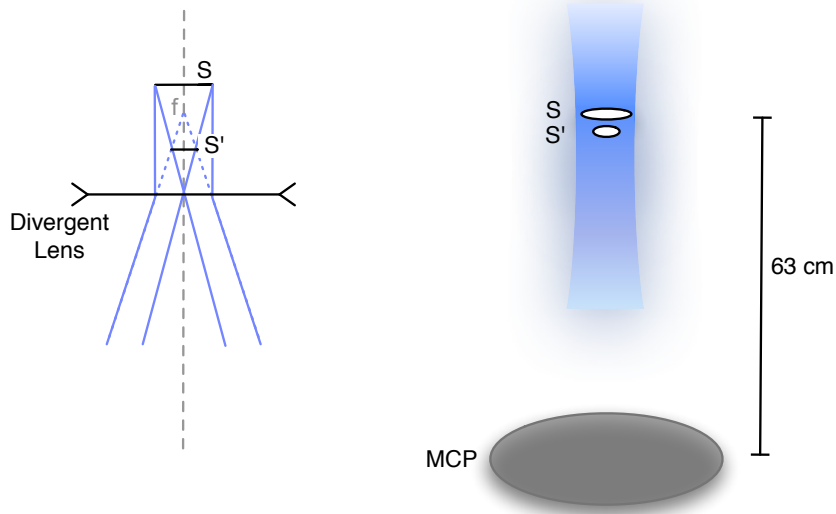


Figure 3.8: On the left: The light generated by an extended source S passes through a divergent lens. The effect of the lens is to create a virtual source S' , between the initial source and the lens, of size smaller than the size of S . On the right: experimental realization of a divergent lens for a cold cloud of Helium atoms. The lens is made by a blue detuned laser shined on the atomic cloud during the time-of-flight. The virtual source is smaller than the initial one, therefore the correlation length at the detector is larger (see equation 3.3). The figure is not in scale.

In the following section we will describe the experimental characteristics of our atomic lens and the experimental sequence used to demagnify the fermionic cloud.

3.3.1 Experimental setup

To create the atomic lens we use a fiber laser (IPG YLD-1BC-1083) detuned on the blue side of the ^3He spectrum by about 300 GHz. The beam propagates vertically and has a waist of $100\ \mu\text{m}$ along the x axis and $150\ \mu\text{m}$ along the y axis. The waist is barely superposed with the trapped atomic cloud. The power of the beam is 300 mW and the laser is linearly polarized.

The experimental procedure used to prepare the ^3He defocused cold clouds is the following. We first create a cold cloud ($0.5\ \mu\text{K}$) of ^3He by using the same procedure as for the previous experiment. After turning off the magnetic trap and waiting for $500\ \mu\text{s}$ for the magnetic field transients to die away, we switch on the defocusing laser for $500\ \mu\text{s}$. The rapid switch on and off of the laser beam is provided by the use of an acousto-optical modulator that is inserted in the beam path. After the application of the laser, we observe the time-of-flight on the detector. Due to the effect of the diverging lens on the atomic cloud, about half of the cloud does not reach the detector

and the atoms are lost. We then increased the number of trapped atoms by about a factor of two in order to have clouds of 2000 – 10000 atoms detected (as in case of the data taken for ^3He at $0.5 \mu\text{K}$ without lens, as shown in table 3.1). During the data acquisition and analysis we checked that the temperature of the cloud along the vertical axis, with and without lens, was stable at about $0.5 \mu\text{K}$.

3.3.2 Experimental results

The data analysis is the same as for the measurements described above. In figure 3.9 we report the antibunching observed with the lens on the xy plane and on the z direction.

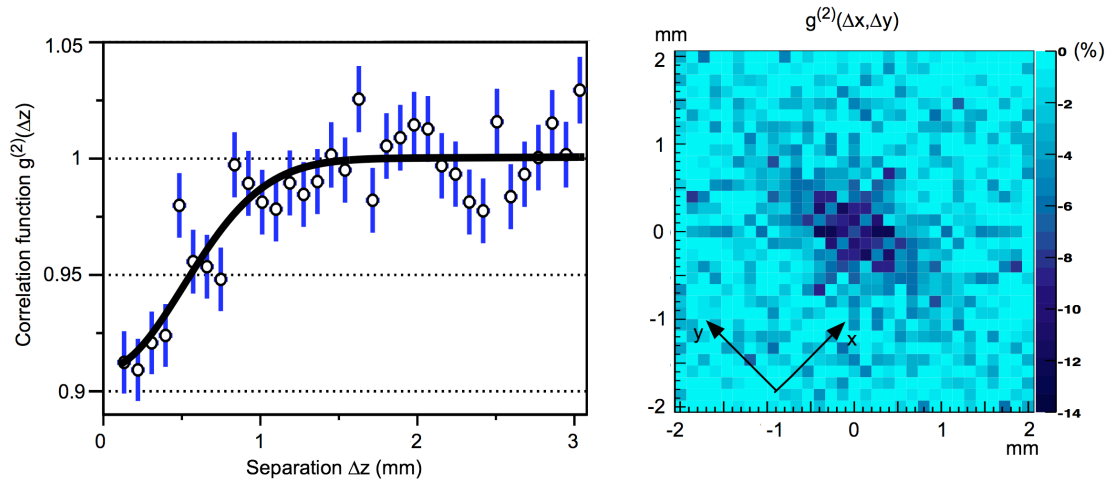


Figure 3.9: Normalized correlation length along the z axis and on the xy plane for a sample of fermions at $0.5 \mu\text{K}$ after the application of the diverging lens. The antibunching height is larger than the one measured without the application of the lens. This fact demonstrates that the effect of the diverging lens is that of decrease the size of the source.

The obtained results are listed in table 3.5 together with the values obtained without applying the lens for mean of comparison. The detector resolution has already been taken into account. For the diverging lens data, the resolution has been measured on a defocused cold cloud by using a gain map acquired just after the acquisition of the correlation data. This should minimize systematics due to the strange behavior of the gain maps and of the resolution function. The value obtained for l_x is still consistent with zero and is not reported in table 3.5.

As one can see the effect of the diverging lens is consistent with our expectations. In the defocusing experiment l_y is 1.4 times larger than in the experiment without laser and the antibunching height (measured on the normalized correlation function on the xy plane, as explained in section 3.1.1) is 0.108 ± 0.003 instead of 0.078 ± 0.003 . We are not able to say if l_x is increased as well because the measured value is still of the order of the resolution. However, the fact that the observed antibunching is larger seems to confirm that l_x is larger as well. Finally l_z is unchanged as expected, since the laser is

Data	l_z (μm)	l_y (μm)	η
^3He , 0.5 μK	750 ± 65	565 ± 47	0.078 ± 0.003
^3He , 0.5 μK with lens	750 ± 80	811 ± 37	0.108 ± 0.003

Table 3.5: Measured values for l_y , l_z and η for ^3He at 0.5 μK with and without defocusing lens. The antibunching height is increased in the data on which we applied the lens as well as the value of the correlation length along y .

vertically propagating and the Rayleigh length is of the order of the centimeter.

The obtained results are, first of all, a demonstration of the fact that the defocusing method is working and can be used to increase the correlation lengths and the contrast of the correlation function. Unfortunately, since the laser waist was small respect to the cloud size, the atomic lens we used presented a lot of aberrations and comparing the experimental results with theoretical predictions is difficult. In fact, before the application of the laser, after 500 μs of free expansion, the RMS size of the cloud is already about 100 μm along the long axis of the trap and is 22 μm along the short axis. The RMS size of the laser is 50 μm on the long axis and 75 μm on the short axis¹, so that even at the beginning of the application of the lens, the laser interacts with a small part of the cloud. Furthermore, during the time of application of the laser, 500 μs , the cloud would expand by a factor of 3 in the absence of the laser action, making aberrations even more important than at the beginning. For these reasons it is very complicated to describe theoretically the action of the laser on the cloud. In the following section we will describe the experiment on the theoretical point of view in the situation in which the laser size is much larger than the cloud size.

3.3.3 Theory

The theoretical results derived in this section cannot be applied to our experimental situation, because the aberrations present in the experiment are not taken into account. However the calculation gives us an idea of the effect that one can have on the antibunching height when the cold cloud is defocused by a laser lens without aberrations.

We can model the atomic cloud as an ideal gas. The density of the trapped sample obeys to a Maxwell-Boltzmann distribution with RMS values $\sigma_i = \sqrt{k_B T / m \omega_i^2}$ for the position and $\sigma_{vi} = \sqrt{k_B T / m}$ for the velocity, with $i = x, y, z$. Here T is the temperature of the sample, m the mass, ω_i the oscillation frequency along the i axis and k_B the Boltzmann constant. The laser propagates in the vertical direction and the Rayleigh length is of the order of 3 cm, therefore the dipolar force acting on the atoms on the z direction is negligible. Consequently the motion of the atoms along the z axis will be described by a simple ballistic expansion in the presence of gravity. The dipolar

¹The laser was focused on the trap. During 500 μs the cloud fall vertically by $\approx 1\mu\text{m}$ that is negligible with respect to the Rayleigh length (3cm). Therefore we can say that the laser interacts with the atoms at its waist.

force has the largest effect on the xy plane. Therefore we will concentrate only on the atomic motion on this plane.

Initial conditions

When the trap is turned off, an atom is at the position x_{trap} with velocity v_{trap} that follow a Maxwell-Boltzmann distribution. Before turning the laser on, the atom moves ballistically for a time \tilde{t} . When the laser is switched on the atom is at the position $x_0 = x_{trap} + v_{trap}\tilde{t}$ and has a velocity $v_0 = v_{trap}$. In the following calculation we will take x_0 and v_0 as the initial position and velocity.

Calculation steps

The calculation can be divided in 3 main steps that are listed here after:

1. At $t = 0$ the laser is switched on for a time τ and the atom, that is at the position x_0 and has a velocity v_0 is submitted to the dipolar force.
2. At $t = \tau$ the laser is switched off and the atom is at the position $x_{dip} = x(\tau)$ with a velocity $v_{dip} = v(\tau)$.
3. Then the atom moves ballistically for a time t_{det} and it reaches the detector at a time $t = \tau + t_{det}$ at a position $x_{det} = v_{dip}t_{det} + x_{dip}$ with a velocity $v_{det} = v_{dip}$.

Analogous equations can be written for the y direction. Since we are interested in the calculation of the magnification factor induced by the laser we will calculate the RMS size of the cloud at the detector. The ratio between the size of the cloud at the detector with and without the application of the laser will give the ratio between the correlation length at the detector with and without laser and the formula 1.39 will give the contrast of the correlation function.

3.3.4 Dipolar force

In this section we will give the equations to describe the motion of the atom submitted to a dipolar force. When a two-level atom interacts with a laser field, it is submitted to a potential given by:

$$U = \frac{\hbar\Delta}{2} \ln(1 + s) \quad (3.5)$$

where Δ is the detuning of the laser with respect to the atomic transition and s is the saturation parameter, given by

$$s = \frac{\Omega^2/2}{\Delta^2 + \Gamma^2/4}. \quad (3.6)$$

Ω is the Rabi frequency for the considered transition and $\Gamma = 2\pi * 1.6$ rad/s is the natural linewidth of the transition. For our experimental parameters $s \ll 1$ and we can write

$$U \approx \frac{\hbar\Delta}{2} s \approx \frac{\hbar}{4} \frac{\Omega^2}{\Delta} \quad (3.7)$$

i.e. the potential is proportional to the light shift induced by the radiation on the atomic level. Writing explicitly the dependence of U from the laser intensity one obtains:

$$U(x, y) = \frac{\hbar}{4} \frac{\Gamma^2}{2\Delta} \frac{I_0}{I_{sat}} \exp\left\{-2\frac{x^2}{w_x^2} - 2\frac{y^2}{w_y^2}\right\} \quad (3.8)$$

I_{sat} is the saturation intensity and is equal to 1.6 W/m². I_0 , w_x and w_y are the intensity and the waist of the laser along the x and y direction. The dynamic equations describing the motion of the atom in the laser field will then be:

$$\begin{aligned} m \frac{d^2x}{dt^2} &= -\frac{\partial U(x, y)}{\partial x} = m \omega_{dipx}^2 x \exp\left\{-2\frac{x^2}{w_x^2} - 2\frac{y^2}{w_y^2}\right\} \\ m \frac{d^2y}{dt^2} &= -\frac{\partial U(x, y)}{\partial y} = m \omega_{dipy}^2 y \exp\left\{-2\frac{x^2}{w_x^2} - 2\frac{y^2}{w_y^2}\right\} \end{aligned} \quad (3.9)$$

with

$$\omega_{dipx,y} = \sqrt{\frac{\hbar}{\pi m} \frac{\Gamma^2}{\Delta} \frac{P}{I_{sat}} \frac{1}{w_{x,y}^3 w_{y,x}}}. \quad (3.10)$$

In the equations above, m is the ³He mass and P is the power of the beam. The system formed by equations 3.9 is not easy to solve and an analytical solution does not exist. Numerically a Montecarlo simulation should allow to find the solution.

If the atoms explore just a small part of the optical potential close to the centre, the solution is analytical. In this situation the Gaussian shape of the laser beam can be approximate by a parabola and the potential is harmonic with a maximum for $x = y = 0$. In the following section we will solve the dynamic equations in this approximation and we will find some experimental situations where the atomic lens would have given a larger antibunching.

Harmonic approximation

In the harmonic approximation the dynamic equations 3.9 are:

$$\frac{d^2x}{dt^2} = \omega_{dipx}^2 x \quad (3.11)$$

$$\frac{d^2y}{dt^2} = \omega_{dipy}^2 y \quad (3.12)$$

and describe an antitrapping potential in both directions x and y . Since the two equations are decoupled we will proceed in what follows by describing the solution for the x direction. We can solve 3.11 with the initial conditions described above that take into account the expansion of the cloud before the application of the laser. The position and the velocity of the atom after the application of the lens for a time τ will then be:

$$x_{dip} = x_0 \cosh(\omega_{dipx}\tau) + \frac{v_0}{\omega_{dipx}} \sinh(\omega_{dipx}\tau) \quad (3.13)$$

$$v_{dip} = x_0 \omega_{dipx} \sinh(\omega_{dipx}\tau) + v_0 \cosh(\omega_{dipx}\tau) \quad (3.14)$$

and the position of the atoms at the detector will be given by:

$$\begin{aligned} x_{det} &= v_{dip} t_{det} + x_{dipx} \\ &= \alpha(\omega_{dipx}, t_{det}, \tau) x_0 + \beta(\omega_{dipx}, t_{det}, \tau) v_0 \end{aligned} \quad (3.15)$$

with

$$\begin{aligned} \alpha(\omega_{dipx}, t_{det}, \tau) &= \omega_{dipx} t_{det} \sinh(\omega_{dipx} \tau) + \cosh(\omega_{dipx} \tau) \\ \beta(\omega_{dipx}, t_{det}, \tau) &= \frac{1}{\omega_{dipx}} \sinh(\omega_{dipx} \tau) + t_{det} \cosh(\omega_{dipx} \tau) \end{aligned}$$

3.3.5 Calculation of the demagnification factor

Now we can calculate the RMS size of the cloud at the detector after the application of the laser, σ_{detx} :

$$\sigma_{detx}^2 = \langle x_{det}^2 \rangle - \langle x_{det} \rangle^2 = \langle x_{det}^2 \rangle \quad (3.16)$$

where $\langle \rangle$ indicates the average over all the positions and velocities. The second equality holds due to the symmetry of the atomic cloud and because we consider the Maxwell-Boltzmann distribution to be centered on zero. We can consider positions and velocities to be independent and then set $\langle x_{det} v_{det} \rangle = 0$. The calculation gives then:

$$\sigma_{detx} = \sigma_x \sqrt{\alpha^2(\omega_{dipx}, t_{det}, \tau) + \omega_x^2 \beta^2(\omega_{dipx}, t_{det}, \tau)} \quad (3.17)$$

where σ_x is the RMS size of the sample in the trap and ω_x is the trap frequency along the x axis. If the laser is not switched on ($\tau = 0$) we find that the cloud expands by a factor $\sqrt{1 + \omega_x^2 t_{det}^2}$, that is the result of the ballistic expansion. The demagnification factor is therefore simply given by $\frac{\sigma_x}{\sigma_{detx}} \sqrt{1 + \omega_x^2 t_{det}^2}$.

3.3.6 Results

The theoretical results derived above are valid only in the harmonic approximation. As we said at the end of section 3.3.2, the conditions in which the experiment has been run do not permit the application of this approximation. However we can calculate the magnification factor that one can obtain with this experimental procedure with laser parameters that make the harmonic approximation valid.

With our detector resolution, in order to observe an antibunching height equals to 1 we should be able to increase L_x by a factor of 20 and L_y by a factor of 6. With this method such a big magnification factors are hardly achievable because they would require a very large waist at least along the x axis. As a consequence we would need a high laser power or/and a small detuning in order to exert a large dipolar force. The last two parameters are delicate because they play an important role on the number of scattered photons Γ_{scatt} and therefore on the heating of the cloud, given by:

$$\Gamma_{scatt} T_{rec} \tau = \frac{1}{4\pi} \frac{\Gamma^3}{\Delta^2 I_{sat}} \frac{P}{w_x w_y} T_{rec} \tau \quad (3.18)$$

where $T_{rec} = 4\mu\text{K}/\text{photon}$ is the heating caused by the absorption of one photon. Increasing the temperature of the cloud during the application of the laser would tend to reduce the contrast of the correlation function and then to reduce the effect of the lens.

It is also interesting to note that if the atoms are falling in a level that is not sensitive to the magnetic field one does not have to wait for the magnetic field transients to go away before switch the lens on. This is the case in the Palaiseau setup. If we can set $\tilde{t} = 0$ the initial cloud size is smaller, therefore we can use a smaller waist and keep the laser on for a shorter time. These conditions translate in a stronger dipolar force and a bigger magnification effect with less heating.

With a lens not affected by aberrations and with our detector resolution one can reasonably observe a correlation function with an antibunching $\eta = 0.26$, almost a factor of 4 bigger than our observation without lens. This can be obtained with $w_x = 700\ \mu\text{m}$, $w_y = 300\ \mu\text{m}$, a detuning of 350 GHz and a power of 700 mW, if the lens is applied just after the trap switch off and is kept on for 800 μs . With these parameters the correlation length along the x axis is increased by a factor 2 and along the y axis by a factor of 2.7. At the end of the application of the lens the atomic cloud would be still more than 2 times smaller than the laser. Therefore about 75% of the atoms see an anharmonicity of less then 20%. With these parameters the heating of the cloud is about 0.1 μK .

Another way to get rid of the resolution would be to decrease the size of the trapped sample directly in the trap by superposing a dipole trap to the magnetic trap. In this case the laser would be on the red side of the resonance and the dipolar force would have the effect of increase the trap oscillation frequencies. There are two possible experimental ways to exploit this idea. The first one is to increase the oscillation frequency by a factor of 20 and 6 along the x and y axis respectively. This is feasible with an optical potential. The second possibility is to load the atoms in a vertical dipolar trap in order to have the long axis of the trap aligned with the vertical direction where the detector has a very good resolution. On the Palaiseau setup we are planning to do the second experiment. For this we have already bought a laser at 1.5 μm that will be superposed to the magnetic trap in order to load the atoms in a vertical trap with trapping frequencies of about 1 – 5 kHz on the xy plane and 50 – 100 Hz along the z axis. With these values for the oscillation frequencies it is possible to observe a contrast of the correlation function equal to 1.

3.4 Conclusion

In this chapter we presented the results obtained during the collaboration with the group of W. Vassen. First of all we described the procedure used to analyze the experimental data. Direct computation of the normalized correlation function according to equation 3.2 would be cumbersome due to the long computation time. Therefore we decided to follow another strategy to normalize the data, taking advantage from the good resolution of our detector over the vertical axis. In this way we can perform the

measurement of the correlation length along the x , y and z axis and of the contrast of the correlation function.

The acquisition of clouds of bosons and fermions at the same temperature allowed us to compare the two correlation functions and to compare them with the theory derived in chapter 1. The measurement of the Hanbury Brown Twiss effect on clouds of fermions at different temperatures allowed the comparison with theory of the behavior of the correlation as a function of the temperature. The agreement with theory is good and almost all the measured values are consistent with theory within two standard deviation. The reason for the observed discrepancies has been commented in this chapter and can be found in the saturation of the detector, a measurement not accurate enough of the detector resolution or in an anomaly of the switching off of the magnetic trap.

In the last part of the chapter we described a second experiment that we carried out in Amsterdam, aimed at the observation of a larger antibunching contrast. In this experiment the source size is artificially made smaller on the xy plane by applying a blue detuned laser on the atoms during the time-of-flight. The action of the laser on the atomic cloud is equivalent to a diverging lens for the light emitted from an extended source. The lens creates a smaller virtual source. A smaller source implies a larger correlation length that is therefore less affected by the resolution of the detector. The measured antibunching is indeed larger than the one measured without application of the lens on the atomic cloud. This experiment is first of all a demonstration of the fact that this method allows to see a larger antibunching and that the height of the correlation function is actually governed by our detector resolution. Unfortunately the lens that we used on the experiment was strongly affected by aberrations and a theoretical estimation of the expected antibunching height is not possible. In order to quantify the maximum contrast observable with this method we derived a theory for a non-aberrating lens and we found that, with our detector resolution and with reasonable laser parameters we can observe an antibunching of 26%, about a factor of four larger than the value observed without the application of the lens.

Part II

Correlated Atom Pairs

Chapter 4

First Generation Experiment

As we said in the introduction of this thesis, the generation of correlated photon pairs by D. C. Burnham and D. L. Weinberg [43] in 1970 paved the way to the realization of several experiments of fundamental interest for the generation of non-classical states of light, such as squeezed or entangled states. As we will show in this chapter, there is an equivalence between the Hamiltonian describing parametric down conversion and the Hamiltonian describing processes such as dissociation of cold molecules or generation of correlated atomic pairs by condensates collisions. This equivalence is a promising way to follow for the generation of a matter wave analogue of these experiments carried out in quantum optics.

The first part of this chapter is devoted to an historical overview in which we will describe some fundamental experiments performed with correlated photon pairs generated by parametric down-conversion.

In the second part of the chapter we will describe an experiment that we carried out during my PhD, where we generated correlated pairs of Helium atoms by the collision of two Bose-Einstein condensates. This experiment has been described in details in the PhD thesis of a former student, Aurélien Perrin [82] and has been object of several publications, theoretical and experimental [38], [84], [85], [86]. In this chapter we will recall the experimental setup and the obtained results. When two condensates collide, some of the atoms in the condensates are scattered in a spherical halo. For momentum and energy conservation, atoms are scattered in pairs flying back to back in the center of mass frame. The use of our three-dimensional single atom detector allows us to demonstrate the existence of a strong correlation between two atoms forming a pair and to fully characterize the correlation function. This is, without any doubt, the major achievement of this experiment. Some other interesting results have been obtained in this experiment, such as the observation of a correlation between atoms flying close together. This is another manifestation of the Hanbury Brown Twiss effect. The comparison of the measured correlation functions with theory is also reported in this chapter.

Going further on in the analogy between correlated photon pairs and correlated atom pairs, it would be very interesting to give an experimental demonstration of the

fact that our system exhibits number squeezing or entanglement. Unfortunately, the experiment presented in this chapter is affected by some limitations that are intrinsic to the way the two condensates collide. In order to overcome these limits we repeated the experiment in another collision geometry, as we will describe in details in chapter 5. The second generation experiment should also allow us to measure some interesting properties of the scattering sphere, such as the thickness and the number of atoms scattered per mode as a function of the scattering angle.

4.1 Correlated pairs of photons

The development of non-linear optics made possible the realization of new sources for the creation of correlated photon pairs. The correlated photon pairs were generated by a parametric down-conversion process in which a single photon from a pump laser at angular frequency ω_0 is converted into a pair of signal and idler photons at angular frequency ω_1 and ω_2 . Momentum and energy conservation impose that:

$$\begin{aligned}\omega_0 &= \omega_1 + \omega_2 \\ \mathbf{k}_0 &= \mathbf{k}_1 + \mathbf{k}_2\end{aligned}\tag{4.1}$$

where \mathbf{k} is the wave vector of the photon in the crystal. The two conditions above are called phase-matching conditions. Parametric down-conversion process is said to be degenerate if $\omega_1 = \omega_2$ and non-degenerate otherwise. Furthermore, since nonlinear crystals are also birefringent we can distinguish between two different kinds of phase-matching: in type-I phase matching idler and signal photons have parallel polarization, while in type-II phase matching the polarizations of the two photons are orthogonal. The phase-matching conditions 4.1 impose that the signal and idler photons emerge on the surface of two cones. The two cones can be concentric, as shown in figure 4.1 or not, depending on the type of phase matching.

The first experiment that demonstrated the existence of correlated photon pairs produced by a parametric amplifier was carried out by D. C. Burnham and D. L. Weinberg in 1970 [43]. In the next section we will describe this experiment and in section 4.1.2 we will describe parametric down-conversion from a theoretical point of view. As we will see, correlated pairs of photons produced by this process show interesting quantum features. In section 4.1.3 we will describe some key experiments that highlighted this quantum character.

4.1.1 Burnham and Weinberg (1970)

Few years after the first observation of parametric down-conversion in a crystal (see for example [87]), D. C. Burnham and D. L. Weinberg [43] performed an experiment to demonstrate that photons emitted in non-linear crystal are correlated in pairs. The experimental setup is shown in figure 4.2 left. A 9 mW He-Cd laser at 325 nm pumps a non-linear crystal. Photons generated by parametric-down conversion are emitted in two cones forming an angle ϕ_1 and ϕ_2 with respect to the pump beam. The coincidence

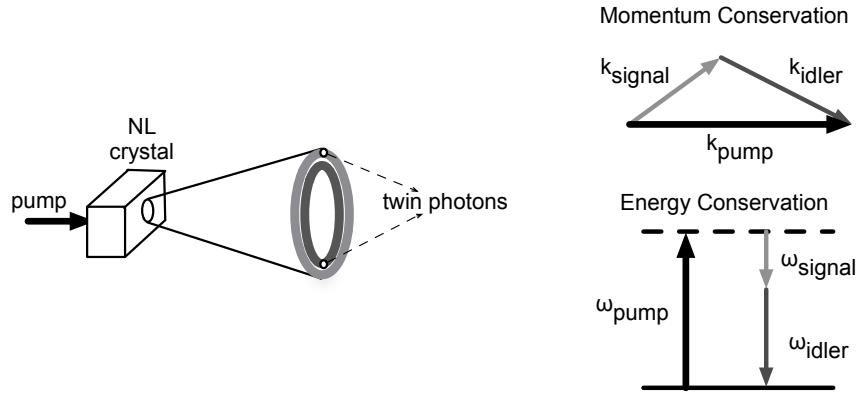


Figure 4.1: Illustration of the phase-matching conditions in parametric down-conversion processes. In case of type-I phase-matching the correlated photons are emitted on two concentric cones, as shown in the left side of the figure. On the right side of the figure energy and momentum conservation are illustrated.

rate is detected by two photomultipliers, one of which is fixed and aligned on the direction of one of the photon beams, while the other one can be moved on the xy plane (see figure 4.2). As in the case of Hanbury Brown Twiss experiments, measuring the coincidence rate is equivalent to measure the second order correlation function of the two photons, signal and idler, on the two detectors. On the right side of figure 4.2 we show the coincidence rate measured as a function of the displacement of one of the photomultipliers along the y axis (perpendicular to the plane of figure 4.2). The coincidence rate R_c shows a peak for a given position of the movable detector. Since the detection rate R_1 , that is the number of photons detected on the movable photomultiplier, stays constant over all the measurement range¹, the peak shown by R_c cannot result from an intensity enhancement of the photon beam. This is the signature of the fact that photons arrive by pairs on the two detectors. The coincidence rate along the x axis was limited by the spatial extension of the light beam. Further measurements [43] proved that photon pairs verify phase-matching conditions 4.1.

Subsequent experiments, using a more precise and sophisticated electronics, measured the signal-idler time correlation. As expected the correlation time is inversely proportional to the frequency width, in a way that doesn't depend on the coherence time of the pump laser [88]. The width of the correlation function along the three axis (xy plane and time) is related to the size of the scattering modes [89].

4.1.2 Theory of the non-degenerate parametric amplifier

We can consider a simple model where only two of the correlated modes are selected and the pump is treated as a classical field at frequency ω_0 . This last approximation is verified because the pump is a laser beam with a large intensity and relative fluctuations

¹The decrease of R_1 for large y is due to scanning the detector off the light cone.

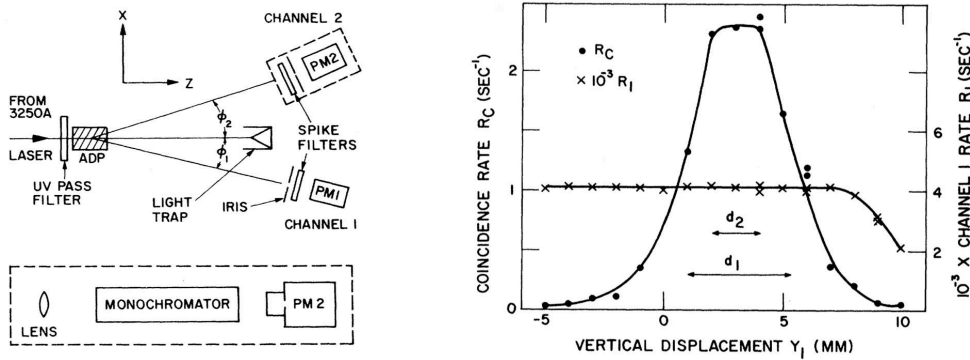


Figure 4.2: On the left, setup used by Burnham and Weinberg to create correlated pairs of photons. The pump laser at 325 nm is shined on the non-linear crystal. The two new beams are at a wavelength of 633 nm and 688 nm and have the same polarization (type-I phase-matching). The generated photons are emitted in two cones of light forming an angle ϕ_1 and ϕ_2 with the direction of the pump beam. The coincidence rate in the two created beams is measured by two photomultipliers. One of the photomultipliers can be translated on the xy plane. On the right, the measured coincidence rate is shown, as a function of the vertical displacement (y axis) of the movable detector. R_c is the coincidence rate on the two detectors, while R_1 is the detection rate on one detector. The peak showed by R_c is the signature of the correlation between signal and idler photons. The figure has been adapted from [43].

can be neglected. The signal and the idler are fully quantum and are described by creation and annihilation operators a_1^\dagger , a_1 and a_2^\dagger , a_2 . The hamiltonian of the system can be written as [15]:

$$H = \hbar\omega_1 a_1^\dagger a_1 + \hbar\omega_2 a_2^\dagger a_2 + i\hbar\chi(a_1^\dagger a_2^\dagger e^{-i\omega_0 t} - a_1 a_2 e^{i\omega_0 t}) \quad (4.2)$$

The coupling constant is proportional to the second order susceptibility of the medium and to the amplitude of the pump. The solutions of the Heisenberg equations of motion in the interaction picture are:

$$\begin{aligned} a_1(t) &= a_1(0) \cosh \chi t + a_2^\dagger(0) \sinh \chi t \\ a_2(t) &= a_2(0) \cosh \chi t + a_1^\dagger(0) \sinh \chi t \end{aligned}$$

If the system initially starts in the vacuum state (i.e. the two modes, signal and idler, are empty) the time dependence of the mean number of photons in the two modes can be written as [15]:

$$\langle n_1(t) \rangle = \langle n_2(t) \rangle = \sinh^2 \chi t \quad (4.3)$$

meaning that vacuum fluctuations are amplified in the process and that the number of photons increases exponentially with time.

A two-mode system like the one generated in a parametric amplifier exhibits interesting quantum correlations between the two modes. For example it has been demonstrated theoretically and experimentally that such two-modes correlations can violate classical inequalities [15], [90], [91], such as the Cauchy-Schwarz inequality.

If the two fields a_1 and a_2 can be treated as classical fields, the Cauchy-Schwarz inequality is [15]:

$$\langle a_1^\dagger a_1 a_2^\dagger a_2 \rangle \leq \left[\langle a_1^{\dagger 2} a_1^2 \rangle \langle a_2^{\dagger 2} a_2^2 \rangle \right]^{1/2} \quad (4.4)$$

The two modes of the non-degenerate parametric amplifier are symmetric, i.e. $\langle n_1 \rangle = \langle n_2 \rangle$ and $\langle n_1^2 \rangle = \langle n_2^2 \rangle$, where $n_i = a_i^\dagger a_i$. Therefore inequality 4.4 becomes:

$$\langle a_1^\dagger a_1 a_2^\dagger a_2 \rangle \leq \langle a_1^{\dagger 2} a_1^2 \rangle \quad (4.5)$$

On the other hand, in quantum mechanics, the appropriate inequality for two non-commuting operators is:

$$\langle a_1^\dagger a_1 a_2^\dagger a_2 \rangle^2 \leq \langle (a_1^\dagger a_1)^2 \rangle \langle (a_2^\dagger a_2)^2 \rangle \quad (4.6)$$

that, if the two modes are symmetric, can be written as [15]:

$$\langle a_1^\dagger a_1 a_2^\dagger a_2 \rangle \leq \langle (a_1^\dagger)^2 (a_1)^2 \rangle + \langle a_1^\dagger a_1 \rangle \quad (4.7)$$

By comparing equations 4.5 and 4.7 we can see that there can be quantum systems that violate the classical Cauchy-Schwarz inequality. Furthermore, the violation of the classical inequality will be the maximum allowed by quantum mechanics when $\langle a_1^\dagger a_1 a_2^\dagger a_2 \rangle = \langle (a_1^\dagger)^2 (a_1)^2 \rangle + \langle a_1^\dagger a_1 \rangle$.

One can show that, if the parametric amplifier exhibits perfect squeezing of the number difference, then the violation of the Cauchy-Schwarz inequality is maximal. In fact one can show that the following conservation law holds:

$$n_1(t) - n_2(t) = n_1(0) - n_2(0) \quad (4.8)$$

Using this relation one can write:

$$\langle n_1(t) n_2(t) \rangle = \langle n_1^2(t) \rangle + \langle n_1(t) [n_2(0) - n_1(0)] \rangle. \quad (4.9)$$

Now, if the system is initially in the vacuum state, then one has simultaneously:

$$\begin{aligned} \langle n_1(t) n_2(t) \rangle &= \langle a_1^\dagger(t) a_1^\dagger(t) a_1(t) a_1(t) \rangle + \langle a_1^\dagger(t) a_1(t) \rangle \\ n_1(t) - n_2(t) &= 0 \end{aligned}$$

The first of these equations corresponds to maximum violation of the classical Cauchy-Schwarz inequality allowed by quantum mechanics, while the second corresponds to perfect squeezing.

Therefore the quantum correlations exhibited by the non-degenerate quantum amplifier violate classical inequalities. These quantum correlations can be further exploited to give squeezing and states similar to those discussed in the Einstein-Podolsky-Rosen paradox. In the following sections we will describe some of the pioneering experiments using these quantum properties of parametric down conversion.

4.1.3 Experiments with correlated photon pairs

Quantum fluctuations in a two-mode parametric oscillator

Several years later, degenerate parametric down-conversion was used to generate squeezed states of light on one of the two beams produced in the process [92], [93]. At the same time, S. Reynaud et al. [94] showed that the photon numbers in signal and idler beams generated in non-degenerate down-conversion are strongly correlated. As shown by equation 4.8, even if the intensity of each beam can fluctuate, the fluctuations of the two beams are identical. Therefore the intensity difference of the two beams will carry no fluctuation at all, i.e. the variance of $I_1 - I_2$ (where I_1 and I_2 are the intensities of each beam) is zero. The first experimental confirmation of the number difference squeezing in twin beams was given by Heidmann et al. [95]. The experimental setup

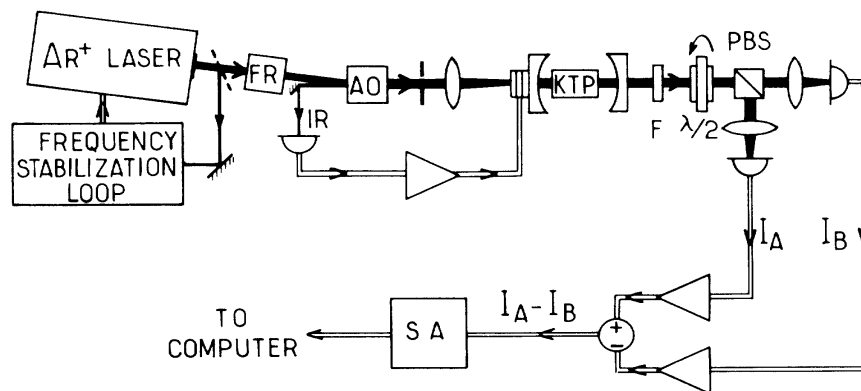


Figure 4.3: Experimental setup used by Heidmann et al. to prove number difference squeezing in twin beams. The twin beams were generated in an OPO, in order to increase light intensity. The two beams, that have different polarization, are separated by a polarizing beam splitter (PBS) and are focussed on two photodiodes. The measured photo-current is then amplified and subtracted. The noise on the current difference is then monitored by a spectrum analyzer. The figure has been taken from [95].

is shown in figure 4.3. In order to increase the intensity of the generated beams, the authors of [95] used an optical parametric oscillator (OPO). In this device, a type-II non-linear crystal is placed inside an optical cavity, that amplifies the intensity of the modes of the twin beams without changing the correlation. The OPO emits two cross polarized twin beams that are separated by a polarizing beam splitter and then focussed onto two photodiodes having the same quantum efficiency. The two photo-currents are then amplified and subtracted and the noise on the resulting difference current is monitored by a spectrum analyzer. A noise reduction of about 30% with respect to the shot-noise limit is observed. Subsequent experiments (see for example [96], [97]) showed a reduction of 88% below the shot-noise limit.

Hong-Ou-Mandel interferometer

Parametric down-conversion was also used to show quantum interference effects. A fundamental experiment has been carried out by C. K. Hong, Z. Y. Ou and L. Mandel in 1987 [98]. They observed the interference between signal and idler photons generated by type-I degenerate down-conversion in a nonlinear crystal. The experimental

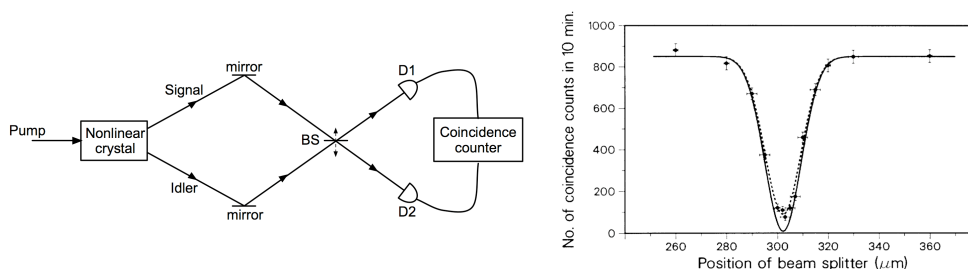


Figure 4.4: On the left side: Experimental setup used by Hong, Ou and Mandel to measure single photon interference. The signal and idler photons generated by parametric down-conversion are combined on a beam splitter. The intensity at the two output ports of the beam splitter is measured with two detectors (D_1 and D_2). The measured detection coincidences are reported on the right side of the figure, as a function of the position of the beam splitter. The plot has been taken from [98]. When the position of the beam splitter is such that the signal and idler paths are equal, a coincidence reduction is detected.

arrangement and the experimental results are shown in figure 4.4. Signal and idler photons are recombined on a 50 : 50 beam splitter, the intensities at the two output ports of the beam splitter are measured and detection coincidences are registered. The beam splitter can be translated in order to change the path lengths of idler and signal photons. If the path lengths are identical, no coincidences are detected. This means that either the two photons went to D_1 or both went to D_2 . Since the two photons are identical, destructive interference of the probability amplitude prevents the possibility that the two photons go to two different output ports. On the contrary, if the difference in the path lengths is larger than the correlation length, no interference occurs and each photon randomly exits either output port, producing coincidences on D_1 and D_2 for 50% of the events.

Einstein-Podolsky-Rosen paradox and Bell's inequalities

The generation of correlated photon pairs paved the way for the generation of entangled states and for fundamental tests of quantum mechanics. In 1935 A. Einstein, B. Podolsky and N. Rosen published a famous paper titled "Can quantum-mechanical description of physical reality be considered complete?" [11] where they formulated a paradox suggesting that the quantum mechanic description of reality could be incomplete. In a *gedanken* experiment, they consider a system composed by two sub-systems that interacted for a finite amount of time, but that are no longer interacting at the

moment of the measurement. This is the case of a correlated photon pair. The central point of the EPR paradox is that, if the two systems are no longer interacting, a measurement made on one system cannot affect the other one. In other words physical reality is described by local variables. This hypothesis has a strong implication: one can exactly measure the value of two non-commuting variables, performing the measurement of one variable on one system and the measurement of the other variable on the second system. This is in contradiction with the Heisenberg uncertainty principle. Therefore, either the EPR hypothesis is false, or the quantum mechanical description of reality is not complete.

Non-locality is the basis for quantum entanglement and has no classical counterpart. Bell designed an ingenious variation of the EPR experiment and proved that there are physical situations in which quantum mechanics prediction differs from the results one would obtain if the EPR hypothesis is verified. Bell's key result was the derivation of an inequality which bear his name. Bell's theorem states that the inequality is always obeyed if the EPR interpretation of the world is correct. Violation of Bell's inequality has been experimentally demonstrated by A. Aspect et al. using correlated photon pairs generated by atomic cascade of calcium [99],[100],[101]. Subsequently, many experiments have been performed to test for violations of Bell's inequalities with very high degree of accuracy. The use of entangled photon pairs generated by down-conversion has increased the sensitivity of the experiments, thus leading to even more convincing demonstrations [102]. The use of optical fibers allowed the demonstration of non-locality over very large distances and with strictly independent observers (see for example [103] and [104]). The violation of Bell's inequalities demonstrates the importance of quantum entanglement and is at the heart of quantum information.

4.2 Correlated pairs of atoms

Greiner et al. (2005)

The experiment of Greiner et al. [37] is the analogue of the experiment of Burnham and Weinberg [43] described in section 4.1. Pairs of atoms are created by the dissociation of ultracold diatomic molecules of fermionic ^{40}K atoms. After dissociation, the two atoms move back to back obeying momentum and energy conservation, as imposed by the dissociation process. The atoms are then detected after a time-of-flight by using absorption imaging. In 2004 Altman et al. proposed a way to measure quantum correlations from the atom shot noise present in absorption images [60]. Combining the theoretical prediction of K.Kheruntsyan and P. D. Drummond [105] and the suggestion by Altman, the authors demonstrated that the atoms generated by dissociation of ultracold molecules are correlated in pairs. The obtained results are shown in figure 4.5. On the left side of figure 4.5 a scheme of molecular dissociation is shown. After dissociation the two atoms propagate back to back, in the centre of mass frame, with momentum $+\mathbf{k}$ and $-\mathbf{k}$ respectively. In the middle of figure 4.5 we show the absorption image after dissociation. The black spot in the middle is a residual cloud of atoms and

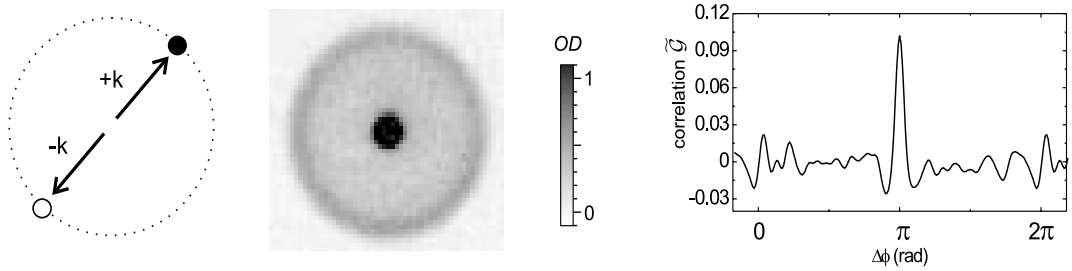


Figure 4.5: On the left: sketch of the molecular dissociation in the centre of mass frame. After dissociation, the correlated atoms are emitted back to back with momentum \mathbf{k} and $-\mathbf{k}$. In the middle: Absorption image of the sphere after dissociation. A spherical halo is clearly visible. The black spot results from a residual cloud of atoms and molecules. On the right: correlation as a function of $\Delta\phi$, that is the angle between two \mathbf{k} vectors. The peak at $\Delta\phi = \pi$ is the signature of the correlation between atoms with opposite momenta. The figure has been adapted from [37].

molecules that did not dissociate. The correlated atom pairs are in the spherical halo around the black spot. On the right side of figure 4.5 we show the non-normalized correlation function as a function of the angle $\Delta\phi$ between the \mathbf{k} vectors of the two atoms. A peak for $\Delta\phi = \pi$ is clearly visible, proving that the atoms of opposite momentum are well correlated in pairs. The width of the correlation peak is limited by the resolution of the detection system. Note that, since the cloud image is integrated along one direction, the authors don't have access to the correlation function along three dimensions in space. For the same reason, a measurement of the thickness of the spherical halo is difficult.

He* correlated pairs

In 2007 we performed an experiment to generate metastable He atom pairs from the collision of two counterpropagating Bose-Einstein condensates [38]. The collision takes place along the long axis of the condensates. After the collision the atoms were detected by a micro-channel plate with a delay-line anode, the same detector used for the Amsterdam-Palaiseau experiment described in the previous chapter of this thesis. Detailed information about the detector can be found in appendix A.

Thanks to the three-dimensional features of this detector it has been possible to deeply study the correlation function as well as the characteristics of the spherical collision shell. In particular we characterized the correlation function in three dimensions, measuring the height and the width of the correlation peaks. We observed a strong correlation peak for atoms propagating back to back, a clear signature of the fact that the atoms are correlated in pairs. We also observed a peak for atoms that have collinear velocity, a signature of the Hanbury Brown Twiss effect relying on the indiscernibility of two atomic pairs [86]. We will come back to this point in section 4.6.4. In both cases, collinear and back to back correlations, the width of the correlation peak is related to the velocity spread of the colliding condensates, that therefore fixes the size of

a scattering mode.

In section 4.5 we will describe in detail the experimental production of the correlated He atom pairs and in section 4.6 we will comment on the obtained results.

As we said in the introduction of this chapter, in order to overcome some of the limits of the experiment done in 2007 we repeated the experiment in another collision geometry. This time the collision takes place along the short axis of the condensates. This new version of the experiment should allow us to study in detail the population of the scattering modes as a function of the angle and, eventually, to observe a squeezing in the difference of the number of atoms scattered into two correlated modes. This experiment will be described in chapter 5 and we will present some preliminary results.

In the next section we would like to draw the attention of the reader on the analogy between the production of correlated photon pairs via parametric down-conversion and the production of correlated atom pairs via the collision of two condensates on a theoretical point of view.

4.3 Analogy with the parametric amplifier

The collision between two condensates can be modeled by a contact potential $V(\mathbf{r}) = g\delta(\mathbf{r})$, where $g = 4\pi\hbar^2 a/m$ depends on the scattering length a . The N body Hamiltonian can therefore be written as² [109]:

$$H = - \int d\mathbf{r} \hat{\Psi}^\dagger(\mathbf{r}, t) \frac{\hbar^2 \nabla^2}{2m} \hat{\Psi}(\mathbf{r}, t) + g \int d\mathbf{r} \hat{\Psi}^\dagger(\mathbf{r}, t) \hat{\Psi}^\dagger(\mathbf{r}, t) \hat{\Psi}(\mathbf{r}, t) \hat{\Psi}(\mathbf{r}, t) \quad (4.10)$$

The trapping potential used for preparing the initial condensate before the collision is omitted since, during the collision, the two condensates are no longer trapped (see section 4.5.1). The field operators $\hat{\Psi}^\dagger(\mathbf{r}, t)$ and $\hat{\Psi}(\mathbf{r}, t)$ are the creation and annihilation operators for a particle at the position \mathbf{r} and verify the bosonic commutation rules:

$$\begin{aligned} [\hat{\Psi}(\mathbf{r}, t), \hat{\Psi}^\dagger(\mathbf{r}', t)] &= \delta(\mathbf{r} - \mathbf{r}') \\ [\hat{\Psi}(\mathbf{r}, t), \hat{\Psi}(\mathbf{r}', t)] &= 0 \end{aligned} \quad (4.11)$$

Since the Hamiltonian 4.10 is of the fourth order in $\hat{\Psi}(\mathbf{r}, t)$, the Heisenberg equation governing the evolution of the field,

$$i\hbar\partial_t \hat{\Psi}(\mathbf{r}, t) = -\frac{\hbar^2 \nabla^2}{2m} \hat{\Psi}(\mathbf{r}, t) + g \hat{\Psi}^\dagger(\mathbf{r}, t) \hat{\Psi}(\mathbf{r}, t) \hat{\Psi}(\mathbf{r}, t) \quad (4.12)$$

is nonlinear and therefore, in general, analytically intractable. However, we can model our system assuming that the two counter-propagating condensates constitute an undepleted source for the process of scattering, exactly as in the case of the parametric

²The Hamiltonian describing the dissociation of a cold cloud of molecules has several analogies with the one describing the collision between two condensates. A detailed treatment has been carried out in several papers by K. Kheruntsyan et al., see for example [106],[107],[108].

amplifier (see section 4.1.2). Therefore we can apply a Bogoliubov approximation and split the field operator into two parts: ψ and $\hat{\delta}$.

The first contribution describes the macroscopically occupied modes, in our case the two Bose-Einstein condensates, where fluctuations are usually small and can be neglected. These modes can be treated classically.

The second contribution, $\hat{\delta}$, describes field modes that show large fluctuations and require a full quantum mechanical treatment. In general this term is small and can be treated in a perturbative way. In our case it represents the scattering modes that are populated by atoms scattered during the condensates collision.

The bosonic field can then be written in the following way:

$$\tilde{\Psi}(\mathbf{r}, t) = \psi_Q(\mathbf{r}, t) + \psi_{-Q}(\mathbf{r}, t) + \hat{\delta}(\mathbf{r}, t) \quad (4.13)$$

where $\pm Q$ denotes the mean momentum of the colliding condensates.

At this point it is already easy to understand the equivalence between Hamiltonian 4.2 and 4.10, in the undepleted pump approximation. Furthermore, the equivalence can become even more explicit if we model the two counter-propagating condensates as plane waves [110]:

$$\psi_{\pm Q}(\mathbf{r}, t) = \sqrt{n_{\pm Q}} e^{\mp i \mathbf{Q} \cdot \mathbf{r}} e^{-i \hbar (Q^2/2m)t} \quad (4.14)$$

where $n_{\pm Q}$ is the density of the particles. In what follows we will assume for simplicity that both waves are equally populated, meaning $n_{\mathbf{Q}} = n_{-\mathbf{Q}} = n$. In a box of size L , the boson field operator can be decomposed into normalized plane waves:

$$\hat{\delta}(\mathbf{r}, t) = L^{-3/2} \sum_{\mathbf{q}} e^{-i \mathbf{q} \cdot \mathbf{r}} a_{\mathbf{q}}(t) \quad (4.15)$$

where $a_{\mathbf{q}}(t)$ is the annihilation operator of an atom of the wave vector \mathbf{q} .

Substituting equations 4.14 and 4.15 into Hamiltonian 4.10 we obtain:

$$H = \sum_{\mathbf{q}} \left(\frac{\hbar^2 q^2}{2m} a_{\mathbf{q}}^\dagger(t) a_{\mathbf{q}}(t) + gn \left(e^{-i \hbar (Q^2/2m)t} a_{\mathbf{q}}^\dagger(t) a_{-\mathbf{q}}^\dagger(t) + h.c. \right) \right) \quad (4.16)$$

If we only consider two modes of opposite momentum $\pm \mathbf{q}$, the Hamiltonian 4.16 is formally equivalent to the Hamiltonian 4.2.

The solution of the Heisenberg equations of motion for annihilation and creation operators can be found analytically and takes the following form:

$$a_{\mathbf{p}}(t) = e^{-i \hbar (Q^2/2m)t} \left[F_1(t, p) a_{\mathbf{p}}(0) - F_2(t, p) a_{-\mathbf{p}}^\dagger(0) \right] \quad (4.17)$$

where

$$\begin{aligned} F_1(t, p) &= \cosh[\sqrt{\Delta(p)}t] - i \hbar \frac{p^2 - Q^2}{2m} \frac{\sinh[\sqrt{\Delta(p)}t]}{\sqrt{\Delta(p)}} \\ F_2(t, p) &= i gn \frac{p^2 - Q^2}{m} \frac{\sinh[\sqrt{\Delta(p)}t]}{\Delta(p)} \\ \Delta(p) &= (2gn/\hbar)^2 - (\hbar(p^2 - Q^2)/2m)^2 \end{aligned} \quad (4.18)$$

From the solution of the Heisenberg equations we can see that modes that are initially empty are occupied as in the case of the parametric amplifier. More precisely, modes can be divided into two classes according to their evolution: modes for which the kinetic energy difference between the incident and the scattered atoms is smaller than the mean field energy ($\Delta(p) > 0$) have their occupation growing exponentially with time and experience Bose enhancement; modes that have $\Delta(p) < 0$ have a population that oscillates around unity. We will come back to this point in section 4.7.2.

We would like to point out that the analogy between the collision of two condensates and the generation of correlated photon pairs is even stronger if we consider four-wave mixing phenomena. Two counterpropagating pump waves interact with a non-linear medium and give rise to two twin beams satisfying phase-matching conditions imposed by the process. Four-wave mixing occurs in non-linear medium with third order non-linear susceptibility. The Hamiltonian of the process is formally equivalent to the one describing parametric amplification processes [111], [112] and indeed four-wave mixing has been observed for atomic matter waves [34], [35], [36].

4.4 A more refined theory

In the previous section, we modeled the two colliding condensates as plane waves. However, in order to model our experiment in a way closer to reality, a more accurate theoretical treatment can be done and two different theoretical approaches can be followed. Our group collaborates with two groups of theoreticians. The group of M. Trippenbach, in Poland, had already published several works about the analytical calculation of the correlation function between atoms issued from the collision of two condensates [113], [110], [109]. The group of K. Kheruntsyan, in Australia, had already studied pair creation during the dissociation of molecules [105], [114], [115], [106], [107]. The calculation done by this group is fully numerical and uses the so-called positive-P method. Details about the calculation procedure can be found in [82]. In the following sections we will describe the two theoretical approaches. They can be applied to the two experiments that we carried out. However, at the actual stage, we only have theoretical results for the first generation experiment and we will discuss how the experimental results compare with them in section 4.7. A further study, going in parallel with the progress of the experimental work will make possible soon a comparison with the second generation experiment as well.

4.4.1 Analytical approach

The approach followed by the group of M. Trippenbach is based on the analytical calculation of the solution of the Heisenberg equations for the Hamiltonian 4.10. The procedure is the one used in the previous section, but the condensates are modeled by Gaussians. We can inject equation 4.13 into the Heisenberg equation 4.12 and, in the spirit of the Bogoliubov approximation, we keep only terms at the first order in $\hat{\delta}$. Furthermore, since the mean-field energy is negligible with respect to the mean

kinetic energy of the two scattering condensates ($\hbar^2 Q^2/2m$), the mean-field terms can be neglected and we obtain:

$$i\hbar\partial_t\hat{\delta}(\mathbf{r},t) = -\frac{\hbar^2\nabla^2}{2m}\hat{\delta}(\mathbf{r},t) + g\left[2\psi_Q(\mathbf{r},t)\psi_{-Q}(\mathbf{r},t) + \psi_Q^2(\mathbf{r},t) + \psi_{-Q}^2(\mathbf{r},t)\right]\hat{\delta}^\dagger(\mathbf{r},t) \quad (4.19)$$

The three terms in brackets correspond to three different processes that are illustrated in figure 4.6. The first one corresponds to annihilation of two particles from counter-propagating condensates and creation of two particles in the field $\hat{\delta}$ of scattered atoms. The second and the third terms correspond to the annihilation of two particles from the same condensate (either ψ_Q or ψ_{-Q}) and creation of two particles in the $\hat{\delta}$ field. Since the second and the third processes are non-resonant, their probability to occur is small and the corresponding terms can be neglected. Therefore the Heisenberg equation can be simplified to:

$$i\hbar\partial_t\hat{\delta}(\mathbf{r},t) = -\frac{\hbar^2\nabla^2}{2m}\hat{\delta}(\mathbf{r},t) + 2g\psi_Q(\mathbf{r},t)\psi_{-Q}(\mathbf{r},t)\hat{\delta}^\dagger(\mathbf{r},t) \quad (4.20)$$

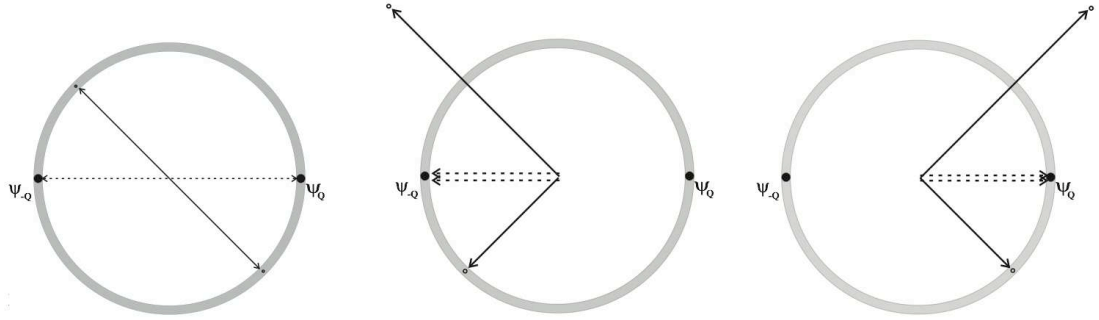


Figure 4.6: Visualisation of the three scattering terms entering in equation 4.19. On the left side we represent the term proportional to $2\psi_Q\psi_{-Q}\hat{\delta}^\dagger$. Two atoms, one from each of the condensates, are annihilated and two atoms conserving momentum and energy are created. In the middle we represent the term proportional to $\psi_{-Q}^2\hat{\delta}^\dagger$. Two atoms are annihilated from ψ_{-Q} and scattered such that momentum is conserved. On the right we show the analogous sketch for the term proportional to $\psi_Q^2\hat{\delta}^\dagger$.

To allow analytical calculations we model the condensates wave-functions as Gaussians with cylindrical symmetry. The spatial widths of the condensates, σ_x along the bias axis and σ_{yz} in the radial direction, are extracted from the initial condensate wave-function which is calculated numerically from the Gross-Pitaevskii equation. Now we have all the ingredients to calculate $\hat{\delta}$.

This approach allows to have an analytical formulation of the thickness of the scattering sphere and of the two-body correlation function. In addition, this method has the advantage to be analytical. This allows to identify of the physical processes (in particular energy and momentum conservation) involved in the pair formation process.

However it doesn't take account of some effects (for example the mean-field interaction between the atoms in the condensate or the expansion of the condensates during the collision, see 4.5.1) that could be important in our experiment. We will come back on these points in section 4.7, where we will compare the theoretical and the experimental results.

4.4.2 Numerical approach

The numerical calculation done by K. Kheruntsyan et al. to simulate our experiment uses the positive-P representation method [15], [116], [82]. The advantage of this method is that, given the Hamiltonian of the interacting many-body system, no additional approximations are imposed to simulate the quantum dynamics governed by the Hamiltonian. The drawback is that it is subject to large sampling errors and boundary problems as the simulation time increases, eventually leading to diverging results. For this reason the simulation of our experiment is restricted to a very short collision time (typically $\approx 25 \mu s$, [84]), which is about 6 times shorter than the experimental collision time for the first generation experiment and about 2 times shorter for the second generation experiment (see section 5.2.1). An extrapolation to longer times is therefore needed. In addition, energy conservation is a less stringent constraint for short collision times and this can possibly lead to a discrepancy between theory and experiment.

The Hamiltonian used to describe the system is 4.10. In the positive-P approach the quantum field operators $\hat{\Psi}(\mathbf{r}, t)$ and $\hat{\Psi}^\dagger(\mathbf{r}, t)$ are represented by two complex fields $\Psi(\mathbf{r}, t)$ and $\tilde{\Psi}(\mathbf{r}, t)$ that are allowed to fluctuate independently (i.e. they are two stochastic complex fields). The dynamics of $\Psi(\mathbf{r}, t)$ and $\tilde{\Psi}(\mathbf{r}, t)$ is governed by the following stochastic equations [117]:

$$\begin{aligned} \frac{\partial \Psi(\mathbf{r}, t)}{\partial t} &= \frac{i\hbar}{2m} \nabla^2 \Psi - \frac{ig}{\hbar} \tilde{\Psi} \Psi \Psi + \sqrt{-\frac{ig}{\hbar} \Psi^2} \zeta_1(\mathbf{r}, t) \\ \frac{\partial \tilde{\Psi}(\mathbf{r}, t)}{\partial t} &= -\frac{i\hbar}{2m} \nabla^2 \tilde{\Psi} + \frac{ig}{\hbar} \Psi \tilde{\Psi} \tilde{\Psi} + \sqrt{\frac{ig}{\hbar} \tilde{\Psi}^2} \zeta_2(\mathbf{r}, t) \end{aligned} \quad (4.21)$$

where $\zeta_1(\mathbf{r}, t)$ and $\zeta_2(\mathbf{r}, t)$ are real independent white noise sources with zero mean and the following correlation:

$$\langle \zeta_j(\mathbf{r}, t) \zeta_k(\mathbf{r}', t') \rangle = \delta_{jk} \delta(\mathbf{r} - \mathbf{r}') \delta(t - t') \quad (4.22)$$

There is an equivalence between statistical averages over the fields $\Psi(\mathbf{r}, t)$ and $\tilde{\Psi}(\mathbf{r}, t)$ and corresponding normally ordered expectation values of operators $\hat{\Psi}(\mathbf{r}, t)$ and $\hat{\Psi}^\dagger(\mathbf{r}, t)$:

$$\langle [\hat{\Psi}^\dagger(\mathbf{x}, t)]^m [\hat{\Psi}(\mathbf{x}', t)]^n \rangle = \langle [\tilde{\Psi}(\mathbf{x}, t)]^m [\Psi(\mathbf{x}', t)]^n \rangle \quad (4.23)$$

As the number of numerical realizations grows towards ∞ , the equivalence 4.23 becomes exact [117]. The initial condition for the simulation is the wave function of the initial trapped condensate modulated with a standing wave that imparts initial momenta $\pm k_{rec}$ in the direction of the collision.

After having numerically solved equations 4.21, one can calculate the correlation function and the thickness of the scattering sphere. The results obtained for the first generation experiment will be given in section 4.7.2 and a comparison with the experimental results will be drawn.

4.5 Experimental setup

The first experimental step consists in the production of a Bose-Einstein condensate. The procedure has been described in chapter 2. Here we recall only the experimental values that are important in this context. In the experiment of ref. [38] we are able to create Bose-Einstein condensates of the order of $10^4 - 10^5$ atoms. The trap has a cigar shape with trapping frequencies of 1150 Hz along the radial direction and 47 Hz along the axial direction. The long axis of the condensate is aligned with the bias field, that defines the quantization axis. We will call the bias axis x in the following. Once the condensate has been produced it is separated in two counterpropagating condensates that collide. The result of the collision is a sphere of atoms verifying momentum and energy conservation. In the next section we will explain in detail the method used to the production of the two condensates.

4.5.1 Production of two colliding condensates

The two colliding Bose-Einstein condensates are produced by using stimulated Raman transitions with different momentum transfers. The Raman transitions are produced by three laser beams L_1 , L_2 and L'_2 . The three beams are blue detuned by $\Delta = 400$ MHz from the transition $2^3S_1 \rightarrow 2^3P_0$ (at 1083 nm). In figure 4.7 we show the level scheme for this transition. Due to the presence of the trapping magnetic field, the magnetic substates of the level 2^3S_1 are not degenerate. The energy difference depends on the value of the bias field. For our trap configuration the energy difference is $h \times \delta = h \times 700$ kHz. L_2 and L'_2 have the same frequencies and the same (σ^-) polarization, while L_1 is π polarized. The frequency difference between L_1 and L_2 is δ . Raman transitions are driven by L_2 and L_1 and by L'_2 and L_1 . Since L_2 and L'_2 have different propagation directions the momentum transferred to the atoms by the couple $L_1 + L_2$ differs from the momentum transferred by $L_1 + L'_2$. In the next subsection we will see the details of this momentum transfer and we will explain why this is responsible of the separation of the initially trapped condensate into two colliding condensates.

Raman transitions not only make the two condensates collide, but also transfer in a coherent way the atoms trapped in the $m_x = 1$ state to the $m_x = 0$ state, where they are no longer trapped. Therefore the atoms that undergo the Raman transition fall under the effect of gravity and are detected by the micro-channel plate without switching off the magnetic trap. This is an important feature of the Raman transfer driven here: as we have already pointed out several times in this thesis we are not really able to control the switch off of the magnetic trap. Eddy currents and residual fields make the trap switch off a really delicate step that can introduce uncontrolled perturbations on the

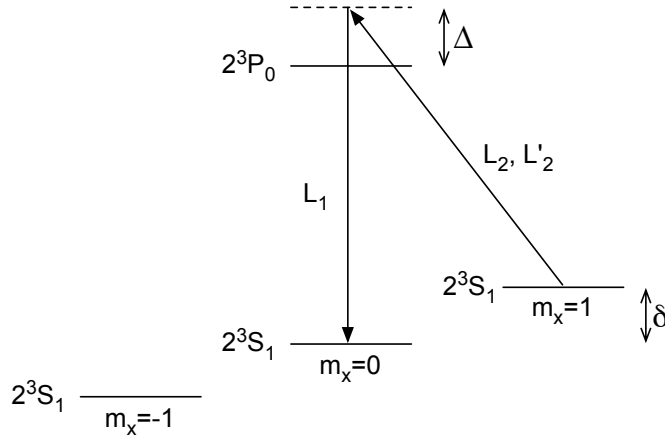


Figure 4.7: Scheme of the Raman transition used to create the two colliding condensates. Since the final state of the Raman transition is insensitive to the magnetic field, the atoms that undergo the Raman transition fall on the micro-channel plate under the effect of gravity and are detected without the need of switching off the magnetic trap.

atomic cloud. Therefore a method allowing time-of-flight detection without switching off the magnetic field is useful.

The relative power and detuning of the Raman beams is chosen so that the Raman transition is insensitive to the initial velocity of the atoms in the condensate. This can be realized providing that

$$2 \frac{|\Omega_1| |\Omega_2|}{|\Delta|} \gg |\delta_{Dopp}| \quad (4.24)$$

where $|\Omega_1|$ and $|\Omega_2|$ are the one photon Rabi frequencies of the two beams driving the considered Raman transition (L_1 and L_2 or L_1 and L'_2) and δ_{Dopp} is the detuning of each atom with respect to the laser beams due to the Doppler effect. We are able to drive Raman oscillations with an efficiency of the order of 90%³ for a pulse duration of ≈ 500 ns. The power of the beams is $\simeq 80$ mW their size is $\simeq 2$ mm (at $1/e^2$).

Momentum transferred by the Raman beams

The geometrical configuration of the three beams will define the momentum transferred from photons to atoms. Figure 4.8 shows the disposition of the three Raman beams in the vacuum chamber. L_1 propagates in the vertical plane and forms an angle of 8° with the vertical axis. As we said above (see figure 4.7), L_1 should be π polarized, i.e. the polarization vector has to be parallel to the bias field. This condition can be satisfied for the beam L_1 . On the other hand L_2 propagates on the horizontal plane

³The estimation of the efficiency of the Raman transfer is made hard by the saturation of the micro-channel plate during the detection of a condensate. The estimation given in the text has been made by decreasing the voltage of the micro-channel plate in order to limit saturation, but it still remains an estimate.

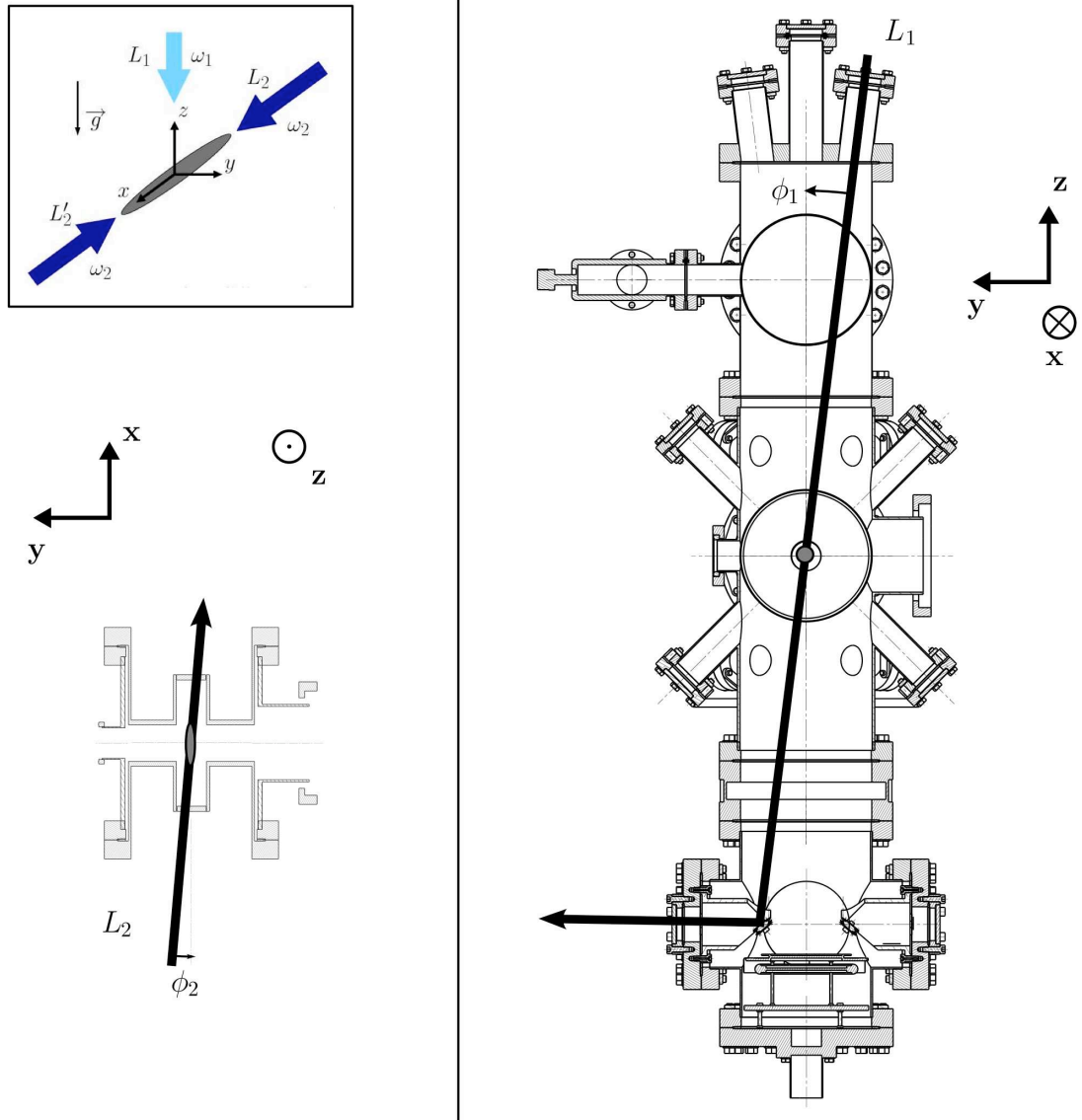


Figure 4.8: Bottom left and right: top view and side view of our science chamber. L_1 propagates in the vertical plane with an angle $\phi_1 = 8^\circ$ with respect to the z axis. It is reflected out of the chamber by a mirror that is in vacuum. L_2 propagates on the horizontal plane with an angle $\phi_2 = 5^\circ$ with respect to the x axis. L'_2 is generated by retroreflecting L_2 and is not shown in figure. The inset on the top of the figure shows the direction of the three Raman beams with respect to the condensate axis.

and has to be circularly σ^- polarized (see figure 4.7). L'_2 is generated by retroreflecting L_2 and has to be σ^- polarized as well. The propagation direction of the beams form an angle of 5° with the bias axis due to a limited optical access. For this reason, L_2 and L'_2 cannot be perfectly circularly polarized and the polarization will not be pure.

In section 4.6.1 we will see the consequence of this fact.

We set the power of the three beams, the relative detuning and the duration of the Raman pulse in order that half of the trapped cloud makes a Raman transition driven by L_1 and L_2 , and half of the cloud makes a Raman transition driven by L_1 and L'_2 . Indicating with \mathbf{e}_π and \mathbf{e}_σ the propagation vectors of L_1 and L_2 respectively, the condensate that is extracted from the trap is in a superposition of two components with different momentum. The atoms that interact with L_1 and L_2 acquire a momentum equal to $\hbar k_{rec}(\mathbf{e}_\sigma - \mathbf{e}_\pi)$, because they absorb a photon from L_2 and emit a photon in L_1 . The atoms that undergo the Raman transition with L_1 and L'_2 acquire a momentum of $\hbar k_{rec}(-\mathbf{e}_\pi - \mathbf{e}_\sigma)$. Therefore, the two colliding condensates travel with a relative momentum of $2\hbar k_{rec}\mathbf{e}_\sigma$.

The efficiency of the three beam process is smaller than the efficiency of the Raman transfer made with only two beams. We estimate the efficiency of the three beam process to be about 60%. This is disappointing if compared with the efficiency of the two beam process. The saturation of the micro-channel plate plays an important role in this case as well, but the difference between the efficiency of the two processes is not completely understood. A possible explanation can be found in the fact that, since the windows are not anti-reflection coated, the two beams L_2 and L'_2 have not the same power. Therefore the Rabi frequency of the Raman transition driven by L_1 and L_2 is not the same as the one of the transition driven by L_1 and L'_2 . In the second generation experiment we changed the experimental sequence in order to overcome this problem, as explained in section 5.3.

4.6 Experimental results

4.6.1 Observation of the collision sphere

As we said in the previous section, the relative velocity of the two colliding condensates is $2v_{rec} = 2\hbar k_{rec}/m$ along the \mathbf{e}_σ axis. Since the angle between \mathbf{e}_σ and the direction of the long axis of the condensate is quite small (only 5°) we can say that the collision takes place along the long axis of the trap. The center of mass of the collision is in a frame initially traveling upward at one recoil velocity and accelerating downward due to gravity. In the centre of mass frame the two condensates moves back to back with momentum $\pm\hbar k_{rec}$ along \mathbf{e}_σ . The relative collision velocity ($2 \times v_{rec} = 2 \times 9.2$ cm/s) is about 8 times larger than the speed of sound of the initial condensate ($v_s = \sqrt{\mu/m} = 2.4$ cm/s), therefore elementary excitations of the condensate correspond to free-particles. A particle in the condensate with momentum $\hbar k_{rec}$ can make an elastic collision with a particle in the other condensate, with momentum $-\hbar k_{rec}$. The atoms behave as classical particles and energy and momentum conservation can be written as:

$$\begin{aligned} \mathbf{k}_{1f} + \mathbf{k}_{2f} &= \mathbf{0} \\ k_{1f}^2 + k_{2f}^2 &= 2k_{rec}^2 \end{aligned} \quad (4.25)$$

where $\hbar\mathbf{k}_{1f}$ and $\hbar\mathbf{k}_{2f}$ are the final momentum of the two particles. The two equations 4.25 imply that, $\hbar\mathbf{k}_{1f}$ and $\hbar\mathbf{k}_{2f}$ have the same modulus, equals to $\hbar k_{rec}$ but opposite direction. Therefore, after collision, atoms are equally distributed on a sphere of radius $\hbar k_{rec}$, in momentum space. This classical model doesn't take into account the initial spread of the two colliding condensates. Due to the Heisenberg principle, the momentum spread of a condensate is inversely proportional to its spatial extension. This will cause a broadening of the spherical shell. In section 4.6.2 we will see how the two things are related. In addition this model doesn't account for the interactions between the atoms during the expansion and it supposes that all the collisions happen at the same time and in the same position. In the following sections we will see how well these hypothesis are verified in our case.

In figure 4.9 we show the scattering sphere obtained by making two condensates collide with the procedure described above. The figure is drawn in velocity space and in the center of mass frame. The x axis is the long axis of the trap, while y is the short axis of the trap, parallel to the plane of the detector. Each frame represents a 2.4 ms time slice of the atomic cloud as it passes the detector plane (xy). We recall that the images are taken after a long time-of-flight (320 ms in this experiment). Therefore the condensates have not a cigar shape anymore, but they are pancakes. In figure 4.9 we see four condensates falling on the detector. The ones indicated by number I and II are the two colliding condensates. As expected they are at $\pm v_{rec}$ along the x axis and they are centered at $0v_{rec}$ along the y direction. The small misalignment of the centre of the two condensates along y is due to the fact that L_2 and L'_2 don't propagate exactly along the x axis (see figure 4.8). Condensate III underwent no momentum transfer and its presence is probably due to the imperfect polarization of the Raman beams. In fact, if the polarization is not pure, an atom can absorb a σ photon and emit a π photon from the same laser beam, undergoing a Raman off resonant transition. Since the two photons come from the same beam the momentum transferred to the atom is zero. Condensate IV contains a smaller number of atoms than condensate III, it underwent no momentum transfer on the plane xy but it has a velocity of $2v_{rec}$ downward. It is probably generated by a four-wave mixing process [34], [35] of condensate III with the colliding condensates I and II. In figure 4.9, the collision sphere is well visible as well. Its radius is about v_{rec} . The number of detected atoms in the sphere can vary from 30 to 300 depending on the number of atoms in the initial condensate and on the efficiency of the Raman process. Since about 40% of the sphere is superposed to the 4 condensates that we mentioned above, we estimate to have on average 2300 atoms in the sphere (assuming a detection efficiency of 10%). In section 4.7.2 we will see how this value compares with theory.

The three dimensional detector permits a study of the scattering sphere in detail and to measure its thickness. In the next section we will give the experimental result of this measurement and we will compare it with theory.

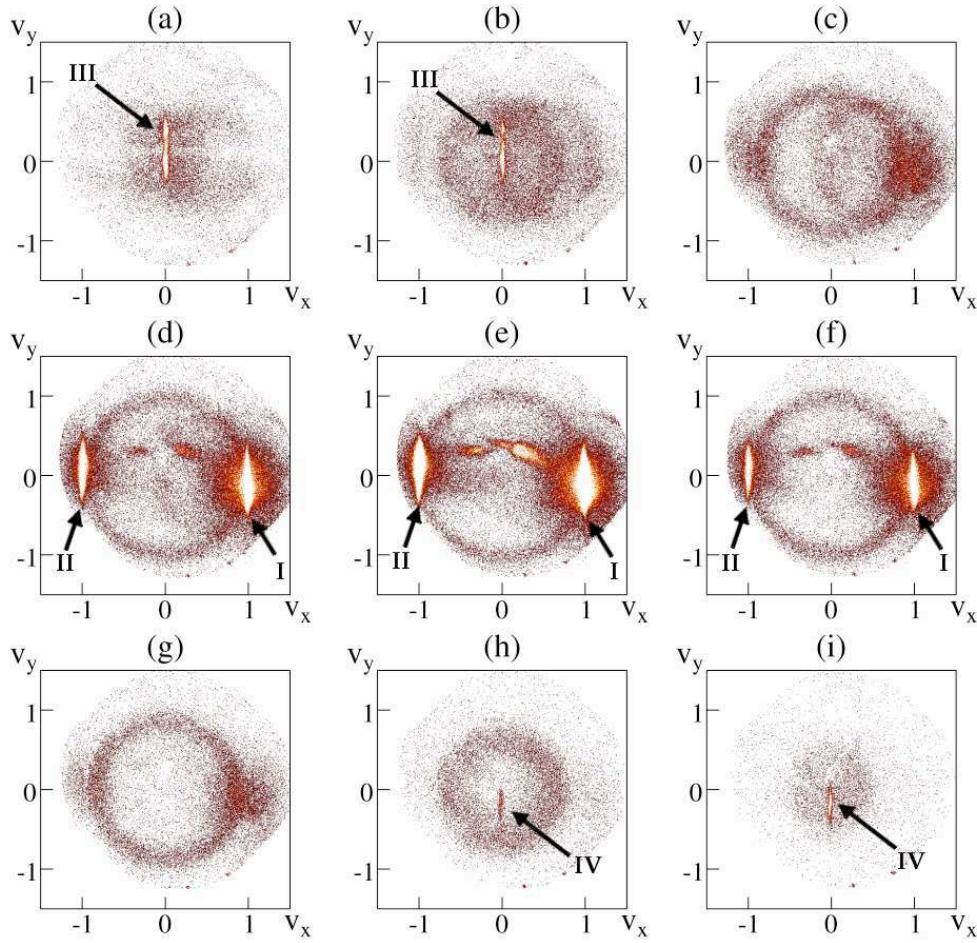


Figure 4.9: Slices of the collision sphere on the xy plane as it falls on the detector. Each slice is averaged over 2.4 ms. The image is averaged over 150 time-of-flights. The two colliding condensates are indicated by numbers I and II. Condensate III has no momentum transfer and is due to the imperfect polarization of our Raman beams. Condensate IV is the result of a four-wave mixing process between condensate III and the two colliding ones. The origin of the spots in the centre of the sphere is not well known. They are probably due to spurious light scattered by the chamber from the Raman beams.

4.6.2 Sphere thickness

In order to precisely measure the sphere thickness we can plot the distribution of the modulus of the momentum of the atoms that belong to the scattering sphere. In doing this we exclude the zones with the four condensates and the zone inside the sphere with the two spots of atoms. This plot is shown in figure 4.10. There are several things that we can note. The distribution of the modulus of \mathbf{k} stays over a tilted background. This is due to the presence of a residual thermal cloud around the condensates that is hard to be properly cut away. In order to estimate the thickness and the radius of the sphere

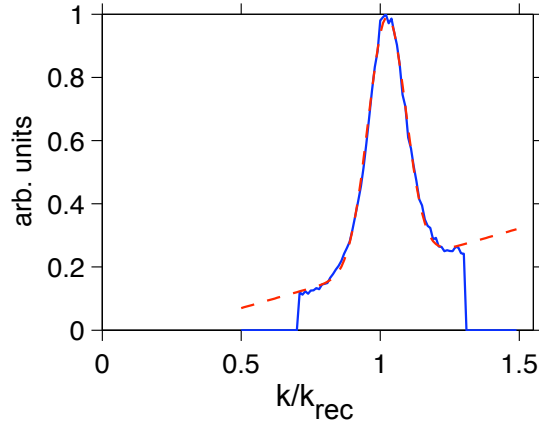


Figure 4.10: Cross section of the scattering halo averaged over all the scattering angles. The sloped background is due to the presence of a residual thermal cloud around the condensates that has not been properly cut away. The red dashed curve is the result of a fit made with a gaussian plus a straight line that takes account of the sloped background.

we can fit the distribution with a straight line plus a gaussian and thereafter subtract the straight line in order to estimate correctly the RMS width. We find $0.067 k_{rec}$. With the same method we can find the centre of the distribution, that is $1.02 k_{rec}$.

As we mentioned in section 4.6.1, the thickness of the sphere is related to the momentum spread of the two colliding condensates, that imposes a minimum width. By numerically solve the Gross-Pitaevski equation in the Thomas-Fermi approximation, for 9.84×10^4 atoms, the initial momentum-space widths are found to be $\sigma_x^{(k)} = 0.0025 k_{rec}$ and $\sigma_{yz}^{(k)} = 0.055 k_{rec}$ [84]. Therefore we would expect to see a strong anisotropy of the scattering halo, reproducing the trap anisotropy. Unfortunately, the presence of the colliding condensates along the x axis makes the measurement of such anisotropy impossible and the sphere thickness is measured chiefly in the yz direction. In addition, since the resolution of our detector in the xy plane is of the order of $0.01 k_{rec}$, the measured width of the sphere would be broadened by the detector resolution (mainly in the x direction). In conclusion, the good agreement between the calculated momentum spread of the initial condensate along the yz direction and the measured thickness of the sphere indicates that the initial momentum spread has the bigger effect in the determination of the sphere thickness. This is also confirmed by the results of the analytical calculation reported in section 4.7.1.

There are other physical arguments that can suggest that the thickness of the sphere is not only determined by the momentum spread of the initial condensate. We will discuss this particular in section 4.7.2.

4.6.3 Back to back correlation

In order to demonstrate that atoms emitted back to back (in the collision center of mass frame) are correlated in pairs, we measured the two-body correlation function $G^{(2)}(\mathbf{k}, -\mathbf{k} + \delta\mathbf{k})$, where \mathbf{k} is a three dimensional vector. Since the number of atoms scattered in the sphere in each shot is small, we measure the correlation function averaged over all the collision sphere (i.e. over all possible values of \mathbf{k}) in order to increase the signal to noise ratio. We therefore measure:

$$G^{(2)}(\delta\mathbf{k}) = \int d^3\mathbf{k} G^{(2)}(\mathbf{k}, -\mathbf{k} + \delta\mathbf{k}) \quad (4.26)$$

As in case of the measurements described in chapter 3 we have to normalize the correlation function in order to measure its width. In the pairs experiment the normalization is even more important because the normalized and non-normalized correlation functions have almost the same width. This was not the case in the Amsterdam-Palaiseau experiment (see figure 3.2). To normalize $G^{(2)}$ we will divide it by the sum of the correlation calculated between atoms belonging to independent clouds. As we have already commented in section 3.1.1, this is the most rigorous normalization procedure. This normalization was not applicable on the Amsterdam-Palaiseau data because it would have taken a too long calculation time. In the pairs experiment however the number of atoms in each sphere is about 100 (compared to 5000 of the Hanbury Brown Twiss experiment), over 1108 acquired time-of-flights, and the computing time is reasonable (only few hours). Therefore we will calculate the correlation on the sum of all the acquired shots and we will use the result to normalize $G^{(2)}(\delta\mathbf{k})$ calculated over the single shot. At the end of this procedure we average $g^{(2)}(\delta\mathbf{k})$ over all the acquired data. More details on the data analysis can be found in [82].

Figure 4.11 shows the normalized correlation function for atoms being scattered back to back. We plot the projection of $g^{(2)}(\delta\mathbf{k})$ over the three axis of the trap. We clearly observe a peak around $\delta\mathbf{k} = \mathbf{0}$, that is the signature of the correlation of atoms emitted back to back.

Width of the correlation

The height and the width of the pair correlation function have been measured by making a Gaussian fit of the 3D histogram containing the normalized correlation function. The fit function has a cylindrical symmetry, like the trap, and is:

$$g^{(2)}(\delta\mathbf{k}) = 1 + \eta \exp\left(-\frac{\delta k_x^2}{2\xi_x^2} - \frac{\delta k_y^2 + \delta k_z^2}{2\xi_{yz}^2}\right) \quad (4.27)$$

The free parameters are η , ξ_x and ξ_{yz} . The fit results for the back to back correlation are listed in the following table:

$\xi_x^{BB}(k_{rec})$	$\xi_{yz}^{BB}(k_{rec})$	η^{BB}
0.017 ± 0.002	0.081 ± 0.004	0.19 ± 0.02

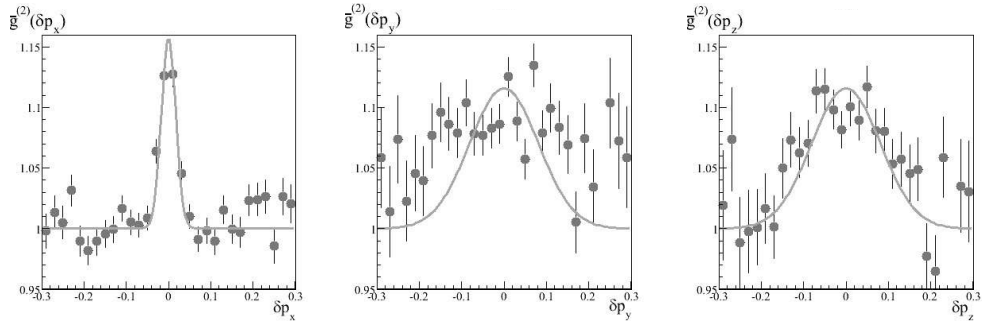


Figure 4.11: Projection of the back to back correlation function along the trap axis plotted in units of $\hbar k_{rec}$. The peak at $\delta \mathbf{p} = 0$ is the signature of the fact that atoms are correlated in pairs of opposite momenta. The solid line is the result of a Gaussian fit. See text for more details.

As in case of the Amsterdam-Palaiseau experiment the height of the correlation function cannot be measured on the projections showed in figure 4.11, because integration modifies the height of the correlation. The solid curves reported in figure 4.11 are the result of a Gaussian fit with the amplitude as the only free parameter. The width has been fixed to the value found with the three-dimensional fit.

The quality of the Gaussian fit is good in the x and z directions. The projection along the y direction seems to be quite noisy compared to the other two and a Gaussian doesn't seem to fit the data points. The origin of this noise has to be found in our analysis procedure. In fact, the first step of the analysis consists in cutting the four condensates falling with the collision sphere. This procedure breaks the cylindrical symmetry of the problem, therefore the noise on the y and z axis can be different [82]. Furthermore the sphere thickness is of the same order of magnitude as the correlation width along y and z , making the normalization problematic. Indeed, the number of detected coincidences decreases when one looks far from $\delta \mathbf{k} = 0$ due to the finite thickness of the halo and the noise on the measurement of the correlation function increases.

One can therefore ask whether the hypothesis of cylindrical symmetry imposed by the fit function 4.27 is verified or not. In section 4.7 we will compare our results with the two theoretical models described previously and we will see that the two models predict a cylindrical symmetry of the correlation function.

The width of the back to back correlation function can be naively inferred with a simple classical model that has been developed by A. Perrin in his PhD thesis [82] and that we report also here. In this model the atoms are treated as billiard balls. The momentum distribution of the two colliding condensates is a three-dimensional Gaussian. The initial momentum of the particles will be randomly chosen following this distribution. After that the momentum of the particles evolves according to the phase-matching conditions 4.25. The scattering direction is chosen randomly as well. Once data are generated with this model, we can analyze them with exactly the same

procedure used for the experimental data. We find that the back to back correlation has a cylindrical shape and the width is not far from the experimental one [82]. Of course this model doesn't account for several physical phenomena that are present in the experiment, such as the mean-field effect, the spatial extension of the condensates, the expansion of the condensates during the collision, but it allows one to have a simple view of the basic process taking place in the experiment.

Height of the correlation

The correlation function that we just measured tells us that if we want to find the partner of an atom of momentum $\hbar\mathbf{k}$ in the collision sphere, we have to look inside the correlation volume measured in the previous section. Inside the correlation volume there will be several atoms but only one of those is "perfectly" correlated with the one of momentum $\hbar\mathbf{k}$. Following this reasoning, we can say that the contrast of the correlation function for $\delta\mathbf{k} = 0$ is given by:

$$1 + \eta^{BB} = \frac{\text{true} + \text{random}}{\text{random}} \quad (4.28)$$

where we call "random" the atoms that are not correlated with the first one. Let's define ΔV the correlation volume defined by the widths found above, N the total number of atoms in the scattering shell and V the total volume of the scattering shell. In a correlation volume we will have 1 true coincidence and $N/V \times \Delta V$ random coincidences. Therefore,

$$1 + \eta^{BB} = \frac{\text{true} + \text{random}}{\text{random}} = 1 + \frac{V}{N\Delta V} \quad (4.29)$$

For our experiment $V/\Delta V \simeq 1300$ and, assuming a detection efficiency of 10%, $N \simeq 2300$ [82]. Therefore we find $\eta^{BB} \approx 0.6$ that is of the same order of magnitude of the measured η^{BB} . The discrepancy can be due to an imprecise determination of N , V or ΔV or to the simplicity of the model developed here. In order to verify the dependence of η^{BB} we measure the height of the correlation function on three data sets with different number of scattered atoms. In figure 4.12 we show our results for the correlation along the x direction. The dependence on the number of atoms is clearly visible.

4.6.4 Collinear correlation

If the correlation between atoms emitted back to back described in section 4.6.3 can be understood in terms of classical mechanics, just by assuming that atoms behave like billiard balls, the effect that we are going to describe in this section is not. In fact, if atoms behaved like classical particles, their distribution on the collision sphere shouldn't depend on the scattering angle, i.e they should be randomly emitted in all directions. Therefore one shouldn't expect to see any correlation peak for atoms having been scattered in the same direction. However, since ${}^4\text{He}$ is a boson, atoms tends to be scattered in bunches. This is a nice demonstration of the Hanbury Brown Twiss effect

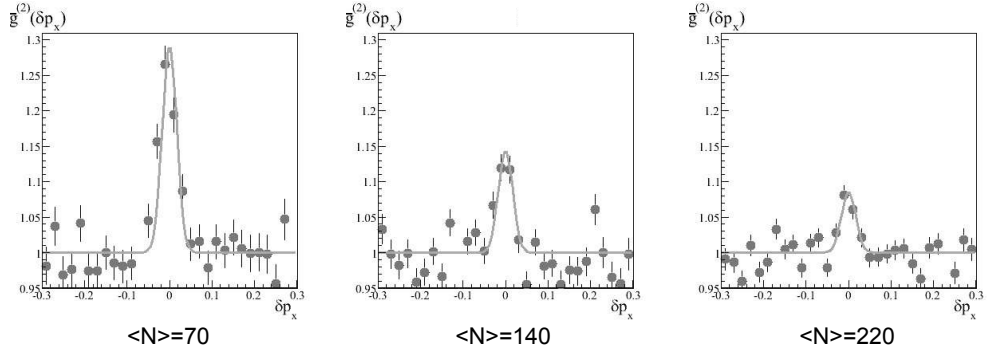


Figure 4.12: Measured two-body correlation function along the x direction for different number of atoms detected on the sphere (in units of $\hbar k_{rec}$). From left to right, the mean number of atoms is 70, 140, 220. As predicted by the simple model explained in this section, the height of the correlation function goes as the inverse of the number of detected atoms.

and it is a demonstration of the importance of quantum mechanics in the description of this experiment.

Following the same procedure as for the measurement of back to back correlations we can measure the correlation between atoms emitted with collinear velocity. This is equivalent to measure:

$$G^{(2)}(\delta\mathbf{k}) = \int d^3\mathbf{k} G^{(2)}(\mathbf{k}, \mathbf{k} + \delta\mathbf{k}) \quad (4.30)$$

Normalization is then carried out as in case of back to back correlations (see section 4.6.3). Figure 4.13 shows the correlation measured on our experimental data for pairs of atoms emitted with collinear velocity.

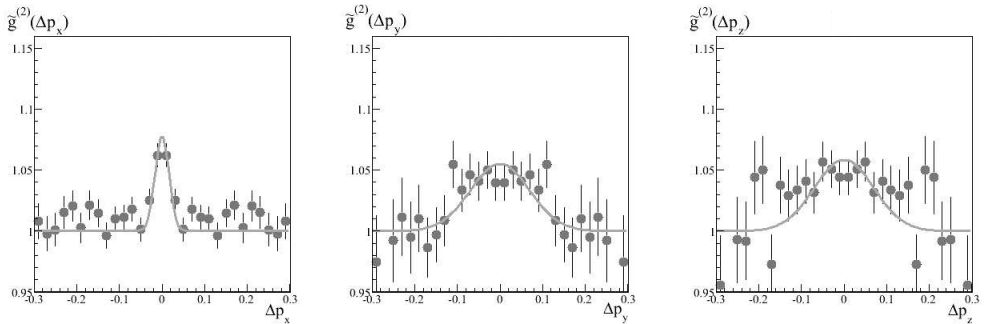


Figure 4.13: Projection of the collinear correlation function along the trap axis in units of $\hbar k_{rec}$. The peak at $\delta\mathbf{p} = 0$ is the signature of the fact that atoms are bosons and tends to be bunched on the detector. This is a further demonstration of the Hanbury Brown Twiss effect. The solid line is the result of a Gaussian fit. See text for more details.

We can explain this correlation with a simple argument, sketched in figure 4.14. We

have to consider a four particle system, formed by two pairs of atoms emitted back to back. In figure 4.14 they are represented by the empty and the full pair of dots⁴. When we detect a particle on detector D_1 and a particle on detector D_2 we don't know if the detected particles belong to the empty or to the full pair of dots. This is equivalent to say that we don't know if the two particles followed the path drawn with a solid line in figure 4.14 or the path drawn with a dashed line. The two possible paths can interfere and this gives rise to the correlation peak (see the simple theoretical argument given in section 1.2 to explain the Hanbury Brown Twiss effect). An analytical calculation done assuming a Gaussian shape for the colliding condensates can be found in [86].

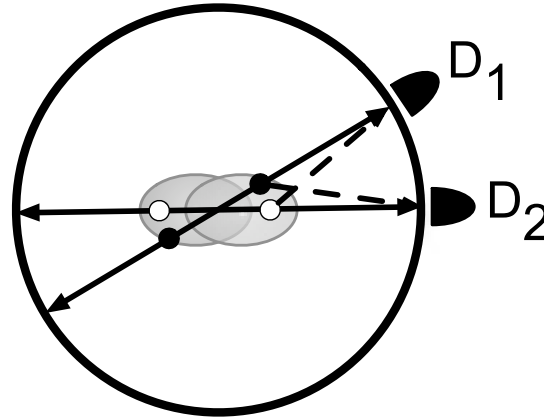


Figure 4.14: This sketch explains the reason why we observe an Hanbury Brown Twiss correlation for two atoms with collinear momenta. The empty and the full dots are two pairs of correlated atoms emitted back to back. The two colliding condensates are represented by the two grey ellipses in the center of the sphere. When a particle is detected by detector D_1 and a particle is detected by D_2 we are not able to say if the detected particle belong to the empty or to the full pair of dots, i.e. we cannot know if the detected particle followed the solid or the dashed path. The two paths interfere and we observe a bunching.

Width and height of the correlation

Height and width of the local correlation function are measured with the method used for the back to back correlation (see section 4.6.3). The results of the three dimensional fit are listed in the following table:

$\xi_x^{CL}(k_{rec})$	$\xi_{yz}^{CL}(k_{rec})$	η^{CL}
0.016 ± 0.003	0.069 ± 0.008	0.10 ± 0.02

As in case of the Hanbury Brown Twiss effect described in the first chapter, the width of the correlation has to be related to the inverse of the spatial extent of the source

⁴The distinction between the two pairs is only graphical. The four atoms are indistinguishable in the quantum mechanics sense.

(i.e. it has to be proportional to the momentum spread of the source). Indeed the measured width in the yz direction is not so different from the estimated width of the source in momentum space $\approx 0.055 k_{rec}$ (for a condensate of 9.84×10^4 atoms). The width on the x direction is limited by the detector resolution. Furthermore the width of the collinear correlation is of the same order of magnitude as the width of the back to back correlation. This is a quite interesting result. In fact, the width of the collinear correlation gives a measurement of the size of the pair production source, or equivalently of a mode of the scattered matter wave field. Since the back to back and collinear widths are close, the pairs produced in the experiment are well emitted in oppositely directed modes.

If the detector resolution had been arbitrarily good, the height of the collinear correlation function should have been equal to 2. As we have already mentioned this is not the case of our detector. A rough estimation of the expected bunching height is given by (compare with equation 1.39):

$$\eta \approx \frac{\sigma_x^{(k)}}{\xi_x^{CL}} \approx 0.15 \quad (4.31)$$

that is in good agreement with the measured value of η^{CL} .

4.6.5 Mode occupancy

In order to estimate the number of atoms per mode in the scattering sphere, we can measure the ratio between the total volume of the sphere V and the correlation volume ΔV . However, the measured correlation volume is strongly affected by the detector resolution, at least in the x direction. Therefore, in order to estimate the mean mode occupation number, we first need to estimate the “real value” of the correlation lengths. This can be done by using the height of the collinear correlation function as a reference. In fact we know that the amplitude of the collinear correlation has to be equal to 2 if measured with an arbitrarily good detector. The collinear correlation length in the x direction has to be ≈ 10 times smaller in order to reach this value. Therefore the “real” correlation volume is 10 times smaller than the measure one. With our experimental values we obtain $N \simeq 2300$ and $V/\Delta V \simeq 1300$ (see section 4.6.3) and then $V/\Delta V_{real} \simeq 1300 \times 10$. Therefore the number of atoms per scattering volume is ≈ 0.2 and the pairs production is in the spontaneous regime [118].

4.6.6 Influence of the gain of the detector

As in the case of the measurement of fermionic antibunching described in the previous chapters of this thesis, we would like to understand what is the role of the detection efficiency on the correlations. In the case of the collinear correlation, we can follow the same reasoning as the one done for fermions in section 1.4.5, equation 1.36. If the detection efficiency varies slowly with respect to the correlation length, it cancels out in the normalization process and the normalized correlation function doesn't depend on it.

The situation is different for the back to back correlation. In fact here we measure the correlation between two atoms that are far apart, on the opposite sides of the detector. Furthermore, we are averaging over all the scattering angles. The result obtained after this average procedure is meaningful only if we assume that $G^{(2)}(\mathbf{k}, -\mathbf{k} + \delta\mathbf{k})$ depends only on $\delta\mathbf{k}$ and not on \mathbf{k} . In this case, calling ϵ_k the detectivity of the zone of the micro-channel plate that detects atoms with momentum \mathbf{k} the correlation function averaged over all the detector will be:

$$\begin{aligned} G_{det}^{(2)}(\delta\mathbf{k}) &= \int d^3\mathbf{k} \epsilon_k \epsilon_{-k+\delta\mathbf{k}} G^{(2)}(\mathbf{k}, -\mathbf{k} + \delta\mathbf{k}) \\ &= G^{(2)}(\delta\mathbf{k}) \int d^3\mathbf{k} \epsilon_k \epsilon_{-k+\delta\mathbf{k}} \end{aligned} \quad (4.32)$$

As we said in section 4.6.3, the normalization is made by dividing the correlation function calculated for each shot by the correlation calculated on the sum of all the acquired shots. The same reasoning as for equation 4.32 can be done on the correlation of the sum of all the shots. The contributions of the detection efficiency will cancel in the normalization procedure and the final result will not depend on the detection efficiency.

4.7 Comparison with theory

4.7.1 Analytical calculation

The perturbative approach described in section 4.4.1 allows one to calculate analytically the second order correlation function and the sphere thickness.

The calculation has been done by M. Trippenbach et al. in [85] for the collision geometry of the first generation experiment. Here we recall the calculation results. The two-body correlation function is given by [85]:

$$\begin{aligned} G^{(2)}(\mathbf{k}_1, \mathbf{k}_2, t) &= \langle \hat{\delta}^\dagger(\mathbf{k}_1, t) \hat{\delta}^\dagger(\mathbf{k}_2, t) \hat{\delta}(\mathbf{k}_2, t) \hat{\delta}(\mathbf{k}_1, t) \rangle \\ &= G^{(1)}(\mathbf{k}_1, \mathbf{k}_1, t) \cdot G^{(1)}(\mathbf{k}_2, \mathbf{k}_2, t) + |G^{(1)}(\mathbf{k}_1, \mathbf{k}_2, t)|^2 + |M(\mathbf{k}_1, \mathbf{k}_2, t)|^2 \end{aligned} \quad (4.33)$$

where $\hat{\delta}$ can be calculated in the way described in section 4.4.1. $M(\mathbf{k}_1, \mathbf{k}_2, t) = \langle \hat{\delta}(\mathbf{k}_1, t) \hat{\delta}(\mathbf{k}_2, t) \rangle$ is the anomalous density and $G^{(1)}(\mathbf{k}_1, \mathbf{k}_2, t) = \langle \hat{\delta}^\dagger(\mathbf{k}_1, t) \hat{\delta}(\mathbf{k}_2, t) \rangle$ is the first order correlation function. As we will see in what follows, the anomalous density describes the back to back correlation while the first order correlation function takes account of the collinear correlation. Since the measurement is done after a long time-of-flight, we can calculate $G^{(2)}$ for a time $t \rightarrow \infty$.

Taking the momenta in units of $\hbar k_{rec}$, to the lowest order in $\hat{\delta}$, the anomalous density is given by [85]:

$$\begin{aligned} M(\mathbf{k}_1, \mathbf{k}_2) &= -i \frac{\alpha \beta^2 \gamma^2}{16\pi} \exp\left(-\frac{\beta^2}{4}(k_{1,x} + k_{2,x})^2\right) \times \\ &\times \exp\left(-\frac{\gamma^2 \beta^2}{4}(\mathbf{k}_{1,r} + \mathbf{k}_{2,r})^2 - \frac{\Delta^2}{4}\right) \left(1 - \operatorname{erf}\left(\frac{i\Delta}{2}\right)\right) \end{aligned} \quad (4.34)$$

with

$$\begin{aligned}\alpha &= \frac{4Na\sigma_x}{\sigma_{yz}^2\sqrt{\pi}} \\ \beta &= Q\sigma_x \\ \gamma &= \frac{\sigma_{yz}}{\sigma_x} \\ \Delta &= \beta \left(1 - \frac{k_1^2 + k_2^2}{2} \right)\end{aligned}$$

In our experiment, for $N = 10^5$ atoms and $Q = k_{rec}$ we have $\alpha = 1053$, $\beta = 227$, $\gamma = 0.05$.

We can decompose $M(\mathbf{k}_1, \mathbf{k}_2)$ into two contributions.

The factor $\left[\exp\left(-\frac{\beta^2}{4}(k_{1,x} + k_{2,x})^2\right) \exp\left(-\frac{\gamma^2\beta^2}{4}(k_{1,r} + k_{2,r})^2\right) \right]$ expresses momentum conservation in the collision process. It is non negligible only when $\mathbf{k}_1 \approx -\mathbf{k}_2$ and decreases exponentially on a width that has the same anisotropy as the condensate momentum density but it is two times larger.

The factor $\exp\left(-\frac{\Delta^2}{4}\right) \left(1 - \operatorname{erf}\left(\frac{i\Delta}{2}\right)\right)$ expresses the conservation of the energy and is non-negligible only for $\Delta \leq 1$. As β is large, $\Delta \simeq 1$ for $k_1 \approx 1$ and $k_2 \approx 1$, that is the requirement expressed by the energy conservation (see equation 4.25).

The result obtained for our experimental parameters (after having normalized equation 4.34 and averaged it over all the scattering angles, see [85]) is reported in figure 4.15. The experimental results (dots) are superposed to the curve obtained with the theoretical calculation (black line). As the figure shows experiment and theory are in very good agreement. This is a verification of the fact that the width of the back to back correlation function is governed by momentum conservation, as expected with the naive model described in section 4.6.3. The calculated width of the correlation along the x axis is much narrower than the experimental one due to the resolution of our detector.

As we said above, the first order correlation function takes account of the collinear correlation. Under the assumption that the following conditions are satisfied:

$$\beta \gg 1 \quad , \quad \frac{\gamma}{|\mathbf{u}_r|} \ll 1 \quad , \quad \frac{1}{|\mathbf{u}_r|\beta\gamma} \ll 1 \quad (4.35)$$

where $\mathbf{u} = (\mathbf{k}_1 + \mathbf{k}_2)/|\mathbf{k}_1 + \mathbf{k}_2|$ and $\mathbf{u}_r = (\mathbf{k}_{1r} + \mathbf{k}_{2r})/|\mathbf{k}_1 + \mathbf{k}_2|$ is the radial component (yz plane) of \mathbf{u} , the first order correlation function is given by [85]:

$$\begin{aligned}G^{(1)}(\mathbf{k}_1, \mathbf{k}_2) &= \frac{\alpha^2\beta\gamma^3}{32\sqrt{2\pi}|\mathbf{u}_r|} \exp\left[\frac{\gamma^2\beta^2}{8}\Delta\mathbf{k}_r^2 - \frac{\beta^2}{8}\Delta k_x^2\right] \times \\ &\times \exp\left(-\frac{\beta^2}{8}(\mathbf{u} \cdot \Delta\mathbf{k})^2\right) \left(1 - \operatorname{erf}\left(\frac{i\beta\mathbf{u} \cdot \Delta\mathbf{k}}{2\sqrt{2}}\right)\right) \times \\ &\times \exp\left(-\frac{2\beta^2\gamma^2\Delta K^2}{\mathbf{u}_r^2}\right)\end{aligned} \quad (4.36)$$

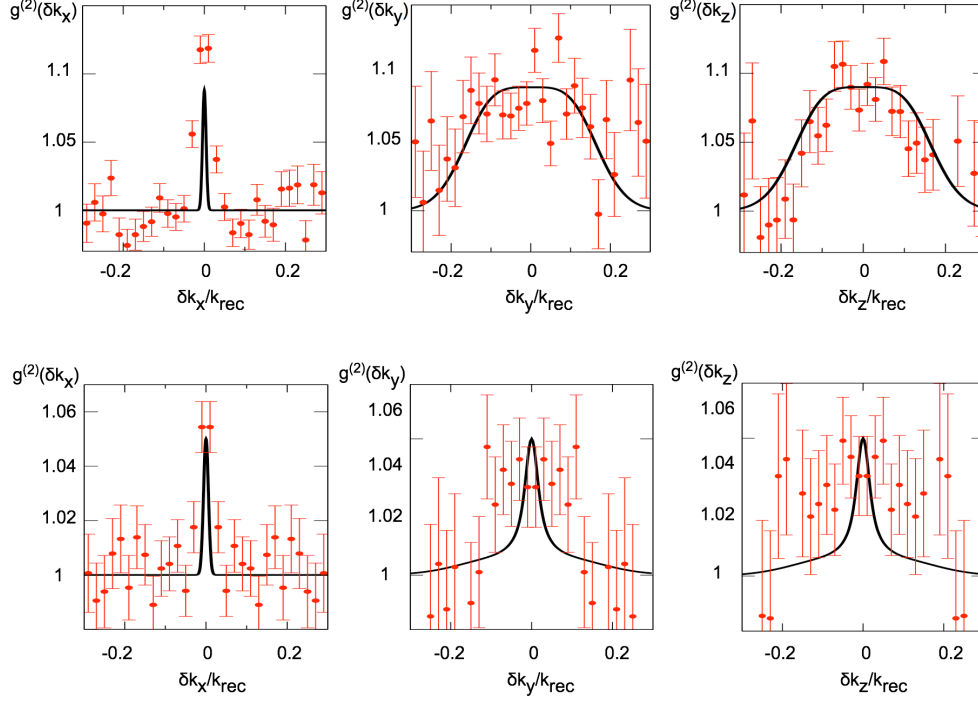


Figure 4.15: Back to back (top line) and collinear (bottom line) normalized correlation function calculated with the analytical model described in section 4.7.1 (solid line) as compared with experimental data. The height of the calculated correlation function has been set in order to take account for the fact that experimental data are projections of the three-dimensional correlation function (see text for more details).

with $\Delta K = \frac{|\mathbf{k}_1 + \mathbf{k}_2|}{2} - 1$ and $\Delta \mathbf{k} = \mathbf{k}_1 - \mathbf{k}_2$. We also assumed $|\Delta \mathbf{k}|$ small. The assumptions 4.35 are verified in our experiment, because the region with $\mathbf{u}_r \approx 0$ is occupied by the two colliding condensates and is excluded from the analysis.

As in the case of the anomalous density, we can decompose $G^{(1)}(\mathbf{k}_1, \mathbf{k}_2)$ into two parts. The first line of equation 4.36 expresses momentum conservation, the second and third lines express energy conservation. The widths imposed by the momentum contribution are $\sqrt{2}$ larger than the width of the back to back correlation⁵. However, in this case, the energy conservation contribution has more important consequences than in the back to back case. In fact, if the energy is strictly conserved, then equation 4.25 implies $k_1 = k_2$ and therefore $\mathbf{u} \cdot \Delta \mathbf{k} = \frac{k_1^2 - k_2^2}{|\mathbf{k}_1 + \mathbf{k}_2|} = 0$. In this case the collinear correlation is the one given by momentum conservation. However, if $\mathbf{u} \cdot \Delta \mathbf{k} \neq 0$, the width of the collinear correlation function is proportional to $1/\beta$ even in the radial direction, in contradiction with the simple classical model developed in section 4.6.4 for which the width of the collinear correlation is proportional to the momentum spread of the initial

⁵A numerical study done by K. Kheruntsyan with the positive-P method demonstrated that the factor of 2 is only due to the Gaussian *ansatz* done for the shape of the colliding condensates.

condensate.

Experimental data and theoretical results are plotted together in figure 4.15, bottom line. As in the case of the back to back correlation, equation 4.36 has been normalized and averaged over all the scattering angles in order to be compared with our data. Once again the width of the correlation along the x direction is much smaller than the experimental width. However, also the width along the y and z direction are much smaller than the experimental ones. This effect comes from the energy conservation requirement that, as we said above, would impose a much narrower width than the one imposed by simply taking only momentum conservation into account.

A possible reason for this discrepancy could be that this method doesn't take account of the mean-field interaction, neither between atoms in the same magnetic substate or between atoms that are in the $m_x = 0$ and $m_x = 1$ substate. Our group has already started a further study to quantify this effect. In addition, this model doesn't take account for the expansion of the two condensates during the collision. This hypothesis seems to be reasonable (we will further discuss it in section 5.2.1), but a quantitative estimation of the effect of condensate expansion is probably needed.

Sphere thickness and density

The same analytical treatment allows to calculate the collision sphere density and thickness. In the hypothesis that the assumptions 4.35 are verified, we find:

$$\rho(\mathbf{k}) = G^{(1)}(\mathbf{k}, \mathbf{k}) = \frac{\alpha^2 \beta \gamma^3}{32\sqrt{2\pi}|\mathbf{u}_\mathbf{r}|} \exp \left[-\frac{2\beta^2 \gamma^2 (k-1)^2}{|\mathbf{u}_\mathbf{r}|} \right] \quad (4.37)$$

The sphere density is peaked around $k = 1$ with a width of $\frac{|\mathbf{u}_\mathbf{r}|}{\beta\gamma} \ll 1$. This theory thus predict an anisotropic halo thickness, but the anisotropy is only strong for $\mathbf{u}_\mathbf{r} \approx 0$. This direction is unaccessible to the first generation experiment, but will be fully accessible in the second generation experiment, as we will see in chapter 5. It is worth noting that the assumptions made above allows the calculation to be entirely analytical. The thickness of the sphere and the collinear correlation function in the $\mathbf{u}_\mathbf{r} \approx 0$ direction would be accessible by doing the calculation numerically.

4.7.2 Positive-P calculation

In this section we will compare our experimental results with the results obtained with the numerical calculation done by K. Kheruntsyan and collaborators [84] that we described in section 4.4.2.

The initial condition for the simulation is the wave function of the initial trapped condensate modulated with a standing wave that imparts initial momenta $\pm k_{rec}$ in the x direction:

$$\begin{aligned} \Psi(\mathbf{r}, 0) &= \langle \hat{\Psi}(\mathbf{r}, 0) \rangle = \sqrt{\rho_0(\mathbf{r})/2} \left(e^{ik_{rec}x} + e^{-ik_{rec}x} \right) \\ \tilde{\Psi}(\mathbf{r}, 0) &= \Psi^*(\mathbf{r}, 0) \end{aligned} \quad (4.38)$$

where ρ_0 is the density profile of the initial condensate (trapped in the $m_x = 1$ state).

The numerical simulation has been run for a initial condensate of 9.84×10^4 atoms and a peak density of $2.5 \times 10^{19} \text{ m}^{-3}$. The duration of the simulation is $25 \mu\text{s}$ and the number of scattered atoms after this time is approximately 1.8% of the total number of atoms in the initial condensate. This number has to be compared to the experimentally measured fraction of 5% at the end of the collision ($\approx 140 \mu\text{s}$). Since the experiment is in the spontaneous regime, we can approximate the behavior of the number of scattered atoms as a function of time as linear (see figure 5.3). In this case the calculated fraction of 1.8% can be extrapolated to 10% at $140 \mu\text{s}$. In the experiment the efficiency of the transfer from $m_x = 1$ to $m_x = 0$ is estimated to be of the order of 60%, while the numerical simulation assumes a transfer efficiency of 100%. In addition the part of the sphere that can be used in the experiment is only 60% of the total volume. Taking these factors into account the number of atoms in the simulated sphere scales down to 4%, in good agreement with the experimentally estimated fraction.

In the following table we report the experimental widths of the back to back and collinear correlation function together with the numerically calculated ones (after a collision time of $25 \mu\text{s}$) [84]:

	$\xi_x^{BB}(k_{rec})$	$\xi_{yz}^{BB}(k_{rec})$	$\xi_x^{CL}(k_{rec})$	$\xi_{yz}^{CL}(k_{rec})$
<i>Exp.</i>	0.017 ± 0.002	0.081 ± 0.004	0.016 ± 0.003	0.069 ± 0.008
<i>Theory</i>	0.0025 ± 0.0001	0.076 ± 0.002	0.0032 ± 0.0001	0.086 ± 0.002

The error on the theoretical values takes account of the error due to stochastic sampling, that is of the order of 3%. The calculated widths along the x axis are, as expected, smaller than the measured ones. The numerically calculated values in the y and z directions are in good agreement with the experimental ones, for both collinear and back to back correlation. The remaining discrepancy between theory and experiment may be due to the evolution of the system after $25 \mu\text{s}$, not accessible with the positive-P method. However, the good agreement leads one to think that the width of the correlation function is mainly governed by the initial momentum distribution of the condensate. This is in agreement with the simple model presented in section 4.6.4, but it disagrees with the analytical calculation shown in section 4.7.1.

Some deviations between the experimental results and the numerical simulation can be due to the fact that in the simulation of the collision process the efficiency of the transfer from the trapped state to the $m_x = 0$ state is assumed to be 100%. Therefore interactions between $m_x = 1$ and $m_x = 0$ atoms are not taken into account. However as we said in section 4.5.1, in the experimental realization of the collision experiment only the 60% of the atoms is extracted from the trap and interactions are not completely negligible. The effect of interactions will be calculated in a future study.

Thickness of the sphere

In sections 4.6.2 and 4.7.1 we said that we would expect the thickness of the sphere to be anisotropic, with an aspect ratio inverted with respect to the trap. Unfortunately, since

the positive-P simulation can be done for a collision time much shorter than the real collision time, the numerical results are not directly comparable with the experiment. In fact, at short collision times the thickness of the sphere is governed by the time-energy uncertainty relation and, for a mean k-vector k_{rec} , the sphere is broadened by:

$$\delta k_{rec} \simeq \frac{m}{\hbar k_{rec} \Delta t} \quad (4.39)$$

Therefore in the numerical simulation the sphere width turns out to be isotropic and the comparison between simulations run with different collision durations [84] shows that it follows equation 4.39. In the experiment, the thickness of the sphere is not governed by the effect described above because the collision time is very long. Therefore a comparison between experiment and theory is not possible.

Another effect that can determine the thickness of the sphere at short collision time can be evaluated, for a uniform system, with the approach used in section 4.3. The mode occupation number can be calculated analytically and the population of modes experiencing Bose enhancement can be taken into account. At short collision times the population of modes that grow exponentially with time is larger than the population of modes that oscillate at the spontaneous noise level. This allows one to calculate the approximate width of the scattering sphere. The calculation has been done in [84] and the sphere thickness turns out to be:

$$\delta k \simeq \frac{4\pi a_0 n_0}{k_{rec}} \quad (4.40)$$

where a_0 is the scattering length between atoms in the $m_x = 0$ level and n_0 is the peak density. The width of the sphere no longer depends on the collision duration, it increases with the effective coupling $a_0 n_0$ and it decreases with the recoil momentum. The positive-P simulation for He atoms simulates the collision for a time shorter than 25 μs , when the thickness of the sphere is governed by equation 4.39. Therefore, also in this case, a direct comparison of the numerical simulation with the result obtained from equation 4.40 is not possible. However numerical simulations in the long time limit can be done for Sodium. In this case the agreement between the numerical result and equation 4.40 is good [84]. Therefore we are tempted to think that equation 4.40 could play a role in the determination of the thickness of the sphere for collision times of the order of the experimental ones. The evaluation of 4.40 for our experimental parameters gives: $\delta k/k_{rec} \simeq 0.05$ [84]. This value has to be added in quadrature to the momentum width of the initial condensate along the radial direction $\sigma_{yz}^{(k)} = 0.055 k_{rec}$, the other quantity that determines the thickness of the sphere in the zone available in the experiment. One obtains $\delta k = 0.074 k_{rec}$, not far from the measured value $\delta k = 0.067 k_{rec}$. This can confirm our hypothesis that the mechanism leading to equation 4.40 can play a role in the experiment. However we note that equation 4.40 is valid if the system enters the stimulated regime, while the experiment is in the spontaneous regime. Therefore the above estimation cannot be fully trusted.

4.8 Conclusion

In this chapter we highlighted the noticeable analogy between correlated photon pairs created by parametric down-conversion and correlated atom pairs issued from the collision of two condensates of metastable helium. We discussed the important implications of correlated photon pairs for the study of quantum mechanics and we described some of the fundamental experiments performed in quantum optics with this system.

In order to describe the creation of pairs in the collision of two condensates from the theoretical point of view, we collaborated with two groups of theoreticians, that use two different methods for the solution of the Heisenberg equations for the system, one analytical and the other numerical. The two methods have been described and we pointed out advantages and drawbacks of both.

During my PhD we performed an experimental demonstration of the fact that atoms created in the collision of two condensates are correlated by pairs. A complete characterization of the correlation function, for atoms scattered back to back and with collinear velocity has been made and reported in this chapter. The experimental data have also been compared with the theoretical results obtained with the analytical and the numerical method described above. Theory and experiments are in general in good agreements, but have both some limitation that, in some cases, makes the comparison difficult. These limits are recalled in the following list:

Experiment:

- Due to the collision geometry, the thickness of the sphere cannot be measured along the x direction because of the presence of the colliding condensates and an eventual anisotropy cannot be shown.
- In section 4.6.1 we pointed out that, due to a four-wave mixing phenomenon, we detect a condensate on the top of the sphere and one on the bottom in addition to the two colliding condensates. This fact is annoying because the four condensates have to be removed from the data before starting the analysis and this causes several problems (see sections 4.6.3 and 5.1.2).
- The transfer efficiency of the trapped atoms in the two colliding condensates is only of the order of 60%. A larger efficiency is preferable because it would imply a larger number of atoms scattered in the collision sphere. In addition interactions between atoms in $m_x = 0$ state and atoms that are still trapped can influence the sphere thickness and the correlations.

Theory:

- The analytical model shows a good agreement with the experiment concerning the back to back correlation but not for the collinear correlation. This can be due to the fact that it doesn't take into account the mean-field effect and the

expansion of the condensates during the collision. Further studies are going to quantify this effect.

- The numerical model shows a good agreement for both collinear and back to back correlation functions, but it can calculate them only for short collision times (about a factor of 6 shorter than in the experiment).
- The analytical model predicts an anisotropic sphere thickness, governed by the momentum spread of the initial condensate, while the numerical calculation cannot give any prediction. However there are physical arguments (discussed in section 4.7.2) that predict an isotropic scattering shell thickness. For these reasons, it would be interesting to measure the sphere thickness on experimental data, on the long direction of the condensate.

In order to overcome the experimental issues outlined above and to make a more thorough study, we devised an experiment in a new collision geometry. The next chapter will be devoted to the description of this second experiment and to the topics that we would like to study in this upgraded version of the experiment.

Chapter 5

Second Generation Experiment

This chapter is devoted to the description of the upgraded version of the atomic pairs experiment described in the previous chapter. In order to measure the sphere thickness and density we decided to perform the experiment in another collision geometry, to get rid of the two condensates falling in the direction of the long axis of the trap. In addition this second version of the experiment will allow us to study an even more intriguing topic, the squeezing of the difference of the number of atoms in two correlated volumes of the sphere.

In the first part of this chapter we will give some theoretical insight of these two topics, we will try to estimate the theoretical expectations and the potential problems that we could encounter. Thereafter we will describe in detail the experimental setup used in the second generation and we will describe advantages and disadvantages of the second version of the experiment with respect to the first version. At the end of the chapter we will present some preliminary results since data acquisition and analysis are still in progress.

5.1 Motivations for an upgraded experiment

5.1.1 Sphere thickness and density

As we said in the previous chapter, an analytical model predicts that the sphere thickness should be anisotropic (see section 4.7.1), with an aspect ratio inverted with respect to the trap. Unfortunately we weren't able to measure it in the first generation experiment because the two colliding condensates are situated in the region where the anisotropy should be the stronger. On the other hand, there are physical arguments that suggest that the sphere thickness should show an aspect ratio smaller than that of the trap, as explained in section 4.7.2. Therefore we would like to perform an experimental check.

The second subject that we would like to study is the density of the scattering sphere and, in particular, how it varies as a function of the scattering angle. In fact one can wonder whether the elongated geometry of the condensate enhances the scattering

of atoms along the long axis of the trap. Gain directionality has been observed in phenomena like superradiance, where a condensate is illuminated by a polarized laser beam. Due to bosonic stimulation scattered photons travels preferentially along the long axis of the condensate, in the so-called end-fire mode [119],[120],[121].

Gain directionality has been studied in a situation similar to our experiment by H. Pu and P. Meystre [122]. They demonstrated that the gain of the amplification of the mode population depends on the geometry of the source and that it is stronger along the long axis of the condensates. Recent numerical simulations carried out by P. Deuar showed that, with 10^5 atoms in the initial condensate, in the collision geometry used in the second generation experiment, we should observe an enhancement of the population scattered along the long axis of the condensate of $\simeq 30\%$ with respect to the population scattered along the short axis [123].

5.1.2 Relative number squeezing

In section 4.1 we showed that correlated pairs of photons produced with parametric down conversion have an interesting property. Since each photon forming a pair is emitted in one of the two correlated modes we expect the number of photons in the two twin modes to be correlated in such a way that their difference does not fluctuate. This effect is called amplitude or number squeezing. It has already been demonstrated several times in nonlinear optics and it would be interesting to check if we can observe it in our correlated atom pairs system. In our experiment we should measure the difference between the number of atoms in two correlated modes for several realizations of the experiment and prove that this quantity is consistent with zero and its fluctuations are sub-Poissonian.

This is actually another way, alternative to the measurement of the correlation function, to prove that atoms (or photons) are emitted in correlated pairs. Furthermore number squeezing doesn't depend on the number of atoms per scattering mode, while the correlation function does. As we have shown in section 4.6.3, the height of the back to back correlation peak decreases as the number of atoms per mode increases, making eventually hard to demonstrate atom-atom correlation by measuring $g^{(2)}$ in case of stimulated scattering regime. On the contrary, number squeezing should be easier to see if the number of atoms per mode is large. In fact, the population difference between two correlated modes i and j is squeezed if its variance is smaller than the Poissonian fluctuation $\langle N_i \rangle + \langle N_j \rangle$, where $\langle N_i \rangle$ and $\langle N_j \rangle$ are the mean populations of the two modes. If the population of each mode is small, an observed number difference squeezing could be non significant. In this case however, the height of the correlation function should be large. The two methods are therefore complementary.

More formally, the normalized variance of the relative number fluctuations between \hat{N}_i and \hat{N}_j is given by [84]:

$$V_{i-j} = \frac{\langle [\Delta(\hat{N}_i - \hat{N}_j)]^2 \rangle}{\langle \hat{N}_i \rangle + \langle \hat{N}_j \rangle} = 1 + \frac{\langle : [\Delta(\hat{N}_i - \hat{N}_j)]^2 : \rangle}{\langle \hat{N}_i \rangle + \langle \hat{N}_j \rangle} \quad (5.1)$$

where $\Delta\hat{X} = \hat{X} - \langle\hat{X}\rangle$ is the fluctuation. The variance has been normalized with respect to the value it would have if the atoms were not correlated but randomly distributed on the sphere (Poissonian statistics). Therefore, with this definition, we have $V_{i-j} = 1$ for randomly distributed atoms. If the atoms are correlated in pairs, we would have a reduction of fluctuations below the shot-noise level and then V_{i-j} would be smaller than one. Perfect squeezing of the relative number fluctuations corresponds to $V_{i-j} = 0$.

Relative number squeezing has been measured on the data generated with the numerical simulation described in section 4.7.2 [84]. The sphere has been divided in four quadrants, indicated in figure 5.1 left, by the letters A, B, C, D. The two colliding condensates have been removed in a way that allows to keep the same volume for the four regions. Quadrants A and C and quadrants B and D contain atoms correlated in

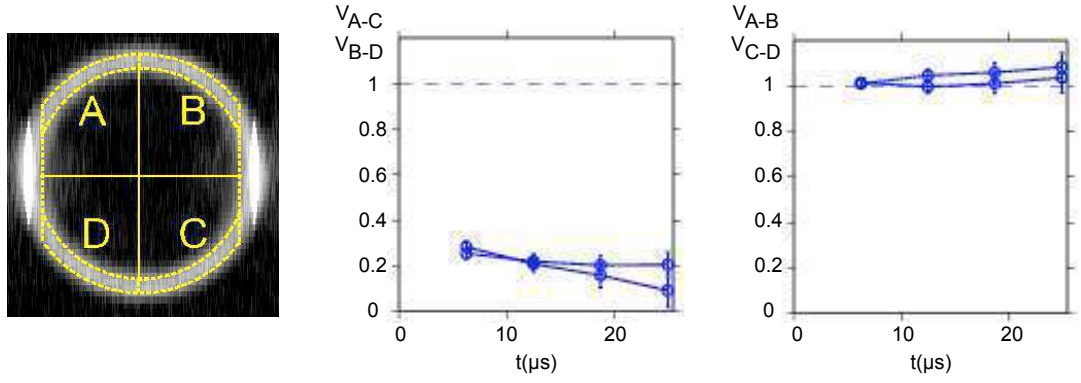


Figure 5.1: On the left side: illustration of the four quadrants A, B, C, D on the scattering sphere. The two colliding condensates are cut in order to keep the symmetry. On the centre and right: normalized variance for the relative number squeezing between correlated quadrants (center) and uncorrelated quadrants (right) as a function of time.

pairs. Therefore the number differences $N_A - N_C$ and $N_B - N_D$ must show squeezing, while $N_A - N_B$ and $N_C - N_D$ should have a variance equal to 1. On the right side of figure 5.1 we show the results given by the positive-P simulation, as a function of time, for V_{A-C} (or equivalently V_{B-D}) and for V_{A-B} (or equivalently V_{C-D}). As expected, the relative number fluctuations between diametrically opposite quadrants shows a normalized variance of 0.2, i.e. a squeezing of 80%. On the other hand, the relative number fluctuations between neighboring (non correlated) quadrants is Poissonian and its variance is equal to 1. There are a few things to note. The first one is that numerical simulations have been done assuming a detection efficiency $\eta = 1$. Squeezing is strongly dependent on the detection efficiency. In fact, if $\eta \neq 1$, if the atoms are randomly distributed on the sphere, the variance of the number difference is:

$$V_{i-j}^{random} = \eta \left(\langle\hat{N}_i\rangle + \langle\hat{N}_j\rangle \right) \quad (5.2)$$

and equation 5.1 becomes:

$$V_{i-j} = 1 + \eta \frac{\langle : [\Delta(\hat{N}_i - \hat{N}_j)]^2 : \rangle}{\langle \hat{N}_i \rangle + \langle \hat{N}_j \rangle}. \quad (5.3)$$

In our experiment the detection efficiency is estimated to be $\eta \approx 10\%$, therefore the above prediction of $\simeq 80\%$ relative number squeezing will be degraded down to a much smaller value of $\simeq 8\%$.

The second thing to note is that even the data produced by the numerical simulation do not show a 100% squeezing. The reason for that can be found in the cut that we have to perform on the sphere to divide it in four quadrants and to remove the colliding condensates. In fact, since each mode has a finite size, given by the width of the correlation function, there is a non-zero probability for one of the atoms forming a pair to be in one of the four quadrants, while its partner falls in a quadrant uncorrelated with the first one or in an excluded zone. This border effect reduces the measured squeezing. For the same reason the larger is the quadrant size, the better is the squeezing [107].

Results of the first generation experiment

We tried to measure number difference squeezing on the data of the first generation experiment. From the experimental point of view, things are a bit more complicated for three reasons. First, we have to remove from the sphere four condensates instead of two, artificially decreasing the observable squeezing, for the reasons mentioned above. Second, the detector efficiency is not homogeneous over all the sphere. This can introduce a systematic error that can cause a displacement of the center of the number difference distribution. Third, the number of atoms detected on the sphere changes from a realization to another. Therefore averaging over different realizations corresponds to averaging distributions with different variances. The latter is solved by normalizing $\Delta N = N_i - N_j$ obtained for each realization of the experiment by $\sqrt{N_i + N_j}$. More details about the data analysis can be found in [82].

In figure 5.2 we show the normalized distribution obtained from our experimental data. The data used here are the same on which we measured the correlation functions shown in section 4.6. The sphere have been divided into two symmetric volumes, one containing atoms with momentum $p_z > 0$, the other containing atoms with momentum $p_z < 0$. The four condensates falling on the sphere have been excluded in order to keep the two volumes symmetric. During the data analysis, we observed that the width of the distribution strongly depends on the size of the zones removed around the four condensates. This is probably due to the existence of thermal clouds around the condensates that are difficult to be properly cut. The measured standard deviation of the number difference distribution fluctuates from 0.96 to 1.01, depending of the size of the excluded zones. Since the standard deviation is normalized to the value it would have in case of randomly distributed pairs, it has to be smaller than one in order to prove that the distribution is squeezed.

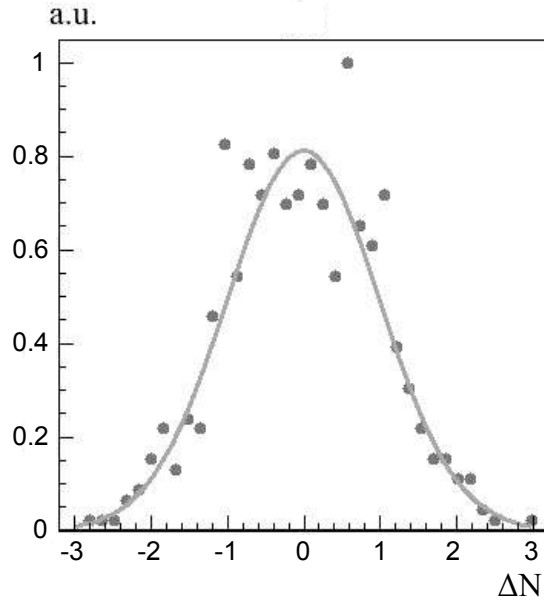


Figure 5.2: Measured distribution of the difference of the number of atoms detected in two correlated volumes of the scattering sphere. The solid line is a Gaussian fit. The RMS value of the distribution is 0.96.

As we said above, squeezing is strongly affected by the detector efficiency. The best value obtained (standard deviation equal to 0.96) would give a squeezing of the order of 80%, assuming a detection efficiency $\eta = 10\%$. This value would be in agreement with the prediction of [84]. However, since the measured variance strongly depends on the way we analyze the data and since we don't know exactly the detection efficiency, these data have to be considered merely encouraging.

5.2 New collision geometry

In the second generation experiment the collision takes place along the short axis of the condensate instead of taking place along the long axis. This presents some advantages and disadvantages with respect to the first experimental realization. The first advantage is that the two colliding condensates are on the top and on the bottom of the sphere. Therefore we would be able to study the sphere in the direction of the long axis of the condensate. Second, the beams used to produce the two colliding condensates have a well defined polarization (we will give more details on this point in section 5.3), reducing the probability of non-resonant Raman transitions with respect to the previous realization. In the first version of the experiment, these transitions and four-wave mixing phenomena were responsible for the observation of the condensates III and IV shown in figure 4.6.1. In addition, the suppression of unwanted condensates would

decrease the size of the zones that have to be removed from the sphere, increasing the signal to noise ratio for the measurement of the correlation function and increasing the observable amount of squeezing. Furthermore, since it is still not clear whether the detector saturation is a local phenomenon or not, the fact of having only two condensates, instead of four, falling on the detector within a short delay (about 20 ms) is preferable. For reasons that we will explain in section 5.3 we decided to make first a Raman transition to transfer the atoms in the untrapped state $m_x = 0$ and then a Bragg pulse to separate the untrapped condensate in two counterpropagating condensates in the state $m_x = 0$. The geometry of the Raman and Bragg beams defines the relative velocity of the condensates that, in the present case, is $\sqrt{2}v_{rec}$. In section 5.3 we will give all the details concerning the experimental realization.

The drawback of the new collision geometry is that the total number of scattered particles during the condensates collision is smaller than in the old geometry. In section 5.2.1 we will discuss the two time scales that play a role in this experiment and we will develop a simple collision model to study the collision rate during the separation of the condensates. A comparison between the two collision geometries will be drawn.

5.2.1 Number of scattered atoms

In both versions of the experiment, the collision between the two condensates happens when the condensates are in the magnetic sublevel $m_x = 0$ where they are no longer trapped. For this reason, there are two physical quantities that govern the number of collisions: the atomic density, that changes due to the free expansion of the condensates, and the separation of the two condensates, determined by their relative velocity. These two physical processes define two different time scales, that we will now estimate.

Rough estimate

In the Thomas-Fermi regime, i.e. when the kinetic energy of the atoms in the condensate is negligible with respect to the interaction energy, the wave function of the trapped condensate is an inverted parabola:

$$\Phi_{TF}(\mathbf{r}) = \left(\frac{\mu - U(\mathbf{r})}{gN} \right)^{1/2} \quad (5.4)$$

where μ is the chemical potential, $U(\mathbf{r})$ is the trapping potential, N is the number of atoms. The interaction constant is defined as $g = 4\pi\hbar^2 a_0/m$ with $a_0 = 5.3$ nm, the scattering length for atoms in $m_x = 0$. The chemical potential is given by:

$$\mu = \frac{1}{2}\hbar\bar{\omega} \left(15Na_0\sqrt{\frac{m\bar{\omega}}{\hbar}} \right)^{2/5} \quad (5.5)$$

where $\bar{\omega}$ is the geometrical average of the trapping frequencies. The spatial extension of the trapped condensate is given by the Thomas-Fermi radius:

$$R_i = \sqrt{\frac{2\mu}{m\omega_i^2}} \quad (5.6)$$

for $i = x, y, z$. For our trapping frequencies, with $N = 10^5$, we find $R_x = 114 \mu\text{m}$ and $R_{yz} = 4 \mu\text{m}$. If we neglect the expansion, the separation time of the two condensates will be:

$$t_x^{sep} = 1.20 \text{ ms} \quad (5.7)$$

in the first collision geometry (two counterpropagating condensates with a velocity of v_{rec} along the x direction) and

$$t_{yz}^{sep} = 70 \mu\text{s} \quad (5.8)$$

in the second collision geometry (two counterpropagating condensates with a velocity of $0.7v_{rec}$ along the radial direction). On the other hand, the condensates will expand very quickly on the radial axis, while the expansion will be negligible on the long axis. A rough estimate of the expansion time of the condensates is given by:

$$t_{yz}^{exp} = \frac{1}{\omega_{yz}} = 140 \mu\text{s} \quad (5.9)$$

At this time, the Thomas-Fermi radius is a factor of $\sqrt{2}$ larger. From this rough estimate we already see that the physical processes governing the two experiments are different: when the collision happens along the long direction, the number of collisions is limited by the expansion of the condensate along the radial direction, while when the collision happens along the radial direction the number of scattered atoms is limited by the separation time of the condensates. This is about two times shorter than t_{yz}^{exp} . In the following section we will estimate more quantitatively the number of collisions in the two cases.

Collision model

In order to determine the total number of atoms scattered during the collision of the two condensates we will use the approach described in [109]. The authors of this paper have shown that a good estimation of the number of scattered atoms is given by:

$$N_{coll}(t) = 2 \int_0^t dt' \int d\mathbf{r} \Delta v \sigma_0 n_1(\mathbf{r}, t') n_2(\mathbf{r}, t') \quad (5.10)$$

where Δv is the relative velocity of the two condensates, $\sigma_0 = 8\pi a_0^2$ is the scattering cross section and $n_1(\mathbf{r}, t)$ and $n_2(\mathbf{r}, t)$ are the densities of the two condensates. The factor of 2 accounts for the fact that there are two atoms scattered for each collision.

The time dependence of the densities of the two condensates takes into account the spatial separation of the condensates and the expansion of the condensates. In order to model the expansion we use the model developed by Y. Castin and R. Dum in [124], in the Thomas-Fermi regime, where the expansion of the condensate can be written in an analytical form. Following this model, the density of the condensates can be written as:

$$n_{1,2}(\mathbf{r}, t) = \frac{\mu}{g\lambda_{\parallel}(t)\lambda_{\perp}^2(t)} \left(1 - \frac{m}{2\mu} \left(\frac{\omega_x^2}{\lambda_{\parallel}^2(t)} x^2 + \frac{\omega_{yz}^2}{\lambda_{\perp}^2(t)} (y^2 + z^2) \right) \right) \quad (5.11)$$

Here $\lambda_{\perp}(t)$ and $\lambda_{\parallel}(t)$ take into account the expansion of the condensate in the radial and in the axial direction respectively. For a strongly elongated condensate $\epsilon = \omega_{\parallel}/\omega_{\perp} \ll 1$ and, defining $\tau = \omega_{\perp}t$, one can write:

$$\begin{aligned}\lambda_{\perp} &\simeq \sqrt{1 + \tau^2} \\ \lambda_{\parallel} &\simeq 1 + \epsilon^2 \left(\tau \arctan(\tau) - \ln \sqrt{1 + \tau^2} \right)\end{aligned}\quad (5.12)$$

As we will see, the collision time is very short (about 50 μs when the collision takes place on the short axis of the condensate and about 150 μs when the collision takes place along the long axis of the condensate) and we can neglect the expansion of the condensate along the long axis of the trap. In order to fix the initial density of the two colliding condensates we proceed as follows: we fix the number of atoms in the trapped condensate and we suppose 100% efficiency for the Raman process. Then we suppose that the Bragg pulse splits the condensate in two parts with the same number of atoms and therefore with a peak density equal to half the peak density of the initial condensate. In case of a non-perfect 50% splitting, the number of atoms in the sphere will be smaller¹. Finally we suppose that the Thomas-Fermi radius of the two colliding condensates is equal to the Thomas-Fermi radius of the initial condensate (i.e. the chemical potential is the same).

In figure 5.3 we compare the number of scattered atoms as a function of time (for 10^5 atoms in the initial condensate) and as a function of the relative velocity, for the two collision geometries. In the left column we report the results obtained in case that the collision takes place along the short axis of the condensate and in the right column for the collision along the long axis.

If we look at the number of scattered atoms as a function of time (first row of figure 5.3), we see that, if the collision happens along the long axis, the collision time is about 300 μs , much longer than in the other geometry (for which it is about 50 μs). In agreement with the rough estimate done at the beginning of this section, the collision time is comparable with the expansion of the two condensates for the first generation experiment, while it is limited by the separation time for the second generation experiment. For this reason, the number of scattered atoms, in the first generation experiment, is about 10 time larger than in the "short axis collision" case. This means that particular care is needed to carry out the second generation experiment, in order to have large condensates, a very good Raman transfer efficiency and a very good 50% Bragg pulse and therefore the maximum number of atoms detected on the sphere.

In the second row of figure 5.3 we show how the number of scattered atoms varies as a function of the relative velocity of the two colliding condensates. The trend of the curve is different in the two collision geometries. If the collision happens along the short axis, the number of scattered atoms is almost insensitive to the relative velocity and decreases if this increases. On the contrary, if the collision happens along the long axis of the condensate, the number of collisions shows a stronger dependence on the relative

¹The number of atoms in the sphere is proportional to the product of the number of atoms in each condensate. This product is maximum if the two condensates have the same number of atoms.

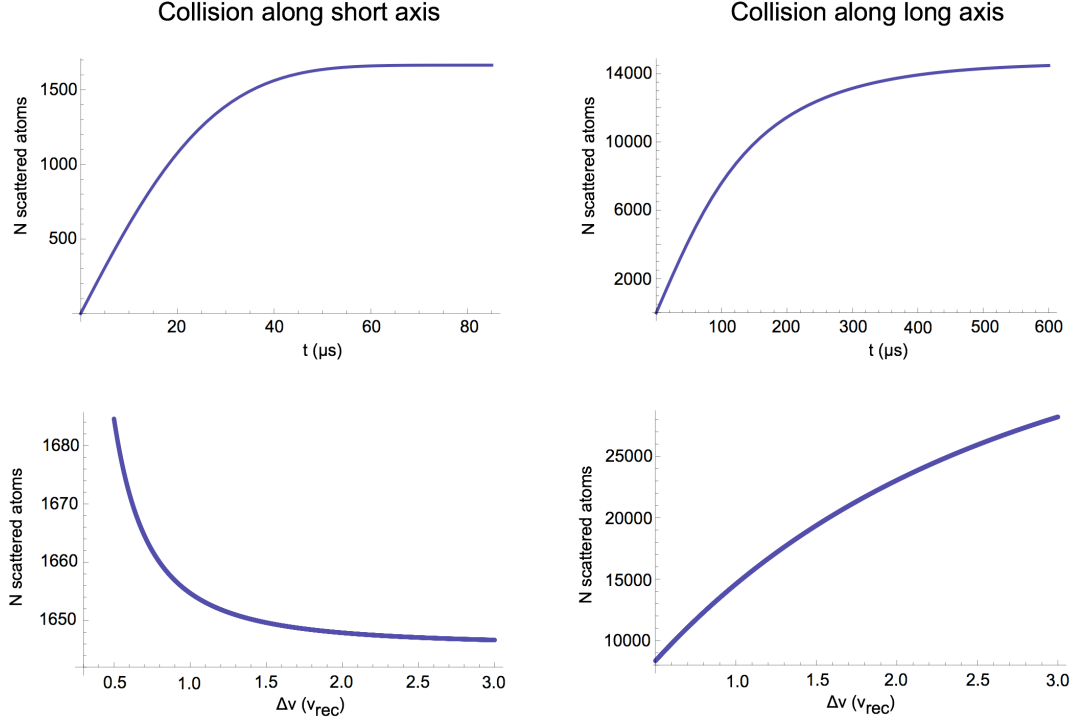


Figure 5.3: Number of scattered atoms as a function of time (first row) and as a function of the relative velocity of two colliding condensates (second row). In the left column we report the results obtained when the collision happens along the short axis of the condensate and in the right column we report the results obtained when the collision happens along the long axis of the condensates. The calculation have been made for 10^5 atoms in the initial condensate. The number of scattered atoms as a function of time (first row) has been calculated for the appropriate collision velocity.

velocity and the number of scattered atoms increases as the relative velocity increases. We can understand this trend if we go back to equation 5.10. In case of collision along the short axis the expansion of the condensates is negligible. This means that we can perform the temporal integration of equation 5.10. The collision time is given by $\Delta t = 2R_{yz}/\Delta v$, therefore:

$$\begin{aligned} N_{coll} &= 2 \Delta t \int d\mathbf{r} \Delta v \sigma_0 n_1(\mathbf{r}) n_2(\mathbf{r}) \\ &= 4R_{yz} \sigma_0 \int d\mathbf{r} \sigma_0 n_1(\mathbf{r}) n_2(\mathbf{r}) \end{aligned}$$

that doesn't depend on the collision velocity. The effective trend of the number of collisions as a function of the collision velocity will be given by the competition between the two effects: if the relative velocity decreases the collision time is longer and the expansion starts to count. If the collision happens along the long axis, the number of collisions is dominated by the density of the condensates and will increase with the relative velocity, as predicted by equation 5.10.

5.3 Experimental setup

We have seen in the previous section that, if the collision between the condensates happens along the short axis, the number of scattered atoms is quite small. Therefore all the experimental steps bringing to the production of the colliding condensates have to be as efficient as possible.

In section 4.5.1 we saw that whereas the transfer efficiency of the two-beam Raman transition is quite good (about 90%), as soon as we retroreflect the horizontal beam in order to split the condensate in two counterpropagating condensates, the transfer efficiency drops to 60%. Even though this behavior has not been completely understood, a possible explanation can be found in the fact that the retroreflected beam L'_2 has a power smaller than L_2 , due to reflections on the windows of the science chamber. This makes the Rabi frequency of the transition driven by the couple $L_1 + L_2$ different from the one of the couple $L_1 + L'_2$. Since the two Rabi frequencies cannot be independently tuned, the power unbalance between L_2 and L'_2 decreases the three-beam process efficiency.

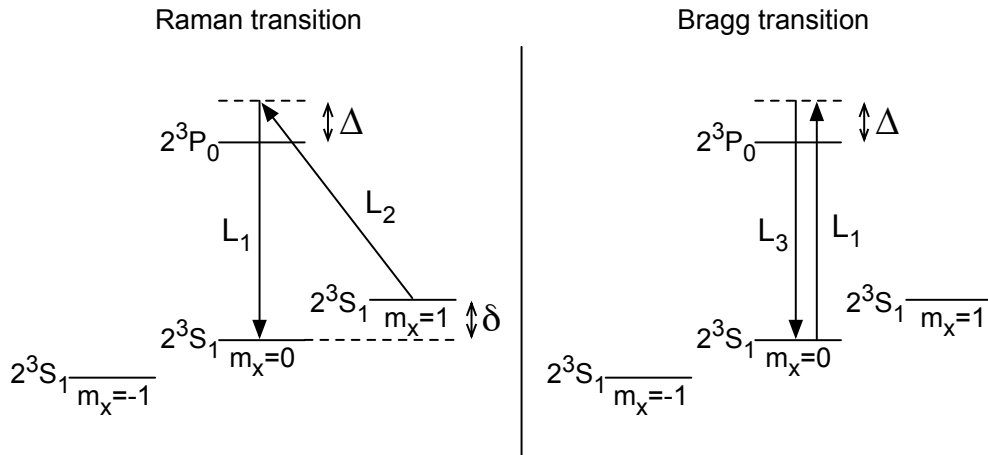


Figure 5.4: Level scheme for the transition used to drive Raman and Bragg transition.

In order to solve this problem we decided to decouple the process that transfers the atoms in the untrapped level from the process that generates the two counterpropagating condensates. Therefore we proceed as follows: a Raman transition is driven by the beams L_1 and L_2 drawn in the level scheme of figure 5.4. Atoms absorb a photon from L_2 and emit a photon in L_1 . Therefore they are transferred from the trapped level $m_x = 1$ to the untrapped level $m_x = 0$ and acquire a momentum $\hbar k_{rec}(\mathbf{e}_2 - \mathbf{e}_1)$, where \mathbf{e}_1 and \mathbf{e}_2 indicate the direction of propagation of the L_1 and L_2 . Thereafter a Bragg transition driven by the beams L_1 and L_3 (see the level scheme of figure 5.4) splits the untrapped cloud into two parts: the duration of the Bragg pulse is such that half of the cloud stays in the state of momentum $\hbar k_{rec}(\mathbf{e}_2 - \mathbf{e}_1)$ and half of the cloud absorbs

a photon from L_1 and emits a photon in L_3 and is therefore transferred in the state of momentum $\hbar k_{rec}(\mathbf{e}_2 - \mathbf{e}_1) + \hbar k_{rec}(\mathbf{e}_1 - \mathbf{e}_3)$, where \mathbf{e}_3 is the direction of propagation of L_3 . The collision is made between these two condensates.

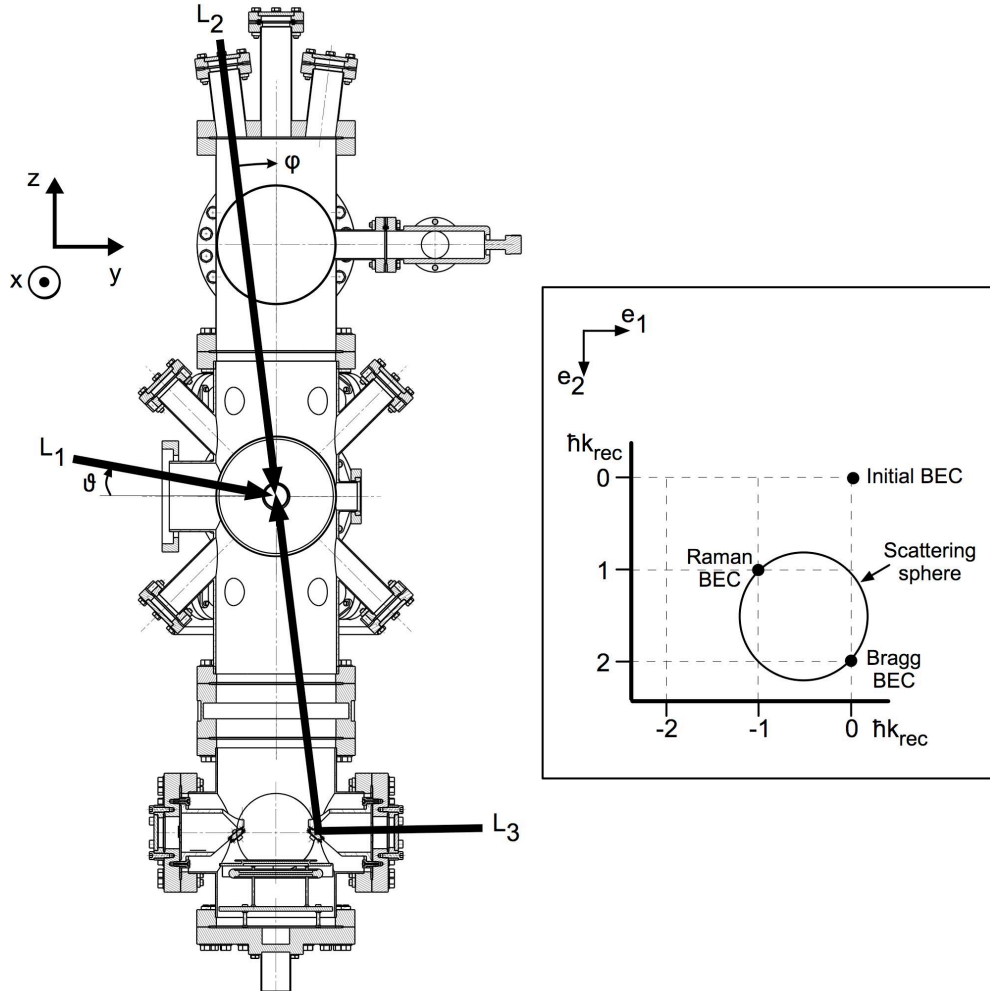


Figure 5.5: Arrangement of the Raman and Bragg beams in the science chamber. The bias field is oriented along the x direction. The three beams are contained in the vertical plane. L_1 forms an angle $\theta \simeq 8^\circ$ with the horizontal plane, whereas L_2 and L_3 forms an angle $\phi \simeq 7^\circ$ with the vertical axis. In the inset we show the section of the collision sphere in the vertical plane in momentum space. The frame axis are the propagation vectors of the three laser beams and to simplify the drawing we imposed $\theta, \phi = 0^\circ$.

Figure 5.5 shows the arrangement of the three beams in the chamber. L_1 is perpendicular to the bias and forms an angle $\theta \simeq 8^\circ$ with the horizontal plane. L_2 and L_3 are counterpropagating (therefore $\mathbf{e}_2 = -\mathbf{e}_3$), they are contained in the vertical plane and they form an angle of $\phi \simeq 7^\circ$ with the vertical direction. The inset of figure 5.5 shows

the collision sphere and the two colliding condensates in the velocity frame. For simplicity, in the inset we pose $\theta, \phi \simeq 0^\circ$. The sphere is centered at $(3/2\mathbf{e}_2 - 1/2\mathbf{e}_1)\hbar k_{rec}$ and its radius is $\hbar k_{rec}|\mathbf{e}_1 + \mathbf{e}_2|/2 = \hbar k_{rec}/2\sqrt{(\cos\theta + \sin\phi)^2 + \cos^2\phi} \simeq \hbar k_{rec}/\sqrt{2}$.

Beams polarization

As one can see from figure 5.4, L_1 and L_3 have to be π polarized, i.e. with linear polarization perpendicular to the bias axis. This can be achieved in the present geometry by assuring that they propagate in the vertical (yz) plane. L_2 has to be σ polarized. Since it propagates in the vertical plane as well, its polarization is set to be linear and perpendicular to the bias axis. In this case, the polarization vector can be written as the sum of two components, one with right circular polarization and one with left circular polarization. Since atoms in $m_x = 1$ are only sensitive to the left circular polarized component, the effective power seen by the atoms is half of the total power. We note that a photon that is σ^+ polarized can drive, together with a σ^- polarized photon, a non-resonant Raman transition from the $m_x = 1$ state to the $m_x = -1$ state. However a simulation shows that the population of this state is smaller than 1% and can be neglected.

The fine adjustment of the polarization is done by using half-wave plates and polarizer beam splitters situated just before the beam enters the science chamber and minimizing the amount of atoms extracted from the condensate due to off-resonant Raman transitions.

Experimental control of Raman and Bragg beams

We already pointed out the fact that Raman and Bragg pulses must have a high Rabi frequency so that the transfer is not sensitive to the velocity spread of the atoms in the condensate (see equation 4.24) and to bias fluctuations, that are of the order of a few kHz. Therefore we work with Rabi frequencies ranging between 100 kHz and 1 MHz. Raman and Bragg beams are switched on and off by acousto-optical modulators driven by low-noise synthesizers. The effective temporal superposition of the light pulses used to drive the Raman or the Bragg transition is assured by the use of RF switches with a controllable delay. With the present setup we can drive pulses of a duration down to 500 ns.

The three beams are generated from the same DBR diode laser that injects a laser amplifier. The light at the output of the amplifier is split into two parts: one goes into an acousto-optical modulator and generate L_1 , the other part goes into a second acousto-optical modulator and is used to generate L_2 and L_3 . In fact, L_2 and L_3 don't need to be on at the same time because one is used for the Raman transition and the other one for Bragg. An electro-optical modulator, triggered after the end of the Raman pulse, is used to switch the polarization of the beam from perpendicular to the bias field (L_2) to parallel to the bias field (L_3). A polarizing beam splitter installed just after the electro-optical modulator switches between the two different optical paths that L_2 and L_3 must follow to go respectively on the top and on the bottom of the

science chamber (see scheme represented in figure 5.6). This way to generate L_2 and L_3 allows to have the maximum amount of power at our disposal for each beam. The transmission efficiency of the electro-optical modulator is 82% and the extinction rate is 0.8%.

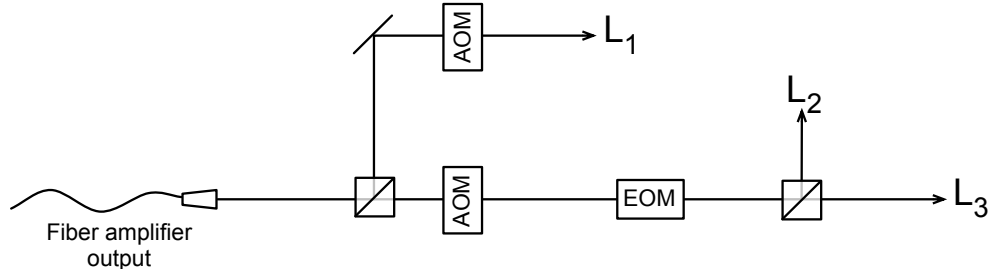


Figure 5.6: Scheme of the optical setup used to generate the three beams needed to drive Raman and Bragg transitions. The laser beam at the output of the fiber amplifier is split into two parts: one passes through an acousto-optical modulator (AOM) and generates the beam L_1 ; the other one passes through an AOM and through an electro-optical modulator (EOM). The latter is used to change the polarization of the beam by 90° between the Raman and the Bragg pulse. A beam splitter installed after the EOM is used then to change the path followed by the laser beam: L_2 drives the Raman transition and enters in the science chamber from the top; L_3 drives the Bragg transition and enters in the science chamber from the bottom (see figure 5.5). Mechanical shutters (not drawn for sake of simplicity) are inserted in the path of the three beams to assure that no light enters the science chamber when not required.

Since the number of atoms scattered in the sphere depends on the density of the cloud, the delay between the Raman and the Bragg pulse is set to the smallest possible value, about $1 \mu\text{s}$. During this delay we trigger the electro-optical modulator and we change the power and the detuning of L_3 by acting on the acousto-optical modulator. At the same time the power of L_1 is changed as well. In this way we can have a control of all the parameters that determine the efficiency of the Raman and Bragg processes. The laser is detuned on the blue side of the atomic resonance by $\Delta/2\pi = 600 \text{ MHz}$.

5.3.1 Theory of the Bragg transitions

As we pointed out in section 5.2.1, since the number of scattered atoms in this geometry is quite small, we want all the processes involved in the production of the two colliding condensates as efficient as possible. In the previous version of the experiment we had already managed to drive two-beam Raman transitions with a good efficiency. In this section we will show what are the requirements to have an efficient Bragg transition.

The difference between a Bragg and a Raman transition resides in the final internal states of the atoms. In a Raman transition the initial and the final internal states are different, while in a Bragg transition they are the same (see figure 5.4). For this reason, it is possible to have a 2N-photon Bragg transition, where the atoms will end in the same final state but with a different final momentum, determined by the number of photons exchanged with the laser beams and by their momentum. By changing the

power and the detuning of the laser beams one can decide which state to populate. We would like to note that, since in this collision geometry the number of scattered atoms doesn't depend too much on the collision velocity (see figure 5.3, second row), we are not interested in driving a $2N$ ($N > 1$) Bragg transition. On the other hand, this could be a nice trick to increase the number of scattered atoms in the other collision geometry. However, in our apparatus, a sphere of radius bigger than v_{rec} would be bigger than the detector and would not be entirely detected. This prevents the measurement of back to back correlations but it still allows the measurement of collinear correlations and of the thickness of the sphere.

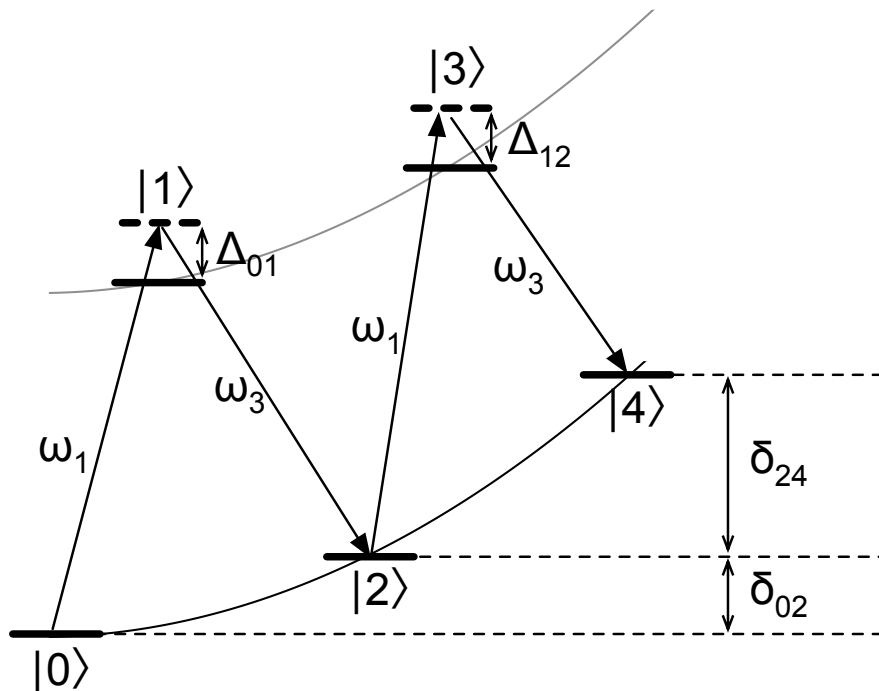


Figure 5.7: Energy diagram of the states that can be excited in a two-photon and a four-photon Bragg process.

In figure 5.7 we show the states that can be populated by driving a two-photon and a four-photon Bragg transition. Due to the quadratic dependence of the energy on the momentum acquired by the atoms, the states involved lay on a parabola. The

initial state is $|0\rangle = |g, \mathbf{p}\rangle$, where g stands for *ground* and \mathbf{p} is the initial momentum of the atoms. If the atoms make a two-photon Bragg transition, they absorb a photon of momentum $\hbar\mathbf{k}_1 = \hbar k_{rec}\mathbf{e}_1$ and they emit a photon of momentum $\hbar\mathbf{k}_3 = \hbar k_{rec}\mathbf{e}_3$. Therefore they will be transferred in the virtual state $|1\rangle = |e, \mathbf{p} + \hbar\mathbf{k}_1\rangle$ (where e stays for *excited*) and will end up in the state $|2\rangle = |g, \mathbf{p} + \hbar(\mathbf{k}_1 - \mathbf{k}_3)\rangle$. For a four-photon transition, they will absorb a third photon of momentum $\hbar\mathbf{k}_1$ and they will emit a fourth photon of momentum $\hbar\mathbf{k}_3$. Therefore they will be transferred to the virtual level $|3\rangle = |g, \mathbf{p} + \hbar(2\mathbf{k}_1 - \mathbf{k}_3)\rangle$ and they will end up in the state $|4\rangle = |g, \mathbf{p} + \hbar(2\mathbf{k}_1 - 2\mathbf{k}_3)\rangle$.

The population of states $|0\rangle$, $|2\rangle$ and $|4\rangle$ is determined by the duration of the interaction between the laser field and the atoms, by the relative detuning between the two laser beams δ and by the two-photon Rabi frequency $\Omega = \Omega_1\Omega_3/(2\Delta)$. In order to perform our experiment we want to keep the population of the state $|4\rangle$ negligible with respect to the population of states $|0\rangle$ and $|2\rangle$ and we want to end up with half of the atoms in $|0\rangle$ and half in $|2\rangle$ in order to have the maximum collision rate. In the following section we will calculate the populations of these states.

Schrödinger equation

The Hamiltonian describing the interaction between the atoms and the laser field can be written, in the dipole approximation, as:

$$H_{INT} = -\mathbf{d} \cdot \mathbf{E}(\mathbf{r}, t) \quad (5.13)$$

where \mathbf{d} is the atomic electric dipole moment. The laser field $\mathbf{E}(\mathbf{r}, t) = \mathbf{E}_1(\mathbf{r}, t) + \mathbf{E}_3(\mathbf{r}, t)$ is the sum of the fields of the two lasers, L_1 and L_3 , driving the Bragg transition, that can be written as:

$$\begin{aligned} \mathbf{E}_1(\mathbf{r}, t) &= \mathcal{E}_1\mathbf{e}_1(e^{i(\mathbf{k}_1 \cdot \mathbf{r} - \omega_1 t)} + c.c.) \\ \mathbf{E}_3(\mathbf{r}, t) &= \mathcal{E}_3\mathbf{e}_3(e^{i(\mathbf{k}_3 \cdot \mathbf{r} - \omega_3 t)} + c.c.) \end{aligned}$$

The Rabi frequency associated to the one-photon process bringing the atom from $|g\rangle$ to $|e\rangle$ and vice-versa is given by:

$$\begin{aligned} \Omega_1 &= \frac{2}{\hbar} \langle e | \mathbf{d} \cdot \mathcal{E}_1 \mathbf{e}_1 | g \rangle \\ \Omega_3 &= \frac{2}{\hbar} \langle g | \mathbf{d} \cdot \mathcal{E}_3 \mathbf{e}_3 | e \rangle \end{aligned}$$

The interaction hamiltonian is therefore written as:

$$\begin{aligned} H_{INT} &= \hbar \frac{\Omega_1}{2} e^{-i\omega_1 t} |1\rangle \langle 0| + \hbar \frac{\Omega_3}{2} e^{-i\omega_3 t} |1\rangle \langle 2| + \\ &+ \hbar \frac{\Omega_1}{2} e^{-i\omega_1 t} |3\rangle \langle 2| + \hbar \frac{\Omega_3}{2} e^{-i\omega_3 t} |3\rangle \langle 4| + c.c. \end{aligned} \quad (5.14)$$

while the atomic Hamiltonian is given by:

$$H_A = \sum_{i=0}^4 \tilde{E}_i |i\rangle \langle i| \quad (5.15)$$

where \tilde{E}_i is the energy of the $|i\rangle$ state and takes account of the energy difference between $|e\rangle$ and $|g\rangle$, of the light shift of the atomic levels and of the momentum acquired by the atom due to emission or absorption of photons.

The wavefunction $|\psi\rangle$ can be written as:

$$|\psi\rangle = \sum_{i=0}^4 C_i e^{-i\tilde{E}_i t} |i\rangle \quad (5.16)$$

In the hypothesis that the spontaneous emission is negligible, the Schrödinger equation is given by the following expressions:

$$\begin{aligned} \dot{C}_0 &= -i \frac{\Omega_1}{2} e^{i\Delta_{01} t} C_1 \\ \dot{C}_1 &= -i \frac{\Omega_1}{2} e^{-i\Delta_{01} t} C_0 - i \frac{\Omega_3}{2} e^{-i(\Delta_{01} + \delta_{02}) t} C_2 \\ \dot{C}_2 &= -i \frac{\Omega_1}{2} e^{i\Delta_{23} t} C_3 - i \frac{\Omega_3}{2} e^{i(\Delta_{01} + \delta_{02}) t} C_1 \\ \dot{C}_3 &= -i \frac{\Omega_1}{2} e^{-i\Delta_{23} t} C_2 - i \frac{\Omega_3}{2} e^{-i(\Delta_{23} + \delta_{24}) t} C_4 \\ \dot{C}_4 &= -i \frac{\Omega_3}{2} e^{i(\Delta_{23} + \delta_{24}) t} C_3 \end{aligned} \quad (5.17)$$

In the equations above, Δ_{01} and Δ_{23} are the detuning of the laser field $\mathbf{E}_1(\mathbf{r}, t)$ with respect to the transition $|0\rangle \rightarrow |1\rangle$ and $|2\rangle \rightarrow |3\rangle$, taking into account the momentum transferred to the atoms. Since $\Delta/2\pi = (\omega_1 - \omega_0)/2\pi = 600$ MHz is much larger than the recoil frequency $\omega_{rec}/2\pi = \hbar k_{rec}^2/2m/2\pi \simeq 40$ kHz we can set $\Delta_{01} \simeq \Delta_{23} \simeq \Delta$.

The quantities δ_{02} and δ_{24} are the effective detunings of the transitions $|0\rangle \rightarrow |2\rangle$ and $|2\rangle \rightarrow |4\rangle$ respectively and are given by:

$$\begin{aligned} \delta_{02} &= \omega_3 - \omega_1 + \frac{(\mathbf{p} + \hbar\mathbf{k}_1 - \hbar\mathbf{k}_3)^2}{2m\hbar} - \frac{\mathbf{p}^2}{2m\hbar} \\ \delta_{24} &= \omega_3 - \omega_1 + \frac{(\mathbf{p} + 2\hbar\mathbf{k}_1 - 2\hbar\mathbf{k}_3)^2}{2m\hbar} - \frac{(\mathbf{p} + \hbar\mathbf{k}_1 - \hbar\mathbf{k}_3)^2}{2m\hbar} \end{aligned}$$

where we supposed that the light shifts of the states $|g\rangle$ and $|e\rangle$ are equal² and therefore cancel away.

In order to obtain the dynamic equations for states $|0\rangle$, $|2\rangle$, $|4\rangle$ we adiabatically eliminate the virtual levels $|1\rangle$ and $|3\rangle$. This is justified when $\Delta \gg \Omega_1, \Omega_3, \delta_{02}, \delta_{24}$. In this case we can integrate the equations for \dot{C}_1 and \dot{C}_3 considering C_0 , C_2 and C_4 constant in time. We therefore obtain:

$$\begin{aligned} \dot{C}_0 &= i \left(\frac{\Omega_1^2}{4\Delta} C_0 + \frac{\Omega_1\Omega_3}{4(\Delta + \delta_{02})} e^{-i\delta_{02} t} C_2 \right) \\ \dot{C}_2 &= i \left(\left(\frac{\Omega_1^2}{4\Delta} + \frac{\Omega_3^2}{4(\Delta + \delta_{02})} \right) C_2 + \frac{\Omega_1\Omega_3}{4\Delta} e^{i\delta_{02} t} C_0 + \frac{\Omega_1\Omega_3}{4(\Delta + \delta_{24})} e^{-i\delta_{24} t} C_4 \right) \end{aligned}$$

²This is true if $\Omega_1 = \Omega_3$.

$$\dot{C}_4 = i \left(\frac{\Omega_3^2}{4(\Delta + \delta_{24})} C_4 + \frac{\Omega_1 \Omega_3}{4\Delta} e^{i\delta_{24}t} C_2 \right) \quad (5.18)$$

We can set $\Delta + \delta_{02} \simeq \Delta + \delta_{24} \simeq \Delta$ and $\Omega_1 = \Omega_3$ and obtain:

$$\begin{aligned} \dot{C}_0 &= i \frac{\Omega}{2} \left(\alpha C_0 + e^{-i\delta_{02}t} C_2 \right) \\ \dot{C}_2 &= i \frac{\Omega}{2} \left(e^{-i\delta_{02}t} C_0 + \beta C_2 + e^{-i\delta_{24}t} C_4 \right) \\ \dot{C}_4 &= i \frac{\Omega}{2} \left(e^{-i\delta_{24}t} C_2 + \alpha C_4 \right) \end{aligned} \quad (5.19)$$

where $\Omega = \Omega_1^2/2\Delta$ is the two-photon Rabi frequency. According to equation 5.18, one clearly has $\alpha = 1$ and $\beta = 2$. However, if one makes the calculation by also taking into account the contribution of states $|-2\rangle = |g, \mathbf{p} - \hbar(\mathbf{k}_1 - \mathbf{k}_3)\rangle$ and $|6\rangle = |g, \mathbf{p} + \hbar(3\mathbf{k}_1 - 3\mathbf{k}_3)\rangle$, other terms appear in equations 5.19. These terms would take into account the pumping from levels $|-2\rangle$ and $|6\rangle$ and one would have $\alpha \simeq 2$. In order to account for this effect we will set $\alpha = 2$ in the following.

Resonance condition

As we said in section 5.3, we want to use the Bragg transition to populate the state $|2\rangle$. In order to be resonant with this state the detuning δ_{02} has to be zero. Therefore

$$\omega_3 - \omega_1 = \frac{\mathbf{p}^2}{2m\hbar} - \frac{(\mathbf{p} + \hbar\mathbf{k}_1 - \hbar\mathbf{k}_3)^2}{2m\hbar} \quad (5.20)$$

The initial momentum of the atoms \mathbf{p} is the momentum transferred by the Raman beams, therefore $\mathbf{p} = -\hbar(\mathbf{k}_3 + \mathbf{k}_1)$ and the 5.20 becomes:

$$\omega_3 - \omega_1 = \frac{\hbar}{2m} \left((\mathbf{k}_1 + \mathbf{k}_3)^2 - (2\mathbf{k}_3)^2 \right) \quad (5.21)$$

If we are resonant with the two-photon transition, we will be detuned by

$$\delta_{24} = \frac{\hbar}{m} (\mathbf{k}_1 - \mathbf{k}_3)^2 \quad (5.22)$$

If $\mathbf{k}_1 \perp \mathbf{k}_3$, the resonance condition is $\omega_3 - \omega_1 = -2\omega_{rec}$ and $\delta_{24} = 4\omega_{rec}$. By solving the system of equations 5.19 we can calculate the population of states $|0\rangle$, $|2\rangle$, $|4\rangle$ and find a situation where the population of $|4\rangle$ is negligible with respect to the other two. In addition, we want to satisfy two requirements: first, we want the velocity spread of the condensate to be negligible with respect to the Rabi frequency; second, we want the total duration of the process (Raman + Bragg) to be small with respect to the expansion of the condensate, in order to have the highest number of collisions.

The evolution of the three populations as a function of time is shown in figure 5.8. The beams are resonant with the two-photon transition and the two-photon Rabi frequency is set to $\Omega = 2\omega_{rec}$ (where $\omega_{rec}/2\pi \simeq 40$ kHz). Therefore with a pulse duration of $3 \mu\text{s}$ we should be able to transfer half of the atoms in the state $|2\rangle$ and leave half in $|0\rangle$. At $t = 3 \mu\text{s}$ the population of the state $|4\rangle$ is $\simeq 5\%$ of the total population.

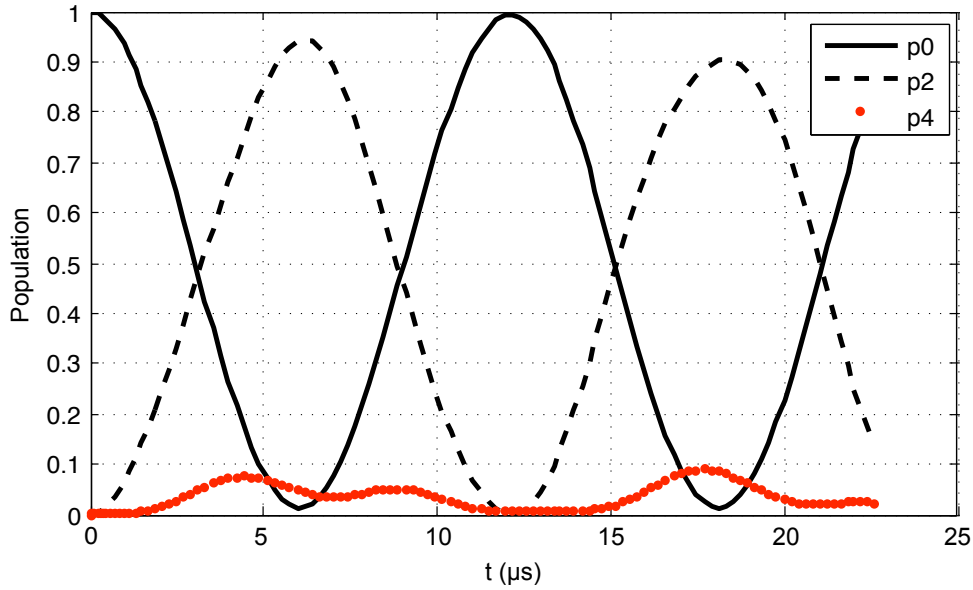


Figure 5.8: Population of the states $|0\rangle$, $|2\rangle$, $|4\rangle$ as a function of time. The relative detuning of the two laser beams is set to be in resonance with the transition $|0\rangle \rightarrow |2\rangle$ and the Rabi frequency is $\Omega = 2\omega_{rec}$. The population of the state $|0\rangle$ is drawn with the solid line, the population of the state $|2\rangle$ with a dashed line and the population of the state $|4\rangle$ with dots. The population of the $|4\rangle$ is always negligible with respect to the other two.

5.3.2 Spontaneous emission

In this second version of the experiment, the detuning Δ of the three beams L_1 , L_2 , L_3 has been set to 600 MHz instead of 400 MHz in order to decrease the spontaneous emission rate. In fact, when an atom is brought to the excited level with the absorption of a photon there is a non-zero probability for the atom to decay to one of the three magnetic sublevels of the 2^3S_1 state spontaneously emitting a photon. Since the direction of emission of this photon is random, the recoil momentum of the atom will be $\hbar k_{rec}$ with a random direction. Therefore atoms that undergo this process will be on a sphere of radius $\hbar k_{rec}$ (in momentum space). Since we detect only atoms falling in $m_x = 0$ (the trap is always kept on), we will detect a third of the atoms that underwent a spontaneous emission process. This can be a big problem. In fact, if the spontaneous emission sphere coincides or intersects the collision sphere, the measurement of the scattering mode population or of the squeezing can be distorted. It will probably have a smallest impact on the back to back correlations, because the atoms on the spontaneous emission sphere are not correlated by pairs of opposite momenta. However it can affect the collinear correlation because atoms on the spontaneous emission sphere will show an Hanbury Brown Twiss like correlation as well. In the following sections we will calculate the spontaneous emission rate and we will show some experimental observations. We will also try to predict the impact of the spontaneous emission spheres

that we can observe in the present experimental situation on the measurements that we want to perform.

Spontaneous emission rate

Let us consider a two level atom in a laser field. For instance we can consider the transition between the states 2^3S_1 with $m_x = 1$ and 2^3P_0 with $m_x = 0$ and the laser field generated by L_2 that is σ^- polarized and is detuned by $\Delta = 600$ MHz on the blue side of the considered transition. The population of the excited level is given by:

$$\rho_e = \frac{1}{2} \frac{s}{1+s} \quad (5.23)$$

with s the saturation parameter:

$$s = \frac{\Omega_1^2/2}{\Delta^2 + \Gamma^2/4} \quad (5.24)$$

where $\Gamma/2\pi = 1.6$ MHz is the natural linewidth of the considered transition. Ω_1 is the one-photon Rabi frequency defined as $\Omega_1 = \Gamma\sqrt{I/(3 \times 2I_{sat})}$, where I is the intensity of the beam and $I_{sat} = 167 \mu\text{W}/\text{cm}^2$ is the saturation intensity. For our beam intensity and size $\Omega_1/2\pi \simeq 20$ MHz. The factor of 3 in the definition of Ω_1 takes account of the appropriate Clebsch-Gordan coefficient. The number of photons emitted in a spontaneous emission process is therefore given by:

$$N_{sp} = \Gamma_{sp} \tau = \rho_e \Gamma \tau \simeq \Gamma \frac{\Omega_1^2}{4\Delta^2} \tau \quad (5.25)$$

where τ is the duration of the laser pulse and Γ_{sp} is the spontaneous emission rate. The last equality holds in our case because $\Delta \gg \Gamma, \Omega_1$. With our experimental parameters, the spontaneous emission rate is about 6×10^{-3} photons per μs per atom. In order to give an estimate of the number of atoms detected in this way, we will consider only the simplest process, in which an atom is excited to the upper level, it decays in $m_x = 0$ with the emission of a photon and is detected. Since the probability of this process to happen is $1/3$, the spontaneous emission rate per atom will be divided by three. If one atom emits on average 2×10^{-3} photons per μs , if the condensate contains 10^5 atoms, we will detect 200 atoms per μs . Since the duration of the Raman and Bragg pulses is around $3 \mu\text{s}$, we can detect 600 atoms on the spontaneous emission sphere. This is not negligible with respect to the number of atoms in the collision sphere that, in section 5.2.1, we estimated to be about 1600. For this reason, we choose the beams geometry by carefully checking that the collision sphere would not be superposed with the spontaneous emission sphere, in order to have a good signal to noise ratio. In the following section we will show where the two spheres would fall on the detector and we will comment on the possible problems.

As we have already noted, this is a simplified picture of the process. In fact there are several other processes that can happen: an atom can absorb a photon and decay

into the $m_x = -1$ state and not be detected or decay in $m_x = 1$ where it can eventually absorb another photon and start the cycle again. In order to calculate exactly the number of atoms decaying in $m_x = 0$ we should take into account the evolution of the process. Therefore the estimation above gives only an order of magnitude.

Experimental observations

Spontaneous emission is quite useful during the alignment of the beams. In fact one can shine on the atoms one beam at a time, with σ polarization and check, for a given duration and intensity, when the number of atoms detected in the spontaneous emission sphere is maximum as a function of the alignment of the beam.

In figure 5.9 we report the spontaneous emission sphere detected when only the L_3 beam is on, with σ polarization. The data have been plot in momentum space in a frame that falls under the effect of gravity. A sphere centered at $\hbar k_{rec}$ is clearly visible. Since the atoms have absorbed one photon from L_3 , they receive a one photon recoil kick towards the top of the chamber and they emit a π polarized photon in a random direction. The three dimensional visualization of the sphere allows one to note that the atoms do not occupy the sphere homogeneously. In fact we can clearly see a hole in the direction of the x axis. This is due to the fact that a linear polarized photon cannot be emitted along the quantization (x) axis. In addition the thickness of the sphere seems to vary as a function of the angle. The statistical properties (density and correlation function) will be the subject of a further study in the short term. The condensate that is visible at $\hbar k_{rec} = 0$ is generated by an off-resonant Raman transition induced by a small amount of linear polarization present in the beam: some of the atoms can absorb a σ photon from the laser beam and emit in a stimulated way a π photon in the same beam, therefore the total momentum transfer for this transition is zero.

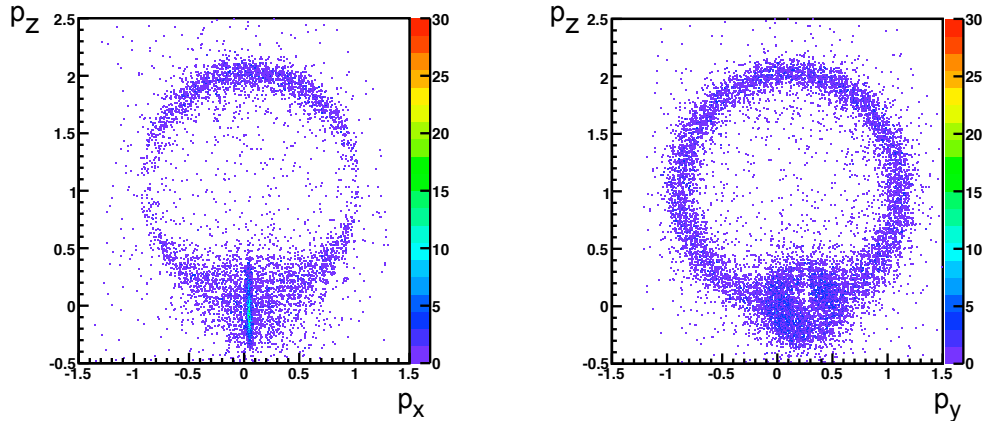


Figure 5.9: Spontaneous emission sphere in momentum space (units of $\hbar k_{rec}$). The sphere has been observed by shining the L_3 beam with σ polarization on the condensate. On the left side we report a slice on the xz plane integrated in the interval $-0.3 < p_y < 0.3$. On the right side we report a slice on the yz plane integrated in the interval $-0.3 < p_x < 0.3$.

Observable spheres

In our experimental situation, atoms are brought to the excited level either by absorbing a photon from L_2 (when we drive the Raman transition) or by absorbing a photon from L_1 (when we drive the Bragg transition). Since we detect only atoms that decay in the substate $m_x = 0$, if the atoms have absorbed a photon from L_2 , the center of the detected spontaneous emission sphere will move (in the free falling frame) with momentum $\hbar k_{rec} \mathbf{e}_2$ and will have a radius equal to $\hbar k_{rec}$. The other possible spontaneous emission sphere can be formed by atoms that undergo the Raman transition and then absorb a photon from L_1 but, instead of terminating the Bragg transfer, emit spontaneously a photon³. This sphere will be centered on $\hbar k_{rec}(\mathbf{e}_2 - \mathbf{e}_1) + \hbar k_{rec} \mathbf{e}_1$, will have a radius equal to $\hbar k_{rec}$ and is therefore coincident with the first one.

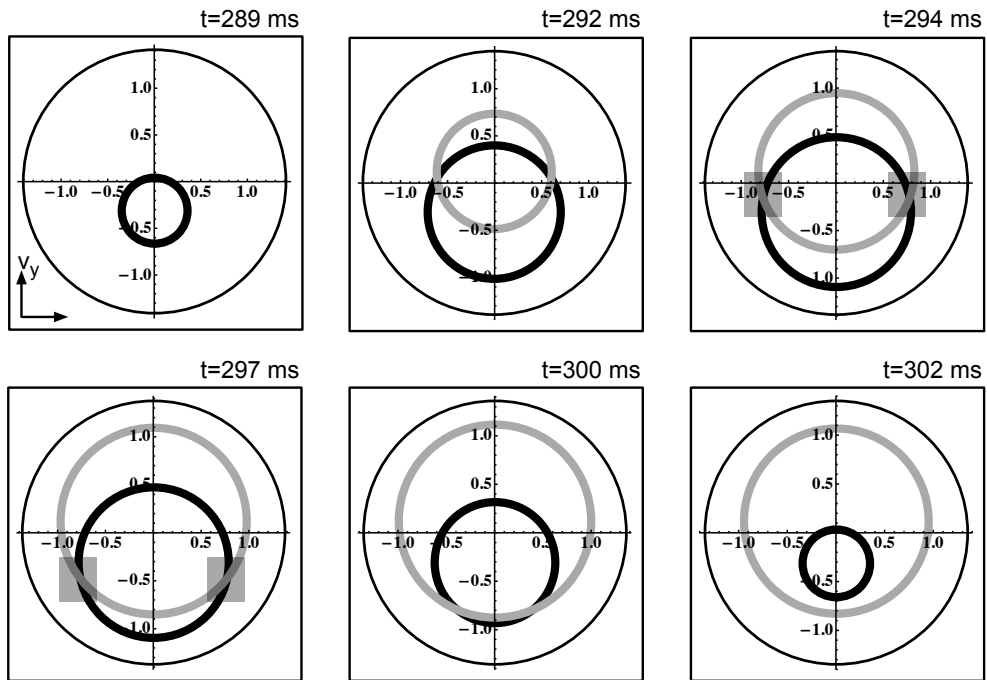


Figure 5.10: Simulation of the experiment (here we have taken $\theta = 8^\circ$ and $\phi = 7^\circ$, see figure 5.5). The scattering sphere (black thick circle) and the spontaneous emission sphere (grey circle) are shown as they fall on the detector. The spheres have been plotted in velocity space, in unity of v_{rec} . The thin black circle represents the detector.

In figure 5.10 we show the result of a simulation of the experiment. Time slices of the scattering sphere (black) and of the spontaneous emission sphere (grey) are shown in velocity space (in unity of the recoil velocity) as they fall on the detector. The black circle represents the detector. The equator of the scattering sphere crosses the detector

³Other spontaneous emission spheres can be observed, however, since they don't intersect the scattering sphere, they are not taken into account.

for $t = 294$ ms. As we can see, at the same time, the spontaneous emission sphere intersects the scattering sphere in the shadowed region, in the direction of the long axis of the condensate (see also the picture at $t = 297$ ms). This region is important for the study of the anisotropy of the sphere and of the mode population as a function of the angle. The presence of the spontaneous emission sphere can eventually spoil the result. The problem can be overcome by estimating the number of atoms present in a region of the spontaneous emission sphere symmetric with respect to the highlighted one and by subsequently subtracting it from the total number of atoms detected in the highlighted region.

5.4 Preliminary results

During the final part of my PhD, we started data acquisition for the second generation experiment after overcoming several technical problems. The analysis that measures the sphere density, correlations and squeezing is long and cumbersome. In this section we will just present some preliminary results.

Figure 5.11 shows the observed scattering sphere in velocity space, in the reference of the center of the sphere. We show slices in the yz plane. Each slice is averaged over $v_x = 0.2 v_{rec}$. The two large spots are the two condensates that underwent the collision, as shown in the inset. As expected no condensate is present on the x direction that is therefore available to study thickness and density of the sphere.

These data have been obtained for a power of 13 mW for the Raman beams and of 6 mW for the Bragg beams. The beam size is 1.88 mm (at $1/e^2$). The Raman pulse duration is 4 μ s and the Bragg pulse duration is 3 μ s.

In order to check the efficiency of the Bragg pulse, we measured the number of atoms remaining in the condensate extracted with the Raman pulse versus the number of atoms transferred by the Bragg pulse. In the left graph of figure 5.12 we plot the number of atoms in the Raman condensate versus the number of atoms in the Bragg condensate. A linear fit gives a slope of 0.9, meaning that the population of the two condensates is very well balanced. We would like to note that this measurement is strongly affected by the saturation of the detector. However, since the saturation depends on the density of the cloud, here it is reasonable to suppose that the number of atoms detected in each condensate is affected in the same way.

A first comparison with theory can be made by looking at the number of scattered atoms as a function of the number of atoms in the initial condensate. This quantity is plotted on the right side of figure 5.12 together with the theoretical expectation computed from equation 5.10 taking into account 10% detection efficiency (dashed line). As one can see the agreement is poor even if we take into account the dispersion of the data. This is due to the fact that saturation is not taken into account. Since the density of the sphere is small compared with the condensate density, we expect that the number of scattered atoms is not affected by the saturation, while the number of atoms in the condensate is. This is supported by the observation that the number of atoms detected in the condensate is systematically smaller than expected. A better agreement

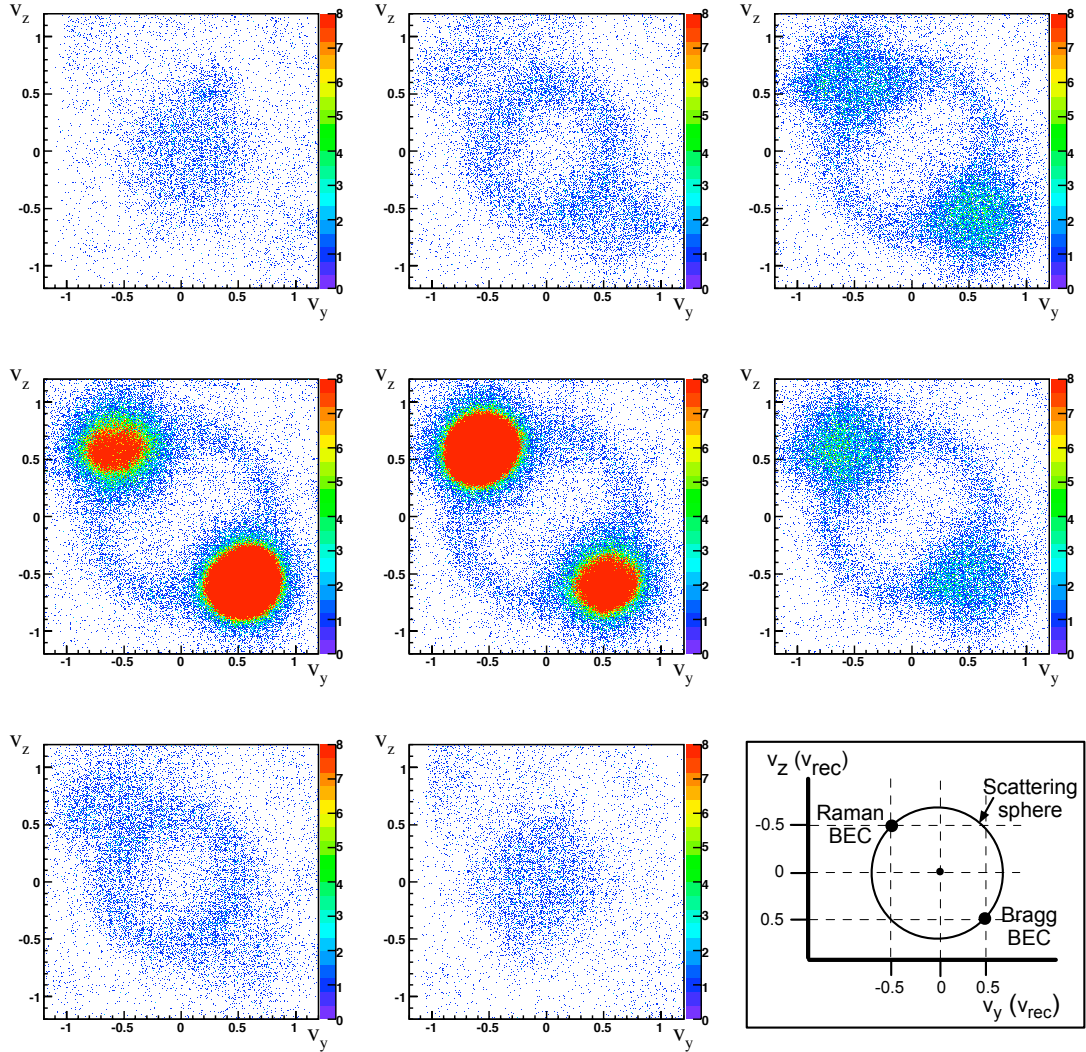


Figure 5.11: Slices of the collision sphere on the yz plane as it falls on the detector, observed in the second version experiment. The sphere has been plotted in velocity space, in units of v_{rec} in the reference of the center of the sphere. Each slice has been averaged over $0.2 v_{rec}$ on the x axis. As the inset shows, the two large spots are the condensate extracted with Raman and Bragg pulses.

is obtained assuming that the number of atoms detected in the condensate is a factor 3.5 smaller than the real number (solid line in figure 5.12). However, this measurement does not allow to distinguish the contribution of the two detector parameters. Therefore the obtained value of the detector saturation strongly depends on the assumed detection efficiency. If we could independently measure the detection efficiency (by calibrating the micro-channel plate or by measuring squeezing), the trend of the number of scattered atoms as a function of the number of colliding atoms would allow us to measure the

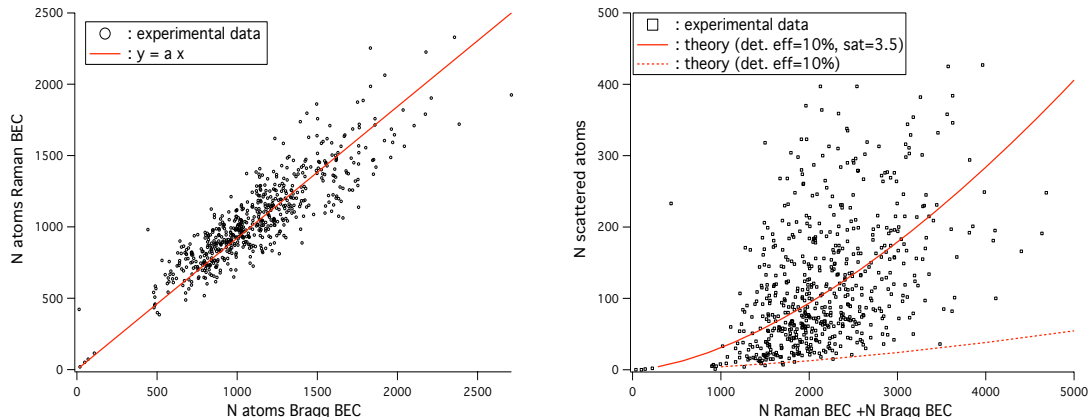


Figure 5.12: On the left side: Number of atoms detected in the condensate with momentum imparted by the Raman pulse as a function of the number of atoms transferred in the second condensate by the Bragg pulse (black circles). The solid line is a linear fit. The slope is 0.92 ± 0.005 , therefore the number of atoms in the two condensates are well balanced, as required. On the right side: Number of scattered atoms as a function of the number of atoms detected in the two colliding condensates (black squares). The dashed line is the theoretical expectation calculated from equation 5.10 assuming a detection efficiency of 10%. The solid line is the theoretical expectation calculated from equation 5.10 assuming a detection efficiency of 10% and that, due to the detection saturation, the number of atoms detected in the condensates is a factor of 3.5 smaller than the real number (see text).

saturation.

Holding the reasonable assumption that the population of the sphere is not affected by the detector saturation, if the detection efficiency is unchanged between the two generations of the experiment (see appendix), the number of scattered atoms is roughly a factor of two less than in the previous version of the experiment (see section 4.6.1). As we pointed out in section 5.2.1, if the number of atoms in the initial condensate is the same, the expected number of scattered atoms is a factor of 10 smaller in the new geometry. Our observation tells us that we succeeded in improving the number of atoms in the initial condensate by roughly a factor of two (see section 5.2.1).

5.5 Conclusion

In this chapter we presented an upgraded version of the He^* pairs experiment. We explained the motivation for a deeper study and we performed a detailed comparison between the two versions of the experiments. We showed that the upgraded version allows us to overcome the limitations of the first version (summarized in the conclusion of chapter 4). In addition, since the number of scattered atoms in the second version is much smaller than in the first version, all the experimental steps for the generation of the colliding condensates have to be optimized with great care. A special attention has been paid to the study of Bragg transitions that we use to split the initial condensate into two counterpropagating condensates. Other possible problems related to spon-

taneous emission of photons during Raman and Bragg transitions have been studied and quantified. In the last section of the chapter some preliminary results have been presented. The observed scattering sphere confirms that the experimental goals of the second generation experiment have been reached: the region along the x direction is available for the measurement of the sphere thickness and the sphere is visible with a significant signal to noise ratio. A detailed analysis of the statistical properties of the sphere (density, correlation functions and squeezing) is in progress at present.

Conclusion

In this thesis we presented two experiments on ultracold gases of metastable Helium: the measurement of the Hanbury Brown Twiss effect on a cloud of fermions and the generation of correlated pairs of bosons in atomic four-wave mixing.

Both experiments constitute the extension, to matter waves, of experiments that have been fundamental for the development of quantum optics. In sharp contrast to photons, ^4He has a readily available fermionic counterpart: ^3He . This isotope has been cooled to degeneracy in the metastable state by the group of W. Vassen in Amsterdam in 2005. This achievement allows one to go beyond the simple analogy between bosonic atoms and photons. In fact, since a fermionic counterpart of photon doesn't exist, it is not possible to directly compare the correlation function for bosons and fermions in an experiment that involves only the light. This has been possible with atoms and it is one of the major achievement of the experiment described in the first part of this thesis. A direct comparison between the correlation function of bosons and fermions produced in the same experimental apparatus and at the same temperature has been performed. Our detection system allowed us to obtain quantitative measurements of the correlation functions of the two isotopes in three dimensions.

The second experiment described in this thesis is the analogue of the experiment performed by Burnham and Weinberg in 1970 with correlated pairs of photons generated in parametric down conversion. In our experiment correlated atom pairs are generated by the collision of two Bose-Einstein condensates. Atomic interactions play the same role as non-linear susceptibility in non-linear crystals. The measurement of the correlation function allows us to demonstrate that atoms flying back to back on the collision sphere are correlated in pairs. Furthermore the observation of a Hanbury Brown Twiss correlation between atoms with collinear velocity demonstrates that our system cannot be interpreted in terms of classical mechanics, but that the bosonic nature of ^4He atoms plays a crucial role.

The realization of a source of correlated atom pairs constitutes the first fundamental step towards the realization of new experiments of quantum atom optics. As the experiment performed by Burnham and Weinberg paved the way to the observation of squeezed and entangled states with photons, it would be very interesting to demonstrate that our atom pairs are entangled and, in the future, to violate Bell's inequalities with atoms. The second version of the pairs experiment described in this thesis goes in this direction. It is aimed to the observation of number squeezing between two

correlated volumes of the scattering sphere. This is the first (and the easiest) step in view of more complicated experiments, that culminate with the violation of Bell's inequalities. In analogy with the experiment carried out by Rarity and Tapster [125] we could perform a Bell test by recombining the atoms belonging to two different pairs. However this experiment is quite hard to perform because the low repetition rate of the experiment together with the low detection efficiency would make the acquisition time unpractically long.

In order to increase the repetition rate one can increase the number of pairs recombined in a single shot. In a scheme like the one of [125] one can use a spherical atom mirror to recombine several pairs at a time or to make several Bragg pulses in different directions in order to recombine several pairs in the same shot. Another approach consists in forcing the atom pairs to be emitted in a small number of momentum mode. Following a suggestion by K. Mølmer [126], Ketterle's group observed atomic four wave mixing by loading a stationary Bose-Einstein condensate into a moving lattice [127]. The presence of the lattice forces atoms to be scattered in two momentum modes imposed by phase matching conditions. Entanglement between particles scattered by the lattice has not been demonstrated experimentally. A recent theoretical work by M. J. Davis et al. [128] suggests a scheme for the detection of entanglement in this system and the experimental requirements seem to be reasonable (even though not trivial). The realization of an experiment of this kind is envisaged in the near future of the He* experiment.

In the very short term, our experimental apparatus will be modified in order to install a dipole trap. After the standard cooling cycle, the sample will be loaded in an anisotropic optical trap with its long axis along the vertical direction. This would allow us to take advantage of the extremely good resolution of our detector on the vertical direction, with an consequent gain in terms of signal to noise ratio in the correlation measurement.

Along a different line, whose exploration began with this thesis and that of M. Schellekens [44], the group is also planning to introduce ^3He in the experimental setup in order to perform quantum atom optics experiments with fermions. This field of research is interesting for several reasons. First, as we said above, quantum optics analogues for experiments with fermions do not exist. Second, it is interesting to compare the behavior of bosons and fermions in the same experiment. For instance, the observation of matter wave amplification, superradiance and four wave mixing has raised the question whether these processes depend on the quantum nature of particles or not. In fact they are normally described as processes which relies on bosonic stimulation, but some theoretical works affirm that they are related to multi-particles interference effects and to the coherence properties of the atomic gas [129], [130], which could be exploited also with fermions. At the moment this question is still waiting for an answer from the experimental side.

The strong interest in quantum atom optics is proved by the ever increasing number of groups all around the world that entered this research field. Besides the experimental results achieved at the Institut d'Optique there have been a number of demonstrations

of quantum atom optics phenomena in recent years. Two and three-body correlations have been used to study strongly correlated systems [131], [132], and non classical correlations have been observed in the Mott insulator phase [59]. Number squeezing has been observed between atoms trapped in different sites of an optical lattice [133]. Along the same line, several groups have developed new detection techniques to perform three dimensional single atom detection for alkali atoms, as for example the group of D. S. Weiss at the Penn State University [134], the group of H. Ott in Mainz [135], or the group of Schmiedmayer in Wien [136]. Nevertheless, the versatility of the detection technique used for the experiments presented in this thesis keeps the He* experiment in Palaiseau on the foreground of this kind of research. From the measurement of the Hanbury Brown Twiss effect for bosons and fermions through the generation of atom pairs, the work done by the He* team sets the stage for new important developments. Without doubts, owing to the commitment and the ability of the team I've the pleasure to work with, these will be soon obtained.

Appendix A

The detector

The detector that we used to perform the measurements described in this thesis is a micro-channel plate (MCP) with a delay-line anode. This detector allows us to perform single atom detection, space and time resolved. In this appendix we will describe the way this detector works and the characteristics of the three different kinds of MCPs that we have used during my PhD. The detector used for the Hanbury Brown Twiss experiment performed in Amsterdam (see chapter 1) has been produced by Burle and is referred as “Burle 1” in the following. It has also been used for the first correlated pairs experiment (see chapter 4). The second detector that we used has been produced by Hamamatsu and is referred as “Hamamatsu”. The third detector has been bought from Burle (now Photonis) as well and is referred as “Burle 2” in the following. It has been used for the second pairs experiment (see chapter 5).

A.1 The micro-channel plate

A micro-channel plate(MCP) is a thin glass plate pierced with many tiny channels. It is fabricated from an array of millions of glass tubes, with a diameter of tens of microns, which is cut into slices around a millimeter thick. The front and the rear face of the MCP are metal coated. MCPs are normally used to detect high energy photons (UV), ions or high energy particles. Due to the large internal energy of the metastable state, metastable Helium can also be detected by a MCP.

Figure A.1 shows a sketch of a MCP and illustrates the way the MCP works. A particle arriving on the input surface of the MCP ejects an electron from the channel wall. The channel then behaves like an electron multiplier. In fact, when an electron enters the channel, is accelerated by an electric field. This electric field is generated by applying a high voltage between the front and the back face of the plate. Since the electric field direction has a small angle with the channel (about 7°), the electron is forced into collision with the channel wall, hence ejecting secondary electrons. Those secondary electrons are then accelerated and hit the channel walls, ejecting other electrons and so on. For each incoming particle about $10^3 - 10^4$ electrons are ejected. The typical duration of this amplification process is about 100 ps.

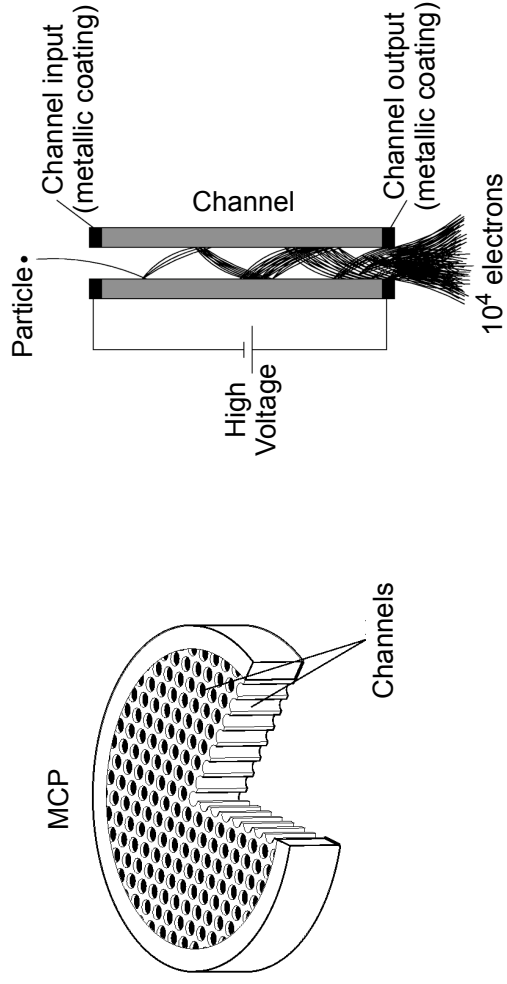


Figure A.1: On the left side: sketch of a MCP (not in scale). On the right side: section of a channel of the MCP and illustration of the working principle.

In order to increase the amplification gain, stacks of 2 or 3 MCPs can be used. Double and triple stacks are commonly called chevron and Z-stack configuration. In order to limit ion feedback the stack is normally mounted by opposing the angles between the MCPs, as shown in figure A.2. In fact a positive ion eventually created in the channel or at the output face of the plate is accelerated toward the input face by the electric field applied across the MCP. Spurious counts can therefore be generated. By correctly orienting the angles of the channels, one prevents the ions to reach the input face of the stack, resulting in a decrease of spurious counts.

In our experiment we use a stack of 2 MCPs in chevron configuration. Each MCP has an active diameter of 7.5 cm. A chevron configuration can produce up to 10^8 electrons for a single count. In table A.1 we summarize the characteristics of the three chevron MCPs used during my PhD.

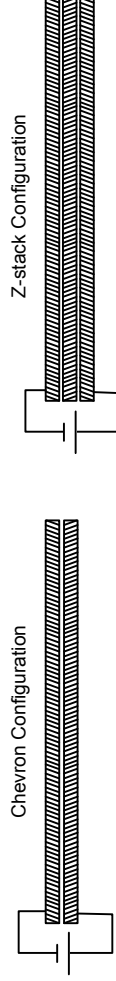


Figure A.2: Chevron and Z-Stack configurations for 2 and 3 MCPs. The orientation of the angle of the channels are inverted in order to prevent ion feedback. If the MCPs forming the stack have similar resistances a single voltage can be applied to the stack.

We note that another source of spurious counts is background gas. Therefore it is important to operate the MCP in good vacuum conditions. This has also the advantage of preventing the formation of electric arcs that can damage the detector.

Company	Burle 1	Hamamatsu	Burle 2
Channel Diameter (μm)	10	25	25
Channel Distance (μm)	12	31	32
Open Area Ratio	70%	57%	> 45%
MCP Active Diameter (cm)	7.5	7.5	7.5
Stack Thickness (mm)	1.2	2.0	3.0
Stack Resistance ($\text{M}\Omega$)	60	80	30
Voltage range (kV)	1.9 – 2.35	1.6 – 2.1	1.9 – 2.4

Table A.1: Technical specifications for the three detectors used during this thesis. The open area ratio is the ratio between the surface occupied by the channel core and that of the entire MCP.

A.2 The delay-line anode

In order to perform a time and space resolved detection of the electron pulses (and therefore of the atoms), electrons going out of the MCP have to be detected. Various detection scheme can be used, such as phosphor screens or charge division devices (resistive anode and delay-line). A comparison between the different kinds has been drawn in the thesis of M. Schellekens [44]. Our choice has gone to a delay-line anode commercially distributed and designed by Roentdek Handels GmbH. We use the model DLD80.

A.2.1 Working principle

The working principle of the delay-line anode is shown in figure A.3. A delay-line is a transmission line over which the electrons going out of the MCP are collected. The electronic pulse is divided into two parts, propagating towards the edges of the delay-line. The arrival time of the two pulses at the two edges can be measured. By knowing the propagation speed of the signal on the line and the line length we can infer the position of the atoms on the line.

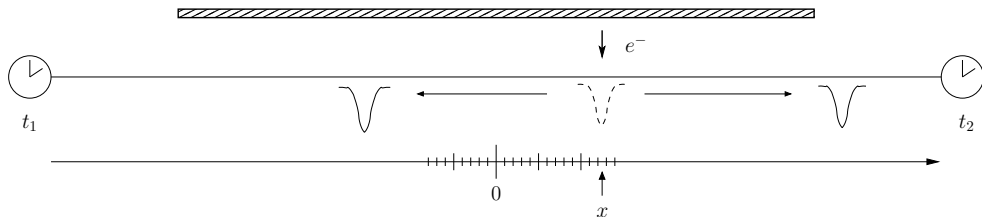


Figure A.3: Delay-line working principle. The electronic pulse at the output of the MCP is collected on the delay-line and is divided in two part, each propagating towards one of the edge of the line. The arrival time of the pulses at the edge of the line can be measured and the initial position of the electron cloud on the line can be measured.

If we consider a line oriented along the x direction, the arrival time of the pulses at the line edge will be given by:

$$t_1 = t_0 + (L/2 + x)/v_L \quad \text{and} \quad t_2 = t_0 + (L/2 - x)/v_L \quad (\text{A.1})$$

where t_0 is the arrival time of the pulse on the line, L is the line length and v_L is the propagation speed of the pulse on the line. The two equations above allow one to calculate the position x of the pulse on the line and its arrival time t_0 on the line (i.e. the arrival time of the particle on the MCP) by measuring t_1 and t_2 . By disposing of two transmission lines, one along the x direction and the other along the y direction, we know the position of the particle on the xy plane and its arrival time on the MCP, that can be converted in a vertical position (see section 1.4.4).

This simple description of the process hides a problem that has to be overcome in the real life. In fact, the propagation speed is of the order of $v_L = c/3$. The time resolution is normally of the order of 200 ps, that translates in a pixel size of 2 cm, definitely too large to perform a precise measurement of the initial position of the particle (our MCP has a diameter of 8 cm and a condensate falling on the MCP has the size of a 2 euros coin).

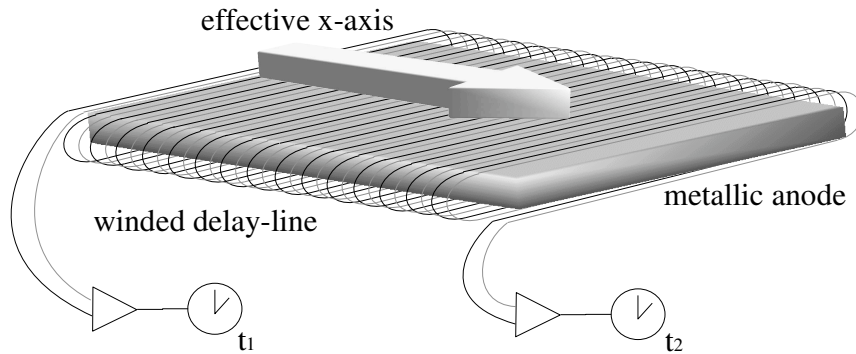


Figure A.4: In order to increase the number of pixels, the propagation speed of the electronic pulse on the delay-line is decreased by winding the line around a metallic plate. The measurement axis becomes the winding axis and the number of pixels along this axis is increased by the number of windings.

A simple way to solve this problem is to wind the delay-line, as illustrated in figure A.4. The delay-line is wound 100 times around a metallic anode. The effective speed of the pulse along the winding axis is therefore artificially reduced by a factor of 100. The winding axis is the effective measurement axis and the pixel size is artificially reduced by the same factor.

In order to measure the position of the atoms in the other direction on the xy plane a second wire is put between the first wire and the anode and is wound in a direction perpendicular to the first one.

The experimental assembly of our detector is shown in figure A.5. The detector (MCP stack plus delay-lines) is mounted on a CF160 flange. The MCP is on the top

of the frame, just above the delay-lines. The delay-lines are shown in the picture on the right side of the figure. The delay lines are at a positive voltage with respect to the rear face of the MCP in order to attract the electron shower. The applied voltages influences the detector resolution and efficiency, as it has been studied in [44].

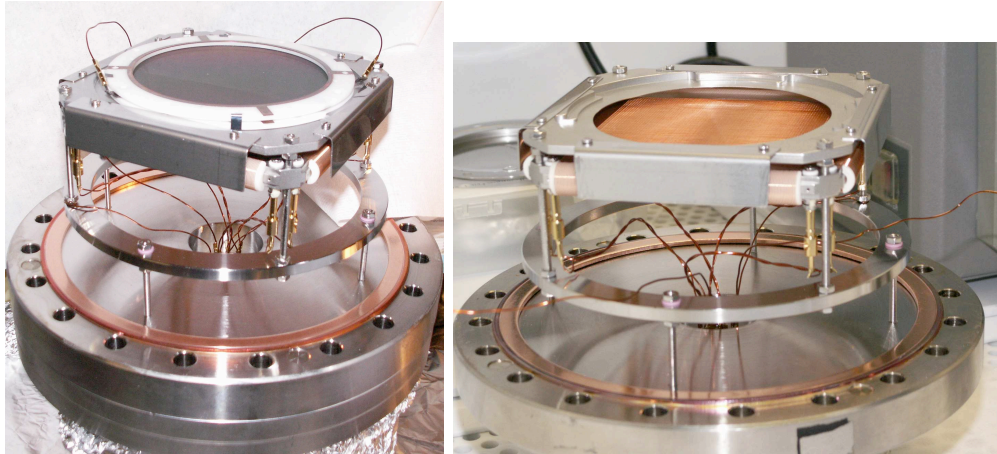


Figure A.5: On the left side: MCP detector with delay-line anode assembly. On the right side: the delay-lines are shown. The MCP has been removed from the mount.

A.2.2 Electronic chain

In order to measure the arrival time of the electronic pulses two methods can be used. The pulses at the edge of the delay lines can be visualized and registered on an oscilloscope. Several informations can be extracted, such as the pulse arrival time, shape, duration and height. However the use of an oscilloscope proves to be particularly expensive in terms of network bandwidth, storage space and computing power. Strictly speaking, the arrival times are the only data required to reconstruct the atom position and therefore we decided to use another method to measure the arrival time. This is based on the use of a Constant Fraction Discriminator (CFD) and a Time to Digital Converter (TDC) that convert the analog signal associated to each pulse as it arrives at the edge of the delay-line into a logic signal, that is written onto a memory. A scheme of the electronic chain is shown in figure A.6. It is important to note that the four signals arriving at the edges of the delay-lines are treated in parallel. Each channel has a CFD and a TDC that are independent on the other channels. The signal is first of all amplified and processed by a CFD. The CFD associates a NIM signal to each pulse. The leading edge of the NIM signal coincides with the time at which the signal at the input of the CFD goes above a given threshold. This threshold is fixed to a given fraction of the height of the pulse being processed. This fraction is fixed by the CFD and is the same for all the pulses. The amplifiers and the CFDs that we use are produced commercially by Roentdek (model DLATR6).

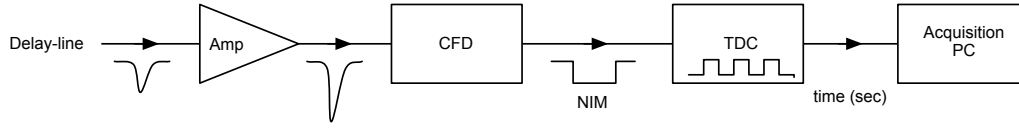


Figure A.6: Sketch of the electronic chain used to measure the arrival time of the electronic pulses at the edge of the delay-line. The pulses are first of all amplified, then the signal is processed by a Constant Fraction Discriminator (CFD), that associates a NIM signal to each pulse. The Time to Digital Converter (TDC) measures the arrival time of the NIM signal by comparing it with a clock.

The NIM signals are then sent to the TDC. The TDC is mainly a counter that compares the arrival time of a logical input pulse with a clock. The coding step of the TDC fixes the time resolution of the pulses and therefore the number of pixels on the xy plane of the detector. The output of the TDC is the arrival time of each pulse. During this thesis we used two different TDCs. The first one had been developed by the Institut de Physique Nucléaire in Orsay and has a coding step of 400 ps. This corresponds to about 400×400 pixels on the xy plane (the pixel size is $200 \mu\text{m}$). It has been used for the first experiment on pair correlation described in this thesis. The second TDC has been developed by the company IsiTech, a spin-off of Paris-Sud University and has a coding step of 275 ps. This corresponds to 600×600 pixels on the xy plane (the pixel size is $133 \mu\text{m}$). This TDC has been used for the Amsterdam data campaign and for the second generation of the pairs experiment. Even if this TDC has a smaller coding step than the first one, we were quite disappointed in discovering that the detector resolution wasn't better than with the first TDC. The only advantage of this TDC with respect to the other one is that, due to the different acquisition and storage protocol used, it accepts a larger input flux.

A.2.3 Determination of the position of the atoms in 3D

When the arrival time of the electronic pulses is recorded on the acquisition computer, we have to process the data in order to determine to which atom the detected pulse belongs. In addition we have to exclude signals coming from technical noise. Therefore a software data treatment is necessary in order to perform these operations and finally reconstruct the position of the atoms in three dimensions. A detailed description of the methods that we use can be found in [44], [82]. With these methods we can reconstruct up to 90% of the atoms, depending on the quality of the MCP and on the noise.

Once we determined which are the four time signals t_{x1} , t_{x2} , t_{y1} , t_{y2} that belong to the same atom, the following simple relations allow us to infer the position of the atom in the xy plane and its arrival time t on the MCP:

$$x = \frac{1}{2}(t_{x1} - t_{x2}) \times v_{eff}$$

$$y = \frac{1}{2}(t_{y1} - t_{y2}) \times v_{eff}$$

$$\begin{aligned}
 t &= \frac{1}{2} \left(t_{x1} + t_{x2} - \frac{L_x}{v_{eff}} \right) \\
 t &= \frac{1}{2} \left(t_{y1} + t_{y2} - \frac{L_y}{v_{eff}} \right)
 \end{aligned} \tag{A.2}$$

where L_x and L_y are the length of the x and y delay-line respectively. The quantity v_{eff} is the effective velocity of the pulses along the delay-line winding axis and it is equal to 0.98mm/ns for our delay-line anode (with an accuracy of 5%). The first and the second equations above allow one to calculate the position of the atom in the xy plane. The third and the fourth ones are equivalent and allow one to calculate the arrival time of the atom on the detector. It is interesting to note that, since we have four equations and three variables, we can determine x , y and t even if we know only three of the four arrival times t_{x1} , t_{x2} , t_{y1} , t_{y2} . However, since we really want to be sure that the reconstructed particle corresponds to a real atom falling on the detector we do not consider this situation.

A.3 Detector characteristics

A.3.1 Pulse-height distribution

As we said above, the electronic pulses at the edge of the delay-lines are first of all amplified. The DLATR6 module allows us to visualize the pulses at the output of each amplifier. The amplified pulses can therefore be visualized with an oscilloscope and their shape can be studied.

For our detector the typical pulse length is of the order of 10 ns. The height is strongly dependent on the number of electrons emitted in the amplification process and depends on the high voltage applied across the MCPs. We can distinguish between two amplification regimes. The pulse height distribution associated to each regime is sketched in figure A.7. When the voltage is in the low range (typically between

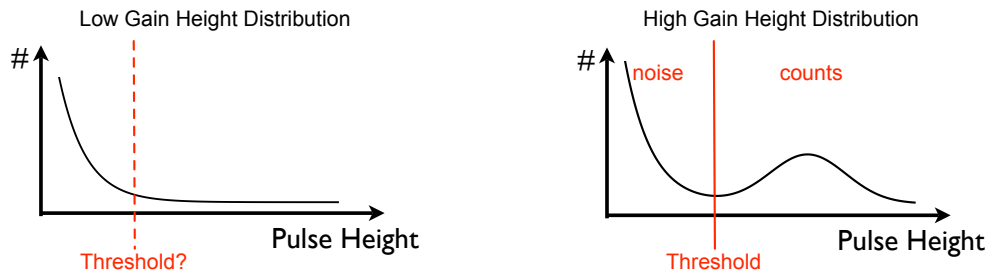


Figure A.7: Pulse height distribution for a chevron MCP working in the low gain region and in the high gain region. At low gain the amplitude distribution is exponential and cannot be distinguished from the background noise. When the gain saturates a double structure appears in the amplitude distribution and it is possible to discriminate between real counts and noise.

1600 V and 1900 V for the Hamamatsu MCP and between 1900 V and 2100 V for the Burle detectors) the amplification gain is low and the amplitude distribution of the electronic pulses is exponential (see left side of figure A.7). In this regime it is impossible to distinguish between pulses generated by real particles and the residual electronic noise. On the other hand, when the voltage is in the high range (for the Hamamatsu detector between 1900 V and 2100 V and for the Burle MCP between 2100 V and 2300 V) the amplification enters the saturated regime (right side of figure A.7). The electronic density inside the channel of the MCP is higher than in the non saturated case and the static electric potential is screened by the electron cloud itself. This has the effect of reducing the amplification and the number of electrons going out of the channels saturates around a value that depends on the characteristics of the MCP. In the pulse height distribution we will therefore distinguish two peaks: one at low amplitudes that shows an exponential decay and is mostly due to electronic noise, one at high amplitudes, bell-shaped, due to real counts. In this regime it is therefore possible to fix a threshold in order to discriminate between noise and real counts. For this reason, particle counting is performed in this regime.

In figure A.8 we show the pulse height distribution obtained for the three detectors used during this PhD thesis. The pulse height distribution have been acquired when the detector was working in the saturated gain regime. The pulse height distribution shows an evident double structure for the two Burle MCPs, while the double structure is much less evident for the Hamamatsu MCP. The threshold that discriminates between real counts and noise was set in the three cases around 50 mV.

A.3.2 Flux saturation

Several times in this thesis we pointed out that our detector saturates when the flux of detected particles is high, such as for example when we detect a cold cloud below or above the condensation threshold. This is due to the fact that the detection of a particle influences the detection of the following particle. In fact, the channel that has been used for the first detection shows an electronic depletion. This depletion is compensated by a strip current, that is normally very low (of the order of μA) because of the high resistance of the MCPs stack ¹. The amplitude of the pulse generated by the second detected particle will be smaller than the amplitude of the first one and eventually smaller than the threshold used to discriminate real counts and noise. Therefore the second particle will eventually not be detected.

During the first year of my PhD, M. Schellekens and I tried to quantify this effect. We measured how the pulse height distribution changes during the detection of a time-of-flight of a ^4He cloud at 1.6 μK . The data are reported in figure A.9. The detector is operated in counting mode, at 2.35 kV. We report on the same graph the particle rate averaged over the whole detector as a function of time, and the averaged pulse height as a function of time. We can clearly see that the pulse height distribution

¹The resistance of the MCP can be reduced by using special coatings. However a reduction of the resistance is limited by an eventual heating of the MCP (that would make the value of the resistance not stable with time) and by the use of high power high voltage supplies.

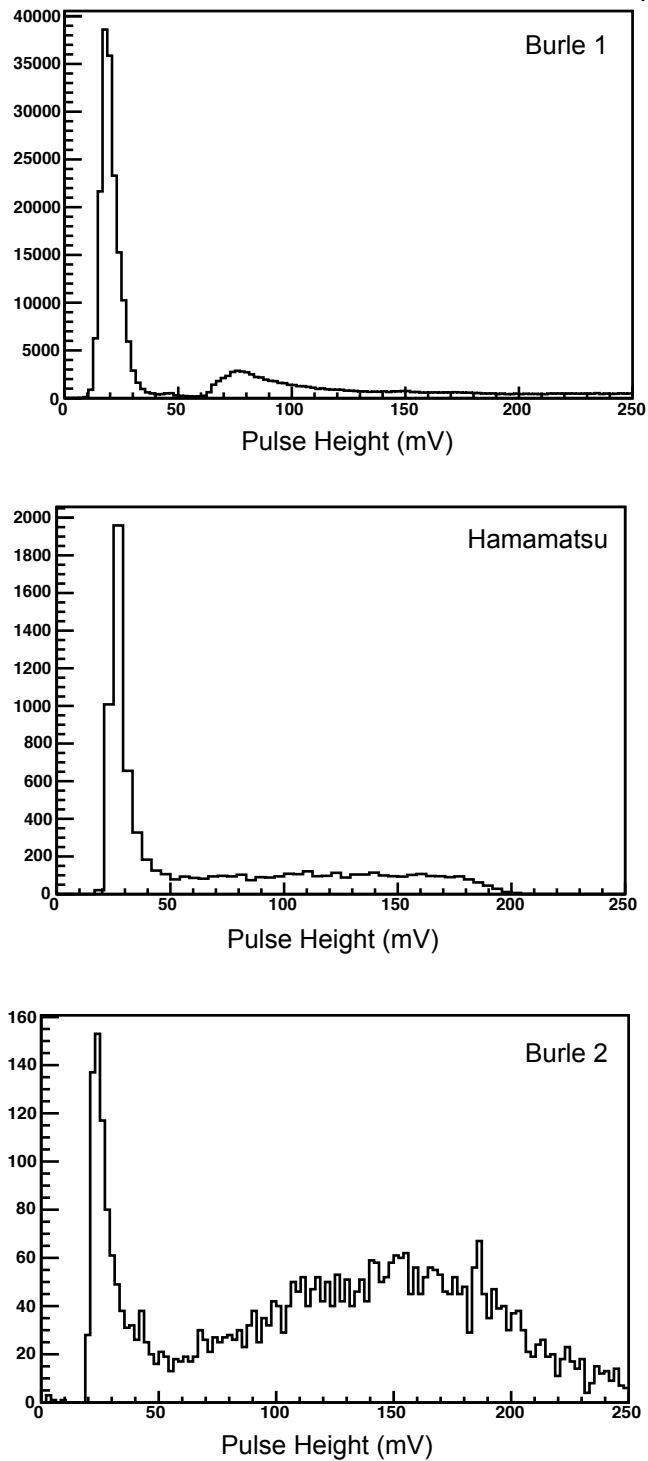


Figure A.8: Pulse height distribution for the three MCPs used during this thesis. The pulse height has been measured in the high gain region (at 2350 V for “Burle 1”, 2100 V for “Hamamatsu”, 2400 V for “Burle 2”). The two Burle MCPs clearly show a double structure, while this is less evident for the Hamamatsu. The vertical scale is not the same for the three graphs.

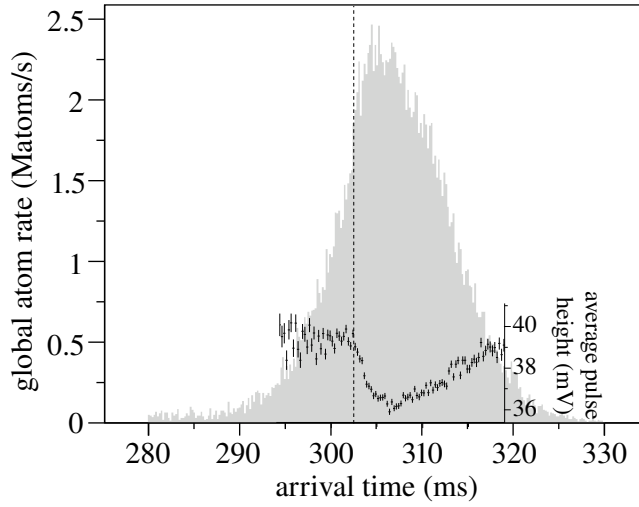


Figure A.9: Measurement of the saturation of the detector. This measurement has been performed on the detector referred as “Burle 1”. We report the time-of-flight of a ^4He cloud at $1.6 \mu\text{K}$ together with the variation of the averaged pulse height. We note a clear drop in the pulse height when the flux of detected atoms reaches 1.7 ± 0.2 Matoms/s. This corresponds to a detected particle rate of 82 ± 10 katoms/cm 2 /s.

drops when the global particle rate goes over 1.7 ± 0.2 Matoms/s. At this temperature this corresponds to a maximum particle rate of 82 ± 10 katoms/cm 2 /s. We observe a reestablishment of the pulse height after 10 – 15 ms. This gives an upper bound for the saturation time constant, since electrons are still being emitted as atoms continue to fall on the plate. Furthermore we note that the time-of-flight is not symmetric with respect to the mean arrival time (estimated to be 308.3 ms), as we would expect for an ultracold cloud following the Maxwell-Boltzmann distribution. This distortion can be attributed to the saturation as well. In fact, when the pulse height drops, the number of atoms being effectively detected decreases in a way that depends on the saturation time constant discussed above.

A.3.3 Background noise

The three MCPs used in this thesis have a different background noise.

“Burle 1” had a very large dark count, up to 1300 counts/s at 2300 V. This noise was spatially very well localized in some hot spots on the edge of the MCP (an image can be found in [44]). These hot spots could easily be excluded from the data.

The Hamamatsu and “Burle 2” showed a very small dark count. It is 40 counts/s at 2100 V for the Hamamatsu MCP, and 100 counts/s at 2350 V for the “Burle 2” MCP. The dark count per unit surface is smaller than 0.5 counts/cm 2 /s. This is negligible with respect to the mean number of counts detected in a cold cloud at around $1 \mu\text{K}$, typically larger than 24 kcounts/cm 2 /s.

The dark count is much higher when the MCPs have just been put under vacuum and lowers progressively with the operation time. It can be due to particles that are trapped inside the channels and that can start an electron avalanche. They disappear as the gas is pumped away. In addition, the fact that the MCP slightly heats up when it is on, contributes to degassing the channels, speeding up the decrease of the dark count.

A.3.4 Detection homogeneity

In order to study the gain map of the detector, we drop onto it an homogeneous flux of atoms, such as the one obtained from a magneto-optical trap. By comparing the number of atoms detected on the different regions of the MCP, we can compare their gain. In figure A.10 we report the gain map of our three detectors, acquired at 2350 V for “Burle 1” and “Burle 2”, and at 2100 V for “Hamamatsu”. In order to compare the three gain maps we normalized the number of counts in each pixel n_i by the mean number of counts per pixel $(\sum n_i)/N$, where N is the number of pixels. The three maps show a higher gain in the central region and gain fluctuations up to 50%. The “Burle 1” presents several zones with a gain close to zero, near to the edges of the MCP.

We experimentally observed that the gain map depends a lot on the mechanical stress imposed on the MCP by its mount. By changing the position of the clamps that hold the MCP it was possible to observe a zone with gain close to zero appear near to the centre of the MCP. This behavior of the gain was more evident for “Burle 1” than for the other two detectors, probably because of the reduced thickness of this MCP with respect to the other two (see table A.1).

Hamamatsu and Burle (Photonis) propose several detection qualities and coatings in order to have a more performing detector. The three MCPs used during this thesis were of the lowest available quality. In the future the purchase of a better quality detector could be interesting in order to increase the actual performances.

A.3.5 Detection efficiency

As we pointed out several times in this thesis, the detection efficiency is a crucial parameter from which depends the understanding and the improvement of a good number of our experimental observations (such as for example, in the correlated pairs experiment, number difference squeezing, height of the back to back correlation function, determination of the number of atoms in the sphere, etc...). In order to precisely measure it, we should have an independent, calibrated, detection system with which compare the number of atoms detected on our detector. This kind of measurement has been done during the collaboration with the group of W. Vassen. In fact, they have two detection systems: a MCP and an absorption imaging system. Few years before our collaboration, they used the absorption imaging system to calibrate the MCP that they use to detect their clouds. During our collaboration we could compare the number of atoms detected on their MCP with the number of atoms detected on ours. This comparison allowed us to estimate the detection efficiency of our detector to be $\simeq 11\%$.

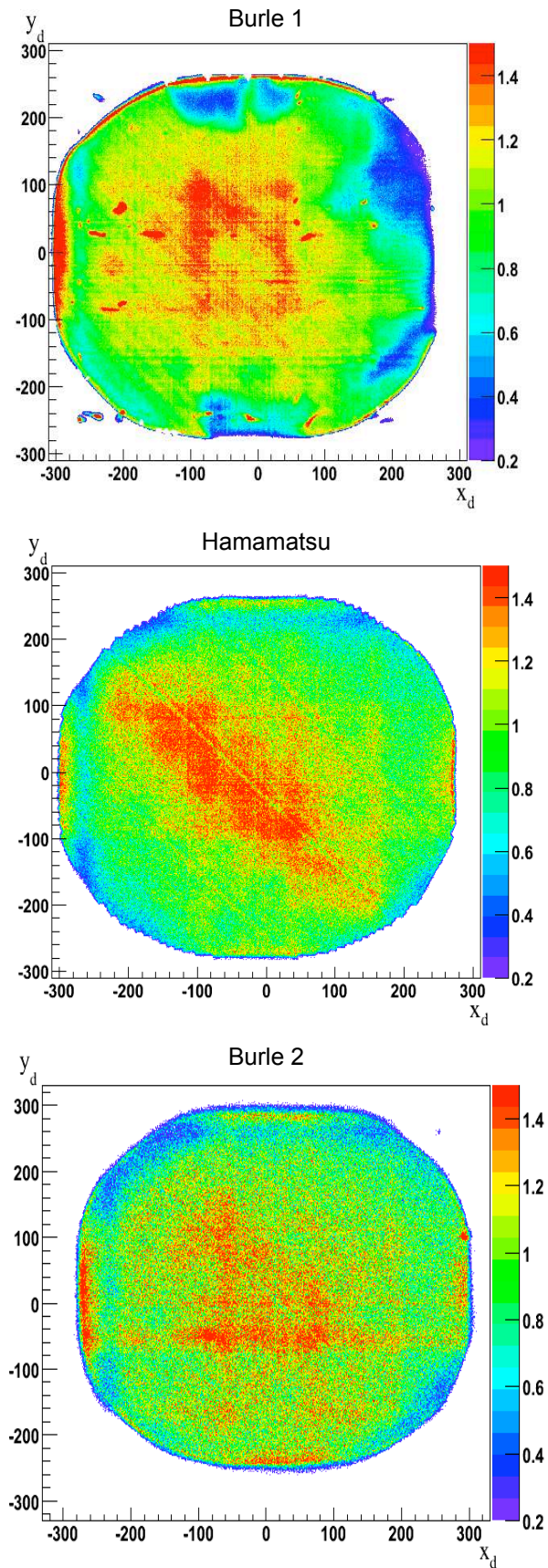


Figure A.10: Gain maps of the three MCPs used during this thesis. The number of atoms per pixel has been divided by the average number of counts per pixel in order to make a comparison among the three maps. The “Burle 1” gain map has been acquired in Amsterdam at 2350 V. The Hamamatsu gain map has been acquired at 2100 V and the “Burle 2” gain map has been acquired at 2350 V.

This estimation has been done on the “Burle1” detector and is a measurement of the global detection efficiency. It is important to note that this measurement only gives an order of magnitude. In fact we know that the MCP detection efficiency decreases with time. Therefore it is possible that the detection efficiency of the Amsterdam MCP at the moment of the comparison with ours wasn’t the same as the one measured few years before with the camera. In addition, the fact that mechanical stress makes the gain map change, can affect a global measurement of the detection efficiency. A more reliable measurement would have been the direct calibration of our MCP with their imaging system. Unfortunately, when we started our collaboration, they had to remove the imaging system in order to install our detector.

The implementation of an absorption imaging system on the Palaiseau setup is planned. It would provide a second diagnostic tool and it would allow us to calibrate the MCP gain and eventually to monitor changes as a function of time.

A way to improve the detection efficiency

In section 5.1.2 we pointed out that the higher the detection efficiency, the easier the measurement of the number difference squeezing is. Therefore we decided to try to increase the detection efficiency by installing a grid above the MCP. Good results obtained with this method have been reported with ions in [137] and have also been observed with metastable Neon atoms in the group of G. Birkl (private communication). The idea is illustrated in figure A.11. Since the open area ratio (i.e. the ratio between

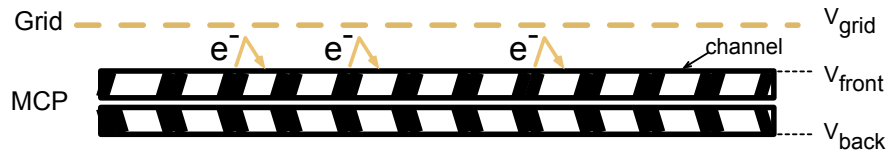


Figure A.11: Scheme used to increase the detection efficiency of the MCP. A grid is installed in front of the MCP. The voltage applied to the grid is negative with respect to the voltage applied on the front face of the MCP ($V_{grid} < V_{front} < V_{back}$). A particle falling in a region between two channels can extract an electron from the surface of the MCP. The electron is pushed inside the closest channel by the electric field create between the grid and the front face of the MCP and eventually start an avalanche process. In this way the particle is detected.

the surface covered with channels and the total MCP surface) is only 60%, one can ask what happens to the atoms that instead of hitting the channel wall, hit a zone between two channels. An electron can be extracted, as a result of the collision, but, since it is not amplified, the atom cannot be detected. In order to amplify these electrons one can create an electric field above the MCP to push the electrons inside the closest channel. They will have a non zero probability to start an electron avalanche inside the channel and therefore there is a non zero probability for the particle to be detected. Such an electric field can be generated by putting a grid above the front face of the MCP. The grid must be negatively charged with respect to the front face of the MCP in order to

repulse the electrons. During her Master stage, M. Bonneau studied the problem by numerically simulating the electric field generated by the grid and she estimated a gain of a factor 1.2 to 2 in the detection efficiency [138].

The grid that we installed above the MCP has a transmission efficiency of 85%, the hole size is $200 \times 200 \mu\text{m}$, the thickness is $4 \mu\text{m}$ and it is installed over the entire MCP active surface at a distance of $5 - 8 \text{ mm}$ from the MCP. In order to test the effect of the grid on the detection efficiency we drop on the detector the atoms loaded in a magneto-optical trap and we observe how the number of detected atoms changes as a function of the voltage applied on the grid. We repeated the experiment for two different voltages applied across the MCP: 1.6 kV and 1.9 kV. The MCP used is the ‘‘Hamamatsu’’. At a voltage of 1.6 kV it works in the low gain region and at 1.9 kV it enters the saturated gain region. The plot of the detected atom number as a function of the grid voltage has been reported in figure A.12. As shown in the figure, the detection

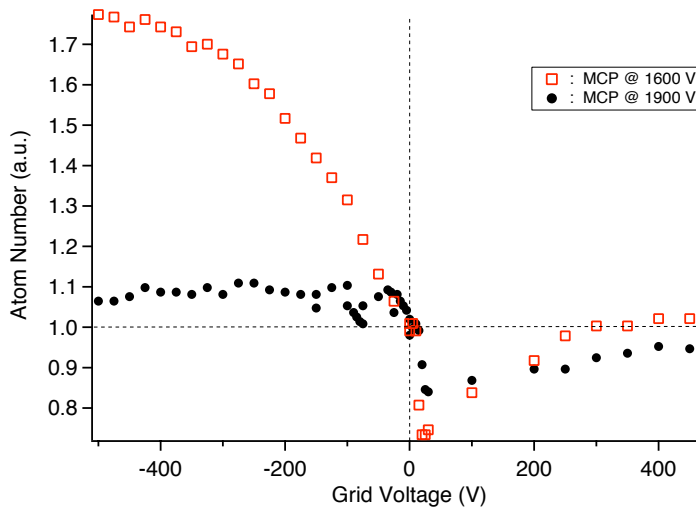


Figure A.12: Detected atom number as a function of the voltage applied to the grid. The graph has been plot for two different voltages applied across the MCP. At 1.6 kV the MCP is in the low gain region, while at 1.9 kV it is in the saturated gain region. The number of detected atoms has been normalized by the number of atoms detected when the voltage applied on the grid is zero. To have an order of magnitude in mind, the number of atoms detected at 1.9 kV is ≈ 70 times larger than the number of atoms detected at 1.6 kV when the grid is at 0 V.

efficiency increases only when the voltage applied across the MCP is low, while at high voltage the detection efficiency stays almost constant. Since all our experiments are performed in counting mode (i.e. in the saturated region gain), the fact that at 1.9 kV the grid has no effect is quite disappointing. We didn’t really understand why the grid didn’t give the expected results. A possible explanation can be found if one think of the electric field experienced by the electrons inside the channel when a voltage is applied on the grid. The electric field inside the channel is perturbed by the potential applied on the grid. Since $V_{grid} < V_{MCP_{Front}} < V_{MCP_{back}}$, when the grid is at a negative

voltage, the electric field inside the channels is larger than when the grid is at zero. This has the effect to increase the amplification gain. Therefore the increase of the number of detected atoms can be due to the fact that the mean pulse height at the output of the MCP is larger and that therefore a larger number of pulses is detected. This effect is large only when the gain is not saturated yet, while it is small when the gain is saturated. If this explanation is true, either the number of electrons ejected when a metastable hits the region between two channels is ridiculous, or these electrons have not enough energy to start an avalanche process.

We would have liked to study this process in more details, for example by studying the pulse height distribution. Unfortunately, for an unknown reason, the grid introduced a large noise on the detector that made any further measurement impossible. We therefore decided to remove the grid.

A.3.6 Detector resolution

One of the methods that can be used to measure the resolution of our detector consists in putting a mask with a defined pattern in front of the detector and measure how well the pattern is imaged. The mask has to be easy to remove, if one wants to measure the resolution several times. In our case this procedure is time demanding since the mask needs to be inside the vacuum chamber. For this reason we use another method to measure the resolution, based on an algorithm that combines the signals coming out from the delay-lines when a cloud falls on the detector.

As we have seen above (equations A.2), the position of the atom along the x axis is given by $\frac{1}{2}(t_{x1} - t_{x2}) \times v_{eff}$ and by $\frac{1}{2}(t_{y1} - t_{y2}) \times v_{eff}$ along the y axis. The resolution is the precision of the measurement of the x and y positions and therefore on the four times t_{x1} , t_{x2} , t_{y1} , t_{y2} . In order to measure it we proceed as follows. For each pixel of the detector and for each shot we calculate:

$$Sum = [(t_{x1} + t_{x2}) - (t_{y1} + t_{y2})] - \langle [(t_{x1} + t_{x2}) - (t_{y1} + t_{y2})] \rangle_N \quad (\text{A.3})$$

where $\langle \rangle_N$ indicates the average over N shots. If our resolution was arbitrarily good, the distribution of Sum would be a Dirac delta centered on 0. Unfortunately the distribution is not a Dirac delta, but it has a finite width, because the value of Sum for a given position (x, y) changes from a realization to another. The standard deviation of the distribution of Sum over M realizations is related to the resolution in the following way:

$$\begin{aligned} \sigma_{Sum}^2 &= \langle Sum^2 \rangle_M - \langle Sum \rangle_M^2 \\ &= \langle Sum^2 \rangle_M \\ &= \langle [(t_{x1} + t_{x2}) - (t_{y1} + t_{y2})]^2 \rangle_M - \langle (t_{x1} + t_{x2}) - (t_{y1} + t_{y2}) \rangle_M^2 \\ &= \sigma_{t_{x1}}^2 + \sigma_{t_{x2}}^2 + \sigma_{t_{y1}}^2 + \sigma_{t_{y2}}^2 \end{aligned} \quad (\text{A.4})$$

In the last passage we supposed the four variables to be independent. This assumption is reasonable because the electronic chains that are used to measure them are different (there is an amplifier, a CFD and a TDC for each signal).

As long as the physical process that generates the four signals is the same, we can suppose that the four variables follow the same distribution and write $\sigma_{t_{x1}} = \sigma_{t_{x2}} = \sigma_{t_{y1}} = \sigma_{t_{y2}}$. This leads to:

$$\sigma_{Sum}^2 = 4\sigma_{t_{x1}}^2. \quad (\text{A.5})$$

Since the RMS single particle resolution on the x direction is $d_x = \sqrt{\sigma_{t_{x1}}^2 + \sigma_{t_{x2}}^2}$, then :

$$d_x = \frac{1}{\sqrt{2}}\sigma_{Sum} \quad (\text{A.6})$$

and the same on the y direction.

Since σ_{Sum} can be measured for any pixel (x,y) , i.e. for any t_{xi}, t_{yi} , this method give access to a measurement of the local resolution and to the resolution averaged over all the detector. The typical values for our detectors are 250 – 300 μm on the xy plane and 0.7 ns on the vertical axis (this translates in a spatial resolution on the vertical axis of ≈ 3 nm).

The study of the local resolution showed that for the “Burle 1” MCP there is a correlation between the detector efficiency and the resolution. Zones with a poor detectivity show a bad resolution, while zones with a good detectivity show a better resolution [82]. For the resolution map of the other two MCPs this correlation is less evident.

A.4 Influence of the resolution on the correlation function

As we pointed out in section 1.4.5, the detector resolution influences the correlation function. The measured correlation function is the convolution between the detector resolution and the correlation function obtained with an arbitrarily good detector. Therefore, a good knowledge of the resolution is crucial for our measurements.

In figure A.13 we show the distribution of $Sum/\sqrt{2}$ averaged over all the detector for the “Burle 1” MCP. This distribution has been obtained on a set of data acquired in Amsterdam. On the left side of figure A.13 the distribution has been fitted with a Gaussian (solid line).

In fact, a careful examination reveals that the resolution function of our detector is not well approximated by a Gaussian because the wings are too broad. A Gaussian fit leaves about 7% of the area of the distribution out of the fit curve. A possibility would have been to try with a Lorentzian function. However, since the correlation function has a Gaussian shape, the convolution with the detector resolution is much simpler if we approximate the resolution function with the sum of three Gaussian. The three Gaussian are centered on zero, have amplitude A_i and standard deviation w_i (with $i = 1, 2, 3$). The fit made with the sum of three Gaussians is shown in figure A.13, on the right (solid line). We proceeded to the fit by first fitting the wings of the distribution with a Gaussian of amplitude A_3 and width w_3 . Then we fitted the wings plus a more central part of the distribution with the sum of two Gaussians, one with fixed parameters A_3 and w_3 and a second one of parameters A_2 and w_2 . Finally we

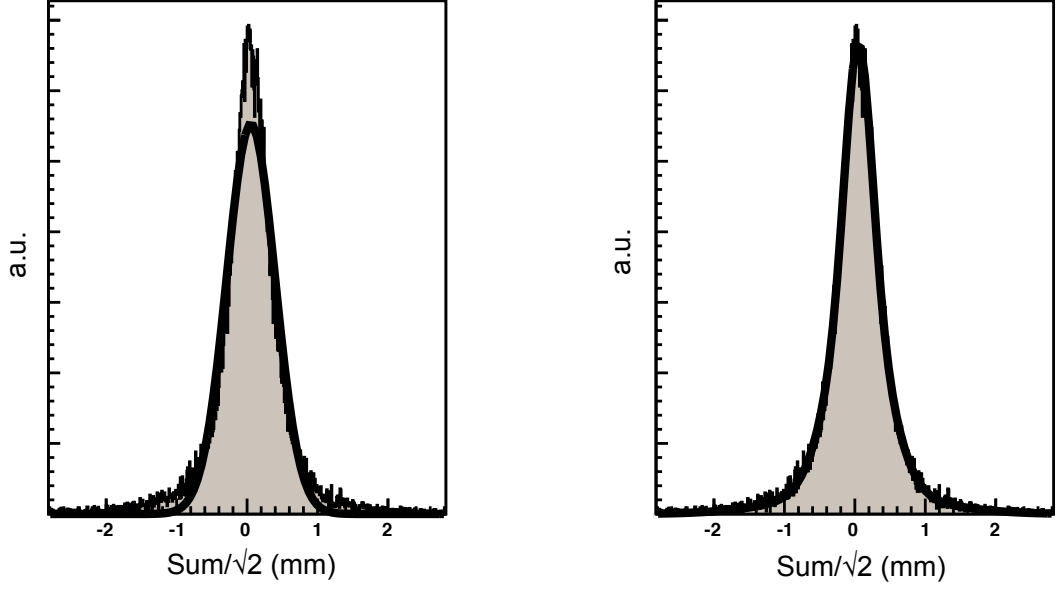


Figure A.13: Plot of the distribution of $Sum/\sqrt{2}$ over all the detector. On the left we show the distribution fitted with a Gaussian. On the right the fit is made with the sum of three Gaussians.

fitted the entire distribution by the sum of three Gaussians, two of which with fixed parameters A_2, A_3, w_2 and w_3 and the third one of parameters A_1, w_1 left free to vary.

Convolution of the correlation function with the resolution function

The convolution of the correlation function (for a cold gas of bosons or fermions as in the Amsterdam experiment) with the resolution function given by the sum of three Gaussians is:

$$g_{3Gauss}^{(2)}(\Delta x, \Delta y, \Delta z) = f_{resol} \otimes g^{(2)}(\Delta x, \Delta y, \Delta z) \quad (\text{A.7})$$

$$= 1 \pm \frac{1}{(\sum_{i=1,2,3} A_i w_i)^2} e^{-\frac{\Delta z^2}{l_z^2}} \prod_{\alpha=x,y} \sum_{i=1,2,3} \frac{A_i w_i l_\alpha}{\sqrt{2w_i^2 + l_\alpha^2}} e^{-\frac{\Delta \alpha^2}{2w_i^2 + l_\alpha^2}} \quad (\text{A.8})$$

where l_α is the correlation length already deconvoluted by the detector resolution.

The contrast of the correlation function, is therefore given by:

$$\eta = \frac{1}{(\sum_{i=1,2,3} A_i w_i)^2} \prod_{\alpha=x,y} \sum_{i=1,2,3} \frac{A_i w_i l_\alpha}{\sqrt{2w_i^2 + l_\alpha^2}} \quad (\text{A.9})$$

The correlation length along x: another method to measure the resolution

We now go back to the more simple model where the detector resolution on the xy plane is modeled by only one Gaussian with standard deviation equal to the one-particle RMS

resolution d_{xy} . In this case it is easy to show that another, independent way to measure the resolution is to measure the correlation length along the x axis. As we have shown in section 1.4.5, the convolution between the correlation function and the one-Gaussian resolution function is (equation 1.38):

$$g_{res}^{(2)}(\Delta x, \Delta y, \Delta z) = 1 - \eta \exp \left\{ -\frac{\Delta x^2}{L_x^2} - \frac{\Delta y^2}{L_y^2} - \frac{\Delta z^2}{L_z^2} \right\}$$

where η is the contrast of the correlation function which is given by (equation 1.39):

$$\eta = g_{res}^{(2)}(0, 0, 0) - 1 = - \prod_{\alpha} \sqrt{\frac{1 + d_{\alpha}^2/s_{det}^2}{1 + (2d_{\alpha})^2/l_{\alpha}^2}}$$

and L_x, L_y, L_z are the measured correlation lengths, convoluted with the detector resolution. The deconvolution gives: $l_{\alpha} = \sqrt{L_{\alpha}^2 - (2d_{\alpha})^2}$ for $\alpha = x, y, z$. In section 1.4.5 we pointed out that the expected value for l_y and l_z is of the order of $700 \mu\text{m}$, while it is of the order of $70 \mu\text{m}$ for l_x (see figure 1.16). Since the detector resolution along the z axis is negligible with respect to L_z , then $L_z \simeq l_z$. Along the y axis the resolution is small compared to the correlation length, but not negligible, therefore the deconvolution is necessary in order to measure l_y . On the other hand, the expected value of the correlation length along the x axis is much smaller (about 7 times) than $2d_x \simeq 500 \mu\text{m}$. Therefore, measuring L_x is equivalent to measure $2d_x$. In order to perform the measurement we fit the correlation on the xy plane with a two-dimensional Gaussian, having as free parameters L_x, L_y and the amplitude. The fit results for L_x are values ranging from $350 \pm 40 \mu\text{m}$ to $470 \pm 60 \mu\text{m}$, that are in reasonable agreement with the value found with the measurement of σ_{Sum} (giving $500 \mu\text{m}$) discussed at the beginning of this section.

Appendix B

Publications

Comparison of the Hanbury Brown-Twiss effect for bosons and fermions

Nature, **445** 402 (2007)

Observation of Atom Pairs in Spontaneous Four-Wave Mixing of Two Colliding Bose-Einstein Condensates

Phys. Rev. Lett., **99** 150405 (2007)

Hanbury Brown and Twiss correlations in atoms scattered from colliding condensates

Phys. Rev. A, **77** 033601 (2008)

Atomic four-wave mixing via condensate collisions

New. J. Phys., **10** 045021 (2008)

LETTERS

Comparison of the Hanbury Brown–Twiss effect for bosons and fermions

T. Jelte¹, J. M. McNamara¹, W. Hogervorst¹, W. Vassen¹, V. Krachmalnicoff², M. Schellekens², A. Perrin², H. Chang², D. Boiron², A. Aspect² & C. I. Westbrook²

Fifty years ago, Hanbury Brown and Twiss (HBT) discovered photon bunching in light emitted by a chaotic source¹, highlighting the importance of two-photon correlations² and stimulating the development of modern quantum optics³. The quantum interpretation of bunching relies on the constructive interference between amplitudes involving two indistinguishable photons, and its additive character is intimately linked to the Bose nature of photons. Advances in atom cooling and detection have led to the observation and full characterization of the atomic analogue of the HBT effect with bosonic atoms^{4–6}. By contrast, fermions should reveal an antibunching effect (a tendency to avoid each other). Antibunching of fermions is associated with destructive two-particle interference, and is related to the Pauli principle forbidding more than one identical fermion to occupy the same quantum state. Here we report an experimental comparison of the fermionic and bosonic HBT effects in the same apparatus, using two different isotopes of helium: ³He (a fermion) and ⁴He (a boson). Ordinary attractive or repulsive interactions between atoms are negligible; therefore, the contrasting bunching and antibunching behaviour that we observe can be fully attributed to the different quantum statistics of each atomic species. Our results show how atom–atom correlation measurements can be used to reveal details in the spatial density^{7,8} or momentum correlations⁹ in an atomic ensemble. They also enable the direct observation of phase effects linked to the quantum statistics of a many-body system, which may facilitate the study of more exotic situations¹⁰.

Two-particle correlation analysis is an increasingly important method for studying complex quantum phases of ultracold atoms^{7–13}. It goes back to the discovery, by Hanbury Brown and Twiss¹, that photons emitted by a chaotic (incoherent) light source tend to be bunched: the joint detection probability is enhanced, compared to that of statistically independent particles, when the two detectors are close together. Although the effect is easily understood in the context of classical wave optics¹⁴, it took some time to find a clear quantum interpretation^{3,15}. The explanation relies on interference between the quantum amplitude for two particles, emitted from two source points S_1 and S_2 , to be detected at two detection points D_1 and D_2 (see Fig. 1). For bosons, the two amplitudes $\langle D_1|S_1\rangle\langle D_2|S_2\rangle$ and $\langle D_1|S_2\rangle\langle D_2|S_1\rangle$ must be added, which yields a factor of 2 excess in the joint detection probability, if the two amplitudes have the same phase. The sum over all pairs (S_1, S_2) of source points washes out the interference, unless the distance between the detectors is small enough that the phase difference between the amplitudes is less than one radian, or equivalently if the two detectors are separated by a distance less than the coherence length. Study of the joint detection rates versus detector separation along the i direction then

reveals a ‘bump’ whose width l_i is the coherence length along that axis^{1,5,16–19}. For a source size s_i (defined as the half width at $e^{-1/2}$ of a gaussian density profile) along the i direction, the bump has a half width at e^{-1} of $l_i = ht/(2\pi ms_i)$, where m is the mass of the particle, t the time of flight from the source to the detector, and h Planck’s constant. This formula is the analogue of the formula $l_i = L\lambda/(2\pi s_i)$ for photons, if $\lambda = h/(mv)$ is identified with the de Broglie wavelength for particles travelling at velocity $v = L/t$ from the source to the detector.

For indistinguishable fermions, the two-body wavefunction is antisymmetric, and the two amplitudes must be subtracted, yielding a null probability for joint detection in the same coherence volume. In the language of particles, it means that two fermions cannot have momenta and positions belonging to the same elementary cell of

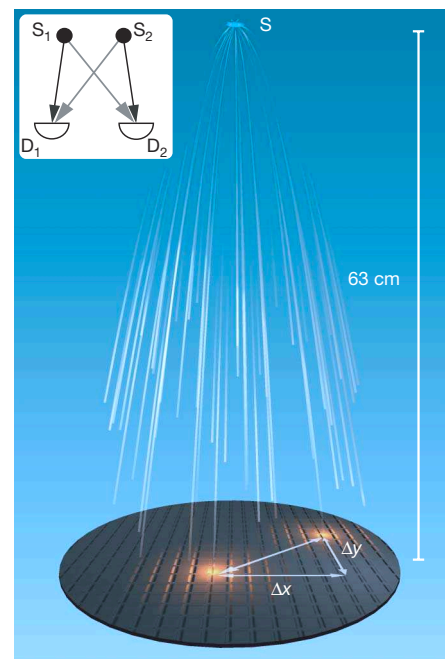


Figure 1 | The experimental set-up. A cold cloud of metastable helium atoms is released at the switch-off of a magnetic trap. The cloud expands and falls under the effect of gravity onto a time-resolved and position-sensitive detector (microchannel plate and delay-line anode) that detects single atoms. The horizontal components of the pair separation Δr are denoted Δx and Δy . The inset shows conceptually the two 2-particle amplitudes (in black or grey) that interfere to give bunching or antibunching: S_1 and S_2 refer to the initial positions of two identical atoms jointly detected at D_1 and D_2 .

¹Laser Centre Vrije Universiteit, De Boelelaan 1081, 1081 HV Amsterdam, The Netherlands. ²Laboratoire Charles Fabry de l’Institut d’Optique, CNRS, Univ. Paris-sud, Campus Polytechnique RD 128, 91127 Palaiseau Cedex, France.

phase space. As a result, for fermions the joint detection rate versus detector separation is expected to exhibit a dip around the null separation. Such a dip for a fermion ensemble must not be confused with the antibunching dip that one can observe with a single particle (boson or fermion) quantum state—for example, resonance fluorescence photons emitted by an individual quantum emitter²⁰. In contrast to the HBT effect for bosons, the fermion analogue cannot be interpreted by any classical model, either wave or particle, and extensive efforts have been directed towards an experimental demonstration. Experiments have been performed with electrons in solids^{21,22} and in a free beam²³, and with a beam of neutrons²⁴, but none has allowed a detailed study and a comparison of the pure fermionic and bosonic HBT effects for an ideal gas. A recent experiment using fermions in an optical lattice²⁵, however, does permit such a study and is closely related to our work.

Here we present an experiment in which we study the fermionic HBT effect for a sample of polarized, metastable $^3\text{He}^*$ atoms ($^3\text{He}^*$), and we compare it to the bosonic HBT effect for a sample of polarized, but not Bose condensed, metastable $^4\text{He}^*$ atoms ($^4\text{He}^*$) produced in the same apparatus at the same temperature. We have combined the position- and time-resolved detector, previously used^{5,26} for $^4\text{He}^*$, with an apparatus with which ultracold samples of $^3\text{He}^*$ or $^4\text{He}^*$ have recently been produced²⁷. Fermions or bosons at thermal equilibrium in a magnetic trap are released onto the detector, which counts individual atoms (see Fig. 1) with an efficiency of approximately 10%. The detector allows us to construct the normalized correlation function $g^{(2)}(\Delta\mathbf{r})$, that is, the probability of joint detection at two points separated by $\Delta\mathbf{r}$, divided by the product of the single detection probabilities at each point. Statistically independent detection events result in a value of 1 for $g^{(2)}(\Delta\mathbf{r})$. A value larger than 1 indicates bunching, while a value less than 1 is evidence of antibunching.

We produce gases of pure $^3\text{He}^*$ or pure $^4\text{He}^*$ by a combination of evaporative and sympathetic cooling in an anisotropic magnetic trap (see Methods). Both isotopes are in pure magnetic substates, with nearly identical magnetic moments and therefore nearly identical trapping potentials, so that trapped non-degenerate and non-interacting samples have the same size at the same temperature. The temperatures of the samples yielding the results of Fig. 2, as measured by the spectrum of flight times to the detector, are $0.53 \pm 0.03 \mu\text{K}$ and $0.52 \pm 0.05 \mu\text{K}$ for $^3\text{He}^*$ and $^4\text{He}^*$, respectively. The uncertainties correspond to the standard deviation of each ensemble. In a single realization, we typically produce 7×10^4 atoms of both $^3\text{He}^*$ and $^4\text{He}^*$. The atom number permits an estimate of the Fermi and Bose–Einstein condensation temperatures of approximately $0.9 \mu\text{K}$ and $0.4 \mu\text{K}$, respectively. Consequently, Fermi pressure in the trapped $^3\text{He}^*$ sample has a negligible (3%) effect on the trap size, and repulsive interactions in the $^4\text{He}^*$ sample have a similarly small effect. The trapped samples are therefore approximately gaussian ellipsoids elongated along the x axis with an r.m.s. size of about $110 \times 12 \times 12 \mu\text{m}^3$. To release the atoms, we turn off the current in the trapping coils and atoms fall under the influence of gravity. The detector, placed 63 cm below the trap centre (see Fig. 1), then records the x – y position and arrival time of each detected atom.

The normalized correlation functions $g^{(2)}(0,0,\Delta z)$ along the z (vertical) axis, for $^3\text{He}^*$ and $^4\text{He}^*$ gases at the same temperature, are shown in Fig. 2. Each correlation function is obtained by analysing the data from about 1,000 separate clouds for each isotope (see Methods). Results analogous to those of Fig. 2 are obtained for correlation functions along the y axis, but the resolution of the detector in the x – y plane (about $500 \mu\text{m}$ half width at e^{-1} for pair separation) broadens the signals. Along the x axis (the long axis of the trapped clouds), the expected widths of the HBT structures are one order of magnitude smaller than the resolution of the detector and are therefore not resolved.

Figure 2 shows clearly the contrasting behaviours of bosons and fermions. In both cases we observe a clear departure from statistical

independence at small separation. Around zero separation, the fermion signal is lower than unity (antibunching) while the boson signal is higher (bunching). Because the sizes of the $^3\text{He}^*$ and $^4\text{He}^*$ clouds at the same temperature are the same, as are the times of flight (pure free fall), the ratio of the correlation lengths is expected to be equal to the inverse of the mass ratio, $4/3$. The observed ratio of the correlation lengths along the z axis in the data shown is 1.3 ± 0.2 . The individual correlation lengths are also in good agreement with the formula $l_z = ht/(2\pi ms_z)$, where s_z is the source size along z . Owing to the finite resolution, the contrast in the signal, which should ideally go to 0 or 2, is reduced by a factor of order ten. The amount of contrast reduction is slightly different for bosons and fermions, and the ratio should be about 1.5. The measured ratio is 2.4 ± 0.2 . This discrepancy has several possible explanations. First, the magnetic field switch-off is not sudden (timescale ~ 1 ms), and this could affect bosons and fermions differently. Second, systematic errors may be present in our estimate of the resolution function. The resolution, however, does not affect the widths of the observed correlation functions along z , and thus we place the strongest emphasis on this ratio as a test of our understanding of boson and fermion correlations in an ideal gas. More information on uncertainties and systematic errors, as well as a more complete summary of the data, are given in Supplementary Information.

Improved detector resolution would allow a more detailed study of the correlation function, and is thus highly desirable. The effect of the resolution could be circumvented by using a diverging atom lens to demagnify the source⁴. According to the formula $l = ht/(2\pi ms)$, a smaller effective source size gives a larger correlation length. We have tried such a scheme by creating an atomic lens with a blue-detuned, vertically propagating, laser beam, forcing the atoms away from its axis (see Methods). The laser waist was not large compared to the cloud size, and therefore our ‘lens’ suffered from strong aberrations, but a crude estimate of the demagnification, neglecting aberrations, gives about 2 in the x – y plane. Figure 3 shows a comparison of

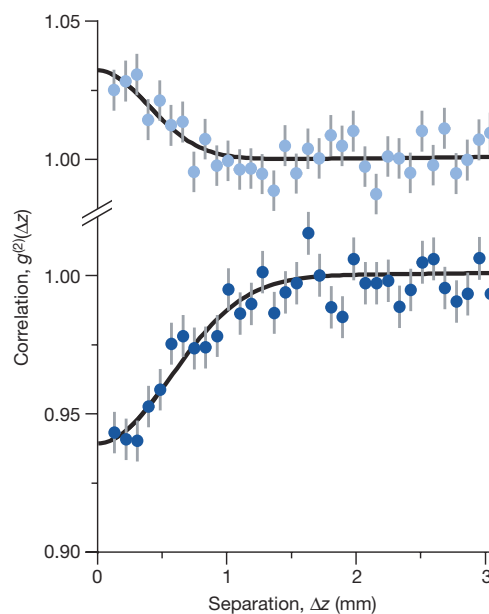


Figure 2 | Normalized correlation functions for $^4\text{He}^*$ (bosons) in the upper plot, and $^3\text{He}^*$ (fermions) in the lower plot. Both functions are measured at the same cloud temperature ($0.5 \mu\text{K}$), and with identical trap parameters. Error bars correspond to the square root of the number of pairs in each bin. The line is a fit to a gaussian function. The bosons show a bunching effect, and the fermions show antibunching. The correlation length for $^3\text{He}^*$ is expected to be 33% larger than that for $^4\text{He}^*$ owing to the smaller mass. We find $1/e$ values for the correlation lengths of 0.75 ± 0.07 mm and 0.56 ± 0.08 mm for fermions and bosons, respectively.

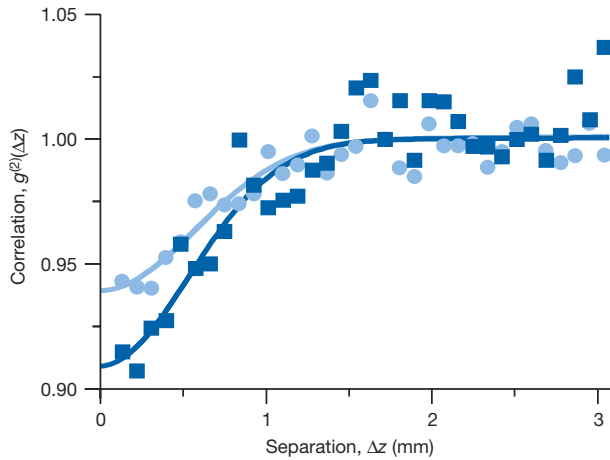


Figure 3 | Effect of demagnifying the source size. We show normalized correlation functions along the z (vertical) axis for ${}^3\text{He}^*$, with (dark blue squares) and without (light blue circles) a diverging atomic lens in the x - y plane. The dip is deeper with the lens, because the increase of the correlation lengths in the x - y plane leads to less reduction of contrast when convolved with the resolution function in that plane.

$g^{(2)}(\Delta z)$ for fermions with and without the defocusing lens. We clearly see a greater antibunching depth, consistent with larger correlation lengths in the x - y plane (we have checked that l_y is indeed increased) and therefore yielding a smaller reduction of the contrast when convolved with the detector resolution function. As expected, the correlation length in the z direction is unaffected by the lens in the x - y plane. Although our atomic lens was far from ideal, the experiment shows that it is possible to modify the HBT signal by optical means.

To conclude, we emphasize that we have used samples of neutral atoms at a moderate density in which interactions do not play any significant role. Care was taken to manipulate bosons and fermions in conditions as similar as possible. Thus the observed differences can be understood as a purely quantum effect associated with the exchange symmetries of wavefunctions of indistinguishable particles.

The possibility of having access to the sign of phase factors in a many-body wavefunction opens fascinating perspectives for the investigation of intriguing analogues of condensed-matter systems, which can now be realized with cold atoms. For instance, one could compare the many-body state of cold fermions and that of ‘fermionized’ bosons in a one-dimensional sample^{28,29}. Our successful manipulation of the HBT signal by interaction with a laser suggests that other lens configurations could allow measurements in position space (by forming an image of the cloud at the detector) or in any combination of momentum and spatial coordinates.

METHODS

Experimental sequence. Clouds of cold ${}^4\text{He}^*$ are produced by evaporative cooling of a pure ${}^4\text{He}^*$ sample, loaded into a Ioffe–Pritchard magnetic trap³⁰. The trapped state is 2^3S_1 , $m_j = 1$, and the trap frequency values are 47 Hz and 440 Hz for axial and radial confinement, respectively. The bias field is 0.75 G, corresponding to a frequency of 2.1 MHz for a transition between the $m_j = 1$ and $m_j = 0$ states at the bottom of the trap. After evaporative cooling, we keep the radio frequency evaporation field (‘r.f. knife’) on at constant frequency for 500 ms, then wait for 100 ms before switching off the trap. In contrast to the experiments of ref. 5, atoms are released in a magnetic-field-sensitive state.

To prepare ${}^3\text{He}^*$ clouds, we simultaneously load ${}^3\text{He}^*$ and ${}^4\text{He}^*$ atoms in the magnetic trap²⁷. The trapping state for ${}^3\text{He}^*$ is 2^3S_1 , $F = 3/2$, $m_F = 3/2$, and axial and radial trap frequencies are 54 Hz and 506 Hz—the difference compared to ${}^4\text{He}^*$ is only due to the mass. The two gases are in thermal equilibrium in the trap, so that ${}^3\text{He}^*$ is sympathetically cooled with ${}^4\text{He}^*$ during the evaporative cooling stage. Once the desired temperature is reached, we selectively eliminate ${}^4\text{He}^*$ atoms from the trap using the r.f. knife. The gyromagnetic ratios for ${}^4\text{He}^*$ and ${}^3\text{He}^*$ are 2 and $4/3$ respectively, so that the resonant frequency of the $m = 1$ to

$m = 0$ transition for ${}^4\text{He}^*$ is $3/2$ times larger than the $m = 3/2$ to $m = 1/2$ transition for ${}^3\text{He}^*$. An r.f. ramp from 3 MHz to 1.9 MHz expels all the ${}^4\text{He}^*$ atoms from the trap without affecting ${}^3\text{He}^*$. We then use the same trap switch-off procedure to release the ${}^3\text{He}^*$ atoms (also in a magnetic-field-sensitive state) onto the detector. We can apply magnetic field gradients to check the degree of spin polarization of either species.

Correlation function. The detailed procedure leading to this correlation is given in ref. 5. Briefly, we convert arrival times to z positions, and then use the three-dimensional positions of each atom to construct a histogram of pair separations Δr in a particular cloud. We then sum the pair distribution histograms for 1,000 successive runs at the same temperature. For separations much larger than the correlation length, this histogram reflects the gaussian spatial distribution of the cloud. To remove this large-scale shape and obtain the normalized correlation function, we divide the histogram by the autoconvolution of the sum of the 1,000 single-particle distributions.

Atom lens experiment. A 300 mW laser beam with an elliptical waist of approximately $100 \times 150 \mu\text{m}^2$ propagates vertically through the trap. The laser frequency is detuned by 300 GHz from the 2^3S_1 to 2^3P_2 transition. After turning off the magnetic trap, and waiting 500 μs for magnetic transients to die away, the defocusing laser is turned on for 500 μs .

Received 15 November; accepted 7 December 2006.

- Hanbury Brown, R. & Twiss, R. Q. Correlation between photons in two coherent beams of light. *Nature* **177**, 27–29 (1956).
- Scully, M. O. & Zubairy, M. S. *Quantum Optics* (Cambridge Univ. Press, Cambridge, UK, 1997).
- Glauber, R. J. in *Quantum Optics and Electronics* (eds DeWitt, C., Blandin, A. & Cohen-Tannoudji, C.) 63–185 (Gordon and Breach, New York, 1965).
- Yasuda, M. & Shimizu, F. Observation of two-atom correlation of an ultracold neon atomic beam. *Phys. Rev. Lett.* **77**, 3090–3093 (1996).
- Schellekens, M. *et al.* Hanbury Brown Twiss effect for ultracold quantum gases. *Science* **310**, 648–651 (2005); published online 15 September 2005 (doi:10.1126/science.1118024).
- Öttl, A., Ritter, S., Köhl, M. & Esslinger, T. Correlations and counting statistics on an atom laser. *Phys. Rev. Lett.* **95**, 090404 (2005).
- Fölling, S. *et al.* Spatial quantum noise interferometry in expanding condensates. *Nature* **434**, 481–484 (2005).
- Spielman, I. B., Phillips, W. D. & Porto, J. V. The Mott insulator transition in two dimensions. Preprint at (<http://arxiv.org/cond-mat/0606216>) (2006).
- Greiner, M., Regal, C. A., Stewart, J. T. & Jin, D. S. Probing pair-correlated fermionic atoms through correlations in atom shot noise. *Phys. Rev. Lett.* **94**, 110401 (2005).
- Altman, E., Demler, E. & Lukin, M. D. Probing many-body states of ultracold atoms via noise correlations. *Phys. Rev. A* **70**, 013603 (2004).
- Grondalski, J., Alsing, P. M. & Deutsch, I. H. Spatial correlation diagnostics for atoms in optical lattices. *Opt. Express* **5**, 249–261 (1999).
- Hellweg, D. *et al.* Measurement of the spatial correlation function of phase fluctuating Bose-Einstein condensates. *Phys. Rev. Lett.* **91**, 010406 (2003).
- Estève, J. *et al.* Observations of density fluctuations in an elongated Bose gas: ideal gas and quasicondensate regimes. *Phys. Rev. Lett.* **96**, 130403 (2006).
- Loudon, R. *The Quantum Theory of Light* 3rd edn (Oxford Univ. Press, Oxford, 2000).
- Fano, U. Quantum theory of interference effects in the mixing of light from phase independent sources. *Am. J. Phys.* **29**, 539–545 (1961).
- Hanbury Brown, R. & Twiss, R. Q. A test of a new stellar interferometer on Sirius. *Nature* **178**, 1046–1048 (1956).
- Baym, G. The physics of Hanbury Brown-Twiss intensity interferometry: From stars to nuclear collisions. *Acta Phys. Pol. B* **29**, 1839–1884 (1998).
- Boal, D. H., Gelbke, C.-K. & Jennings, B. K. Intensity interferometry in subatomic physics. *Rev. Mod. Phys.* **62**, 553–602 (1990).
- Viana Gomes, J. *et al.* Theory for a Hanbury Brown Twiss experiment with a ballistically expanding cloud of cold atoms. *Phys. Rev. A* **74**, 053607 (2006).
- Kimble, H. J., Dagenais, M. & Mandel, L. Photon antibunching in resonance fluorescence. *Phys. Rev. Lett.* **39**, 691–695 (1978).
- Henny, M. *et al.* The fermionic Hanbury Brown and Twiss experiment. *Science* **284**, 296–298 (1999).
- Oliver, W. D., Kim, J., Liu, R. C. & Yamamoto, Y. Hanbury Brown and Twiss-type experiment with electrons. *Science* **284**, 299–301 (1999).
- Kiesel, H., Renz, A. & Hasselbach, F. Observation of Hanbury Brown-Twiss anticorrelations for free electrons. *Nature* **418**, 392–394 (2002).
- Iannuzzi, M., Orecchini, A., Sacchetti, F., Facchi, P. & Pascazio, S. Direct experimental evidence of free-fermion antibunching. *Phys. Rev. Lett.* **96**, 080402 (2006).
- Rom, T. *et al.* Free fermion antibunching in a degenerate atomic Fermi gas released from an optical lattice. *Nature* **444**, 733–736 (2006).
- Jagutzki, O. *et al.* A broad-application microchannel-plate detector system for advanced particle or photon detection tasks: Large area imaging, precise multi-hit timing information and high detection rate. *Nucl. Instrum. Methods Phys. Res. A* **477**, 244–249 (2002).

27. McNamara, J. M., Jelten, T., Tychkov, A. S., Hogervorst, W. & Vassen, W. Degenerate Bose-Fermi mixture of metastable atoms. *Phys. Rev. Lett.* **97**, 080404 (2006).
28. Girardeau, M. Relationship between systems of impenetrable bosons and fermions in one dimension. *J. Math. Phys. (NY)* **1**, 516–523 (1960).
29. Olshanii, M. Atomic scattering in the presence of an external confinement and a gas of impenetrable bosons. *Phys. Rev. Lett.* **81**, 938–941 (1998).
30. Tychkov, A. S. *et al.* Metastable helium Bose-Einstein condensate with a large number of atoms. *Phys. Rev. A* **73**, 031603(R) (2006).

Supplementary Information is linked to the online version of the paper at www.nature.com/nature.

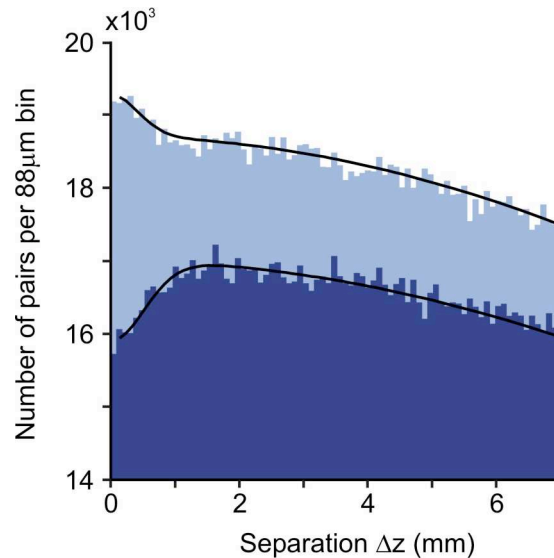
Acknowledgements This work was supported by the access programme of Laserlab Europe. The LCVU group in Amsterdam is supported by the 'Cold Atoms' programme of the Dutch Foundation for Fundamental Research on Matter (FOM) and by the Space Research Organization Netherlands (SRON). The Atom Optics group of LCFIO is a member of the IFRAF institute and of the Fédération LUMAT of the CNRS, and is supported by the French ANR and by the SCALA programme of the European Union.

Author Information Reprints and permissions information is available at www.nature.com/reprints. The authors declare no competing financial interests. Correspondence and requests for materials should be addressed to C.I.W. (christoph.westbrook@institutoptique.fr) or W.V. (w.vassen@few.vu.nl).

Supplementary material for "Hanbury Brown Twiss effect for bosons versus fermions"

1. Unnormalised pair histogram

In order to give the reader an idea of the "raw" data, we show in Supplementary figure 1 some unnormalised pair histograms. The data correspond to the normalised plots shown in Fig. 2 in the main text. In addition to the bunching and antibunching feature for separations below 1 mm, the histogram also shows a broad structure which is due to the approximately Gaussian shape of the cloud. The broad structure is eliminated by the normalisation procedure described in Ref. 5 of the main text and summarised in Methods.



Supplementary figure. 1. Unnormalised pair histograms for bosons (light blue) and fermions (dark blue). The black lines represent a fit to the sum of two Gaussian functions.

2. Fit results

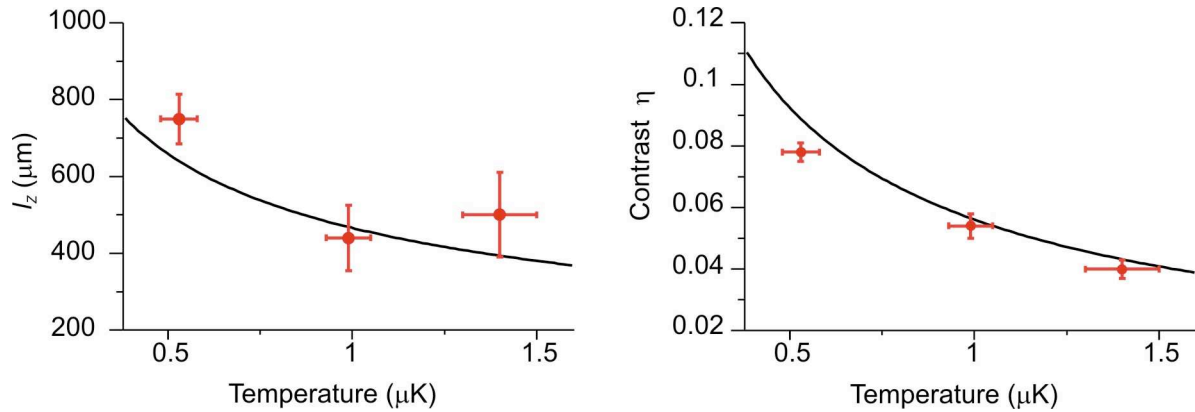
If one neglects finite resolution effects, the normalised correlation function should be well described by a Gaussian function:

$$g^{(2)}(\Delta x, \Delta y, \Delta z) = 1 \pm \exp\left(-\left[\left(\frac{\Delta x}{l_x}\right)^2 + \left(\frac{\Delta y}{l_y}\right)^2 + \left(\frac{\Delta z}{l_z}\right)^2\right]\right), \quad (1)$$

where the + sign refers to bosons and the – sign to fermions. We denote the correlation lengths in the 3 different spatial directions i , by l_i . In practice this function must be convolved with the resolution function of the detector. The resolution function is determined by the method discussed in Ref. 26. The resolution along the z direction is approximately 3 nm and is neglected. The convolution in the x - y plane is described in Ref. 19 for the case of a Gaussian resolution function. Careful measurements have revealed that the wings of the resolution function are broader than those of a Gaussian and we thus use an empirically determined analytical function to approximate the pair resolution function. Its $1/e$ halfwidth is about 500 μm . Since the correlation length in the x direction is more than an order of magnitude smaller than the resolution, we set $l_x = 0$. The convolution also affects the height of

the signal so that $g^{(2)}(0,0,0) = 1 \pm \eta$. The parameter η is referred to as the contrast. The fit parameters are thus l_y , l_z and η .

Data were taken for fermions ($^3\text{He}^*$) at 0.5 μK , 1.0 μK and 1.4 μK . The corresponding fit results for l_z and η are plotted in Supplementary Figure 2. In addition, we have data for two other situations, one using $^4\text{He}^*$ at 0.5 μK , and another using $^3\text{He}^*$ at 0.5 μK and a diverging lens. All 5 runs are summarised in table 1. In the graphs, we have plotted the formula $l_z = \hbar t / 2\pi m s_z$, extracting the size s_z from the measured temperature, trap oscillation frequency and assuming the cloud is an ideal gas. For the contrast η , we plot the expected variation based on the measured resolution function.



Supplementary figure. 2. Summary of data taken for $^3\text{He}^*$ clouds at three different temperatures. The solid lines show the expected results (see text).

Run	l_z (μm)	l_y (μm)	η
$^3\text{He}^*$, 0.5 μK	750 ± 70	570 ± 50	0.078 ± 0.003
$^3\text{He}^*$, 1 μK	440 ± 90	360 ± 90	0.054 ± 0.004
$^3\text{He}^*$, 1.4 μK	500 ± 110	0 *	0.040 ± 0.003
$^4\text{He}^*$, 0.5 μK	560 ± 80	570 ± 100	0.033 ± 0.003
$^3\text{He}^*$, 0.5 μK , with lens	750 ± 80	810 ± 40	0.108 ± 0.003

*In this run, the fitted width of the correlation function along y is actually smaller than the resolution.

Thus no reasonable value can be extracted for l_y .

Supplementary table 1. Summary of fit results for all data sets

Generally the data are in good agreement with the predictions of the ideal gas model. In the run with the lens, we have made no quantitative comparison with a calculation because it would involve taking into account the severe aberrations of the lens. Qualitatively however, we see that, as expected, the correlation length along z is unchanged while that along y , as well as the contrast, are increased. The fitted values of η do not correspond to those one would deduce from the data in Figs. 2 and 3 in the main text. This is because, as in Ref. 5, we computed the correlation function along the z axis over an area slightly larger than the width of the resolution function. This procedure improves the signal to noise ratio and preserves the form and the width of the correlation function but slightly modifies its height.

We observe three small anomalies: first, the contrast η for both bosons and fermions at $0.5 \mu\text{K}$ is below the prediction and the ratio, after correction for the resolution, is 2.4 ± 0.2 instead of the expected value 1.5. Second, the correlation length l_y for fermions at $0.5 \mu\text{K}$ seems quite low resulting in a ratio of fermions to bosons of 1.0 ± 0.2 instead of 1.3. Third, the width of the antibunching dip in the normalised pair separation histogram along y for fermions at $1.4 \mu\text{K}$ is *smaller* than the width of the measured resolution function, meaning that the fitted value of l_y is consistent with zero.

A systematic error may be present in the estimation of the detector resolution. After moving the detector from Orsay to Amsterdam, we noticed that the detector resolution, differed by up to 30% from day to day. A systematic error in the resolution has approximately the same relative effect on the value of η . It would also have an effect on the value of l_y . Uncontrolled variations in the resolution may thus account for the above anomalies. The correlation length in the vertical direction l_z however, should not be affected by an imprecise knowledge of the resolution in the x - y plane. The good agreement we find with our expectations along this axis is the strongest argument that the correlations we observe are consistent with the ideal gas model.

A second possible source of systematic error is related to the switch-off of the magnetic trap. Eddy currents cause a typical time scale of 1 ms in this turn-off³⁰. Since, unlike in Ref. 5, the released atoms are in a magnetic field sensitive state, partially adiabatic effects or focussing by residual curvatures could affect our measurement of the temperature or of the effective source size viewed from the detector. We have no independent estimate of the magnitude of these effects and can simply conclude that the reasonable agreement with our model means that these effects are not very large.

Observation of Atom Pairs in Spontaneous Four-Wave Mixing of Two Colliding Bose-Einstein Condensates

A. Perrin, H. Chang, V. Krachmalnicoff, M. Schellekens, D. Boiron, A. Aspect, and C. I. Westbrook*

Laboratoire Charles Fabry de l'Institut d'Optique, CNRS, Univ Paris-Sud, Campus Polytechnique, RD128, 91127 Palaiseau cedex, France

(Received 23 April 2007; published 12 October 2007)

We study atom scattering from two colliding Bose-Einstein condensates using a position sensitive, time resolved, single atom detector. In analogy to quantum optics, the process can also be thought of as spontaneous, degenerate four-wave mixing of de Broglie waves. We find a clear correlation between atoms with opposite momenta, demonstrating pair production in the scattering process. We also observe a Hanbury Brown–Twiss correlation for collinear momenta, which permits an independent measurement of the size of the pair production source and thus the size of the spatial mode. The back-to-back pairs occupy very nearly two oppositely directed spatial modes, a promising feature for future quantum optics experiments.

DOI: [10.1103/PhysRevLett.99.150405](https://doi.org/10.1103/PhysRevLett.99.150405)

PACS numbers: 03.75.Nt, 34.50.–s

Recent years have seen the emergence of “quantum atom optics”, that is the extension of the many analogies between atom optics and traditional optics to the quantum optical domain in which phenomena like vacuum fluctuations and entanglement play a central role. In optics, the advent of correlated photon pairs [1] has provided a fruitful avenue of investigation, with examples including single photon sources and entangled states [2]. Partly inspired by this work, there have been many proposals concerning atom pairs, especially the production and observation of entanglement [3–7]. Many authors have also theoretically investigated other aspects of the pair production mechanism in both atomic collisions and in the breakup of diatomic molecules [7–13].

As emphasized in Ref. [4], pair production can be studied in two limits. If many atoms are created in a single mode, stimulated emission of atoms is important, and one can speak of two mode squeezing in analogy with Ref. [14]. The opposite limit, in which the occupation number of the modes is much less than unity, corresponds to the spontaneous production of atom pairs, entangled either in spin or momentum in analogy with Refs. [15,16]. Experiments on stimulated atomic four-wave mixing [17–19] and on parametric amplification in an optical lattice [20,21] are in the first limit, and pairs of “daughter BEC’s” with opposite velocities have been clearly observed. Experiments in the regime of individual atom pairs include the many experiments investigating the scattered halo in collisions of cold atoms either in the s -wave regime [22–24] or for higher partial waves [25,26]. None of these experiments, however, has demonstrated correlated pairs. The only evidence of atom pair production with cold atoms has been reported in absorption images of atoms from the breakup of molecules near a Feshbach resonance [27].

Here, we report on the observation of individual atom pairs with opposite velocities produced in the collision of

two condensates. A time and position resolved, single atom detector [28] permits us to reconstruct the three dimensional distribution of the scattered atoms: a spherical shell in velocity space. We also reconstruct the two-particle correlation function in 3D and find a strong correlation between atoms emitted back to back. This process can be interpreted as a spontaneous four-wave mixing process constrained by a phase matching condition as in the non linear optical analog which produces twin photons [2]. It can also be seen as the result of pairwise elastic collisions between atoms, constrained by momentum conservation. We measure the width of the velocity correlation function for a back to back atom pair and show that it corresponds very nearly to the uncertainty limited momentum spread of the colliding BECs.

This interpretation is confirmed by the observation of the velocity correlation function for two atoms scattered in the *same* direction. This latter effect, predicted in Refs. [7,10,13], is another manifestation of the Hanbury Brown–Twiss effect (HBT). As in high energy collisions [29], the effect allows us to measure the size of the collision volume.

The fact that the width of the HBT peak is close to that of the back-to-back correlation confirms that for a given atom on the collision sphere, its partner is scattered into a single mode of the matter wave field. This observation is crucial for future experiments in which one would like to bring pairs back together in order to confirm their entanglement in the spirit of Ref. [16] or observe other quantum effects [30].

We produce condensates of 10^4 – 10^5 atoms in the $m_x = 1$ sublevel of the 2^3S_1 state of metastable helium (He^*). The condensates are stored in a cylindrically symmetric magnetic trap with axial and radial trapping frequencies of 47 and 1150 Hz, respectively. The bias field is 0.25 G in the x direction (see Fig. 1), and defines the quantization axis. The uncertainty limited velocity spread of the colliding

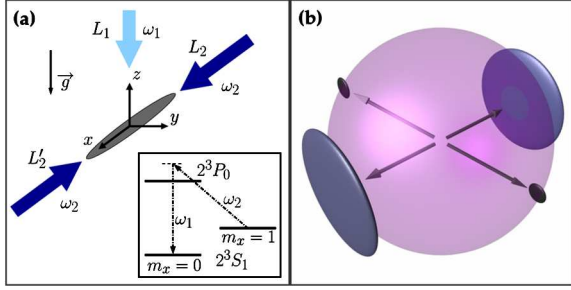


FIG. 1 (color online). (a) View of the magnetically trapped condensate (in the $m_x = 1$ state) and the three laser beams which create two cigar shaped counterpropagating free condensates (in the $m_x = 0$ state) by σ^-/π Raman transfers induced by $L_1 - L_2$ and $L_1 - L'_2$, respectively (see inset). L_1 is π -polarized (along x) while L_2 and L'_2 are σ^- -polarized. (b) Representation in velocity space of the expected atomic density after the collision. The scattered atoms are on a sphere and the remaining condensates, pancake-shaped after expansion, lie on the edge of the sphere along the x axis. A collision process involving an atom of each condensate is also represented. The shape of the scattering modes is related to the uncertainty limited momentum spread of the condensates.

atoms is thus anisotropic and we calculate it numerically using the Gross-Pitaevskii equation [31]. For a condensate with 3×10^4 atoms, we find rms axial and radial velocity spreads of $v_x^{\text{rms}} = 0.0044v_{\text{rec}}$ and $v_{yz}^{\text{rms}} = 0.091v_{\text{rec}}$, where $v_{\text{rec}} = 9.2$ cm/s is the single photon recoil velocity, $\hbar k/m$ where k is the photon wave vector and m is the atomic mass. The spread in these values due to the spread in condensate number is about $\pm 20\%$.

To generate two colliding Bose-Einstein condensates, we use two stimulated Raman transitions with different momentum transfers, produced by phase coherent laser beams L_1 , L_2 , and L'_2 , as shown in Fig. 1 [31]. These transitions have two purposes: first they transfer atoms to the magnetic field insensitive state $m_x = 0$ so that they freely fall to the detector and second, they separate the condensate into two components with velocities $v_{\text{rec}}(\mathbf{e}_1 \pm \mathbf{e}_2)$, where \mathbf{e}_1 and \mathbf{e}_2 are the unit vectors along the propagation axes of the laser beams L_1 and L_2 respectively. The beams are pulsed on for a duration of ~ 500 ns and couple about 60% of the atoms to the $m_x = 0$ state. We do not switch off the magnetic trap, therefore atoms remaining in $m_x = 1$ stay trapped. The two colliding condensates travel with a relative velocity of $2v_{\text{rec}}$, at least 8 times larger than the speed of sound in the initial condensate. This ensures that elementary excitations of the condensate correspond to free particles. Since they are no longer trapped, the two colliding condensates expand radially, reducing the collision rate. A numerical model [8], assuming an expansion identical to that of a single condensate with the same total number of atoms, shows a roughly exponential decrease in the pair production rate with a time constant of ~ 150 μs .

After the collision, atoms fall onto a 8 cm microchannel plate detector placed 46.5 cm below the trap center. This

detector measures the arrival time of the atoms and their positions in the x - y plane [28,32]. Figure 2 shows successive 2.4 ms time slices showing the atom positions as they cross the detector plane. The time of flight for the center of mass to reach the detector is 320 ms. Since this time of flight is large compared to the collision duration, and the observed patterns are large compared to the collision volume, the observed 3D atom positions accurately reflect the velocity distribution after collision. In the following, we will only refer to the velocities of the detected atoms.

In Fig. 2, one clearly sees a spherical shell of radius of v_{rec} , represented by circles of varying diameter [see also Fig. 1(b)]. In the midplane of the sphere one can see the unscattered, pancake-shaped condensates I, II which locally saturate the detector. Other features are also visible in Fig. 2. In frames (a),(b) one sees a condensate, III, which underwent no momentum transfer, possibly due to the imperfect polarization of the Raman beams which can produce an off resonant, single beam Raman transition [31]. A fourth condensate, IV, probably resulting from four-wave mixing [17] of condensate III and the main unscattered condensates I, II is visible in frames (h),(i). Frames (b),(c) show a collision sphere due to the collision of I with atoms remaining trapped in $m_x = 1$ and with condensate III. The two spots within the sphere in frames (d)–(f) are not understood.

To avoid effects of local saturation of the detector in our analysis, we exclude regions around the 4 condensates, representing about 40% of the sphere. On the remaining area of the sphere we detect between 30 and 300 atoms on

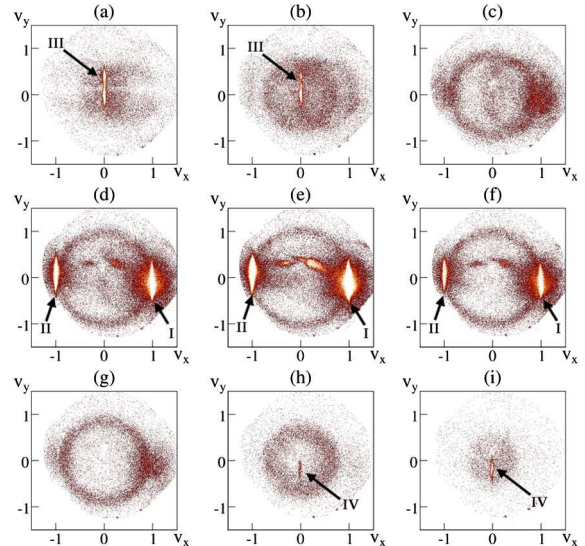


FIG. 2 (color online). (a)–(i) Images of the collision of two condensates. Each frame represents a 2.4 ms time slice of the atomic cloud as it passes the plane of the detector (x - y). 150 shots have been averaged to obtain these images. The two colliding condensates I, II and the collision sphere are clearly visible. Other features visible in the images are discussed in the text. The axes are marked in units of the recoil velocity.

each shot, with an average of about 100 per shot. Assuming a detection efficiency of 10% [32], this means that $\sim 5\%$ of the atoms are scattered from the two condensates. This number is consistent with the expected s -wave cross section [33] and the estimated evolution of the density during the collision.

We examine the pair correlation function for atoms in back to back directions by constructing, within the set of all the scattered atoms in one shot, a three-dimensional histogram containing all the pairs with a velocity sum $\mathbf{V} = \mathbf{V}_1 + \mathbf{V}_2$ close to zero. We then sum the histograms over 1100 shots. Another histogram containing all the pairs of the sum of all shots gives the accidental coincidence rate for uncorrelated atoms and is used as a normalization. We thus recover the normalized second order correlation function, averaged over the sphere [31], $g^{(2)}(\mathbf{V})$ of the distribution of relative velocities of atom pairs on the sphere. Figure 3(a) shows the behavior of $g^{(2)}(\mathbf{V})$ around $\mathbf{V} = \mathbf{0}$ projected along the three space axes. The peak indicates that, given the detection of an atom on the sphere, there is an enhanced probability of detecting a second one on the opposite side. Cartesian coordinates are best suited to plotting the data because of the competing spherical symmetry of the scattering process and the cylindrical symmetry of the source.

To analyze these results further, we perform a three-dimensional Gaussian fit to the normalized histogram:

$$g^{(2)}(V_x, V_y, V_z) = 1 + \eta e^{-[(V_x^2/2\sigma_x^2) - (V_y + V_z)^2/(2\sigma_z^2)]}. \quad (1)$$

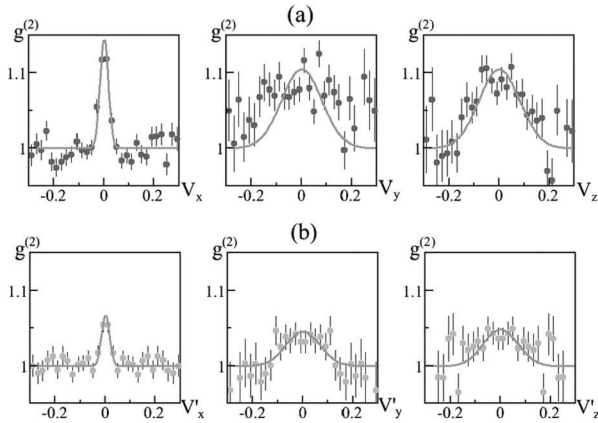


FIG. 3. Back-to-back [panel (a)] and collinear [panel (b)] correlation peaks. (a) Projection of $g^{(2)}(\mathbf{V} = \mathbf{V}_1 + \mathbf{V}_2)$ along the different axes of the experiment and around $\mathbf{V} = \mathbf{0}$. The projection consists in averaging the correlation in the two other directions over a surface equal to the products of the corresponding correlation lengths. This averaging makes the height smaller than the 3D fitted value $\eta^{\text{BB}} = 0.19 \pm 0.02$. The peak is the signature for correlated atoms with opposite velocities. (b) Projection of $g^{(2)}(\mathbf{V}' = \mathbf{V}_1 - \mathbf{V}_2)$ along the different axes of the experiment. This peak is due to the Hanbury Brown–Twiss bunching effect. All velocities are expressed in units of the recoil velocity.

The fit gives $\eta^{\text{BB}} = 0.19 \pm 0.02$, $\sigma_x^{\text{BB}} = 0.017 \pm 0.002 v_{\text{rec}}$, and $\sigma_{yz}^{\text{BB}} = 0.081 \pm 0.004 v_{\text{rec}}$. The observed width in the x direction is limited by the rms pair resolution of the detector, $0.14 v_{\text{rec}}$ [31,36]. In the y and z directions, the observed width is close to the uncertainty limited velocity scale v_{yz}^{rms} discussed above. It is therefore reasonable to conclude that the anisotropy in the correlation function is closely related to the anisotropy of the momentum distribution in the source. Detailed modeling accounting accurately for this width is in progress, but for purposes of this Letter, we will simply compare the width with that of the correlation function for collinear atoms as described below.

The procedure to construct the correlation function for nearly collinear velocities (the HBT effect) is the same as that for the back-to-back correlation function. Defining the relative velocity $\mathbf{V}' = \mathbf{V}_1 - \mathbf{V}_2$, we show in Fig. 3(b) the correlation function $g^{(2)}(\mathbf{V}')$ around $\mathbf{V}' = \mathbf{0}$. Using the fitting function, Eq. (1), we find: $\eta^{\text{CL}} = 0.10 \pm 0.02$, $\sigma_x^{\text{CL}} = 0.016 \pm 0.003 v_{\text{rec}}$, and $\sigma_{yz}^{\text{CL}} = 0.069 \pm 0.008 v_{\text{rec}}$. As in the back to back case, the width in the x direction is limited by the resolution while in the y - z plane it is close to v_{yz}^{rms} . If we think of the HBT effect as giving a measure of the size of the pair production source, the width of the collinear correlation function defines the size of a mode of the scattered matter wave field. The fact that the back-to-back and collinear widths are so close, at least in the directions we can resolve, is further, strong evidence that, at least in the directions we resolve, the pairs we produce are in oppositely directed modes.

We now turn to the height of the peaks η . In the collinear case we expect the value of η^{CL} to be unity for a detector resolution much smaller than the peak width. Since in the x direction the width is clearly limited by the resolution, a crude estimate for η^{CL} is the ratio of the ideal width to the observed one: $\eta^{\text{CL}} \approx v_x^{\text{rms}}/\sigma_x = 0.3$. The discrepancy with the fitted value may have to do with our crude estimate of the effective source size along x and therefore of v_x^{rms} .

In the back-to-back case, the height of the peak is not limited to unity. A simple model of the peak height compares the number of true pairs to random coincidences in a volume ΔV defined by the widths observed in Fig. 3:

$$1 + \eta^{\text{BB}} = \frac{\text{true} + \text{random}}{\text{random}} = 1 + \frac{V}{N\Delta V}. \quad (2)$$

Here N is the number of atoms scattered on a single shot (but not necessarily detected) and V is the volume of the scattering shell. A rough estimate of $\Delta V/V$ is $1/1400$. As mentioned above, we detect on average 100 atoms on the analyzed 60% of the sphere. Assuming again a quantum efficiency of 10%, a rough estimate of the average number N is 1700 so that we find $\eta^{\text{BB}} \approx 0.8$ which gives the correct order of magnitude. We emphasize that ΔV is limited by the detector resolution in the x direction and is therefore about 10 times larger than the volume corresponding to a single mode. Thus, as stated in the introduc-

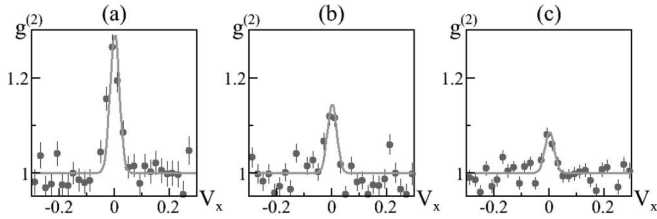


FIG. 4. Projections of $g^{(2)}(\mathbf{V})$ along the x axis and around $\mathbf{V} = \mathbf{0}$. Bin of mean number of detected atoms of (a) 50, (b) 125, and (c) 190.

tion, the number of scattered atoms per mode is small compared to unity, and we are in the separated entangled pair production regime. We can verify the $1/N$ dependence of Eq. (2) by binning the data according to the number of scattered atoms per shot. Dividing the 1100 shots into 3 bins of different atom numbers we do observe the expected trend as shown in Fig. 4.

A detailed model of the pair production process must include a more careful description of the collision geometry of colliding and expanding condensates as well as the effect of the condensates' mean field on the scattered atoms, something which is neglected in the above discussion. A rough estimate of the mean field effect is found by adding the chemical potential to the kinetic energy of a scattered atom. This gives an additional velocity broadening of order $0.03v_{\text{rec}}$, not entirely negligible compared to the observed widths. Several workers are developing such models. The correlation functions we observe lend themselves to an investigation of Cauchy-Schwartz inequalities [2]. A cross correlation (back-to-back) greater than an autocorrelation (collinear) violates a Cauchy-Schwartz inequality for classical fields. Sub-Poissonian number differences between opposite directions should also be present [7]. A future publication will discuss these aspects of the experiment.

We acknowledge valuable discussions with K. Kheruntsyan, K. Mølmer, and M. Trippenbach. Our group is a member of the IFRAF institute, and is supported by the french ANR, the QUDEDIS program, and the SCALA program of the European Union.

*christoph.westbrook@institutoptique.fr

- [1] D. C. Burnham and D. L. Weinberg, Phys. Rev. Lett. **25**, 84 (1970).
- [2] See, for example, D. Walls and G. Milburn, *Quantum Optics* (Springer, New York, 1991).
- [3] H. Pu and P. Meystre, Phys. Rev. Lett. **85**, 3987 (2000).
- [4] L.-M. Duan, A. Sørensen, J. I. Cirac, and P. Zoller, Phys. Rev. Lett. **85**, 3991 (2000).

- [5] K. V. Kheruntsyan, M. K. Olsen, and P. D. Drummond, Phys. Rev. Lett. **95**, 150405 (2005).
- [6] T. Opatrný and G. Kurizki, Phys. Rev. Lett. **86**, 3180 (2001).
- [7] C. M. Savage, P. E. Schwenn, and K. V. Kheruntsyan, Phys. Rev. A **74**, 033620 (2006).
- [8] Y. B. Band, M. Trippenbach, J. P. Burke, and P. S. Julienne, Phys. Rev. Lett. **84**, 5462 (2000).
- [9] P. Naidon and F. Masnou-Seeuws, Phys. Rev. A **68**, 033612 (2003).
- [10] P. Ziń *et al.*, Phys. Rev. Lett. **94**, 200401 (2005).
- [11] P. Ziń, J. Chwedeńczuk, and M. Trippenbach, Phys. Rev. A **73**, 033602 (2006).
- [12] A. A. Norrie, R. J. Ballagh, and C. W. Gardiner, Phys. Rev. A **73**, 043617 (2006).
- [13] P. Deuar and P. D. Drummond, Phys. Rev. Lett. **98**, 120402 (2007).
- [14] A. Heidmann *et al.*, Phys. Rev. Lett. **59**, 2555 (1987).
- [15] Z. Y. Ou and L. Mandel, Phys. Rev. Lett. **61**, 50 (1988); Y. H. Shih and C. O. Alley, Phys. Rev. Lett. **61**, 2921 (1988).
- [16] M. A. Horne, A. Shimony, and A. Zeilinger, Phys. Rev. Lett. **62**, 2209 (1989); J. G. Rarity and P. R. Tapster, Phys. Rev. Lett. **64**, 2495 (1990).
- [17] L. Deng *et al.*, Nature (London) **398**, 218 (1999).
- [18] J. M. Vogels, K. Xu, and W. Ketterle, Phys. Rev. Lett. **89**, 020401 (2002).
- [19] J. M. Vogels, J. K. Chin, and W. Ketterle, Phys. Rev. Lett. **90**, 030403 (2003).
- [20] N. Gemelke *et al.*, Phys. Rev. Lett. **95**, 170404 (2005).
- [21] G. K. Campbell *et al.*, Phys. Rev. Lett. **96**, 020406 (2006).
- [22] A. P. Chikkatur *et al.*, Phys. Rev. Lett. **85**, 483 (2000).
- [23] K. Gibble, S. Chang, and R. Legere, Phys. Rev. Lett. **75**, 2666 (1995).
- [24] N. Katz, E. Rowen, R. Ozeri, and N. Davidson, Phys. Rev. Lett. **95**, 220403 (2005).
- [25] C. Buggle, J. Leonard, W. von Klitzing, and J. T. M. Walraven, Phys. Rev. Lett. **93**, 173202 (2004).
- [26] N. R. Thomas, N. Kjærgaard, P. S. Julienne, and A. C. Wilson, Phys. Rev. Lett. **93**, 173201 (2004).
- [27] M. Greiner, C. A. Regal, J. T. Stewart, and D. S. Jin, Phys. Rev. Lett. **94**, 110401 (2005).
- [28] M. Schellekens *et al.*, Science **310**, 648 (2005).
- [29] G. Baym, Acta Phys. Pol. B **29**, 1839 (1998).
- [30] C. K. Hong, Z. Y. Ou, and L. Mandel, Phys. Rev. Lett. **59**, 2044 (1987).
- [31] See EPAPS Document No. E-PRLTAO-99-043742 for the experimental details for interested readers. For more information on EPAPS, see <http://www.aip.org/pubservs/epaps.html>.
- [32] T. Jelte *et al.*, Nature (London) **445**, 402 (2007).
- [33] We extrapolate from [34,35] a value of 5.3 nm for the scattering length between $m = 0$ atoms.
- [34] S. Moal *et al.*, Phys. Rev. Lett. **96**, 023203 (2006).
- [35] P. J. Leo, V. Venturi, I. B. Whittingham, and J. F. Babb, Phys. Rev. A **64**, 042710 (2001).
- [36] J. Viana Gomes *et al.*, Phys. Rev. A **74**, 053607 (2006).

Observation of atom pairs in spontaneous four wave mixing of two colliding Bose-Einstein Condensates: supplementary information

A. Perrin, H. Chang, V. Krachmalnicoff, M. Schellekens, D. Boiron, A. Aspect
and C. I. Westbrook

Here we give some additional technical details concerning the experiment for interested readers.

Raman laser beams: Figure 1 shows the approximate geometry of the Raman laser beams which generate the two colliding condensates. More precisely, an approximately vertical beam propagates in the direction defined by $\mathbf{e}_1 = \cos\theta\mathbf{e}_z + \sin\theta\mathbf{e}_y$ with $\theta \approx 7^\circ$, and where \mathbf{e} represents a unit vector. This beam is π -polarized (parallel to the x -axis). A second, horizontal beam propagates in the direction defined by $\mathbf{e}_2 = \cos\phi\mathbf{e}_x + \sin\phi\mathbf{e}_y$ with $\phi \approx 5^\circ$. The polarization is circular and corresponds nearly to σ^- . Perfect σ^- polarization with respect to the x axis is not possible unless $\phi = 0$. The laser beams are blue-detuned by 400 MHz from the $2^3S_1 - 2^3P_0$ transition (wavelength 1083 nm) and have a relative detuning of about 700 kHz to match the Raman resonance between the two Zeeman sublevels. The horizontal beam is retro-reflected. The intensity of laser L_1 is 100 mW/cm² whereas the intensities of laser L_2 and L'_2 are 50 mW/cm². The waist of these beams is 2.8 mm so that the intensity over the condensate is approximately constant.

The Raman detuning, 700 kHz is not very large compared to the Fourier limited width of the pulses. If in addition, the polarization of one beam is not exactly π or σ , a single beam (L_1 , L_2 or L'_2) can drive a Raman transition with no momentum transfer. This is the likely mechanism for the production of the condensate III in Fig. 2. In subsequent experiments we have observed that a better polarizer for L_1 substantially reduces the number of atoms in condensate III.

Detector resolution: In earlier work, we showed that the single particle resolution was of order 300 μm corresponding to a velocity resolution of 0.1 v_{rec} . The two particle resolution is a factor of $\sqrt{2}$ larger.

Size of the condensate: In the Thomas Fermi limit and for 3×10^4 atoms the chemical potential is $\mu/h = 3.5$ kHz. The Thomas-Fermi radii R are 90 μm and 3.5 μm in the axial and radial directions. Since the number of atoms is not large, the Thomas Fermi approximation is questionable. To go beyond that approximation we calculate the BEC profiles numerically, by solving the Gross-Pitaevskii equation. The deduced profile only differs from the Thomas-Fermi one by the appearance of wings in the profile along the radial axes. This makes the velocity distribution of the condensates slightly different. Our numerically estimated rms ve-

locities given in the main text are about $2\hbar/mR$.

In addition to governing the width of the correlation functions, the quantity v^{rms} should determine the thickness of the scattering sphere. We observe an rms width of 0.08 v_{rec} averaged over the detected part of the sphere, close to the value of v_{yz}^{rms} (0.091 v_{rec}). Along the x direction the thickness of the sphere should be smaller corresponding to v_x^{rms} (0.0044 v_{rec}), but the presence of the unscattered condensates renders that direction inaccessible. Thus the measured thickness of the sphere corroborates our estimate of the size and velocity distribution of the source.

Definition of $g^{(2)}(\mathbf{V})$: Our histogramming procedure to find the correlation function for back to back pairs corresponds to first calculating the averaged unnormalized correlation function $\overline{G^{(2)}}$:

$$\overline{G^{(2)}}(\mathbf{V}) = \int d^3\mathbf{V}_1 G^{(2)}(\mathbf{V}_1, -\mathbf{V}_1 + \mathbf{V}) \quad (1)$$

For collinear pairs we compute

$$\overline{G^{(2)}}(\mathbf{V}') = \int d^3\mathbf{V}_1 G^{(2)}(\mathbf{V}_1, \mathbf{V}_1 + \mathbf{V}') \quad (2)$$

These results are normalized as explained in the main text to obtain $g^{(2)}(\mathbf{V})$ and $g^{(2)}(\mathbf{V}')$.

Comment on Fig. 3: The figure plots a projected and averaged correlation function. This procedure tends to reduce the peak heights. The plotted curve in each panel is a Gaussian with a width determined by the 3D fit and a height determined by fitting the height of the averaged and projected data.

In the second panel of Fig. 3 a (the y axis), the points lie systematically above the line. This may be due to the fact that because of our elimination of the areas around the condensates, most of the data for the y direction comes from points close to the $y - z$ plane. This means that the main contribution to the correlation data along y comes from different points along the radius of the sphere. Since the thickness of the sphere is of similar shape and size as the correlation function itself, the normalization has the same shape as the correlation data rendering the normalization of the wings of the curve very sensitive to noise. Thus the correlation functions along x and z give a better view of the quality of the data. The fit however makes use of all the data points at once and suffers less from this problem.

**Erratum: Observation of Atom Pairs in Spontaneous Four-Wave Mixing
of Two Colliding Bose-Einstein Condensates
[Phys. Rev. Lett. 99, 150405 (2007)]**

A. Perrin, H. Chang, V. Krachmalnicoff, M. Schellekens, D. Boiron, A. Aspect, and C. I. Westbrook
(Received 17 April 2008; published 8 May 2008)

DOI: [10.1103/PhysRevLett.100.189904](https://doi.org/10.1103/PhysRevLett.100.189904)

PACS numbers: 03.75.Nt, 34.50.-s, 99.10.Cd

On page 3, column 1, second paragraph, Eq. (1) should read:

$$g^{(2)}(V_x, V_y, V_z) = 1 + \eta e^{-(V_x^2/2\sigma_x^2) - [(V_y^2 + V_z^2)/(2\sigma_{yz}^2)]}. \quad (1)$$

In the same paragraph, the phrase “. . . the pair resolution of the detector, $0.14v_{\text{rec}}$,” should read “. . . the pair resolution of the detector, $0.014v_{\text{rec}}$.” In the EPAPS document No. E-PRLTAO-99-043742, in the paragraph entitled “Detector resolution:,” the quantity “ $0.1v_{\text{rec}}$ ” should read “ $0.01v_{\text{rec}}$.”

Hanbury Brown and Twiss correlations in atoms scattered from colliding condensates

Klaus Mølmer

Lundbeck Foundation Theoretical Center for Quantum System Research, Department of Physics and Astronomy, University of Aarhus, DK-8000 Århus C, Denmark

A. Perrin, V. Krachmalnicoff, V. Leung, D. Boiron, A. Aspect, and C. I. Westbrook

Laboratoire Charles Fabry de l'Institut d'Optique, CNRS, Université Paris-sud Campus Polytechnique, RD128, 91127 Palaiseau, France

(Received 1 October 2007; published 4 March 2008)

Low energy elastic scattering between clouds of Bose condensed atoms leads to the well known s -wave halo with atoms emerging in all directions from the collision zone. In this paper we discuss the emergence of Hanbury Brown and Twiss coincidences between atoms scattered in nearly parallel directions. We develop a simple model that explains the observations in terms of an interference involving two pairs of atoms each associated with the elementary s -wave scattering process.

DOI: [10.1103/PhysRevA.77.033601](https://doi.org/10.1103/PhysRevA.77.033601)

PACS number(s): 03.75.Gg, 34.50.-s

I. INTRODUCTION

In a number of experiments, Bose-Einstein condensates have been prepared to collide with each other with well defined collision energies and momenta. At the microscopic level, when two particles with equal mass and opposite velocities collide in an s -wave collision, the collision partners will propagate away from each other with the same probability amplitude in all directions, but their individual momenta are correlated in opposite directions, as their total center-of-mass momentum is conserved in the collision process. In experiments with colliding condensates, the scattering into all directions has been clearly observed as a so-called s -wave halo of scattered particles [1]. The observation of pair correlations of particles leaving the collision region back-to-back (see Fig. 1), requires efficient detection of all momentum components of individual atoms, and this correlation has recently been observed as a significant coincidence signal in a collision experiment with Bose-Einstein condensates of metastable atomic helium [2]. The same experiment also observed an increased coincidence of particles scattered into *the same* direction. This phenomenon is due to the bosonic nature of the particles and to the fact that several independent scattering processes occur simultaneously.

We shall present a theoretical analysis of this Hanbury Brown and Twiss correlation phenomenon, aiming at a simple model which explains its qualitative and quantitative character in experiments. It is important to emphasize that the appearance of atoms moving in the same direction is not compatible with momentum conservation in a single collision process of two counterpropagating atoms, and our discussion will, indeed, refer to effects that rely on a many-body treatment of the collision of larger ensembles. In order to get physical insight, we will separate the problem in two: first, we treat independent pairwise collisions in which the collisional interaction gives rise to pairs of scattered atoms, and second, we treat the evolution of the many-body state describing the ensemble of scattered atoms neglecting the interactions in order to apply analytic methods. The validity of this separation and means to improve the theory, if necessary, will be discussed.

In Sec. II, we present a full second quantized description of the collision of a large number of identical bosons. We

shall write down the second quantized many-body Hamiltonian, and discuss how the elementary processes of interest relate to the different terms in this Hamiltonian. We treat the case where all the atoms initially populate two counterpropagating single particle states which are only weakly depleted by the collisions, and which will hence serve as c -number field sources for creation of pairs. This is in analogy with the quantum optics treatment of spontaneous four-wave mixing, where photon pairs are generated from the interaction of two incident laser beams, described by classical electromagnetic waves. In Sec. III, we discuss the Bogoliubov transformation, which provides a very accurate approximation to the time evolution of the system. We shall not, however, apply this transformation in a quantitative treatment, but rather show that its formal structure already predicts the collinear [Hanbury Brown and Twiss (HBT)] correlation and motivates a quite general analytical Ansatz for the quantum state of the scattered atoms. In Sec. IV, we shall consider the leading two- and four-atom terms in an expansion of the quantum state of scattered atoms, and show that they hold the key to the observed Hanbury Brown and Twiss correla-

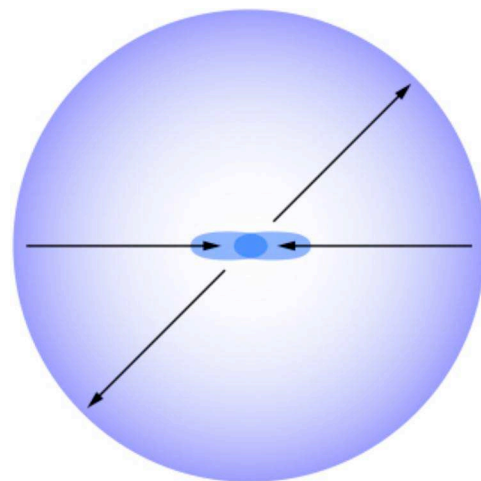


FIG. 1. (Color online) Diagrammatic representation of two condensates colliding and giving rise to an s -wave halo of scattered particles. Particles are scattered pairwise back-to-back.

tions. In Sec. V, we shall use energy conservation and phase matching considerations to motivate a simple analytical model, from which we show that the coincidence of scattered particles in the same direction, though a many-body effect, can be understood quantitatively from the properties of the simple two-atom scattering wave function. Section VI concludes the paper with a discussion of the insights offered by our analysis.

II. COLLIDING BOSE-EINSTEIN CONDENSATES

The Hamiltonian,

$$H = \int d\vec{r} \hat{\Psi}^\dagger(\vec{r}) \left(-\frac{\hbar^2}{2m} \Delta + V(\vec{r}) + \frac{g}{2} \hat{\Psi}^\dagger(\vec{r}) \hat{\Psi}(\vec{r}) \right) \hat{\Psi}(\vec{r}), \quad (1)$$

with field operators obeying the Bosonic commutator relations $[\Psi(\vec{r}), \Psi^\dagger(\vec{r}')] = \delta(\vec{r} - \vec{r}')$, gives a good description of bosons interacting at low collision energies via a short range potential. The interaction is represented by a delta-function interaction term with strength g , proportional to the s -wave scattering length. The atoms may be subject to a wide range of trapping or guiding potentials $V(\vec{r})$, or they may propagate freely ($V=0$), and the initial state of the system may be specified according to experimental preparation procedures to describe, for example, a single condensate or several macroscopically populated components. We are interested in the situation, in which two condensates with well defined momenta, and hence relatively large spatial extent, propagate toward each other. The conventional second quantized Hamiltonian fully describes the problem, and a Monte Carlo-type simulation of the dynamics [3–5], and perhaps even simpler simulation approaches based on truncated Wigner function expansions [6,7], may solve this problem in full generality by full three-dimensional (3D) propagation of stochastic Schrödinger-type equations.

We assume that elastic collisions occur with a sufficiently small cross section that the colliding condensates are only weakly depleted due to the collision term in Eq. (1). The Hamiltonian has terms describing the kinetic energy and the potential energy of atoms moving in the external potential and finally, a term describing the mean field repulsive or attractive potential due to the other atoms of the colliding condensates. But the product of two creation and two annihilation operators in the interaction term does not only read as density dependent correction to the potential energy in the Gross-Pitaevskii equation: the product of two creation operators may also cause the creation of a pair of atoms with momenta entirely different from the incident ones, extracted consistently from the condensates by the product of annihilation operators. The pairs of atoms “created” in the scattering process are the ones that are detected as the s -wave halo around the condensate collision region in Fig. 1.

We can think of each point in the collision zone as a point source for a pair of initially close atoms (atoms only collide at short range), which are subsequently separated by free propagation, perturbed by the interaction with the condensate components. This propagation, together with the coherent addition of pair amplitudes originating from the entire colli-

sion zone leads to a complicated many-body entangled state, but energy conservation, imposed after a sufficiently long interaction time, and momentum conservation, imposed by phase matching, serves to justify our simpler model, described below.

III. BOGOLIUBOV APPROXIMATION

If the original condensates are only weakly depleted by the scattering, we may follow Refs. [8–10] and expand the atomic field annihilation operator,

$$\hat{\Psi}(\vec{r}, t) = \psi_{\vec{k}_0}(\vec{r}, t) + \psi_{-\vec{k}_0}(\vec{r}, t) + \hat{\Psi}'(\vec{r}, t), \quad (2)$$

as a sum of mean field terms $\psi_{\pm\vec{k}_0}$ describing the incident wave packets, and noise terms $\hat{\Psi}'(\vec{r}, t)$, describing field components of the initially unpopulated scattering modes. We shall assume that there is no active external potential during the collision, and for convenience we omit the prime on the noise operator terms in the following. The Bogoliubov approximation consists of applying the Gross-Pitaevskii equation to the propagation in time of the mean field part and of obtaining the Heisenberg equations of motion for the field operators from an expansion of the Hamiltonian (1) to second order in the noise operator terms.

These equations of motion are linear in the field creation and annihilation operators,

$$i\hbar \partial_t \hat{\Psi}(\vec{r}, t) = \left(-\frac{\hbar^2}{2m} \Delta + 2g |\psi_{\vec{k}_0}(\vec{r}, t) + \psi_{-\vec{k}_0}(\vec{r}, t)|^2 \right) \hat{\Psi}(\vec{r}, t) + g [\psi_{\vec{k}_0}(\vec{r}, t) + \psi_{-\vec{k}_0}(\vec{r}, t)]^2 \hat{\Psi}^\dagger(\vec{r}, t). \quad (3)$$

By expanding the operator solution to this equation as a formal Bogoliubov transformation,

$$\hat{\Psi}(\vec{r}, t) = \int d\vec{r}' [f(\vec{r}, \vec{r}', t) \hat{\Psi}(\vec{r}', 0) + g(\vec{r}, \vec{r}', t) \hat{\Psi}^\dagger(\vec{r}', 0)], \quad (4)$$

the Heisenberg equations of motion (3) can be rewritten as partial differential equations for the c -number functions f and g , and the atomic annihilation operators are at any given time explicitly expressed as linear combinations of the annihilation and creation operators at time zero, where the initial state is assumed to be known (incident condensate wave functions, no scattered atoms). The mean atom number and any higher order correlation function of the field can therefore be expressed algebraically in terms of the expansion coefficients of the Bogoliubov transformation and the known vacuum expectation values of field operator products. Although obviously related, the use of the Bogoliubov transformation here is different from the Bogoliubov approximation used to identify low-lying, collective excitation modes in a condensate. The analysis rather follows the philosophy of squeezed light generation with optical parametric oscillators in quantum optics, where the Bogoliubov method is used to diagonalize a multimode Hamiltonian with pair creation and annihilation operators [11] (see also [12,13]). By use of the Bogoliubov approximation, the full many-body problem has

been reduced to partial differential equations of a complexity comparable to the single particle Schrödinger equation, and one only has to solve time dependent wave equations in three spatial dimensions as done in Refs. [8–10].

Here we shall demonstrate some properties of the solution that follow by purely analytical arguments, i.e., without access to the precise solution. Since the initial state of the atomic scattering modes (momentum components) of interest is the vacuum state, which has a Gaussian (Wigner) probability distribution for the multimode field variables, and the Bogoliubov transformation is linear in field operators, the state will, independently of the precise form of the transformation, at all later times be a Gaussian with vanishing mean field expectation value [14]. If we restrict the analysis to a single final momentum state (mode), by a partial trace over all other modes, the state of this mode is also a Gaussian state with vanishing mean amplitude. It is thus fully characterized by the second moments of the Hermitian linear combinations $q_{\vec{k}} \equiv (\hat{\Psi}^\dagger(\vec{k}) + \hat{\Psi}(\vec{k}))/\sqrt{2}$, $p_{\vec{k}} \equiv i(\hat{\Psi}^\dagger(\vec{k}) - \hat{\Psi}(\vec{k}))/\sqrt{2}$ of the field operators. We now wish to establish that our Gaussian distribution is symmetric, i.e., $\text{Var}(q_{\vec{k}}) = \text{Var}(p_{\vec{k}})$. This indeed follows if the “anomalous” moments $\langle \hat{\Psi}^\dagger(\vec{k})^2 \rangle = \langle \hat{\Psi}(\vec{k})^2 \rangle = 0$, i.e., if there is no coherence between states differing by two atoms propagating in the given direction. We now apply the physical argument, that the collisional Hamiltonian does not produce such coherence, since the collision process can only produce pairs of atoms propagating in opposite directions, and states, e.g., with zero and two atoms with momentum \vec{k} must also contain zero and two atoms with momentum around $-\vec{k}$. The anomalous moments vanish due to the orthogonality of these parts of the wave function.

It is well known in quantum optics, that a symmetric Gaussian state is equivalent to an incoherent mixture of number states with exponential number distribution, also known as a thermal state with the density matrix [11],

$$\rho_1 = (1 - |t|^2) \sum |t^{2n}|^n \langle n |. \quad (5)$$

The state conditioned upon detection, and annihilation, of a single particle reads,

$$\rho_c = \nu \hat{a} \rho_1 \hat{a}^\dagger = \frac{(1 - |t|^2)^2}{|t|^2} \sum_n |t^{2n}|^n |n - 1\rangle \langle n - 1|, \quad (6)$$

where ν is a normalization constant. A straightforward calculation shows that this state has precisely twice as many bosons on average as (5), and hence that the probability to detect two bosons by a low efficiency detector is twice the square of the single quantum detection probability. It thus follows that the coincidence counting rate for observing two atoms leaving the collision zone in the same, narrowly defined, direction, $\langle \hat{\Psi}^\dagger(\vec{k}) \hat{\Psi}^\dagger(\vec{k}) \hat{\Psi}(\vec{k}) \hat{\Psi}(\vec{k}) \rangle$ is twice the square of the mean counting rate, and twice the coincidence rate for seeing atoms in two unrelated directions.

Without performing any calculations, we therefore understand qualitatively the observed coincidences observed in the experiments [2] as the direct consequence of the thermal counting statistics (Gaussian quadrature distribution) of the

output flux in all scattering directions. This is the famous Hanbury Brown and Twiss effect [17–20] observed originally as photon bunching in chaotic light resulting from the addition of the contributions of many incoherent emitters. We note that the factor n in the expansion (6) is a bosonic amplification factor stemming from the \sqrt{n} coefficients accompanying the annihilation operator acting on the quantum state. The effects of this amplification factor are also observed in condensate formation [21] and matter wave amplification [22] experiments. In order to provide a natural estimate of the HBT momentum correlation function, one could develop the field correlations by solution of the linear Bogoliubov-de-Gennes equations for the problem [8–10] which by the corresponding linear transformation of operators provides the first and second order momentum correlation functions and hence the momentum range within which the bunching effect takes place. Here, we will rather keep track of the binary scattering states, and in particular of the counterpropagating partners, which will give us an alternative and very useful physical interpretation of the effect.

The Bogoliubov transformation of field operators is equivalent to a multimode unitary squeezing operation [11], which is indeed nothing but the time evolution operator of a Hamiltonian with quadratic terms in field creation and annihilation operators. Such an operator can be ordered as a product of three exponentials [15,16]: one involving a sum of products of pairs of creation operators, one involving a sum of products of creation and annihilation operators and one involving a sum of products of pairs of annihilation operators. When acting on the initial vacuum state vector, only the unit term of the series expansion of the latter two exponentials contribute, and the state can therefore be written in terms of a quadratic form of creation operators of atoms, e.g., in the momentum space representation,

$$|\Psi\rangle = N_\Psi \exp\left(\int d\vec{k}_1 d\vec{k}_2 \psi(\vec{k}_1, \vec{k}_2) \hat{\Psi}^\dagger(\vec{k}_1) \hat{\Psi}^\dagger(\vec{k}_2)\right) |\text{vac}\rangle. \quad (7)$$

The function $\psi(\vec{k}_1, \vec{k}_2)$ generally depends in a complex manner on the dynamical evolution. It is of course related to the scattering wave function of a single pair of atoms, and we shall come back to this relationship in connection with the model studied in Sec. V of the paper. The use of second quantization automatically yields the bosonic symmetry of our state, but in addition we can require that the pair amplitude function obey the explicit exchange symmetry $\psi(\vec{k}_1, \vec{k}_2) = \psi(\vec{k}_2, \vec{k}_1)$. For now, let us assume, that the propensity for atoms to be scattered into opposite directions also implies that $\psi(\vec{k}_1, \vec{k}_2)$ takes nonvanishing values for all directions of the scattered particles, but only if $\vec{k}_1 \sim -\vec{k}_2$. The function $\psi(\vec{k}_1, \vec{k}_2)$ is not a normalized wave function: the larger its amplitude the more particle pairs are created, and higher order terms of the exponential play more and more important roles. The many-body state $|\Psi\rangle$ is normalized by the prefactor N_Ψ in (7).

We now proceed to determine the density-density correlations of atoms detected in two different directions, labeled by

momentum states (\vec{k}, \vec{k}') , i.e., the expectation value

$$F(\vec{k}, \vec{k}') \propto \langle \hat{\Psi}^\dagger(\vec{k}) \hat{\Psi}^\dagger(\vec{k}') \hat{\Psi}(\vec{k}') \hat{\Psi}(\vec{k}) \rangle \quad (8)$$

The state (7) is a Gaussian state, and by Wick's theorem [23] this expectation value can be written down in terms of only pair-expectation values. We shall address the contribution from the four-atom component in the expansion of the exponential in (7), as this provides a straightforward interpretation of the origin and the behavior of the atomic Hanbury Brown and Twiss correlations.

IV. TWO-ATOM AND FOUR-ATOM STATES

The state (7) can be written explicitly,

$$|\Psi\rangle = N_\Psi \left(|\text{vac}\rangle + \int d\vec{k}_1 d\vec{k}_2 \psi(\vec{k}_1, \vec{k}_2) \hat{\Psi}^\dagger(\vec{k}_1) \hat{\Psi}^\dagger(\vec{k}_2) |\text{vac}\rangle + \frac{1}{2} \left(\int d\vec{k}_1 d\vec{k}_2 \psi(\vec{k}_1, \vec{k}_2) \hat{\Psi}^\dagger(\vec{k}_1) \hat{\Psi}^\dagger(\vec{k}_2) \right)^2 |\text{vac}\rangle + \dots \right). \quad (9)$$

The zero order term is the vacuum state. The first order term is a two-atom state of atoms propagating back-to-back, and the second order term of the series expansion of (7) is the four-atom state

$$|\Psi_4\rangle \equiv \left(\int d\vec{k}_1 d\vec{k}_2 \psi(\vec{k}_1, \vec{k}_2) \hat{\Psi}^\dagger(\vec{k}_1) \hat{\Psi}^\dagger(\vec{k}_2) \right)^2 |\text{vac}\rangle, \quad (10)$$

which we will show accounts for the observed HBT effect. The squared pair creation operator in (10) can be expanded as a fourfold integral. To obtain the correlation function (8), we have to apply the product of the two annihilation operators on $|\Psi_4\rangle$ and determine the squared norm of the resulting state,

$$F(\vec{k}, \vec{k}') \propto \|\hat{\Psi}(\vec{k}) \hat{\Psi}(\vec{k}') |\Psi_4\rangle\|^2. \quad (11)$$

Using the field commutator relations, we can shift the annihilation operators to the right of all creation operators in (11). This yields a total of 12 terms, which by relabeling and use of the exchange symmetry can be reduced to a sum of three different contributions,

$$\begin{aligned} \hat{\Psi}(\vec{k}) \hat{\Psi}(\vec{k}') |\Psi_4\rangle &\propto \int d\vec{k}_1 d\vec{k}_2 \{ \psi(\vec{k}_1, \vec{k}_2) \psi(\vec{k}, \vec{k}') \\ &+ \psi(\vec{k}_1, \vec{k}) \psi(\vec{k}_2, \vec{k}') \\ &+ \psi(\vec{k}_1, \vec{k}') \psi(\vec{k}_2, \vec{k}) \} \hat{\Psi}^\dagger(\vec{k}_1) \hat{\Psi}^\dagger(\vec{k}_2) |\text{vac}\rangle. \end{aligned} \quad (12)$$

and thus its squared norm:

$$\begin{aligned} F(\vec{k}, \vec{k}') &\propto \int d\vec{k}_1 d\vec{k}_2 \{ \psi(\vec{k}_1, \vec{k}_2) \psi(\vec{k}, \vec{k}') + \psi(\vec{k}_1, \vec{k}) \psi(\vec{k}_2, \vec{k}') \\ &+ \psi(\vec{k}_1, \vec{k}') \psi(\vec{k}_2, \vec{k}) \}^2. \end{aligned} \quad (13)$$

This is the main result of the paper. Dealing explicitly with

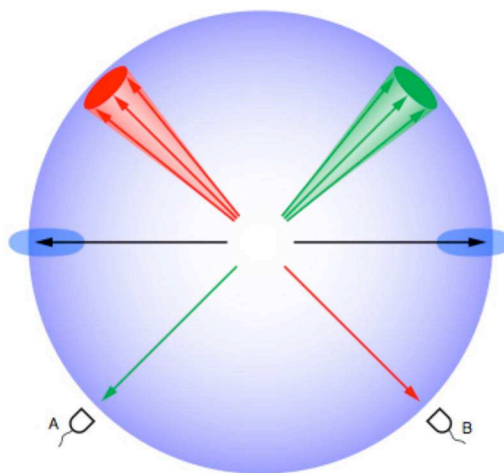


FIG. 2. (Color online) State of four atoms, scattered pairwise back-to-back. Atoms detected by detectors A and B in an arbitrary pair of directions have partners recoiling in the opposite directions within a certain width imposed by the uncertainty on total and relative momentum of the atoms. The quantum state of the detected pair is obtained by a partial trace over the recoiling momentum components, and the coincidence counting yield in the detectors is just the product of the single detector count signals

the four atom component it is easy to see what happens. In Fig. 2, we illustrate the case of detection of a particle pair in random directions. Because, as noted below Eq. (4), $\psi(\vec{k}, \vec{k}')$ vanishes unless \vec{k} and \vec{k}' are anti-parallel, the first term in Eq. (10) only contributes if the detectors correspond to opposite directions. For opposite or random directions such as in Fig. 2, there is also no cross term between the second two terms because one vanishes whenever the other is finite. If (\vec{k}, \vec{k}') are nearly parallel, as illustrated in Fig. 3, the last two terms evaluate the two different ψ -terms at the detector directions and at the direction specified by the integration variables.

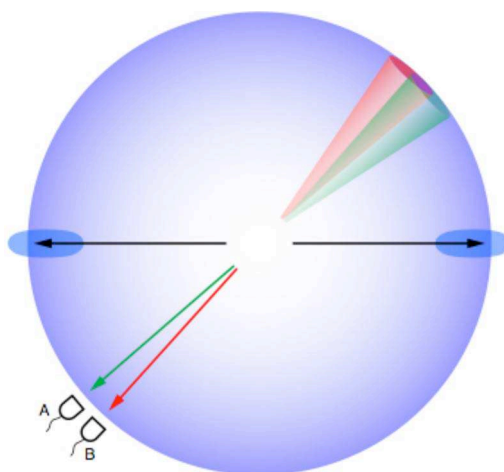


FIG. 3. (Color online) State of four atoms, with two atoms detected in nearly parallel directions. The detected atoms are not unambiguously identified with their recoiling partners if their momentum distributions are wide enough to overlap. This leads to an interference term in the coincidence counting yield in detectors A and B as expressed by the formal expression (13).

This means that values of the integration variables \vec{k}_1, \vec{k}_2 exist (opposite to the detector directions), where both of the last terms in (13) contribute, namely if \vec{k}_1 and \vec{k}_2 are within the “recoil cone” of both detection directions \vec{k} and \vec{k}' . For identical \vec{k} and \vec{k}' this interference give precisely the factor 2 increase of coincidences compared to the case of random directions. We also note that the enhanced coincidences occur within a solid angle specified precisely by this “recoil cone”. The next section develops our model one step further and carries out the calculation for the special choice of a Gaussian for the function $\psi(\vec{k}_1, \vec{k}_2)$.

V. RESULT FOR A SIMPLE ANSATZ FOR $\psi(\vec{k}_1, \vec{k}_2)$

As stated above, the Bogoliubov approximation to the actual state can be found numerically by solution of linear wave equations. In this section, we shall rather take a simpler approach by making an Ansatz for the shape of the function ψ by appealing to the dynamics and the conservation laws valid in the bipartite collision dynamics.

Energy conservation, which is effectively enforced during the temporal solution of the Schrödinger equation, suggests that the atomic pair state $\psi(\vec{k}_1, \vec{k}_2)$ describes particles with the same energy as the incident condensate particles. Momentum conservation suggests that they also have the same total momentum as the colliding pair. Due to the finite size of the colliding clouds, this does not strictly imply that the two atoms must have exactly opposite momenta. The finite size of the collision zone implies a quantum mechanical momentum uncertainty, and if contributions from small regions (with correspondingly large total momentum uncertainty) are added coherently the resulting phase matching condition is not sharp if the entire collision zone has finite size. There are therefore quantum fluctuations of both the modulus and direction of the momenta. When the particles escape from the collision zone as illustrated in Fig. 1, they are also repelled by the mean field interaction with the two condensate components. Here we will not try to describe accurately the effect of this interaction, which is in any case small when atoms leave a condensate after receiving an initial kinetic energy large compared to the chemical potential [24]. Note, however, that such mean field repulsion has in fact turned out to be tractable in the atom laser output from a condensate, where a generalized ABCD matrix formalism yields an analytical description of the propagation [25].

We define coordinates such that the nearly parallel \vec{k}, \vec{k}' of interest are close to the negative z -direction. Their partners at \vec{k}_1, \vec{k}_2 must both be close to the positive z -direction, and we shall assume the z -coordinates to be equal and opposite and only look at their x and y components. Their widths are related to the wave functions of the colliding condensates, both due to the amplitude of collisions out of these condensates and due to the mean field repulsion, and they are thus in general anisotropic. We restrict for simplicity the integration to one transverse coordinate (putting vector arrows on the arguments will yield the 2D result), and we assume that a single pair is described by a wave function, where the wave function amplitude for the recoiling partner has a bell shaped

profile, that we for simplicity approximate by a Gaussian, centered at minus the coordinates of the detected particle. The width of this wave function is parametrized by a momentum width K which thus represents both the momentum width of the colliding condensate particles and the acceleration due to the mean field.

Assuming thus the last two terms in (13) to be of such Gaussian shape, and ignoring the first term which vanishes for the geometry studied, we can explicitly calculate the coincidence signal:

$$\begin{aligned} F(\vec{k}, \vec{k}') &\propto \int dk_1 dk_2 \exp\{-[(k_1 + k)^2 + (k_2 + k')^2]/2K^2\} \\ &\quad + \exp\{-[(k_1 + k')^2 + (k_2 + k)^2]/2K^2\} \\ &\quad \times 1 + \exp[-(k - k')^2/2K^2], \end{aligned} \quad (14)$$

where we recall that k and k' here refer to (small) transverse coordinates of the detector directions with respect to a given axis, i.e., $(k - k')$ is the radial momentum of the outgoing particles multiplied with their mutual (small) angle in radians.

We recover the Hanbury Brown and Twiss correlations, and we observe that the correlations persist for final state momenta within a distance from each other of the order of the quantum mechanical uncertainty of the total momentum of the atom pair escaping the collision zone. This is in accord with our interpretation in terms of the interference between the indistinguishable components illustrated as the overlapping recoil cones in Fig. 1(c), that leads to the last term in (14) depending on both k and k' , whereas the direct terms lose the k and k' dependence due to the Gaussian integrals.

It is interesting to note, that Eq. (14) follows from a two-state amplitude $\psi(k, k') \propto \exp(-(k + k')^2/2K^2)$ for transverse momentum components of atoms propagating in nearly opposite directions, and therefore the two atom component of Eq. (9) predicts a correlation of atoms in opposite directions with the dependence $|\psi(k, k')|^2 \propto \exp(-(k + k')^2/K^2)$. The Hanbury Brown and Twiss bunching thus occurs within a Gaussian width that is $\sqrt{2}$ times larger than the range of correlation of recoiling atomic momenta. This prediction for the Gaussian wave functions has been verified by more detailed analysis of the full 3D propagation [5]. One way to understand the broadening is to recognize that the density dependence of the pair production mechanism results in a source which is spatially narrower than the condensates themselves.

Although we have based our analysis on the four-atom component of the full many body states, we have argued that a calculation based on the full state would yield the same results, and in particular that the HBT correlation amounts to a factor of two in parallel directions while the correlation in opposite directions is not limited by this factor. When multiple scattering is neglected, the complete many-body problem is solved by the Bogoliubov-de-Gennes equations, and the resulting Gaussian or thermal character of the many-body state is fully accounted for by the second moments. This does not imply, however, that one would get the same quantitative results for scattering of few and many atoms. If the

normalized wave function for a single scattered pair in the case of a low scattering probability is denoted $\chi(\vec{k}_1, \vec{k}_2)$, it may be reasonable to describe the collision process by the effective Hamiltonian $H = \kappa \int d\vec{k}_1 d\vec{k}_2 \chi(\vec{k}_1, \vec{k}_2) \hat{\Psi}^\dagger(\vec{k}_1) \hat{\Psi}^\dagger(\vec{k}_2) + \text{H.c.}$, where κ is a coupling strength. The unitary time evolution operator is the exponential of this operator multiplied by $(t/i\hbar)$ or integrated over a suitable time interval. We note that this does not generally result in an expression for $\psi(\vec{k}_1, \vec{k}_2)$ in (7) which is proportional to $\chi(\vec{k}_1, \vec{k}_2)$. In the case of single mode squeezing, it is known that one must evaluate the hyperbolic tangent function of the squeezing parameter to convert the squeezing operator to the normal order form [11], and in our general multimode case, normal ordering is accomplished by evaluating the tanh function of a matrix argument [15,16]. For small arguments, in the perturbative regime of spontaneous four wave mixing, tanh is a linear function, and we get the same momentum dependence. Outside the perturbative regime, we retain the factor 2 bunching effect by our general argument, but the precise shape of the correlation peak may be modified.

VI. DISCUSSION

We have presented a simple interpretation of the observed Hanbury Brown and Twiss correlations observed in the elastic scattering of Bose-Einstein condensates. We emphasize, that in order to make quantitative predictions, it is necessary to make a more elaborate calculation of the pair formation and the propagation of the atoms both in free space and in the regions where the mean field of the condensate components act as a perturbing potential. Such a description is offered by the Bogoliubov theory in Refs. [8–10], and we note that [10] as well as [4] also provide numerical evidence for the density correlations discussed in the present paper. Our interpretation relies on the structural property of the solutions to the Bogoliubov theory (7), but it proceeds by applying a different physical reasoning which recognizes that the two detected particles are accompanied by collision partners propagating in the opposite directions, and we hence observe part of a four-atom state. This is an appealing picture, in particular because the prediction of the coincidence signal, and in particular its width, relates to the transverse spreading of the pair wave functions of oppositely propagating atoms after the bipartite collisions.

As we discussed in the text, when observed from only one direction, the reduced density matrix of the expanding atomic cloud is similar to a thermal state. This density matrix is sufficient to predict the outcome of any measurement on the observed part of the system, and it explains the experimental findings as an analog of the observed bunching of the photons from a thermal/chaotic light source. The optical Hanbury Brown and Twiss experiment has a characteristic transverse spatial scale over which the correlation falls to unity, related to the transverse momentum distribution of the photons impinging on the detector, and in a similar manner we have a finite transverse coherence length in the atomic

scattering experiment. We discussed the isotropic s-wave scattering, with possible corrections due to anisotropy of the colliding clouds and spatial phase matching. In addition, one may apply a periodic background potential, which may alter the energy dependence on the momentum vector of moving atoms, and hence modify the scattering profile [26,27], and with confinement to one dimension, it may lead to highly selective population of specific momentum states with strong, observable quantum correlations [28,29].

It is interesting to recall that a mixed quantum state, i.e., a density matrix, can always be formally obtained as the reduced state of a larger quantum system which is in a pure state, and in particular any thermal quantum state of a bosonic degree of freedom can be modeled by a pure squeezed state in a doubled tensor space. This is known as the “thermofields” formulation [30], and for example the single mode thermal state (5) can be obtained as the trace over one of the modes of a non-degenerate two mode squeezed state, as obtained, e.g., from a non-degenerate optical parametric oscillator (OPO),

$$|\psi_{\text{OPO}}\rangle \propto \sum_n r^n |n, n\rangle. \quad (15)$$

In our four-atom analysis, the apparently thermal state arriving at nearby detectors is precisely part of such a larger system. The advantage of this insight is that the spatial scale of the extended state, in our case the probability distribution of the total momentum of scattered atoms, directly yields the density correlations in the reduced density matrix. More elaborate analyses [31] have shown how density-density correlations in the image of expanding gases can reveal a wide range of more complex many-body properties, as confirmed by experiments [32].

Finally, if the collision occurs between two different bosonic species, the same kind of correlations will occur for the density correlations of each species, but not for the cross correlation, where the recoiling atoms are distinguishable, and hence do not interfere. For collisions between bosons and fermions the situation is different. Electrons have been demonstrated to show antibunching related to their fermionic character [33], and antibunching has also been demonstrated for neutral fermionic atoms [34,35]. Collisions between a Bose condensate and a degenerate Fermi gas, where all fermions initially occupy orthogonal states, but where Pauli blocking forbids more than one atom ending up in the same final state should lead to observable antibunching effects in the scattered bosons.

ACKNOWLEDGMENTS

The authors gratefully acknowledge discussions with Karen Kheruntsyan and financial support from the European Union integrated project SCALA and the ESF cold atom network QUDEDIS. The Atom Optics group of LCFIO is a member of the IFRAF institute, and is supported by the French ANR and by the Atom Chips program of the European Union.

- [1] K. Gibble, S. Chang, and R. Legere, *Phys. Rev. Lett.* **75**, 2666 (1995); A. P. Chikkatur, A. Görlitz, D. M. Stamper-Kurn, S. Inouye, S. Gupta, and W. Ketterle, *ibid.* **85**, 483 (2000); J. M. Vogels, K. Xu, and W. Ketterle, *ibid.* **89**, 020401 (2002); N. Katz, J. Steinhauer, R. Ozeri, and N. Davidson, *ibid.* **89**, 220401 (2002); C. Buggle, J. Leonard, W. von Klitzing, and J. T. M. Walraven, *ibid.* **93**, 173202 (2004); N. R. Thomas, N. Kjærgaard, P. S. Julienne, and A. C. Wilson, *ibid.* **93**, 173201 (2004).
- [2] A. Perrin, H. Chang, V. Krachmalnicoff, M. Schellekens, D. Boiron, A. Aspect, and C. I. Westbrook, *Phys. Rev. Lett.* **99**, 150405 (2007).
- [3] M. J. Steel, M. K. Olsen, L. I. Plimak, P. D. Drummond, S. M. Tan, M. J. Collett, D. F. Walls, and R. Graham, *Phys. Rev. A* **58**, 4824 (1998).
- [4] P. Deuar and P. D. Drummond, *Phys. Rev. Lett.* **98**, 120402 (2007).
- [5] A. Perrin, C. M. Savage, D. Boiron, V. Krachmalnicoff, C. I. Westbrook, and K. Kheruntsyan, e-print arXiv:0712.2145v1.
- [6] A. Sinatra, C. Lobo, and Y. Castin, *Phys. Rev. Lett.* **87**, 210404 (2001).
- [7] A. A. Norrie, R. J. Ballagh, and C. W. Gardiner, *Phys. Rev. A* **73**, 043617 (2006).
- [8] P. Ziń, J. Chwedeńczuk, A. Veitia, K. Rzażewski, and M. Trippenbach, *Phys. Rev. Lett.* **94**, 200401 (2005).
- [9] J. Chwedeńczuk, P. Ziń, K. Rzażewski, and M. Trippenbach, *Phys. Rev. Lett.* **97**, 170404 (2006).
- [10] P. Ziń, J. Chwedeńczuk, and M. Trippenbach, *Phys. Rev. A* **73**, 033602 (2006).
- [11] C. M. Caves and B. L. Schumaker, *Phys. Rev. A* **31**, 3068 (1985).
- [12] U. V. Poulsen and K. Mølmer, *Phys. Rev. A* **63**, 023604 (2001).
- [13] U. V. Poulsen and K. Mølmer, *Phys. Rev. A* **76**, 013614 (2007).
- [14] A. K. Ekert and P. L. Knight, *Phys. Rev. A* **43**, 3934 (1991).
- [15] C. F. Lo, *Phys. Rev. A* **51**, 1706 (1995).
- [16] Hong-yi Fan, *J. Opt. B: Quantum Semiclassical Opt.* **5**, R147 (2003).
- [17] R. Hanbury Brown and R. Q. Twiss, *Nature (London)* **178**, 1046 (1956).
- [18] R. Q. Twiss, A. G. Little, and R. Hanbury Brown, *Nature (London)* **180**, 324 (1957).
- [19] G. A. Rebka and R. V. Pound, *Nature (London)* **180**, 1035 (1957).
- [20] B. L. Morgan and L. Mandel, *Phys. Rev. Lett.* **16**, 1012 (1966).
- [21] H.-J. Miesner, D. M. Stamper-Kurn, M. R. Andrews, D. S. Durfee, S. Inouye, and W. Ketterle, *Science* **279**, 1005 (1998).
- [22] S. Inouye, T. Pfau, S. Gupta, A. P. Chikkatur, A. Görlitz, D. E. Pritchard, and W. Ketterle, *Nature (London)* **402**, 641 (1999).
- [23] W. H. Louisell, *Quantum Statistical Properties of Radiation* (John Wiley and Sons, New York, 1973).
- [24] N. P. Robins, C. Figl, S. A. Haine, A. K. Morrison, M. Jeppesen, J. J. Hope, and J. D. Close, *Phys. Rev. Lett.* **96**, 140403 (2006).
- [25] Y. Le Coq, J. H. Thywissen, S. A. Rangwala, F. Gerbier, S. Richard, G. Delannoy, P. Bouyer, and A. Aspect, *Phys. Rev. Lett.* **87**, 170403 (2001); J.-F. Riou, W. Guerin, Y. Le Coq, M. Fauquembergue, V. Josse, P. Bouyer, and A. Aspect, *ibid.* **96**, 070404 (2006).
- [26] N. Katz, E. Rowen, R. Ozeri, and N. Davidson, *Phys. Rev. Lett.* **95**, 220403 (2005).
- [27] K. Mølmer, *New J. Phys.* **8**, 170 (2006).
- [28] K. M. Hilligsøe and K. Mølmer, *Phys. Rev. A* **71**, 041602(R) (2005).
- [29] G. K. Campbell, J. Mun, M. Boyd, E. W. Streed, W. Ketterle, and D. E. Pritchard, *Phys. Rev. Lett.* **96**, 020406 (2006).
- [30] S. M. Barnett and P. L. Knight, *J. Opt. Soc. Am. B* **2**, 467 (1985).
- [31] E. Altman, E. Demler, and M. D. Lukin, *Phys. Rev. A* **70**, 013603 (2004); J. Grondalski, P. Alsing, and I. Deutsch, *Opt. Express* **5**, 249 (1999); J. Viana Gomes, A. Perrin, M. Schellekens, D. Boiron, C. I. Westbrook, and M. Belsley, *Phys. Rev. A* **74**, 053607 (2006).
- [32] S. Fölling, F. Gerbier, A. Widera, O. Mandel, T. Gericke, and I. Bloch, *Nature (London)* **434**, 481 (2005); M. Schellekens, R. Hoppeler, A. Perrin, J. Viana Gomes, D. Boiron, A. Aspect, and C. I. Westbrook, *Science* **310**, 648 (2005).
- [33] H. Kiesel, A. Renz, and F. Hasselbach, *Nature (London)* **418**, 392 (2002).
- [34] T. Jelte, J. M. McNamara, W. Hogervorst, W. Vassen, V. Krachmalnicoff, M. Schellekens, A. Perrin, H. Chang, D. Boiron, A. Aspect, and C. I. Westbrook, *Nature (London)* **445**, 402 (2007).
- [35] T. Rom, Th. Best, D. van Oosten, U. Schneider, S. Fölling, B. Paredes, and I. Bloch, *Nature (London)* **444**, 733 (2006).

Atomic four-wave mixing via condensate collisions

A Perrin¹, C M Savage², D Boiron¹, V Krachmalnicoff¹,
C I Westbrook¹ and K V Kheruntsyan^{3,4}

¹ Laboratoire Charles Fabry de l'Institut d'Optique, CNRS, Univ Paris-Sud,
Campus Polytechnique, RD128, 91127 Palaiseau Cedex, France

² ARC Centre of Excellence for Quantum-Atom Optics, Department of Physics,
Australian National University, Canberra ACT 0200, Australia

³ ARC Centre of Excellence for Quantum-Atom Optics,
School of Physical Sciences, University of Queensland, Brisbane,
QLD 4072, Australia

E-mail: christoph.westbrook@institutoptique.fr and
karen.kheruntsyan@uq.edu.au

New Journal of Physics **10** (2008) 045021 (26pp)

Received 11 December 2007

Published 30 April 2008

Online at <http://www.njp.org/>

doi:10.1088/1367-2630/10/4/045021

Abstract. We perform a theoretical analysis of atomic four-wave mixing via a collision of two Bose–Einstein condensates of metastable helium atoms, and compare the results to a recent experiment. We calculate atom–atom pair correlations within the scattering halo produced spontaneously during the collision. We also examine the expected relative number squeezing of atoms on the sphere. The analysis includes first-principles quantum simulations using the positive P -representation method. We develop a unified description of the experimental and simulation results.

⁴ Author to whom any correspondence should be addressed.

Contents

1. Introduction	2
2. Summary of experimental results	4
2.1. Overview of the experiment	4
2.2. Main results	5
3. Qualitative analysis	6
3.1. Width of the pair correlation functions	6
3.2. Width of the scattered halo	7
4. Model	9
5. Results and discussion	10
5.1. Main numerical example	10
5.2. Shorter collision time	13
5.3. Smaller collision velocity	15
5.4. Smaller scattering length	17
5.5. Relative number squeezing and violation of Cauchy–Schwartz inequality	19
6. Summary	21
Acknowledgments	22
Appendix A. Duration of the collision	22
Appendix B. Occupation number of the scattering modes and amplitude of the BB correlation	22
Appendix C. Width of the s-wave scattering sphere in the undepleted ‘pump’ approximation	23
Appendix D. Positive-P simulation parameters	24
References	25

1. Introduction

Recent years have seen the introduction of powerful new tools for studying degenerate quantum gases. For example, on the experimental side correlation measurements offer a new experimental probe of many-body effects [1]–[11]. On the theoretical side, the challenges posed by the new experimental techniques are being met by quantum dynamical simulations of large numbers of interacting particles in realistic parameter regimes. These are becoming possible due to the advances in computational power and improvements in numerical algorithms (for recent examples, see [12]–[15]).

In this paper, we study metastable helium ($^4\text{He}^*$), which is currently unique in *quantum atom optics* in that it permits a comparison of experimentally measured [16] and theoretically calculated quantum correlations. This is one of the first examples in which experimental measurements can be considered in the context of first-principles calculations. Our goal in this paper is to confront a theoretical analysis with the results of recent experiments on atomic four-wave mixing via a collision of two Bose–Einstein condensates (BECs) of metastable $^4\text{He}^*$ atoms [16]. Figure 1 is a schematic momentum space diagram of these experiments. Two condensates, whose atoms have approximately equal but opposite momenta, \mathbf{k}_1 and $\mathbf{k}_2 \simeq -\mathbf{k}_1$,

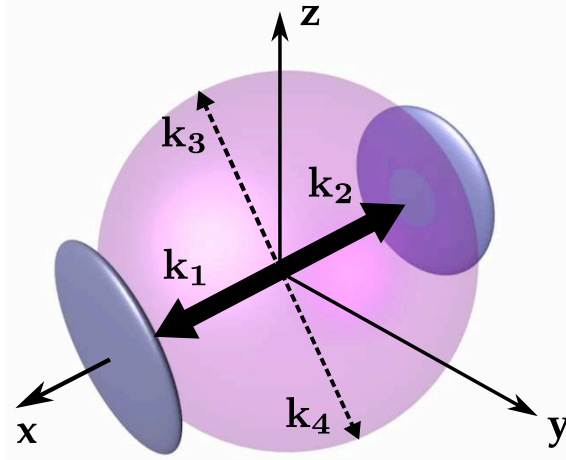


Figure 1. Schematic momentum space diagram of the atomic four-wave mixing interaction. Optical Raman pulses generate untrapped condensates with momenta \mathbf{k}_1 and $\mathbf{k}_2 = -\mathbf{k}_1$ parallel to the x -axis (dark disks). These undergo a four-wave mixing interaction to produce correlated atomic pairs on a spherical shell of radius k_1 .

interact by four-wave mixing, while they spatially overlap, to produce correlated atomic pairs with approximately equal but opposite momenta, \mathbf{k}_3 and \mathbf{k}_4 , satisfying momentum conservation, $\mathbf{k}_1 + \mathbf{k}_2 = \mathbf{k}_3 + \mathbf{k}_4$. Figure 1 corresponds to the experimental data shown in figure 2 of [16], since after time-of-flight expansion, atomic momentum is mapped into atomic position.

We perform first-principles quantum simulations of the collision dynamics using the positive P -representation method [17]–[20]. The advantage of this method is that given the Hamiltonian of the interacting many-body system, no additional approximations are imposed to simulate the quantum dynamics governed by the Hamiltonian. The drawback on the other hand, is that it usually suffers from large sampling errors and the boundary term problem [21] as the simulation time t_{sim} increases, eventually leading to diverging results.

An empirically estimated upper bound for the positive- P simulation time (beyond which the stochastic trajectories start to make large excursions in phase space, leading to boundary term problem and uncontrollable sampling errors [21]) for the evolution of condensates with s -wave scattering interactions is given approximately by [22]

$$t_{\text{sim}} \lesssim 2.5m(\Delta V)^{1/3}/[4\pi\hbar a\rho_0^{2/3}], \quad (1)$$

where m is the atom mass, a is the s -wave scattering length, ρ_0 is the condensate peak density, and $\Delta V = \Delta x \Delta y \Delta z$ is the volume of the elementary cell of the computational lattice, with lattice spacings of Δx , Δy and Δz . Applying this formula to metastable helium, we see that this is a particularly challenging case among commonly condensed atoms due to its small atomic mass and relatively large scattering length. Our simulations are restricted to short interaction times (typically $\lesssim 25 \mu\text{s}$), which are about six times shorter than the experimental interaction time of [16]. Despite this, our positive- P simulations provide useful insights into the experimental observations; in addition, they can serve as benchmarks for approximate theoretical methods (such as the Hartree–Fock–Bogoliubov method [23]–[26] or the truncated Wigner method [12, 13]) to establish the range of their validity.

We note that the simulations of BEC collisions of [12, 13] using the truncated Wigner method are in a different regime than the ones carried out here using the positive- P method. More specifically, the authors of [12, 13] simulate condensates at much higher densities, for which the approximations of the method [13, 27] are satisfied. The advantage of the Wigner method over the positive- P is that it does not suffer from boundary term problem and can be used to simulate condensate collisions for longer durations.

In the present paper, we calculate atom pair correlations within the scattering halo produced spontaneously during the collision (see figure 1). The scattering halo is a spherical shell in momentum space. In the limit of small occupation of the scattered modes, the s-wave nature of the collisions ensures an approximately uniform atom population over the halo. We consider the strength and the width of the correlation signal, as well as the momentum width of the halo. We also analyze relative atom number squeezing and the violation of the classical Cauchy–Schwartz inequality.

In section 2 of this paper, we will summarize the experimental results we wish to analyze. In section 3, we discuss order of magnitude estimates. In section 4, we describe simulations using the positive P -representation method, and in section 5, we discuss the results of our simulations. Section 6 summarizes our work.

2. Summary of experimental results

2.1. Overview of the experiment

The starting point of the experiment is a $^4\text{He}^*$ condensate of 10^4 – 10^5 atoms confined in a magnetic trap whose frequencies are: $\omega_x/2\pi = 47$ Hz and $\omega_y/2\pi = \omega_z/2\pi = 1150$ Hz. A sudden Raman outcoupling drives the trapped $^4\text{He}^*$ from the $m_x = 1$ Zeeman sublevel into the magnetic field insensitive state $m_x = 0$ [16]. The Raman transition also splits the initial ($m_x = 1$) condensate into two roughly equally populated condensates with opposite velocities along the x -direction. The magnitude of each velocity is equal to the recoil velocity $v_r = 9.2$ cm s $^{-1}$, defined by the momentum of the photons used to create the colliding condensates $\hbar k_r$, $k_r = 5.8 \times 10^6$ m $^{-1}$. The relative velocity $2v_r$ of the two condensates is about eight times higher than the speed of sound $c_s = \sqrt{\mu/m}$ of the initial condensate, ensuring that the relevant elementary excitations of the condensates correspond to free particles.

During the separation of the condensates, elastic collisions occurring between atoms with opposite velocities scatter a small fraction (5%) of the total initial atom number into the halo. The system is shown in three dimensions (3D) in an accompanying video of the experimental results after a 320 ms time of flight⁵. For the purposes of this paper, the experiment consists in the acquisition of the 3D positions of the particles scattered into the collision halo after the time of flight. This information permits the reconstruction of the 3D momentum vectors of the individual particles after they have ceased interacting with each other.

⁵ A 3D, animated rendition of the atomic positions 320 ms after release from the trap, available from stacks.iop.org/NJP/10/045021/mmedia. The vertical positions are derived from the arrival times as described in [16]. Each point corresponds to the detection of one atom and the animation shows the sum of 50 separate runs. The ellipsoids at the sides are the colliding condensates. The ellipsoids at the top and bottom result from imperfect Raman polarizations and stimulated atomic four-wave mixing (see [16]). The four condensates are excluded from the analysis given in the text.

2.2. Main results

Knowledge of the momentum vectors in turn permits the construction of two-particle correlation functions in momentum space. The correlation function shows features for particles traveling both back-to-back (BB) and collinearly. The BB correlation results from binary, elastic collisions between atoms, whereas the collinear (CL) correlation is a two particle interference effect involving members of two different pairs: a Hanbury Brown–Twiss correlation [28]. Both correlation functions are anisotropic because of the anisotropy of the initial colliding condensates.

To quantify these correlations, we first introduce the unnormalized normally-ordered second-order correlation function between the densities at two points in momentum space,

$$G^{(2)}(\mathbf{k}_1, \mathbf{k}_2) = \langle : \hat{n}(\mathbf{k}_1) \hat{n}(\mathbf{k}_2) : \rangle. \quad (2)$$

Here, $\hat{n}(\mathbf{k}) = \hat{a}^\dagger(\mathbf{k})\hat{a}(\mathbf{k})$ is the momentum density operator, $\hat{a}^\dagger(\mathbf{k})$ and $\hat{a}(\mathbf{k})$ are the Fourier transforms of the field creation and annihilation operators $\hat{\Psi}^\dagger(\mathbf{x})$ and $\hat{\Psi}(\mathbf{x})$, and the colons $::$ stand for normal ordering of the operators according to which all creation operators stand to the left of the annihilation operators, so that

$$\langle : \hat{n}(\mathbf{k}_1) \hat{n}(\mathbf{k}_2) : \rangle = \langle \hat{a}^\dagger(\mathbf{k}_1) \hat{a}^\dagger(\mathbf{k}_2) \hat{a}(\mathbf{k}_2) \hat{a}(\mathbf{k}_1) \rangle. \quad (3)$$

Because of a low data rate, the correlation measurements must be averaged over the entire collision sphere to get statistically significant results. The average CL second-order correlation as a function of the relative displacement Δk_i in the k_i -direction ($i = x, y, z$) is defined as

$$g_{\text{CL}}^{(2)}(\Delta k_i) = \frac{\int_{\mathcal{D}} d^3\mathbf{k} G^{(2)}(\mathbf{k}, \mathbf{k} + \mathbf{e}_i \Delta k_i)}{\int_{\mathcal{D}} d^3\mathbf{k} \langle \hat{n}(\mathbf{k}) \rangle \langle \hat{n}(\mathbf{k} + \mathbf{e}_i \Delta k_i) \rangle}, \quad (4)$$

where \mathbf{e}_i is the unit vector in the k_i -direction. The normalization of $g_{\text{CL}}^{(2)}(\Delta k_i)$ ensures that for uncorrelated densities $g_{\text{CL}}^{(2)}(\Delta k_i) = 1$. The integration domain \mathcal{D} in (4) selects a certain region of interest in momentum space and can be defined, for example, to contain only a narrow spherical shell and to eliminate the initial colliding condensates. Due to the averaging, the dependence of the correlation functions on the direction \mathbf{k} is lost.

The average BB correlation function $g_{\text{BB}}^{(2)}(\Delta k_i)$ between two diametrically opposite points, one of which is additionally displaced by Δk_i in the k_i -direction, is defined similarly to $g_{\text{CL}}^{(2)}(\Delta k_i)$:

$$g_{\text{BB}}^{(2)}(\Delta k_i) = \frac{\int_{\mathcal{D}} d^3\mathbf{k} G^{(2)}(\mathbf{k}, -\mathbf{k} + \mathbf{e}_i \Delta k_i)}{\int_{\mathcal{D}} d^3\mathbf{k} \langle \hat{n}(\mathbf{k}) \rangle \langle \hat{n}(-\mathbf{k} + \mathbf{e}_i \Delta k_i) \rangle}. \quad (5)$$

The experimental observations can be summarized as follows. The width of both correlation functions along the axial direction of the condensate, the x -axis, is limited by the resolution of the detector and hence contains little information about the collision. In the radial direction (with respect to the symmetry of the colliding condensates), one observes a peak which can be fitted to a Gaussian function with rms widths $\sigma_{y,z}^{\text{CL}}$ and $\sigma_{y,z}^{\text{BB}}$ for the CL and BB cases, respectively. The experimental results are summarized in the following table

$\sigma_{y,z}^{\text{BB}}/k_r$	$\sigma_{y,z}^{\text{CL}}/k_r$	$\sigma_{y,z}^{\text{CL}}/\sigma_{y,z}^{\text{BB}}$
0.081 ± 0.004	0.069 ± 0.008	0.85 ± 0.15

(6)

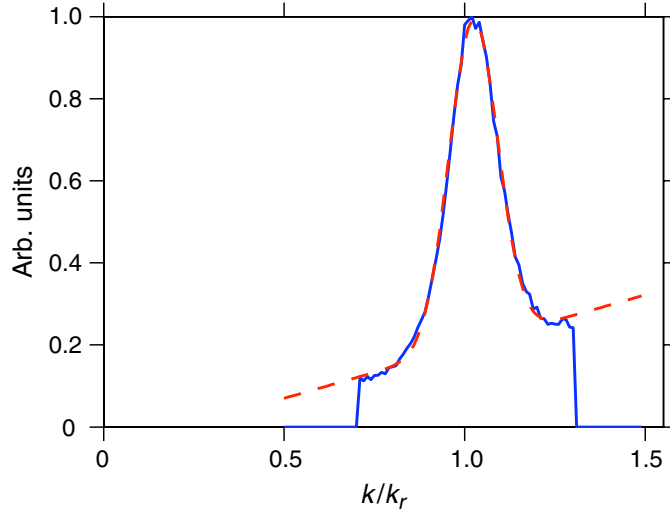


Figure 2. Cross-section of the scattering halo. A sloped background is present due to thermal atoms in the trap. This background has been fitted to a straight line and subtracted in order to estimate the rms width, $\delta k \simeq 0.067k_r$.

One can also use the data to deduce the averaged radial width δk of the scattering halo. Figure 2 shows a cross-section of the halo, averaged over all accessible scattering angles. The presence of the unscattered condensates prevents observation of the shell along the x -axis, but along the accessible directions we find $\delta k \simeq 0.067k_r$.

3. Qualitative analysis

In this section, we discuss some simple, analytical estimates of the measured quantities. In later sections, we will do more precise, numerical calculations which will verify the results of this section.

3.1. Width of the pair correlation functions

As discussed in [16], the width of the BB and CL correlation functions should be on the order of the momentum width of the initial condensate, which in turn is proportional to the inverse width of its spatial profile. For a Gaussian density profile of the initial condensate in position space $\rho(\mathbf{x}) = \langle \hat{\Psi}^\dagger(\mathbf{x})\hat{\Psi}(\mathbf{x}) \rangle = \rho_0 \exp[-\sum_{i=x,y,z} r_i^2/(2w_i^2)]$, and therefore a Gaussian density distribution in momentum space, $n(\mathbf{k}) = \langle \hat{n}(\mathbf{k}) \rangle \propto \exp[-\sum_{i=x,y,z} k_i^2/(2\sigma_i^2)]$, with $\sigma_i = 1/2w_i$, an approximate theoretical treatment based on a simple ansatz for the pair wavefunction predicts a Gaussian dependence of the BB and CL correlation functions on the relative wavevectors Δk_i [28]:

$$G^{(2)}(\mathbf{k}, -\mathbf{k} + \mathbf{n}_i \Delta k_i) \propto \exp\left(-\frac{\Delta k_i^2}{2(\sigma_i^{\text{BB}})^2}\right), \quad (7)$$

$$G^{(2)}(\mathbf{k}, \mathbf{k} + \mathbf{n}_i \Delta k_i) \propto \exp\left(-\frac{\Delta k_i^2}{2(\sigma_i^{\text{CL}})^2}\right). \quad (8)$$

The widths of the BB (σ_i^{BB}) and CL (σ_i^{CL}) correlations are related to the momentum-space width σ_i of the initial (source) condensate via [28]

$$\sigma_i^{\text{BB}}/\sigma_i = \sqrt{2}, \quad (9)$$

$$\sigma_i^{\text{CL}}/\sigma_i = 2, \quad (10)$$

and therefore the width of the BB correlation is $\sqrt{2}$ times smaller than the width of the CL correlation. Similar predictions of correlation widths have been made and discussed in [13, 24].

In section 5.1, the initial momentum-space widths are found to be $\sigma_x = 0.0025k_r$ and $\sigma_{y,z} = 0.055k_r$, assuming $N = 9.84 \times 10^4$ atoms. Expressing the experimentally measured widths in units of $\sigma_{y,z}$, we can rewrite (6) as

$\sigma_{y,z}^{\text{BB}}/\sigma_{y,z}$	$\sigma_{y,z}^{\text{CL}}/\sigma_{y,z}$	$\sigma_{y,z}^{\text{CL}}/\sigma_{y,z}^{\text{BB}}$
1.47 ± 0.07	1.25 ± 0.15	0.85 ± 0.15

(11)

and therefore, equation (9) is in agreement with the measured width of the radial BB correlation function, whereas (10) overestimates the width of the CL correlation function by almost 60%. As we show below, first-principles simulations using the positive- P method and incorporating atom–atom interactions result in widths which are closer to the experimental values.

The discrepancy between the two theoretical approaches (which apparently is larger for the CL correlations than for the BB ones) comes mostly from the fact that the above calculation is made for a Gaussian shape of the initial BEC density profile, whereas in practice and in the positive- P simulations the spatial density of a harmonically trapped condensate is closer to an inverted parabola (as in the Thomas–Fermi limit) rather than to a Gaussian. An alternative theoretical model [29], based on the undepleted source condensate approximation and a numerical solution to the linear operator equations of motion for scattered atoms, also confirms that for short times the momentum-space correlation widths are narrower if the source condensate has a parabolic spatial density profile, compared to the case of a Gaussian density profile.

3.2. Width of the scattered halo

A second, experimentally accessible quantity in a BEC collision is the width $\hbar\delta k_i$ in momentum space of the halo on which the scattered atoms are found. Clearly the momentum spread σ_i (in $i = x$ -, y - or z -direction) of the colliding condensates imposes a minimum width

$$\delta k_i \gtrsim \sigma_i. \quad (12)$$

This limit suggests that the halo could be anisotropic. As noted above, however, the experiment in [16] is not highly sensitive to such an anisotropy, and measures the width chiefly in the y - and z -directions.

Other physical considerations also affect this width, and suggest that the halo should rather be isotropic, in which case we can drop the index from δk . Here, we discuss two mechanisms that impose a finite radial width on the halo.

If the pairs are produced during a finite time interval Δt , the total energy of the pair is necessarily broadened by $\hbar/\Delta t$. This is true even if the relative momentum is well defined.

For a mean k -vector k_r , the finite interaction time between the colliding BECs results in a broadening of

$$\delta k \simeq \frac{m}{\hbar k_r \Delta t}, \quad (13)$$

where we assumed $\delta k/k_r \ll 1$. In the experiment, the collision time is sufficiently long that the above effect does not impose a limitation on the width of the sphere. In the positive- P simulations, however, numerical stability problems limit the maximum collision time that can be simulated, as discussed in section 5, and this time does indeed impose a width on the halo. For short collision times, where the scattering is in the spontaneous regime, our numerical results for the width δk are in good agreement with the simple estimate of equation (13).

For long collision times, it can happen that so many atoms are scattered that Bose enhancement and stimulated effects become important. In this case, the width of the scattering shell can be estimated by a slightly more involved approximate approach based on analytic solutions for the uniform system within the undepleted ‘pump’ (source condensate) approximation [30]. Under this approximation, the present system is equivalent to the dissociation of a condensate of molecular dimers studied in detail in [14, 31, 32]. The latter system in turn is analogous to parametric down-conversion in optics [33]. The details of the approximate solutions, common to condensate collisions and molecular dissociation, and the relationship between them are given in appendix C. The resulting width of the halo found from this approach is

$$\delta k \simeq \frac{4\pi a \rho_0}{k_r}. \quad (14)$$

We see that in this regime, the width is proportional to the scattering length a and the peak density ρ_0 , but it no longer depends on the collision duration.

The physical interpretation of equation (14) is that with the stronger effective coupling (or nonlinearity) $a\rho_0$, one can excite and amplify spectral components that are further detuned from the exact resonance condition $\hbar\Delta_k = 0$ (or further ‘phase mismatched’). The inverse dependence on collision momentum k_r can be understood via the quadratic dependence of the energy on momentum k : to get the same excitation at a given energy offset $\hbar\Delta_k$, (C.3), one requires smaller absolute momentum offset δk at larger k_r than at small k_r .

Positive- P simulations covering the transition from the spontaneous to stimulated regimes are available for ^{23}Na condensate collisions as in [15]. The numerical results in this case are in agreement with the simple analytic estimate of equation (14). More specifically, we find that for collision durations between 300 and 640 μs the actual numerical results for the width of the spherical halo vary, respectively, between $\delta k/k_r \simeq 0.13$ and $\delta k/k_r \simeq 0.087$, whereas equation (14) predicts $\delta k/k_r \simeq 0.096$.

For $^4\text{He}^*$, on the other hand, the small mass and the larger scattering length of $^4\text{He}^*$ atoms limit the maximum simulation time to $t_{\text{sim}} \lesssim 25 \mu\text{s}$. This is far from the stimulated regime, and therefore we do not have a direct comparison of the numerical results with equation (14). The experiment is also not in the stimulated regime. We are nevertheless tempted by the numerical ^{23}Na result to extrapolate equation (14) to $^4\text{He}^*$ BEC collisions in the long time limit and we obtain $\delta k/k_r \simeq 0.05$. Adding this width in quadrature to the momentum width of the initial condensate, $\sigma_{y,z} \simeq 0.055k_r$, gives $\sqrt{(0.05k_r)^2 + (0.055k_r)^2} = 0.074k_r$, not far from the experimentally observed radial momentum width of $\delta k \simeq 0.067k_r$. We thus suggest that the mechanism leading to equation (14) may play a role in the experiment.

4. Model

The effective field theory Hamiltonian governing the dynamics of the collision of BECs is given by

$$\hat{H} = \int d\mathbf{x} \left\{ \frac{\hbar^2}{2m} |\nabla \hat{\Psi}|^2 + \frac{\hbar U_0}{2} \hat{\Psi}^\dagger \hat{\Psi}^\dagger \hat{\Psi} \hat{\Psi} \right\}, \quad (15)$$

where $\hat{\Psi}(\mathbf{x}, t)$ is the field operator with the usual commutation relation $[\hat{\Psi}(\mathbf{x}, t), \hat{\Psi}^\dagger(\mathbf{x}', t)] = \delta^{(3)}(\mathbf{x} - \mathbf{x}')$, m is the atomic mass, the first term is the kinetic energy, and the second term describes the s-wave scattering interactions between the atoms. The trapping potential for preparing the initial condensate before the collision is omitted since we are only modeling the dynamics of the outcoupled condensates in free space. The use of the effective delta function interaction potential $U(x - y) = U_0 \delta(x - y)$ assumes a UV momentum cutoff k^{\max} . In our numerical simulations, the momentum cutoff is imposed explicitly via the finite computational lattice. If the lattice spacings (Δx , Δy and Δz) in each spatial dimension are chosen to be much larger than the s-wave scattering length a , then the respective momentum cutoffs satisfy $k_{x,y,z}^{\max} \ll 1/a$. In this case the coupling constant U_0 is given by the familiar expression $U_0 \simeq 4\pi \hbar a/m$ [34] without the need for explicit renormalization.

To model the dynamics of quantum fields describing the collision of two BECs, we use the positive P -representation approach [17]. In this approach, the quantum field operators $\hat{\Psi}(\mathbf{x}, t)$ and $\hat{\Psi}^\dagger(\mathbf{x}, t)$ are represented by two complex stochastic c -number fields $\Psi(\mathbf{x}, t)$ and $\tilde{\Psi}(\mathbf{x}, t)$ whose dynamics is governed by the following stochastic differential equations [15]:

$$\frac{\partial \Psi(\mathbf{x}, t)}{\partial t} = \frac{i\hbar}{2m} \nabla^2 \Psi - iU_0 \tilde{\Psi} \Psi \Psi + \sqrt{-iU_0 \Psi^2} \zeta_1(\mathbf{x}, t), \quad (16a)$$

$$\frac{\partial \tilde{\Psi}(\mathbf{x}, t)}{\partial t} = -\frac{i\hbar}{2m} \nabla^2 \tilde{\Psi} + iU_0 \Psi \tilde{\Psi} \tilde{\Psi} + \sqrt{iU_0 \tilde{\Psi}^2} \zeta_2(\mathbf{x}, t). \quad (16b)$$

Here, $\zeta_1(\mathbf{x}, t)$ and $\zeta_2(\mathbf{x}, t)$ are real independent noise sources with zero mean, $\langle \zeta_j(\mathbf{x}, t) \rangle = 0$, and the following non-zero correlation:

$$\langle \zeta_j(\mathbf{x}, t) \zeta_k(\mathbf{x}', t') \rangle = \delta_{jk} \delta^{(3)}(\mathbf{x} - \mathbf{x}') \delta(t - t'). \quad (17)$$

The stochastic fields $\Psi(\mathbf{x}, t)$ and $\tilde{\Psi}(\mathbf{x}, t)$ are independent of each other [$\tilde{\Psi}(\mathbf{x}, t) \neq \Psi^*(\mathbf{x}, t)$] except in the mean, $\langle \tilde{\Psi}(\mathbf{x}, t) \rangle = \langle \Psi^*(\mathbf{x}, t) \rangle$, where the brackets $\langle \dots \rangle$ refer to stochastic averages with respect to the positive P -distribution function. In numerical realizations, this is represented by an ensemble average over a large number of stochastic realizations (trajectories). Observables described by quantum mechanical ensemble averages over normally ordered operator products have an exact correspondence with stochastic averages over the fields $\Psi(\mathbf{x}, t)$ and $\tilde{\Psi}(\mathbf{x}, t)$:

$$\langle [\hat{\Psi}^\dagger(\mathbf{x}, t)]^m [\hat{\Psi}(\mathbf{x}', t)]^n \rangle = \langle [\tilde{\Psi}(\mathbf{x}, t)]^m [\Psi(\mathbf{x}', t)]^n \rangle. \quad (18)$$

The initial condition for our simulations is a coherent state of a trapped condensate, modulated with a standing wave that imparts initial momenta $\pm k_r$ (where $k_r = m v_r / \hbar$ and v_r is the collision velocity) in the x -direction,

$$\Psi(\mathbf{x}, 0) = \langle \hat{\Psi}(\mathbf{x}, 0) \rangle = \sqrt{\rho_0(\mathbf{x})/2} (e^{ik_r x} + e^{-ik_r x}), \quad (19)$$

with $\tilde{\Psi}(\mathbf{x}, 0) = \Psi^*(\mathbf{x}, 0)$. Here, $\rho_0(\mathbf{x})$ is the density profile given by the ground state solution to the Gross–Pitaevskii equation in imaginary time. The above initial condition models a sudden

Raman outcoupling of a BEC of trapped $^4\text{He}^*$ atoms in the $m_x = 1$ sublevel into the magnetic field insensitive state $m_x = 0$, using two horizontally counter-propagating lasers and a third vertical laser [16]. In this geometry, the Raman transitions split the initial ($m_x = 1$) condensate into two equally populated condensates and simultaneously impart velocities of $\pm v_r$ onto the two halves. As a result, the two outcoupled condensates undergo a collision and expand in free space. Accordingly, in our dynamical simulations, the field $\hat{\Psi}(\mathbf{x}, t)$ represents the atoms in the untrapped state $m_x = 0$, having the s-wave scattering length of $a_{00} = 5.3$ nm ([16] and references therein), while the initial density profile $\rho_0(\mathbf{x})$ refers to that of the trapped atoms in the $m_x = 1$ state having the scattering length of $a_{11} = 7.51$ nm [35]. The same distinction in terms of the scattering length in question applies to the definition of the interaction strength $U_0 \simeq 4\pi\hbar a/m$, in which a has to be understood as a_{11} for the trapped condensate or as a_{00} for the outcoupled cloud.

In our simulations, we assume for simplicity that the outcoupling from the trapped $m_x = 1$ state is 100% efficient, in which case the entire population is transferred into the $m_x = 0$ state and therefore we have only to model s-wave scattering interactions between the atoms in the $m_x = 0$ state. In the experiment, on the other hand, the transfer efficiency is only about 60% and therefore the collisions between the atoms in the $m_x = 0$ and $m_x = 1$ are not completely negligible and may be responsible for some of the deviations between the present theoretical results and the experimental observations.

5. Results and discussion

5.1. Main numerical example

Here, we present the results of positive- P numerical simulations of collisions of two condensates of $^4\text{He}^*$ atoms ($m \simeq 6.65 \times 10^{-27}$ kg) as in the experiment of [16]. The key parameters in our main numerical example are the collision velocity, $v_r = 9.2$ cm s $^{-1}$, and the peak density of the initial trapped condensate, $\rho_0 = 2.5 \times 10^{19}$ m $^{-3}$. The trap frequencies are matched exactly with the experimental values, $\omega_x/2\pi = 47$ Hz and $\omega_y/2\pi = \omega_z/2\pi = 1150$ Hz. The s-wave scattering length for the magnetically trapped atoms in the $m_x = 1$ sublevel is $a_{11} = 7.5$ nm; the s-wave scattering length for the outcoupled atoms in the $m_x = 0$ sublevel is $a_{00} = 5.3$ nm. Other simulation parameters are given in appendix D.

The initial state of the trapped condensate is found via the solution of the Gross–Pitaevskii equation in imaginary time. Given the above trap frequencies and the peak density as a target, we find that the total number of atoms in the main example is $N = 9.84 \times 10^4$. With these parameters, the average kinetic energy of colliding atoms is $E_{\text{kin}}/k_B = mv_r^2/2k_B \simeq 2.0 \times 10^{-6}$ K, which is about 7.4 times larger than the mean-field energy of the initial condensate $E_{\text{MF}}/k_B = 4\pi\hbar^2 a_{11} \rho_0 / mk_B \simeq 2.7 \times 10^{-7}$ K.

The duration of simulation in the main example is $t_f = 25$ μs . This is considerably smaller than the estimated duration of collision in the experiment, 140 μs (see appendix A). The number of scattered atoms in our numerically simulated example at $t_f = 25$ μs is ~ 1750 , representing $\sim 1.8\%$ of the total number of atoms in the initial BEC. Operationally, the fraction of scattered atoms is determined as the total number of atoms contained within the scattering halo (see figure 3 showing two orthogonal slices through the momentum density distribution) after eliminating the regions of momentum space occupied by the two colliding condensates. We implement the elimination by simply discarding the data points corresponding to $|k_x| > 0.99k_r$,

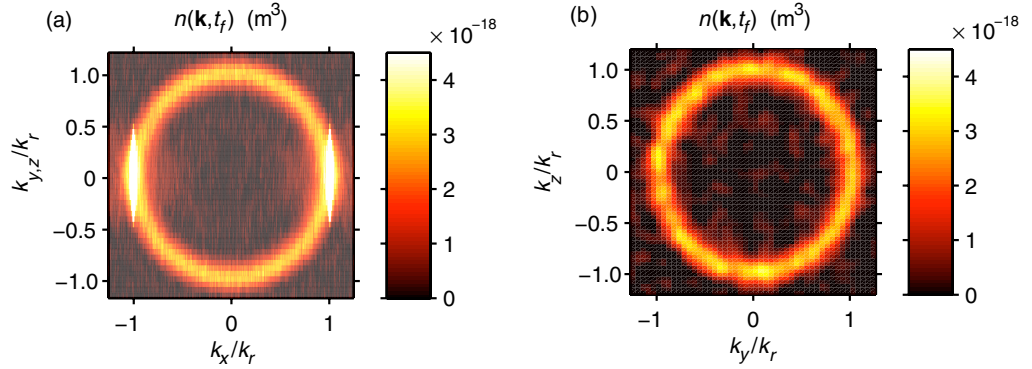


Figure 3. Slices through $k_z = 0$ (a) and $k_x = 0$ (b) of the 3D atomic density distribution in momentum space $n(\mathbf{k}, t_f)$ after $t_f = 25 \mu\text{s}$ collision time. Due to the symmetry in the transverse direction (orthogonal to x), the average density through $k_y = 0$ coincides with that of $k_z = 0$. The color scale is chosen to clearly show the halo of spontaneously scattered atoms and cuts off the high-density peaks of the two colliding condensates (shown in white on the left panel).

which fully contain the colliding condensates. This cuts off a small fraction of the scattered atoms as well, but the procedure is simple to implement operationally and is unambiguous.

In order to compare our calculated fraction of scattered atoms at $t_f = 25 \mu\text{s}$ with the experimentally measured fraction of 5% at the end of collision at $\sim 140 \mu\text{s}$, we first note that these timescales are relatively short and correspond to the regime of spontaneous scattering. The number of scattered atoms increases approximately linearly with time, therefore our calculated fraction of 1.8% can be extrapolated to about 10% to correspond to the expected fraction at $\sim 140 \mu\text{s}$. Next, one has to scale this value by a factor 0.6^2 to account for the fact that in the experiment only 60% of the initial number of atoms was transferred to the $m_x = 0$ state of the colliding condensates. Accordingly, our theoretical estimate of 10% should be proportionally scaled down to 4% conversion, in good agreement with the experimentally estimated fraction of 5% (see also appendix A).

In figure 4, we plot the radial momentum distribution of scattered atoms (solid line), obtained after angle averaging of the full 3D distribution within the region $|k_x| \leq 0.8k_r$. The numerical result is fitted with a Gaussian $\propto \exp[-(k - k_0)^2 / (2\delta k^2)]$ (dashed line), centered at $k_0 = 0.98k_r$, and having the radial width of $\delta k = 0.10k_r \simeq 5.8 \times 10^5 \text{ m}^{-1}$, where $k = |\mathbf{k}|$. The fitted radial width of $\delta k = 0.10k_r$ of the numerical simulation is in reasonable agreement with the simple estimate of equation (13), which gives $\delta k \simeq 0.075k_r$ for $\Delta t = 25 \mu\text{s}$.

Figure 5 shows the numerical results for the BB and CL correlations (solid lines with circles), defined in equations (4) and (5). Due to the symmetry of the y - and z -directions, the results in these directions are practically the same. In order to verify the hypothesis that the shape and therefore the width of the pair correlation functions is governed by the width of the momentum distribution of the source condensate, we also plot the actual initial momentum distributions of the source condensate in the two orthogonal directions (with the understanding that the horizontal axis Δk_i now refers to the actual wavevector component k_i). The actual data points for the correlation functions and for the momentum distribution of the source are shown by the circles and squares, respectively, and are fitted with Gaussian curves for simplicity and

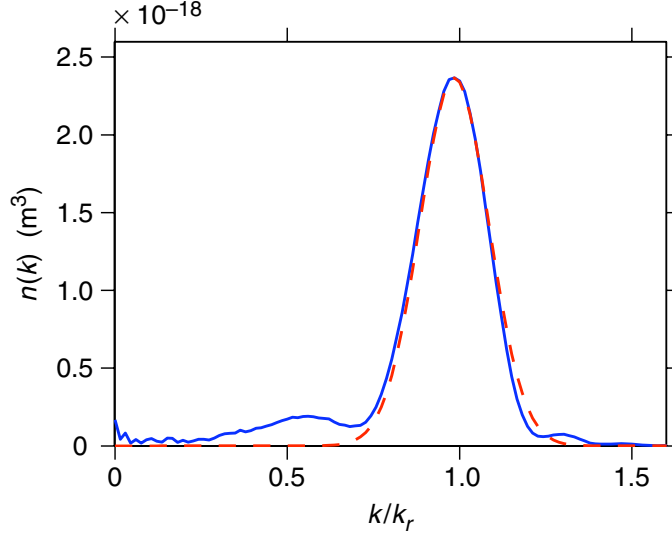


Figure 4. Angle averaged (radial) momentum distribution $n(k)$ of the scattered atoms (solid line) and a simple Gaussian fit (dashed line) used to define the radial width $\delta k = 0.10k_r$ of the halo around the peak momentum $k_0 = 0.98k_r$ (see text).

to guide the eye. The Gaussian fits for the correlation functions (solid lines) give:

$$g_{\text{BB}}^{(2)}(\Delta k_i) - 1 = 9.2 \exp\{-\Delta k_i^2/[2(\sigma_i^{\text{BB}})^2]\}, \quad (20)$$

$$g_{\text{CL}}^{(2)}(\Delta k_i) - 1 = \exp\{-\Delta k_i^2/[2(\sigma_i^{\text{CL}})^2]\}, \quad (21)$$

where the correlation widths σ_i^{BB} and σ_i^{CL} are shown in the table (22) below. The Gaussian fits (dashed lines) for the slices of the initial momentum distribution $n_0(k_i) \propto \exp\{-k_i^2/[2(\sigma_i)^2]\}$ are scaled to the same peak value as $g_{\text{BB/CL}}^{(2)}(0) - 1$ and have $\sigma_x = 0.0025k_r$ and $\sigma_{y,z} = 0.055k_r$.

By comparing the solid and the dashed lines, we see that the shape of the correlation functions indeed closely follow the shape of the momentum distribution of the source. More specifically, we find that the following results provide the best fit to our numerical data:

$\sigma_x^{\text{BB}}/\sigma_x$	$\sigma_{y,z}^{\text{BB}}/\sigma_{y,z}$	$\sigma_x^{\text{CL}}/\sigma_x$	$\sigma_{y,z}^{\text{CL}}/\sigma_{y,z}$
1.18	1.39	1.27	1.57

(22)

The ratios between the CL and BB correlation widths are $\sigma_x^{\text{CL}}/\sigma_x^{\text{BB}} \simeq 1.08$ and $\sigma_{y,z}^{\text{CL}}/\sigma_{y,z}^{\text{BB}} \simeq 1.13$. The errors due to stochastic sampling on all quoted values of the correlation widths are smaller than 3%.

The values for $\sigma_{y,z}^{\text{CL}}/\sigma_{y,z}$ and $\sigma_{y,z}^{\text{BB}}/\sigma_{y,z}$ can be compared with the respective experimentally measured values of table (11) and we see reasonably good agreement, even though the numerical data are for a much shorter collision time. The remaining discrepancy between the numerical data at $t_f = 25 \mu\text{s}$ and the experimentally measured values after a $\sim 140 \mu\text{s}$ interaction time may be due to the evolution of the condensates past $25 \mu\text{s}$, not attainable within the positive- P method. The above numerical results for the correlation widths can also be compared with the simple analytic estimate based on the Gaussian ansatz treatment of equations (9) and (10). We find that the approximate analytic results overestimate the BB and CL widths by ~ 20 and 40% , respectively, in the present example.

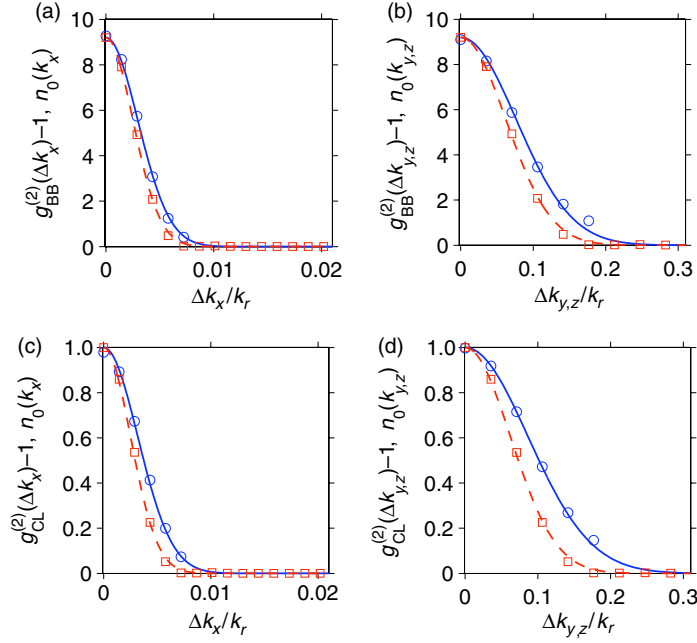


Figure 5. BB and CL atom–atom pair correlation, $g_{\text{BB/CL}}^{(2)}(\Delta k_i) - 1$ as a function of the displacement Δk_i ($i = x, y$ and z) in units of the collision momentum k_r , after $t_f = 25 \mu\text{s}$ collision time. The circles are the numerical results, angle-averaged over the halo of scattered atoms after elimination of the regions occupied by the two colliding condensates; the solid lines are simple Gaussian fits to guide the eye (see text). For comparison, we also plot the initial momentum distribution $n_0(k_i)$ of the colliding condensates; the actual data points are shown by the squares and are fitted by a dashed-line Gaussian.

The amplitude of the correlation functions can also be inferred by simple models. In fact, the CL correlation function is a manifestation of the Hanbury Brown and Twiss effect since it involves pairs from two independent spontaneous scattering events and we expect an amplitude of $g_{\text{CL}}^{(2)}(0) = 2$ [28]. This is in agreement with the positive- P simulations. The BB correlation amplitude, on the other hand, can be substantially higher and display super-bunching ($g_{\text{BB}}^{(2)}(0) \gg 1$) [14, 24] since the origin of this correlation is a simultaneous creation of a pair of particles in a single scattering event.

In a simple qualitative model [16], the amplitude of the BB correlation can be linked to the inverse population of the atomic modes on the halo. As we show in appendix B, this model follows the trends observed in our first-principles numerical simulations.

5.2. Shorter collision time

Here, we present the results of numerical simulation for the same parameters as in our main numerical example from section 5.1, except that the data are analyzed at $t_f = 12.5 \mu\text{s}$, which is half the previous interaction time. We found in section 5.1 that σ_{yz}^{BB} , σ_{yz}^{CL} and the width of the halo δk are all nearly the same. In section 3, however, we argue that the widths of the correlation functions and the halo are governed by different limits (equations (9), (10) and (13) or (14), respectively). The example in this section illustrates this point.

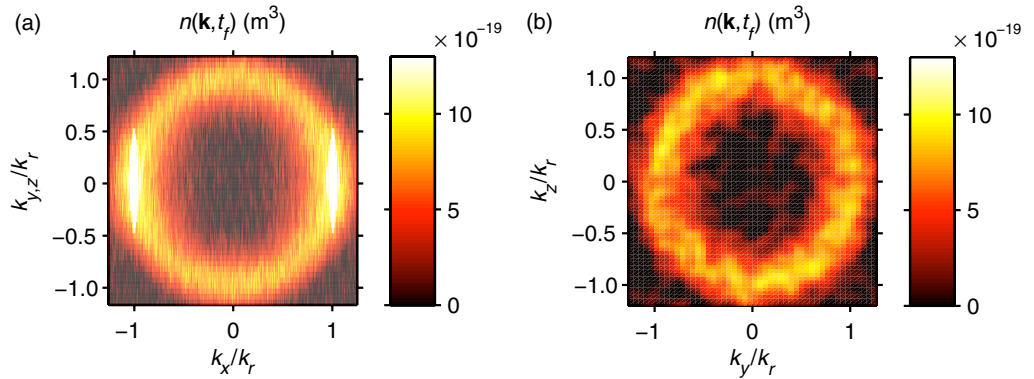


Figure 6. Same as in figure 3, except for $t_f = 12.5 \mu\text{s}$ collision time.

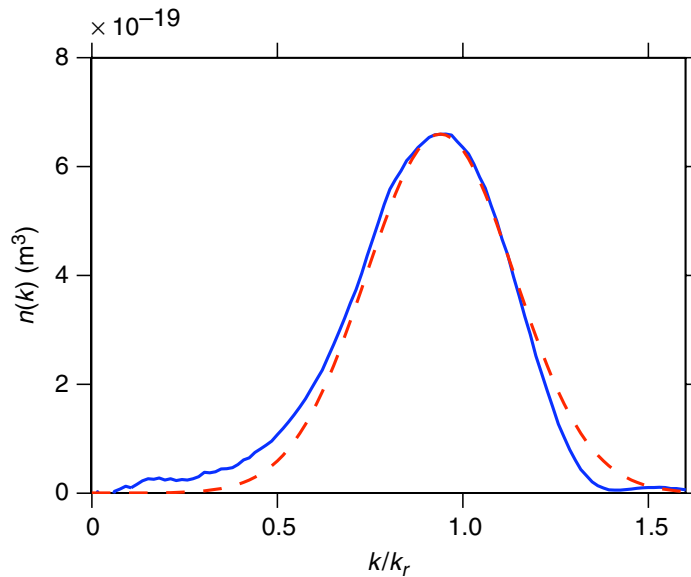


Figure 7. Same as in figure 4, except for $t_f = 12.5 \mu\text{s}$ collision time. The width and the peak of the fitted Gaussian here are: $\delta k = 0.20k_r$ and $k_0 = 0.95k_r$.

Figure 6 shows two orthogonal slices of the s-wave scattering sphere in momentum space (cf figure 3), whereas figure 7 is the corresponding radial distribution after angle averaging. The most obvious feature of the distribution is that it is broader than at $t_f = 25 \mu\text{s}$ and the fitted Gaussian gives the radial width of $\delta k = 0.20k_r$. This is precisely twice the width in figure 4 and is in agreement with the simple qualitative estimate of equation (13).

The BB and CL correlation functions after $t_f = 12.5 \mu\text{s}$ collision time are qualitatively very similar to those shown in figure 5, except that the Gaussian fits are

$$g_{\text{BB}}^{(2)}(\Delta k_i) - 1 = 35.6 \exp\{-\Delta k_i^2/[2(\sigma_i^{\text{BB}})^2]\}, \quad (23)$$

$$g_{\text{CL}}^{(2)}(\Delta k_i) - 1 = \exp\{-\Delta k_i^2/[2(\sigma_i^{\text{CL}})^2]\}, \quad (24)$$

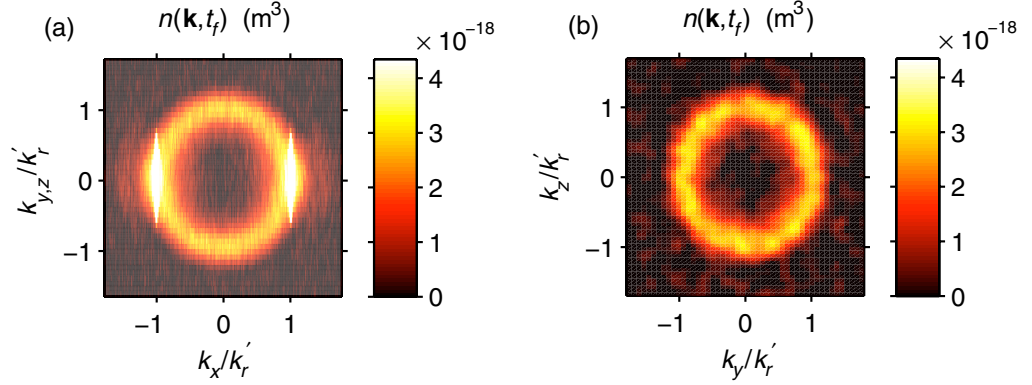


Figure 8. Same as in figure 3, except for $\sqrt{2}$ times smaller collision velocity, $v_r' = 6.46 \text{ cm s}^{-1}$ ($k_r' = 4.09 \times 10^6 \text{ m}^{-1}$). The axes for the momentum components k_i ($i = x, y$ and z) are in units of smaller recoil momentum than in figure 3, and therefore the absolute radius of the s-wave scattering sphere is smaller in the present example.

with the correlation widths given by

$\sigma_x^{\text{BB}}/\sigma_x$	$\sigma_{y,z}^{\text{BB}}/\sigma_{y,z}$	$\sigma_x^{\text{CL}}/\sigma_x$	$\sigma_{y,z}^{\text{CL}}/\sigma_{y,z}$
1.16	1.28	1.27	1.48

(25)

The ratios between the widths are $\sigma_x^{\text{CL}}/\sigma_x^{\text{BB}} \simeq 1.09$ and $\sigma_{y,z}^{\text{CL}}/\sigma_{y,z}^{\text{BB}} \simeq 1.16$.

For the correlation functions, the main difference compared to the case for $25 \mu\text{s}$ is that the peak value of the BB correlation is now larger, reflecting the lower atomic density on the scattering halo. The correlation widths, on the other hand, are practically unchanged, at least within the numerical sampling errors of the positive- P simulations; the errors are at the level of the third significant digit in the quoted values, which we suppress. The number of scattered atoms in this example is about 850, which is approximately half the number at $25 \mu\text{s}$, confirming the approximately linear dependence on time in the spontaneous scattering regime.

5.3. Smaller collision velocity

In this example, we present the results of simulations in which the collision velocity is smaller by a factor $\sqrt{2}$ than before, $v_r' = 6.5 \text{ cm s}^{-1}$ ($k_r' = 4.1 \times 10^6 \text{ m}^{-1}$), while all other parameters are unchanged. In practice, this can be achieved by changing the propagation directions of the Raman lasers that outcouple the atoms from the trapped state. As in the previous example, the halo width illustrates equation (13).

The results of positive- P simulations for the momentum density distribution at $t_f = 25 \mu\text{s}$ are shown in figures 8 and 9. The most obvious feature of the distribution is again the fact that it is now broader than in our main example of section 5.1. The width of the Gaussian function fitted to the numerically calculated radial momentum distribution is given by $\delta k = 0.21 k_r'$. This is again in excellent agreement with the simple analytic estimate of equation (13), which predicts the broadening to be inversely proportional to the collision velocity. We also note that the peak momentum (relative to k_r') in the present example is slightly shifted towards the center of the

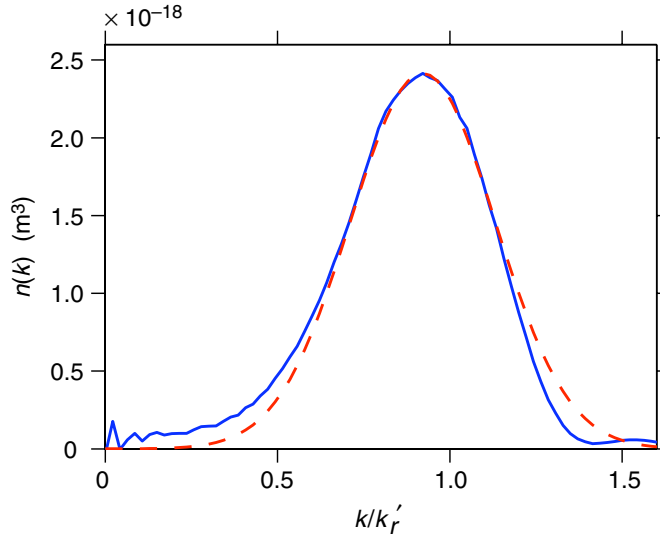


Figure 9. Same as in figure 4 except for $\sqrt{2}$ times smaller collision velocity v_r' ($k_r' = 4.1 \times 10^6 \text{ m}^{-1}$). The width and the peak of the fitted Gaussian are $\delta k = 0.21k_r' = 8.6 \times 10^5 \text{ m}^{-1}$ and $k_0 = 0.92k_r'$.

halo, $k_0 = 0.92k_r'$, which is a feature predicted in [30] to occur when the ratio of the kinetic energy to the interaction energy per particle is reduced.

The BB and CL correlation functions in this example are again qualitatively very similar to those shown in figure 5, except that the Gaussian fits are

$$g_{\text{BB}}^{(2)}(\Delta k_i) - 1 = 9.0 \exp\{-\Delta k_i^2/[2(\sigma_i^{\text{BB}})^2]\}, \quad (26)$$

$$g_{\text{CL}}^{(2)}(\Delta k_i) - 1 = \exp\{-\Delta k_i^2/[2(\sigma_i^{\text{CL}})^2]\}, \quad (27)$$

with the correlation widths given by

$\sigma_x^{\text{BB}}/\sigma_x$	$\sigma_{y,z}^{\text{BB}}/\sigma_{y,z}$	$\sigma_x^{\text{CL}}/\sigma_x$	$\sigma_{y,z}^{\text{CL}}/\sigma_{y,z}$
1.16	1.35	1.31	1.51

(28)

where $\sigma_x/k_r' \simeq 0.0035$ and $\sigma_x/k_r' \simeq 0.078$. The ratios between the CL and BB correlation widths are $\sigma_x^{\text{CL}}/\sigma_x^{\text{BB}} \simeq 1.13$ and $\sigma_{y,z}^{\text{CL}}/\sigma_{y,z}^{\text{BB}} \simeq 1.12$.

As we see from these results, the absolute widths of the correlation functions are practically unchanged compared to the main numerical example (22). This provides further evidence that, at least for short collision times, the correlation widths are governed by the momentum width of the source condensate, which is unchanged in the present example compared to the case of section 5.1.

The number of scattered atoms in this example is about 1270, which is approximately $\sqrt{2}$ times smaller than in section 5.1 and corresponds to $\sim 1.3\%$ conversion. This scaling is in agreement with the rate equation approach [24], according to which the number of scattered atoms is proportional to the square root of the collision energy and hence to the collision momentum, which is $\sqrt{2}$ times smaller here.

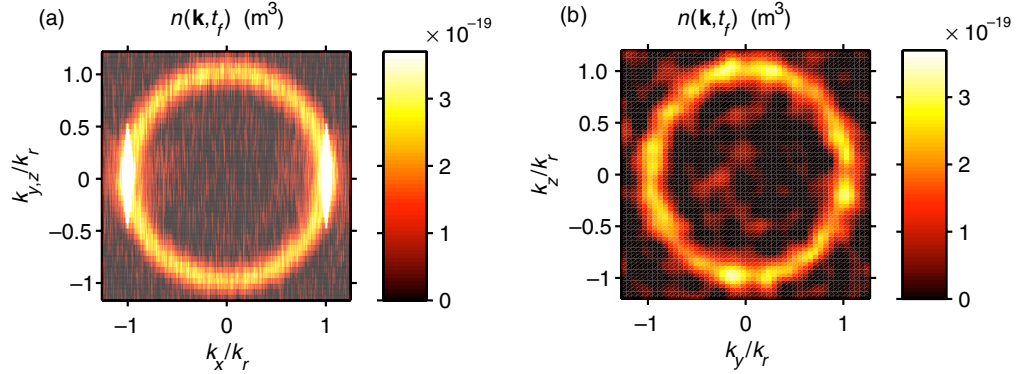


Figure 10. Same as in figure 3 except for the scattering lengths of $a_{00} = 2.65$ nm and $a_{11} = 3.75$ nm, which are twice as small as before.

5.4. Smaller scattering length

Finally, we present the results of numerical simulations for the same parameters as in our main numerical example from section 5.1, except that the scattering lengths a_{11} and a_{00} are artificially halved, i.e. $a_{00} = 2.65$ nm and $a_{11} = 3.75$ nm. The trap frequencies are unchanged and we modify the chemical potential to arrive at the same peak density of the initial BEC in the trap, $\rho_0 \simeq 2.5 \times 10^{19} \text{ m}^{-3}$. The total number of atoms is now smaller, $N \simeq 3.5 \times 10^4$. One effect of changing the scattering length is that it changes the size and shape of the trapped cloud, and therefore also its momentum distribution. The shape is slightly closer to a Gaussian and therefore also to the treatment in [28].

Due to the smaller scattering length, the density distribution in position space of the initial trapped condensate is now narrower and conversely the momentum distribution of the colliding condensates is broader. On the other hand, the width of the halo (see figures 10 and 11 at $t_f = 25 \mu\text{s}$) of scattered atoms is practically unchanged compared to the example of figure 4, as it is governed by the energy–time uncertainty consideration (13), for the spontaneous scattering regime. The only quantitative difference is the lower peak density on the scattering sphere, which is due to the weaker strength of atom–atom interactions resulting in a slower scattering rate. The number of scattered atoms at $25 \mu\text{s}$ is ~ 180 , corresponding to 0.51% conversion of the initial total number $N \simeq 3.5 \times 10^4$. The fraction 0.51% itself corresponds approximately to a scaling law of $\sim a^{3/2}$, which is the same as the scaling of the total initial number of trapped atoms in the Thomas–Fermi limit for a fixed peak density.

Since the widths of the correlation functions are governed by the width of the momentum distribution of the initial colliding condensates, we expect corresponding broadening of the correlation functions as well (see figure 12). To quantify this effect, we fit the momentum distribution of the initial BEC by a Gaussian $\propto \exp\{-k_i^2/[2(\sigma_i)^2]\}$, where $\sigma_x = 0.0036k_r$ and $\sigma_{y,z} = 0.068k_r$ (cf with $\sigma_x = 0.0025k_r$ and $\sigma_{y,z} = 0.055k_r$ in figure 5, which are $\sim \sqrt{2}$ smaller). The Gaussian fits to the correlation functions in figure 12 are

$$g_{\text{BB}}^{(2)}(\Delta k_i) - 1 = 49 \exp\{\Delta k_i^2/[2(\sigma_i^{\text{BB}})^2]\}, \quad (29)$$

$$g_{\text{CL}}^{(2)}(\Delta k_i) - 1 = 0.94 \exp\{\Delta k_i^2/[2(\sigma_i^{\text{CL}})^2]\}, \quad (30)$$

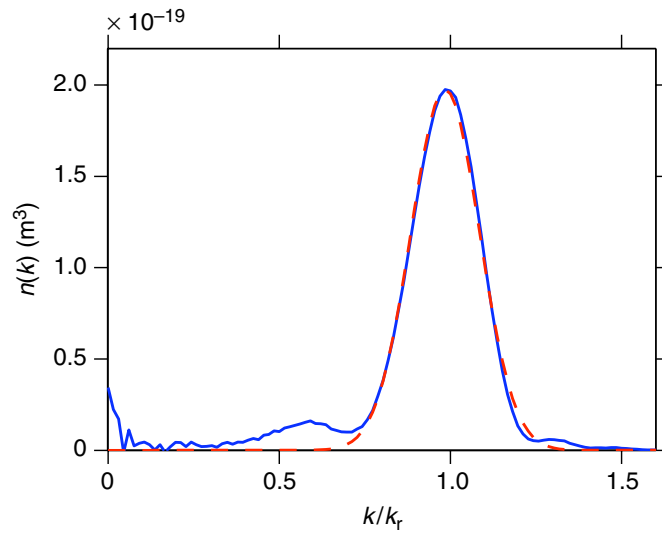


Figure 11. Same as in figure 4 except for twice as small values of the scattering lengths a_{00} and a_{11} . The width and the peak of the fitted Gaussian are $\delta k = 0.10k_r$ and $k_0 = 0.98k_r$, which are the same as in figure 4.

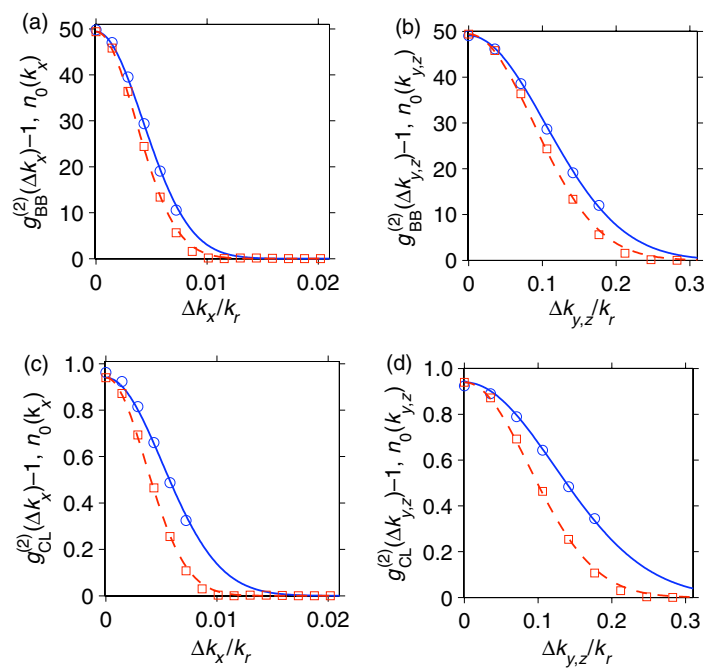


Figure 12. Same as in figure 5 except for twice as small s-wave scattering lengths a_{11} and a_{00} .

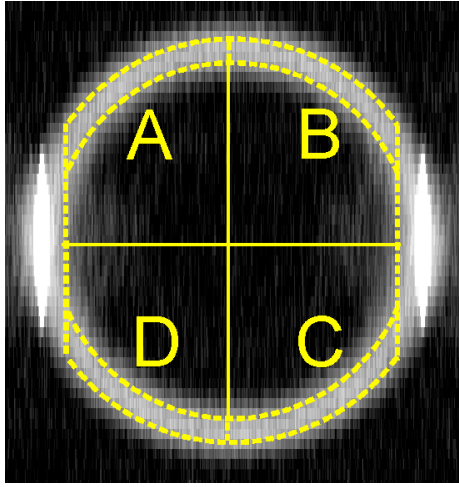


Figure 13. Illustration of the four regions of the momentum space density, forming the quadrants *A*, *B*, *C* and *D* on the *s*-wave scattering sphere, on which we analyze the data for relative number squeezing.

where the widths σ_i^{BB} and σ_i^{CL} are given by

$\sigma_x^{\text{BB}}/\sigma_x$	$\sigma_{y,z}^{\text{BB}}/\sigma_{y,z}$	$\sigma_x^{\text{CL}}/\sigma_x$	$\sigma_{y,z}^{\text{CL}}/\sigma_{y,z}$
1.18	1.53	1.42	1.81

(31)

We see that the relative widths are practically unchanged, implying that the absolute widths are broadened. The ratios between the CL and BB correlation widths are slightly increased and are given by $\sigma_x^{\text{CL}}/\sigma_x^{\text{BB}} \simeq 1.20$ and $\sigma_{y,z}^{\text{CL}}/\sigma_{y,z}^{\text{BB}} \simeq 1.18$.

These numerical results make the present example—with the diminished role of atom–atom interactions—somewhat closer to the simple analytic predictions of equations (9) and (10) based on a Gaussian ansatz for non-interacting condensates.

5.5. Relative number squeezing and violation of Cauchy–Schwartz inequality

Another useful measure of atom–atom correlations is the normalized variance of the relative number fluctuations between atom numbers \hat{N}_i and \hat{N}_j in a pair of counting volume elements denoted via *i* and *j*,

$$V_{i-j} = \frac{\langle [\Delta(\hat{N}_i - \hat{N}_j)]^2 \rangle}{\langle \hat{N}_i \rangle + \langle \hat{N}_j \rangle} = 1 + \frac{\langle : [\Delta(\hat{N}_i - \hat{N}_j)]^2 : \rangle}{\langle \hat{N}_i \rangle + \langle \hat{N}_j \rangle}, \quad (32)$$

where $\Delta\hat{X} = \hat{X} - \langle \hat{X} \rangle$ is the fluctuation. This definition uses the conventional normalization with respect to the shot-noise level characteristic of Poissonian statistics, such as for a coherent state, $\langle \hat{N}_i \rangle + \langle \hat{N}_j \rangle$. In this case, the variance $V_{i-j} = 1$, which corresponds to the level of fluctuations in the absence of any correlation between \hat{N}_i and \hat{N}_j . Variance smaller than one, $V_{i-j} < 1$, implies reduction (or squeezing) of fluctuations below the shot-noise level and is due to quantum correlation between the particle number fluctuations in \hat{N}_i and \hat{N}_j . Perfect (100%) squeezing of the relative number fluctuations corresponds to $V_{i-j} = 0$.

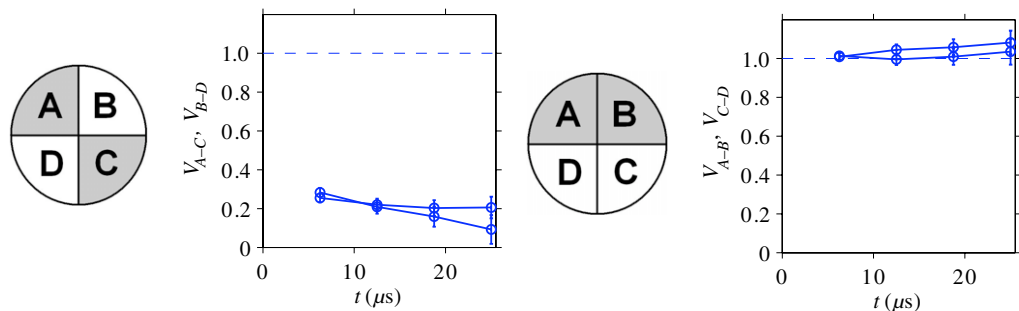


Figure 14. Relative number variance in the diametrically opposite and neighboring quadrants, $V_{A-C/B-D}$ and $V_{A-B/C-D}$, as a function of time.

In the context of the present model for the BEC collision experiment and possible correlation measurements between atom number fluctuations on diametrically opposite sides of the s-wave scattering sphere, we assign the indices $i, j = A, B, C$ and D in equation (32) to one of the four quadrants as illustrated in figure 13. The total atom number operator \hat{N}_i in each quadrant \mathcal{D}_i within the s-wave scattering sphere is defined after elimination of the regions in momentum space occupied by the two colliding condensates

$$\hat{N}_i(t) = \int_{\mathcal{D}_i} dk_x dk_y \int_{-\infty}^{+\infty} dk_z \hat{n}(\mathbf{k}, t). \quad (33)$$

Operationally, this is implemented by discarding the data points beyond $|k_x| > 0.8k_r$. In addition, the quadrants \mathcal{D}_i are defined on a 2D plane after integrating the momentum distribution along the z -direction, which in turn only takes into account the 3D data points satisfying $|1 - k^2/k_r^2| < 0.28$, i.e. lying in the narrow spherical shell $k_r \pm \delta k$ with $\delta k \simeq 0.14k_r$. The elimination of the inner and outer regions of the halo is done to minimize the sampling error in our simulations, since these regions have vanishingly small population and produce large noise in the stochastic simulations.

The choice of the quadrants as above is a particular implementation of the procedure of binning, known to result in a stronger correlation signal and larger relative number squeezing [11, 36]. Due to strong BB pair correlations, we expect the relative number fluctuations in the diametrically opposite quadrants to be squeezed, $V_{A-C}, V_{B-D} < 1$, while the relative number variance in the neighboring quadrants, such as V_{A-B} and V_{C-D} , is expected to be larger than or equal to one. The positive- P simulations confirm these expectations and are shown in figure 14, where we see strong ($\sim 80\%$) relative number squeezing for the diametrically opposite quadrants, $V_{A-C, B-D} \simeq 1 - 0.8 = 0.2$.

These results assume a uniform detection efficiency of $\eta = 1$, whereas if the efficiency is less than 100% ($\eta < 1$), then the second term in equation (32) should be multiplied by η . This implies, that for $\eta = 0.1$ as an example, the above prediction of $\sim 80\%$ relative number squeezing will be degraded down to a much smaller but still measurable value of $\sim 8\%$ squeezing ($V_{A-C, B-D} \simeq 1 - 0.08 = 0.92$). Even with perfect detection efficiency, our simulations do not lead to ideal (100%) squeezing. This can be understood in terms of a small fraction of collisions that take place with a center-of-mass momentum offset that is (nearly) parallel to one of the borders between the quadrants. As a result, the respective scattered pairs

fail to appear in diametrically opposite quadrants during the (finite) propagation time (see also [36]).

For the symmetric case with $\langle \hat{N}_i \rangle = \langle \hat{N}_j \rangle$ and $\langle \hat{N}_i^2 \rangle = \langle \hat{N}_j^2 \rangle$, the variance V_{i-j} can be rewritten as

$$V_{i-j} = 1 + \langle \hat{N}_i \rangle [g_{ii}^{(2)} - g_{ij}^{(2)}], \quad (34)$$

where the second-order correlation function $g_{ij}^{(2)}$ is defined according to

$$g_{ij}^{(2)} = \frac{\langle : \hat{N}_i \hat{N}_j : \rangle}{\langle \hat{N}_i \rangle \langle \hat{N}_j \rangle}. \quad (35)$$

Equation (34) helps to relate the relative number squeezing, $V_{i-j} < 1$, to the violation of the classical Cauchy–Schwartz inequality $g_{12}^{(2)} > g_{11}^{(2)}$, studied extensively in quantum optics with photons [33, 37]. The analysis presented here (see also [36] on molecular dissociation) shows that the Cauchy–Schwartz inequality, and its violation, is a promising area of study in *quantum atom optics* as well.

6. Summary

An important conclusion that we can draw from the numerical simulations is that the predicted widths of the correlation functions are remarkably robust against the parameter variations we were able to explore (in section 5.1 through 4). This gives us confidence in our physical interpretation of the width as being chiefly due to the initial momentum width of the condensate. The discrepancy with the analytical calculation of [28] seems to be primarily due to the different cloud shapes used. The width of the halo varies with the parameters we tested in a predictable way and also confirms the discussion in section 3.

As for comparison with the experiment, the numerically calculated widths of the scattering halo and the correlation functions coincide with the experimental ones to within better than 20% in most cases. The main discrepancy with the experiment is in the *ratio* of the BB and CL correlation widths. From the experimental point of view, these ratios are more significant than the individual widths since some sources of uncertainty, such as the number of atoms and the size of the condensates, cancel. The discrepancy may mean that the CL correlations are not sufficient to characterize the size and momentum distribution in the source at this level of accuracy. The discrepancies may of course also be due to the numerous experimental imperfections, especially the fact that the Raman outcoupling was only 60% efficient, and therefore an appreciable trapped $m_x = 1$ condensate was left behind. This defect may be remedied in future experiments. On the other hand, the current simulations neglect the unavoidable interaction of the scattered atoms with unscattered, $m_x = 0$ condensates as they leave the interaction region. This interaction could alter the trajectories of the scattered atoms in a minor, but complicated way. Future numerical work must examine this possibility further.

Still, the overall message of this work is that a first principles quantum field theory approach can quantitatively account for experimental observations of atomic four-wave mixing experiments. This work represents the first time that this sort of numerical simulation has been carefully confronted with an experiment. An interesting extension would be to examine the regime of stimulated scattering. It has been predicted that a highly anisotropic BEC could lead to an anisotropic population of the scattering halo [38, 39]. This effect would be a kind of atomic

$\Delta k_y = 3.06 \times 10^5 \text{ m}^{-1}$ and $\Delta k_z = 2.04 \times 10^5 \text{ m}^{-1}$. The momentum cutoffs are $k_x^{(\text{max})} = 1.75 \times 10^7 \text{ m}^{-1}$, $k_y^{(\text{max})} = 7.66 \times 10^6 \text{ m}^{-1}$ and $k_z^{(\text{max})} = 7.15 \times 10^6 \text{ m}^{-1}$.

The momentum cutoff in the collision direction, $k_x^{(\text{max})}$, is more than 3 times larger than the collision momentum k_r , and hence it captures all relevant scattering processes of interest, including the energy non-conserving scatterings $(k_r) + (k_r) \rightarrow (3k_r) + (-k_r)$ and $(-k_r) + (-k_r) \rightarrow (-3k_r) + (k_r)$ [15]. In all our figures, the regions of momentum space covering $k_x \simeq \pm 3k_r$ are not shown for the clarity of presentation of the main halo. These scattering processes, which produce a weak but not negligible signal at $k_x \simeq \pm 3k_r$, i.e. outside the main halo, are enhanced by Bose stimulation due to the large population of the colliding condensate components at $k_x \simeq \mp k_r$, respectively. In the remaining y- and z-directions, such processes are absent and therefore the number of lattice points and the momentum cutoffs can be smaller.

Since the momentum distribution of the initial condensate is narrowest in the k_x -direction, one may question whether the resolution of $\Delta k_x = 2.49 \times 10^4 \text{ m}^{-1}$ with 1400 lattice points is sufficient. We check this by repeating the simulations with $4200 \times 40 \times 40$ lattice points and quantization lengths of $L_x = 753 \mu\text{m}$ and $L_y = L_z = 15.4 \mu\text{m}$, which give smaller lattice spacing $\Delta k_x = 8.24 \times 10^3 \text{ m}^{-1}$, together with $\Delta k_y = \Delta k_z = 4.08 \times 10^5 \text{ m}^{-1}$, $k_x^{(\text{max})} = 1.75 \times 10^7 \text{ m}^{-1}$ and $k_y^{(\text{max})} = k_z^{(\text{max})} = 8.16 \times 10^6 \text{ m}^{-1}$. Our results on the new lattice reproduce the previous ones, within the sampling errors of the stochastic simulations. We typically average over 2800 stochastic trajectories, and take 128 time steps in the simulations over $25 \mu\text{s}$ collision time. A typical simulation of this size takes about 100 h on 7 CPUs running in parallel at 3.6 GHz clock speed.

References

- [1] Jelte T *et al* 2007 *Nature* **445** 402
- [2] Hellweg D, Cacciapuoti L, Kottke M, Schulte T, Sengstock K, Ertmer W and Arlt J J 2003 *Phys. Rev. Lett.* **91** 010406
- [3] Esteve J, Trebbia J B, Schumm T, Aspect A, Westbrook C I and Bouchoule I 2006 *Phys. Rev. Lett.* **96** 130403
- [4] Rom T, Best T, van Oosten D, Schneider U, Fölling S, Paredes B and Bloch I 2006 *Nature* **444** 733
- [5] Öttl A, Ritter S, Köhl M and Esslinger T 2005 *Phys. Rev. Lett.* **95** 090404
- [6] Ritter S, Öttl A, Donner T, Bourdel T, Köhl M and Esslinger T 2007 *Phys. Rev. Lett.* **98** 090402
- [7] Hofferberth S, Lesanovsky I, Schumm T, Schmiedmayer J, Imambekov A, Gritsev V and Demler E 2007 *Preprint* 0710.1575
- [8] Schellekens M, Hoppeler R, Perrin A, Viana Gomes J, Boiron D, Westbrook C I and Aspect A 2005 *Science* **310** 648
- [9] Yasuda M and Shimizu F 1996 *Phys. Rev. Lett.* **77** 3090
- [10] Fölling S, Gerbier F, Widera A, Mandel O, Gericke T and Bloch I 2005 *Nature* **434** 481
- [11] Greiner M, Regal C A, Stewart J T and Jin D S 2005 *Phys. Rev. Lett.* **94** 110401
- [12] Norrie A A, Ballagh R J and Gardiner C W 2005 *Phys. Rev. Lett.* **94** 040401
- [13] Norrie A A, Ballagh R J and Gardiner C W 2006 *Phys. Rev. A* **73** 043617
- [14] Savage C M, Schwenn P E and Kheruntsyan K V 2006 *Phys. Rev. A* **74** 033620
- [15] Deuar P and Drummond P D 2007 *Phys. Rev. Lett.* **98** 120402
- [16] Perrin A, Chang H, Krachmalnicoff V, Schellekens M, Boiron D, Aspect A and Westbrook C I 2007 *Phys. Rev. Lett.* **99** 150405
- [17] Drummond P D and Gardiner C W 1980 *J. Phys. A: Math. Gen.* **13** 2353
- [18] Gardiner C W and Zoller P 2000 *Quantum Noise* (Berlin: Springer)

- [19] Steel M J, Olsen M K, Plimak L I, Drummond P D, Tan S M, Collett M J, Walls D F and Graham R 1998 *Phys. Rev. A* **58** 4824
- [20] Drummond P D and Corney J F 1999 *Phys. Rev. A* **60** R2661
- [21] Gilchrist A, Gardiner C W and Drummond P D 1997 *Phys. Rev. A* **55** 3014
- [22] Deuar P and Drummond P D 2006 *J. Phys. A: Math. Gen.* **39** 1163
- [23] Ziń P, Chwedeńczuk J, Veitia A, Rzażewski K and Trippenbach M 2005 *Phys. Rev. Lett.* **94** 200401
- [24] Ziń P, Chwedeńczuk J and Trippenbach M 2006 *Phys. Rev. A* **73** 033602
- [25] Morgan S A, Rusch M, Hutchinson D A W and Burnett K 2003 *Phys. Rev. Lett.* **91** 250403
- [26] Yurovsky V A 2002 *Phys. Rev. A* **65** 033605
- [27] Sinatra A, Lobo C and Castin I 2002 *J. Phys. B: At. Mol. Opt. Phys.* **35** 3599
- [28] Molmer K, Perrin A, Krachmalnicoff V, Leung V, Boiron D, Aspect A and Westbrook C I 2008 *Phys. Rev. A* **77** 033601
- [29] Ögren H M and Kheruntsyan K V (unpublished)
- [30] Bach R, Trippenbach M and Rzażewski K 2002 *Phys. Rev. A* **65** 063605
- [31] Kheruntsyan K V and Drummond P D 2002 *Phys. Rev. A* **66** 031602
- [32] Davis M J, Thwaite S J, Olsen M K and Kheruntsyan K V 2008 *Phys. Rev. A* **77** 023617
- [33] Walls D and Milburn G 1991 *Quantum Optics* (New York: Springer)
- [34] Abrikosov A A, Gorkov L P and Dzyaloshinski I E 1963 *Methods of Quantum Field Theory in Statistical Physics* (New York: Springer)
- [35] Moal S, Portier M, Kim J, Dugué J, Rapol U D, Leduc M and Cohen-Tannoudji C 2006 *Phys. Rev. Lett.* **96** 023203
- [36] Savage C M and Kheruntsyan K V 2007 *Phys. Rev. Lett.* **99** 220404
- [37] Zou X, Wang L and Mandel L 1991 *Opt. Commun.* **84** 351
- [38] Vardi A and Moore M G 2002 *Phys. Rev. Lett.* **89** 090403
- [39] Pu H and Meystre P 2000 *Phys. Rev. Lett.* **85** 3987
- [40] Inouye S, Chikkatur A, Stamper-Kurn D M, Stenger J, Pritchard D and Ketterle W 1999 *Science* **285** 571
- [41] Gross M and Haroche S 1982 *Phys. Rep.* **93** 301
- [42] Wong C Y and Zhang W N 2007 *Phys. Rev. C* **76** 034905
- [43] Collocut G R and Drummond P D 2001 *Comput. Phys. Commun.* **142** 219
- [44] Castin Y and Dum R 1996 *Phys. Rev. Lett.* **77** 5315
- [45] Trippenbach M, private communication

analogue of superradiance observed when off-resonant light is shone on a condensate [40, 41]. In addition, our results may be useful beyond the cold atom community: theoretical descriptions of correlation measurements in heavy ion collisions [42] may benefit from some of our insights.

Acknowledgments

We acknowledge stimulating discussions with A Aspect, K Mølmer, M Trippenbach, P Deuar and M Davis, and thank the developers of the XMDS software [43]. CS and KK acknowledge support from the Australian Research Council and the Queensland State Government. Part of this work was done at the Institut Henri Poincaré—Centre Emile Borel; KK thanks the institute for hospitality and support. The atom optics group is supported by the SCALA program of the EU and by the IFRAF institute.

Appendix A. Duration of the collision

In order to estimate the collision duration one can consider a simple classical model of the collision [24]. Denoting by $\rho_1(\mathbf{x}, t)$ and $\rho_2(\mathbf{x}, t)$ the density distributions of the two condensates, the number of scattered atoms $N_{\text{sc}}(t)$ at a given time can be written

$$N_{\text{sc}}(t) = 2 \int_0^t dt' \int d^3\mathbf{x} 2\sigma_0 v_r \rho_1(\mathbf{x}, t') \rho_2(\mathbf{x}, t'), \quad (\text{A.1})$$

where $\sigma_0 = 8\pi a_{00}^2$ is the cross-section for a collision of two particles. In this latter formula $a_{00} \simeq 5.3$ nm is the scattering length between $m_x = 0$ atoms [16].

The time-dependent density of the two condensates can be calculated from the expansion of a condensate in the Thomas–Fermi regime described in [44]. This approach suggests two different timescales for the collision duration. First, the separation of the two condensates occurs in a time defined by the ratio of the longitudinal size of the condensates and their relative velocity $t_{\text{sep}} = R_x/v_r$. Taking for R_x the Thomas–Fermi radius of the initial condensate, one can show that t_{sep} is on the order of 1 ms. At the same time, the condensates expand during their separation on a timescale $t_{\text{exp}} = 1/\omega_y = 1/\omega_z \simeq 140$ μs . This latter effect appears to be predominant in the evaluation of equation (A.1) and t_{exp} can be taken as a definition of the collision duration Δt . The numerical evaluation of equation (A.1) gives $N_{\text{sc}}(\Delta t) \simeq 0.66 N_{\text{sc}}(\infty)$ and the estimated total number of scattered atoms corresponds to the experimentally observed 5% of the initial total number of atoms in the trapped condensate.

Appendix B. Occupation number of the scattering modes and amplitude of the BB correlation

In order to estimate the occupation number of the scattering modes one needs to compare the number of scattered atoms N_{sc} to the number of scattering modes N_m . To achieve this one has to first consider the volume of a scattering mode V_m , given by the first-order coherence volume (also dubbed ‘phase grain’ in [12, 15]). Such a volume corresponds in fact to the coherence volume of the source condensate, and in practice it can also be deduced from the measurement of the width of the CL correlation function $g_{\text{CL}}^{(2)}(\Delta k_i)$ as one expects in a Hanbury Brown–Twiss

experiment. For simplicity, we match the scattering mode volume V_m to the coherence volume of the source condensate in momentum space,

$$V_m \simeq \beta \sigma_x (\sigma_{yz})^2, \quad (\text{B.1})$$

where β is a geometrical factor which depends on the geometry of the modes. Approximating the source condensate in momentum space by a Gaussian $\propto \exp[-x^2/(2\sigma_x^2) - (y^2 + z^2)/(2\sigma_{y,z}^2)]$, one has $\beta = (2\pi)^{3/2}$.

The number of scattering modes N_m can in turn be estimated from knowledge of the total volume of the scattering shell V ,

$$N_m = \frac{V}{V_m}, \quad (\text{B.2})$$

where the volume V is determined from the value of the width of the scattering shell δk :

$$\begin{aligned} V &= \int d^3\mathbf{k} \exp[-(k - k_r)^2/(2\delta k^2)] \\ &\simeq 4\pi \sqrt{2\pi} k_r^2 \delta k, \end{aligned} \quad (\text{B.3})$$

for $\delta k \ll k_r$. If we apply this estimate to the results of the main numerical example (see section 5.1), we find $N_m \simeq 26\,400$. As $N_{sc} = 1750$, this implies an occupation number per mode of $N_{sc}/N_m \simeq 0.066$. Such an estimate confirms that the system is indeed in the spontaneous regime and that bosonic stimulation effects are negligible.

The simple model of [16] for the BB correlation predicts that its height is given by

$$g_{BB}^{(2)}(0) = 1 + N_m/N_{sc}. \quad (\text{B.4})$$

Using the above estimate of N_m and the actual value of N_{sc} found from the numerical simulations, we obtain that the height of the BB correlation peak should be approximately given by ~ 16 . This compares favorably with the actual numerical result of 10.2. Similarly, we obtain the BB correlation peak of: ~ 62 in the example with the shorter collision time (compare with the numerical result of 36.6); ~ 18 in the example with the smaller collision velocity (compare with 10); and ~ 70 in the example with the smaller scattering length (compare with 50).

Appendix C. Width of the s-wave scattering sphere in the undepleted ‘pump’ approximation

To estimate the width of the halo of scattered atoms beyond the spontaneous regime we use the analytic solutions for a uniform system in the so-called undepleted ‘pump’ approximation in which the number of atoms in the colliding condensates are assumed constant. This approximation is applicable to short collision times. Nevertheless, it formally describes the regime of stimulated scattering and can be used to estimate the width of the s-wave scattering sphere as we show here.

The problem of BEC collisions in the undepleted ‘pump’ approximation was studied in [30]; the solutions for the momentum distribution of the s-wave scattered atoms are formally equivalent to those obtained for dissociation of a BEC of molecular dimers in the undepleted molecular condensate approximation [14, 31]. For a uniform system with periodic boundary conditions, one has the following analytic solution for momentum mode occupation numbers:

$$n_{\mathbf{k}}(t) = \frac{\bar{g}^2}{\bar{g}^2 - \Delta_k^2} \sinh^2 \left(\sqrt{\bar{g}^2 - \Delta_k^2} t \right). \quad (\text{C.1})$$

Here, the constant \bar{g} is given by

$$\bar{g} = 2U_0\rho_0 = \frac{8\pi\hbar a_{00}\rho_0}{m}, \quad (\text{C.2})$$

where $U_0 = 4\pi\hbar a_{00}/m$ corresponds to the coupling constant g/\hbar of [30], and we note that the results of [30] contain typographical errors and have to be corrected as follows [45]: given the Hamiltonian of (1), with $g = 4\pi\hbar^2 a/m$, the coupling g in (2), (7), (9) and (10), as well as in the definition of $\Delta(p)$ after (9), should be replaced by $2g$. In the problem of molecular dissociation, the constant \bar{g} corresponds to $\bar{g} = \chi\sqrt{\rho_0}$ [14], where χ is the atom–molecule coupling and ρ_0 is the molecular BEC density.

The parameter Δ_k in equation (C.1) corresponds to the energy offset from the resonance condition

$$\hbar\Delta_k \equiv \frac{\hbar^2 k^2}{2m} - \frac{\hbar^2 k_r^2}{2m}, \quad (\text{C.3})$$

where $\hbar k_r$ is the collision momentum; in molecular dissociation, $\hbar^2 k_r^2/m$ corresponds to the effective dissociation energy $2\hbar|\Delta_{\text{eff}}|$, using the notation of [14].

From equation (C.1), we see that modes with $\bar{g}^2 - \Delta_k^2 > 0$ experience Bose enhancement and grow exponentially with time, whereas the modes with $\bar{g}^2 - \Delta_k^2 < 0$ oscillate at the spontaneous noise level. The absolute momenta of the exponentially growing modes lie near the resonant momentum $\hbar k_r$, and therefore we can use the condition $\bar{g}^2 - \Delta_k^2 = 0$ to define the approximate width of the s-wave scattering sphere. First, we write $k = k_r + \Delta k$ and assume for simplicity that k_r is large enough so that $\Delta k \ll k_r$. Then the condition $\bar{g}^2 - \Delta_k^2 = 0$ can be approximated by

$$1 - \left(\frac{\hbar k_r \Delta k}{m\bar{g}} \right)^2 \simeq 0. \quad (\text{C.4})$$

This can be solved for Δk and used to define the width $\delta k = \Delta k/2$ of the s-wave scattering sphere as

$$\frac{\delta k}{k_r} \simeq \frac{m\bar{g}}{2\hbar k_r^2} = \frac{4\pi a_{00}\rho_0}{k_r^2}. \quad (\text{C.5})$$

The reason for defining it as half of Δk is to make δk closer in definition to the half-width at half maximum and to the rms width around k_r .

The above simple analytic estimate (C.5) gives $\delta k/k_r \simeq 0.05$ for the present ${}^4\text{He}^*$ parameters. For comparison, the actual width of the analytic result (C.1) varies between $\delta k/k_r \simeq 0.12$ and $\delta k/k_r \simeq 0.027$ for durations between $\bar{g}t = 1$ and $\bar{g}t = 7$, corresponding, respectively, to $t \simeq 20 \mu\text{s}$ and $t \simeq 140 \mu\text{s}$ in the present ${}^4\text{He}^*$ example.

Appendix D. Positive- P simulation parameters

The positive- P simulations in our main numerical example of section 5 are performed on a computational lattice with $1400 \times 50 \times 70$ points in the (x, y, z) -directions, respectively. The length of the quantization box along each dimension is $L_x = 252 \mu\text{m}$, $L_y = 20.52 \mu\text{m}$ and $L_z = 30.76 \mu\text{m}$. The computational lattice in momentum space is reciprocal to the position space lattice and has the lattice spacing of $\Delta k_i = 2\pi/L_i$, giving $\Delta k_x = 2.49 \times 10^4 \text{m}^{-1}$,

Bibliography

- [1] A. A. MICHELSON and E. MORLEY. “On the relative motion of the earth and the luminiferous ether”. *American Journal of Science*, **34** 333 (1887)
- [2] A. EINSTEIN. “Über die Entwicklung unserer Anschauungen über das Wesen und die Konstitution der Strahlung (The development of our views on the composition and essence of radiation)”. *Phys. Z.*, **10** 817 (1909)
- [3] M. BORN and E. WOLF. *Principles of Optics* (Cambridge University Press, 2005)
- [4] M. PLANCK. “The genesis and present state of development of the quantum theory. Nobel lecture” (1918). <http://nobelprize.org>
- [5] M. FOX. *Quantum Optics. An introduction* (Oxford Master Series in Physics, 2006)
- [6] R. H. BROWN and R. Q. TWISS. “Correlation between photons in two coherent beams of light”. *Nature*, **177** 27 (1956)
- [7] E. M. PURCELL. “The question of correlation between photons in coherent light rays”. *Nature*, **178** 1449 (1956)
- [8] R. J. J. GLAUBER. “The quantum theory of optical coherence”. *Phys. Rev.*, **130** 2529 (1963)
- [9] R. J. GLAUBER. “Nobel lecture: One hundred years of light quanta”. *Rev. Mod. Phys.*, **78** 1267 (2006)
- [10] H. J. KIMBLE, M. DAGENAIS and L. MANDEL. “Photon antibunching in resonance fluorescence”. *Phys. Rev. Lett.*, **39** 691 (1977)
- [11] A. EINSTEIN, B. PODOLSKY and N. ROSEN. “Can quantum-mechanical description of physical reality be considered complete?” *Phys. Rev.*, **47** 777 (1935)
- [12] E. SCHRÖDINGER. “Discussion on probability relations between separated systems”. *Proc. Camb. Phil. Soc.*, **31** 555 (1935)

- [13] N. BOHR. “Can quantum-mechanical description of physical reality be considered complete?” *Phys. Rev.*, **48** 696 (1935)
- [14] J. S. BELL. “On the Einstein-Podolsky-Rosen paradox”. *Phys.*, **1** 195 (1964)
- [15] D. F. WALLS and G. J. MILBURN. *Quantum Optics* (Springer, 2008), 2nd edition
- [16] S. CHU. “Nobel lecture: The manipulation of neutral particles”. *Rev. Mod. Phys.*, **70** 685 (1998)
- [17] C. N. COHEN-TANNOUDJI. “Nobel lecture: Manipulating atoms with photons”. *Rev. Mod. Phys.*, **70** 707 (1998)
- [18] W. D. PHILLIPS. “Nobel lecture: Laser cooling and trapping of neutral atoms”. *Rev. Mod. Phys.*, **70** 721 (1998)
- [19] R. BLATT and D. WINELAND. “Entangled states of trapped atomic ions”. *Nature*, **453** 1008 (2008)
- [20] J. I. CIRAC and P. ZOLLER. “Quantum computations with cold trapped ions”. *Phys. Rev. Lett.*, **74** 4091 (1995)
- [21] C. MONROE, D. M. MEEKHOF, B. E. KING, W. M. ITANO and D. J. WINELAND. “Demonstration of a fundamental quantum logic gate”. *Phys. Rev. Lett.*, **75** 4714 (1995)
- [22] H. HÄFFNER, C. ROOS and B. R. “Quantum computing with trapped ions”. *Phys. Rep.*, **469** 155 (2008)
- [23] M. H. ANDERSON, J. R. ENSHER, M. R. MATTHEWS, C. E. WIEMAN and E. A. CORNELL. “Observation of Bose-Einstein condensation in a dilute atomic vapor”. *Science*, **269** 198 (1995)
- [24] K. B. DAVIS, M. O. MEWES, M. R. ANDREWS, N. J. VAN DRUTEN, D. S. DURFEE, D. M. KURN and W. KETTERLE. “Bose-Einstein condensation in a gas of sodium atoms”. *Phys. Rev. Lett.*, **75** 3969 (1995)
- [25] C. C. BRADLEY, C. A. SACKETT, J. J. TOLLETT and R. G. HULET. “Evidence of Bose-Einstein Condensation in an atomic gas with attractive interactions”. *Phys. Rev. Lett.*, **75** 1687 (1995)
- [26] M. R. ANDREWS, C. G. TOWNSEND, H.-J. MIESNER, D. S. DURFEE, D. M. KURN and W. KETTERLE. “Observation of interference between two Bose condensates”. *Science*, **275** 637 (1997)
- [27] M. KÖHL, T. W. HÄNSCH and T. ESSLINGER. “Measuring the temporal coherence of an atom laser beam”. *Phys. Rev. Lett.*, **87** 160404 (2001)

-
- [28] M.-O. MEWES, M. R. ANDREWS, D. M. KURN, D. S. DURFEE, C. G. TOWNSEND and W. KETTERLE. “Output coupler for Bose-Einstein condensed atoms”. *Phys. Rev. Lett.*, **78** 582 (1997)
- [29] M. KOZUMA, L. DENG, E. W. HAGLEY, J. WEN, R. LUTWAK, K. HELMERSON, S. L. ROLSTON and W. D. PHILLIPS. “Coherent splitting of Bose-Einstein condensed atoms with optically induced bragg diffraction”. *Phys. Rev. Lett.*, **82** 871 (1999)
- [30] A. D. CRONIN, J. SCHMIEDMAYER and D. PRITCHARD. “Atom interferometers”. *arXiv:0712.3703* (2009)
- [31] B. DEMARCO and D. S. JIN. “Onset of Fermi degeneracy in a trapped atomic gas”. *Science*, **285** 1703 (1999)
- [32] F. SCHRECK, L. KHAYKOVICH, K. L. CORWIN, G. FERRARI, T. BOURDEL, J. CUBIZOLLES and C. SALOMON. “Quasipure Bose-Einstein condensate immersed in a Fermi sea”. *Phys. Rev. Lett.*, **87** 080403 (2001)
- [33] A. G. TRUSCOTT, K. E. STRECKER, W. I. MCALEXANDER, G. B. PARTRIDGE and R. G. HULET. “Observation of fermi pressure in a gas of trapped atoms”. *Science*, **291** 2570 (2001)
- [34] L. DENG, E. W. HAGLEY, J. WEN, M. TRIPPENBACH, Y. BAND, P. S. JULIENNE, J. E. SIMSARIAN, K. HELMERSON, S. L. ROLSTON and W. D. PHILLIPS. “Four-wave mixing with matter waves”. *Nature*, **398** 218 (1999)
- [35] J. M. VOGELS, K. XU and W. KETTERLE. “Generation of macroscopic pair-correlated atomic beams by four-wave mixing in Bose-Einstein condensates”. *Phys. Rev. Lett.*, **89** 020401 (2002)
- [36] J. M. VOGELS, J. K. CHIN and W. KETTERLE. “Coherent collisions between Bose-Einstein condensates”. *Phys. Rev. Lett.*, **90** 030403 (2003)
- [37] M. GREINER, C. A. REGAL, J. T. STEWART and D. S. JIN. “Probing pair-correlated fermionic atoms through correlations in atom shot noise”. *Phys. Rev. Lett.*, **94** 110401 (2005)
- [38] A. PERRIN, H. CHANG, V. KRACHMALNICOFF, M. SCHELLEKENS, D. BOIRON, A. ASPECT and C. I. WESTBROOK. “Observation of atom pairs in spontaneous four-wave mixing of two colliding Bose-Einstein condensates”. *Phys. Rev. Lett.*, **99** 150405 (2007)
- [39] A. ROBERT, O. SIRJEAN, A. BROWAEYS, J. POUPARD, S. NOWAK, D. BOIRON, C. I. WESTBROOK and A. ASPECT. “A Bose-Einstein condensate of metastable atoms”. *Science*, **292** 461 (2001)

- [40] M. SCHELLEKENS, R. HOPPELER, A. PERRIN, J. V. GOMES, D. BOIRON, A. ASPECT and C. I. WESTBROOK. “Hanbury Brown Twiss effect for ultra-cold quantum gases”. *Science*, **310** 648 (2005)
- [41] J. M. MCNAMARA, T. JELTES, A. S. TYCHKOV, W. HOGERVORST and W. VASSEN. “Degenerate bose-fermi mixture of metastable atoms”. *Physical Review Letters*, **97** 080404 (2006)
- [42] T. JELTES, J. M. MCNAMARA, W. HOGERVORST, W. VASSEN, V. KRACHMALNICOFF, M. SCHELLEKENS, A. PERRIN, H. CHANG, D. BOIRON, A. ASPECT and C. I. WESTBROOK. “Comparison of the Hanbury Brown-Twiss effect for bosons and fermions”. *Nature*, **445** 402 (2007)
- [43] D. C. BURNHAM and D. L. WEINBERG. “Observation of simultaneity in parametric production of optical photon pairs”. *Phys. Rev. Lett.*, **25** 84 (1970)
- [44] M. SCHELLEKENS. *L’effet Hanbury Brown et Twiss pour les atoms froids*. Ph.D. thesis, Université Paris-Sud (2007)
- [45] J. V. GOMES. *Thermométrie et propriétés de cohérence d’un gaz quantique ultra-froid d’hélium métastable*. Ph.D. thesis, Université Paris-Sud (2007)
- [46] M. O. SCULLY and M. S. ZUBAIRY. *Quantum Optics* (Cambridge University Press, 2006)
- [47] R. H. BROWN and R. Q. TWISS. “A new type of interferometer for use in radio astronomy”. *Phil. Mag.*, **45** 663 (1954)
- [48] G. BAYM. “The physics of Hanbury Brown Twiss intensity interferometry: from stars to nuclear collisions”. *Acta Physica Polonica B*, **29** 1839 (1998)
- [49] R. H. BROWN. *Boffin* (Adam Hilger, Bristol, 1991)
- [50] R. H. BROWN. *The Intensity Interferometer* (Taylor & Francis LTD, London, 1974)
- [51] W. D. OLIVER, J. KIM, R. C. LIU and Y. YAMAMOTO. “Hanbury Brown and Twiss-type experiment with electrons”. *Science*, **284** 299 (1999)
- [52] M. HENNY, S. OBERHOLZER, C. STRUNK, T. HEINZEL, K. ENSSLIN, M. HOLLAND and C. SCHÖNENBERGER. “The fermionic Hanbury Brown and Twiss experiment”. *Science*, **284** 296 (1999)
- [53] H. KIESEL, A. RENZ and F. HASSELBACH. “Observation of Hanbury Brown-Twiss anticorrelations for free electrons”. *Nature*, **418** 392 (2002)
- [54] M. IANNUZZI, A. ORECCHINI, F. SACCHETTI, P. FACCHI and S. PASCAZIO. “Direct experimental evidence of free-fermion antibunching”. *Physical Review Letters*, **96** 080402 (2006)

-
- [55] T. ROM, T. BEST, D. VAN OOSTEN, U. SCHNEIDER, S. FÖLLING, B. PAREDES and I. BLOCH. “Free fermion antibunching in a degenerate atomic Fermi gas released from an optical lattice”. *Nature*, **444** 733 (2006)
- [56] M. BÜTTIKER. “Bunches of photons–antibunches of electrons”. *Science*, **284** 275 (1999)
- [57] S. OBERHOLZER, M. HENNY, C. STRUNK, C. SCHÖNENBERGER, T. HEINZEL, K. ENSSLIN and M. HOLLAND. “The Hanbury Brown and Twiss experiment with fermions”. *Physica E: Low-dimensional Systems and Nanostructures*, **6** 314 (2000)
- [58] J. C. H. SPENCE. “Spaced-out electrons”. *Nature*, **418** 377 (2002)
- [59] S. FÖLLING, F. GERBIER, A. WIDERA, O. MANDEL, T. GERICKE and I. BLOCH. “Spatial quantum noise interferometry in expanding ultracold atom clouds”. *Nature*, **434** 481 (2005)
- [60] E. ALTMAN, E. DEMLER and M. D. LUKIN. “Probing many-body states of ultracold atoms via noise correlations”. *Phys. Rev. A*, **70** 013603 (2004)
- [61] W. H. LOUISELL. *Quantum Statistical Properties of Radiation* (Wiley, 1973)
- [62] J. V. GOMES, A. PERRIN, M. SCHELLEKENS, D. BOIRON, C. I. WESTBROOK and M. BELSLEY. “Theory for a Hanbury Brown Twiss experiment with a ballistically expanding cloud of cold atoms”. *Phys. Rev. A*, **74** 053607 (2006)
- [63] A. S. TYCHKOV, T. JELTES, J. M. MCNAMARA, P. J. J. TOL, N. HERSCHBACH, W. HOGERVORST and W. VASSEN. “Metastable helium Bose-Einstein condensate with a large number of atoms”. *Phys. Rev. A*, **73R** 031603 (2006)
- [64] P. J. J. TOL, N. HERSCHBACH, E. A. HESSELS, W. HOGERVORST and W. VASSEN. “Large numbers of cold metastable helium atoms in a magneto-optical trap”. *Phys. Rev. A*, **60R** 761 (1999)
- [65] G. V. SHLYAPNIKOV, J. T. M. WALRAVEN, U. M. RAHMANOV and M. W. REYNOLDS. “Decay kinetics and Bose condensation in a gas of spin-polarized triplet helium”. *Phys. Rev. Lett.*, **73** 3247 (1994)
- [66] O. SIRJEAN, S. SEIDELIN, J. V. GOMES, D. BOIRON, C. I. WESTBROOK, A. ASPECT and G. V. SHLYAPNIKOV. “Ionization rates in a Bose-Einstein condensate of metastable helium”. *Phys. Rev. Lett.*, **89** 220406 (2002)
- [67] C. J. MYATT, E. A. BURT, R. W. GHRIST, E. A. CORNELL and C. E. WIEMAN. “Production of two overlapping Bose-Einstein condensates by sympathetic cooling”. *Phys. Rev. Lett.*, **78** 586 (1997)

- [68] M. PRZYBYTEK and B. JEZIORSKI. “Bounds for the scattering length of spin-polarized helium from high-accuracy electronic structure calculations”. *J. Chem. Phys.*, **123** 134315 (2005)
- [69] P. O. FEDICHEV, M. W. REYNOLDS and G. V. SHLYAPNIKOV. “Three-body recombination of ultracold atoms to a weakly bound s level”. *Phys. Rev. Lett.*, **77** 2921 (1996)
- [70] V. KRACHMALNICOFF. *Spettroscopia di precisione dell³He: verso una determinazione della struttura iperfine e dello shift isotopico*. Master’s thesis, Università degli Studi di Firenze degli Studi di Firenze (2005)
- [71] T. JELTES. *Quantum Statistical effects in ultracold gases of metastable helium*. Ph.D. thesis, Vrije Universiteit, Amsterdam (2008)
- [72] N. VANSTEENKISTE, C. GERZ, R. KAISER, L. HOLLBERG, C. SALOMON and A. ASPECT. “A frequency-stabilized LNA laser at $1.083\mu\text{m}$: application to the manipulation of ^4He atoms”. *J. Phys. II*, **1** 1407 (1991)
- [73] W. ROOIJAKKERS, W. HOGERVORST and W. VASSEN. “An intense collimated beam of metastable helium atoms by two-dimensional laser cooling”. *Opt. Comm.*, **123** 321 (1996)
- [74] A. S. TYCHKOV. *Bose-Einstein condensation of metastable helium atoms*. Ph.D. thesis, Vrije Universiteit, Amsterdam (2008)
- [75] A. BROWAEYS. *Piégeage magnétique d’un gaz d’Hélium métastable : vers la condensation de Bose-Einstein*. Ph.D. thesis, Université Paris-Sud (2000)
- [76] R. STAS. *Trapping fermionic and bosonic helium atoms*. Ph.D. thesis, Vrije Universiteit, Amsterdam (2005)
- [77] T. BERGEMAN, G. EREZ and H. J. METCALF. “Magnetostatic trapping fields for neutral atoms”. *Phys. Rev. A*, **35** 1535 (1987)
- [78] S. SEIDELIN. *Collisions dans un gaz d’hélium métastable au voisinage de la dégénérescence quantique*. Ph.D. thesis, Université Paris-Sud (2004)
- [79] P. O. SCHMIDT, S. HENSLER, J. WERNER, T. BINHAMMER, A. GÖRLITZ and T. PFAU. “Doppler cooling of an optically dense cloud of magnetically trapped atoms”. *J. Opt. Soc. Am. B*, **20** 960 (2003)
- [80] W. KETTERLE, D. S. DURFEE and D. M. STAMPER-KURN. “Making, probing and understanding bose-einstein condensates”. In M. INGUSCIO, S. STRINGARI and C. WIEMAN, editors, “Bose-Einstein condensation in atomic gases, Proceedings of the International School of Physics ”Enrico Fermi”, Course CXL”, 67–176 (IOS Press, Amsterdam, 1999)

-
- [81] S. SEIDELIN, J. V. GOMES, R. HOPPELER, O. SIRJEAN, D. BOIRON, A. ASPECT and C. I. WESTBROOK. “Getting the elastic scattering length by observing inelastic collisions in ultracold metastable helium atoms”. *Phys. Rev. Lett.*, **93** 090409 (2004)
- [82] A. PERRIN. *Observation de paires d’atomes corrélés au travers de la collision de deux condensats de Bose-Einstein*. Ph.D. thesis, Université Pierre et Marie Curie (2007)
- [83] F. SCHRECK. *Mixtures of ultracold gases: Fermi sea and Bose-Einstein condensate of Lithium isotopes*. Ph.D. thesis, Université Pierre et Marie Curie - Paris VI (2002)
- [84] A. PERRIN, C. M. SAVAGE, D. BOIRON, V. KRACHMALNICOFF, C. I. WESTBROOK and K. V. KHERUNTSYAN. “Atomic four-wave mixing via condensate collisions”. *New. J. Phys.*, **10** 045021 (2008)
- [85] J. CHWEDŃCZUK, P. ZIŃ, M. TRIPPENBACH, A. PERRIN, V. LEUNG, D. BOIRON and C. I. WESTBROOK. “Pair correlations of scattered atoms from two colliding Bose-Einstein condensates: Perturbative approach”. *Phys. Rev. A*, **78** 053605 (2008)
- [86] K. MÖLMER, A. PERRIN, V. KRACHMALNICOFF, V. LEUNG, D. BOIRON, A. ASPECT and C. I. WESTBROOK. “Hanbury Brown and Twiss correlations in atoms scattered from colliding condensates”. *Phys. Rev. A*, **77** 033601 (2008)
- [87] S. E. HARRIS, M. K. OSHMAN and R. L. BYER. “Observation of tunable optical parametric fluorescence”. *Phys. Rev. Lett.*, **18** 732 (1967)
- [88] S. FRIBERG, C. K. HONG and L. MANDEL. “Measurement of time delays in the parametric production of photon pairs”. *Phys. Rev. Lett.*, **54** 2011 (1985)
- [89] B. R. MOLLOY. “Photon correlations in the parametric frequency splitting of light”. *Phys. Rev. A*, **8** 2684 (1973)
- [90] M. D. REID and D. F. WALLS. “Violations of classical inequalities in quantum optics”. *Phys. Rev. A*, **34** 1260 (1986)
- [91] X. ZOU, L. WANG and L. MANDEL. “Violation of classical probability in parametric down-conversion”. *Opt. Comm.*, **84** 351 (1991)
- [92] L.-A. WU, H. J. KIMBLE, J. L. HALL and H. WU. “Generation of squeezed states by parametric down conversion”. *Phys. Rev. Lett.*, **57** 2520 (1986)
- [93] R. PASCHOTTA, M. COLLETT, P. KÜRZ, K. FIEDLER, H. A. BACHOR and J. MLYNEK. “Bright squeezed light from a singly resonant frequency doubler”. *Phys. Rev. Lett.*, **72** 3807 (1994)

- [94] S. REYNAUD, C. FABRE and E. GIACOBINO. “Quantum fluctuations in a two-mode parametric oscillator”. *J. Opt. Soc. Am. B*, **4** 1520 (1987)
- [95] A. HEIDMANN, R. J. HOROWICZ, S. REYNAUD, E. GIACOBINO, C. FABRE and G. CAMY. “Observation of quantum noise reduction on twin laser beams”. *Phys. Rev. Lett.*, **59** 2555 (1987)
- [96] O. AYTÜR and P. KUMAR. “Pulsed twin beams of light”. *Phys. Rev. Lett.*, **65** 1551 (1990)
- [97] J. GAO, F. CUI, C. XUE, C. XIE and P. KUNCHI. “Generation and application of twin beams from an optical parametric oscillator including an α -cut KTP crystal”. *Opt. Lett.*, **23** 870 (1998)
- [98] C. K. HONG, Z. Y. OU and L. MANDEL. “Measurement of subpicosecond time intervals between two photons by interference”. *Phys. Rev. Lett.*, **59** 2044 (1987)
- [99] A. ASPECT, P. GRANGIER and G. ROGER. “Experimental tests of realistic local theories via Bell’s theorem”. *Phys. Rev. Lett.*, **47** 460 (1981)
- [100] A. ASPECT, P. GRANGIER and G. ROGER. “Experimental realization of Einstein-Podolsky-Rosen-Bohm gedankenexperiment: A new violation of Bell’s inequalities”. *Phys. Rev. Lett.*, **49** 91 (1982)
- [101] A. ASPECT, J. DALIBARD and G. ROGER. “Experimental test of Bell’s inequalities using time- varying analyzers”. *Phys. Rev. Lett.*, **49** 1804 (1982)
- [102] P. G. KWIAT, K. MATTLE, H. WEINFURTER, A. ZEILINGER, A. V. SERGIENKO and Y. SHIH. “New high-intensity source of polarization-entangled photon pairs”. *Phys. Rev. Lett.*, **75** 4337 (1995)
- [103] W. TITTEL, J. BRENDEL, H. ZBINDEN and N. GISIN. “Violation of Bell inequalities by photons more than 10 km apart”. *Phys. Rev. Lett.*, **81** 3563 (1998)
- [104] G. WEIHS, T. JENNEWEIN, C. SIMON, H. WEINFURTER and A. ZEILINGER. “Violation of Bell’s inequality under strict Einstein locality conditions”. *Phys. Rev. Lett.*, **81** 5039 (1998)
- [105] K. V. KHERUNTSYAN and P. D. DRUMMOND. “Quantum correlated twin atomic beams via photodissociation of a molecular Bose-Einstein condensate”. *Phys. Rev. A*, **66** 031602 (2002)
- [106] C. M. SAVAGE, P. E. SCHWENN and K. V. KHERUNTSYAN. “First-principles quantum simulations of dissociation of molecular condensates: Atom correlations in momentum space”. *Phys. Rev. A*, **74** 033620 (2006)
- [107] C. M. SAVAGE and K. V. KHERUNTSYAN. “Spatial pair correlations of atoms in molecular dissociation”. *Phys. Rev. Lett.*, **99** 220404 (2007)

-
- [108] M. ÖGREN and K. V. KHERUNTSYAN. “Atom-atom correlations and relative number squeezing in dissociation of spatially inhomogeneous molecular condensates”. *Phys. Rev. A*, **78** 011602 (2008)
- [109] P. ZIŃ, J. CHWEDEŃCZUK and M. TRIPPENBACH. “Elastic scattering losses from colliding Bose-Einstein condensates”. *Phys. Rev. A*, **73** 033602 (2006)
- [110] R. BACH, M. TRIPPENBACH and K. RZAŻEWSKI. “Spontaneous emission of atoms via collisions of Bose-Einstein condensates”. *Phys. Rev. A*, **65** 063605 (2002)
- [111] M. SARGENT III, D. A. HOLM and M. S. ZUBAIRY. “Quantum theory of multiwave mixing. I. general formalism”. *Phys. Rev. A*, **31** 3112 (1985)
- [112] N. A. ANSARI and M. S. ZUBAIRY. “Violation of Cauchy-Schwarz and Bell’s inequalities in four-wave mixing”. *Phys. Rev. A*, **38** 2380 (1988)
- [113] Y. B. BAND, M. TRIPPENBACH, J. P. BURKE and P. S. JULIENNE. “Elastic scattering loss of atoms from colliding Bose-Einstein condensate wave packets”. *Phys. Rev. Lett.*, **84** 5462 (2000)
- [114] K. V. KHERUNTSYAN, M. K. OLSEN and P. D. DRUMMOND. “Einstein-Podolsky-Rosen correlations via dissociation of a molecular Bose-Einstein condensate”. *Phys. Rev. Lett.*, **95** 150405 (2005)
- [115] K. V. KHERUNTSYAN. “Matter-wave amplification and phase conjugation via stimulated dissociation of a molecular Bose-Einstein condensate”. *Phys. Rev. A*, **71** 053609 (2005)
- [116] P. D. DRUMMOND, P. DEUAR and J. F. CORNEY. “Quantum many-body simulations using gaussian phase-space representations”. *arXiv:quant-ph/0608247* (2006)
- [117] P. DEUAR and P. D. DRUMMOND. “Correlations in a BEC collision: First-principles quantum dynamics with 150 000 atoms”. *Phys. Rev. Lett.*, **98** 120402 (2007)
- [118] L.-M. DUAN, A. SØRENSEN, J. I. CIRAC and P. ZOLLER. “Squeezing and entanglement of atomic beams”. *Phys. Rev. Lett.*, **85** 3991 (2000)
- [119] S. INOUE, A. P. CHIKKATUR, D. M. STAMPER-KURN, J. STENGER, D. E. PRITCHARD and W. KETTERLE. “Superradiant Rayleigh scattering from a Bose-Einstein condensate”. *Science*, **285** 571 (1999)
- [120] H. PU, W. ZHANG and P. MEYSTRE. “Wave mixing of optical pulses and Bose-Einstein condensates”. *Phys. Rev. Lett.*, **91** 150407 (2003)
- [121] M. G. MOORE and P. MEYSTRE. “Theory of superradiant scattering of laser light from Bose-Einstein condensates”. *Phys. Rev. Lett.*, **83** 5202 (1999)

- [122] H. PU and P. MEYSTRE. “Creating macroscopic atomic Einstein-Podolsky-Rosen states from Bose-Einstein condensates”. *Phys. Rev. Lett.*, **85** 3987 (2000)
- [123] P. DEUAR. private communication (2009)
- [124] Y. CASTIN and R. DUM. “Bose-Einstein condensates in time dependent traps”. *Phys. Rev. Lett.*, **77** 5315 (1996)
- [125] J. G. RARITY and P. R. TAPSTER. “Experimental violation of Bell’s inequality based on phase and momentum”. *Phys. Rev. Lett.*, **64** 2495 (1990)
- [126] K. M. HILLIGSÖE and K. MÖLMER. “Phase-matched four wave mixing and quantum beam splitting of matter waves in a periodic potential”. *Phys. Rev. A*, **71** 041602 (2005)
- [127] G. K. CAMPBELL, J. MUN, M. BOYD, E. W. STREED, W. KETTERLE and D. E. PRITCHARD. “Parametric amplification of scattered atom pairs”. *Phys. Rev. Lett.*, **96** 020406 (2006)
- [128] A. J. FERRIS, M. K. OLSEN and M. K. DAVIS. “Atomic entanglement generation and detection via degenerate four-wave-mixing of a Bose-Einstein condensate in an optical lattice”. *arXiv:0902.1793* (2009)
- [129] W. KETTERLE and S. INOUE. “Does matter wave amplification work for fermions?” *Phys. Rev. Lett.*, **86** 4203 (2001)
- [130] M. G. MOORE and P. MEYSTRE. “Atomic four-wave mixing: Fermions versus bosons”. *Phys. Rev. Lett.*, **86** 4199 (2001)
- [131] T. KINOSHITA, T. WENGER and D. S. WEISS. “Local pair correlations in one-dimensional Bose gases”. *Phys. Rev. Lett.*, **95** 190406 (2005)
- [132] B. L. TOLRA, K. M. O’HARA, J. H. HUCKANS, W. D. PHILLIPS, S. L. ROLSTON and J. V. PORTO. “Observation of reduced three-body recombination in a correlated 1D degenerate Bose gas”. *Phys. Rev. Lett.*, **92** 190401 (2004)
- [133] J. ESTEVE, C. GROSS, A. WELLER, S. GIOVANAZZI and M. K. OBERTHALER. “Squeezing and entanglement in a Bose-Einstein condensate”. *Nature*, **455** 1216 (2008)
- [134] K. D. NELSON, X. LI and D. S. S. WEISS. “Imaging single atoms in a three-dimensional array”. *Nat. Phys.*, **3** 556 (2007)
- [135] T. GERICKE, P. WÜRTZ, D. REITZ, T. LANGEN and H. OTT. “High-resolution scanning electron microscopy of an ultracold quantum gas”. *Nat. Phys.*, **4** 949 (2008)

- [136] R. BÜCKER, A. PERRIN, S. MANZ, T. BETZ, C. KOLLER, T. PLISSON, J. ROTTMANN, T. SCHUMM and J. SCHMIEDMAYER. “Single-atom-sensitive fluorescence imaging of ultracold quantum gases”. *arXiv:0907.0674* (2009)
- [137] B. DECONIHOUT, F. VURPILLOT, M. BOUET and L. RENAUD. “Improved ion detection efficiency of microchannel plate detectors”. *Rev. Sci. Instr.*, **73** 1734 (2002)
- [138] M. BONNEAU. *Optique atomique quantique: amélioration de l’efficacité de détection des atomes et caractérisation d’une diode laser en cavité étendue*. Master’s thesis, Université Paris-Sud (2008)

RESUME

Cette thèse présente deux expériences sur des gaz ultrafroids d'hélium métastable qui constituent l'extension, à des ondes de matière, d'expériences fondamentales en optique quantique. Le succès de ces expériences repose sur l'utilisation d'un détecteur d'atomes uniques capable de reconstruire la position des atomes en trois dimensions.

Dans la première expérience nous avons comparé, sur le même dispositif expérimental, la fonction de corrélation à deux corps des atomes appartenant à un nuage froid de fermions identiques à celle d'un nuage froid de bosons identiques à la même température. Comme bosons et fermions suivent deux statistiques quantiques différentes, les deux fonctions de corrélation sont différentes : les bosons ont tendance à arriver groupés sur le détecteur, alors que les fermions ont tendance à arriver dégroupés, à cause du principe d'exclusion de Pauli.

Dans la deuxième expérience nous avons étudié la corrélation entre paires d'atomes bosoniques générées dans la collision de deux condensats de Bose-Einstein. La mesure de la fonction de corrélation nous a permis de démontrer que les atomes d'impulsion opposée, dans le référentiel du centre de masse, sont corrélés par paires. De plus l'observation d'une corrélation de type Hanbury Brown Twiss entre paires d'atomes diffusés dans la même direction démontre que notre système ne peut pas être interprété en termes de mécanique classique, mais que la statistique bosonique y joue un rôle important. Une nouvelle génération de cette expérience permettra de mesurer la dépendance angulaire de la population des modes atomiques diffusés et d'étudier le squeezing de la différence de population entre modes opposés.

mots-clés: atomes froids - optique atomique quantique - effet Hanbury Brown Twiss - fonction de corrélation - gaz de Fermi - condensat de Bose-Einstein - mélange à quatre ondes - galette de micro-canaux

ABSTRACT

This thesis presents two experiments on ultracold gases of metastable Helium that constitute the extension, to matter waves, of experiments that have been fundamental for the development of quantum optics. Both experiments have been realized by using a single atom detector, that allows one to reconstruct the position of the atoms in three dimensions.

In the first experiment we directly compared the two-body correlation function for a cold cloud of identical fermions and for a cold cloud of identical bosons at the same temperature issued from the same experimental apparatus. Since bosons and fermions obey different quantum statistics, the two-body correlation functions are different: identical bosons tend to be detected bunched in pairs, while identical fermions tend to antibunch because of the Pauli exclusion principle.

In the second experiment we studied the correlation between pairs of bosonic atoms generated in the collision of two Bose-Einstein condensates. The measurement of the correlation function allows us to demonstrate that atoms flying back to back in the centre of mass frame are correlated in pairs. Furthermore the observation of a Hanbury Brown Twiss correlation between atoms with collinear velocity demonstrates that our system cannot be interpreted in terms of classical mechanics, but that the bosonic statistics plays a crucial role. A new version of the experiment will allow us to measure the angular dependence of the population of the scattering modes and the number difference squeezing between two correlated modes.

keywords: cold atoms - quantum atom optics - Hanbury Brown Twiss effect - correlation function - Fermi gas - Bose-Einstein condensate - four wave mixing - micro-channel plate